Cranfield UNIVERSITY

Image Processing and Agent-Based framework for the Geolocation of Emitters

by A. Mikhalev

Supervisor:
Prof. R.F. Ormondroyd

Cranfield University
Defence College of Management and Technology
Shrivenham, Swindon, Wiltshire SN6 8LA. United Kingdom.

Department of Informatics and Sensors

PhD thesis

Abstract

The research presented in this thesis is about a task of geolocation of radio frequency emitters. In this research the problem of geolocation of non-collaborative emitter was addressed. This thesis presents the novel algorithm for the RF emitter geolocation based on the image process technique known as Hough Transform. The comparison of this algorithm with traditional approaches to geolocation showed a number of benefits, like robustness, accuracy and advanced fusion capability. The application of the Hough Transform to data fusion allowed to use the modern concepts of agent-based fusion and cluster level fusion, thus moving the solution of the problem of the geolocation to upper level of fusion hierarchy. The work on Hough Transform lead to a comparison of the Bayesian and non-Bayesian approaches in solving the task of geolocation. Exploitation of the comparison lead to the derivation of a generalized estimator. This estimator highlighted a number of mathematical functions which can be exploited for geolocation and data fusion. These functions has been tested for the purpose of data fusion in geolocation and it was found that Hough Transform is a useful alternative approach for the data fusion for geolocation of RF emitter.

Acknowledgment

I would like to express my deepest and sincere appreciation to my supervisor Professor R.F Ormondroyd for his constant encouragement, guidance and support during my Ph.D. studies. Our discussions and arguments helped greatly in refining the ideas in this thesis from their original hazy form into ones that can be considered clear and concise.

I also would like to thank Dr Nikolai Ptitsyn for his introduction of the Hough Transform for image processing.

During my research I found a number of exciting connections: first between estimation theory and image processing, then between image processing and general probability theory, then the set theory. Recently, some connections emerged from the estimation theory and the image processing to chaos and uncertainty theory. Each connection produced an exciting moment, each of them was an unexpected one. It was a great fun and entertainment, because each time trying to answer one questions a received another 10 as answer, pushing boundaries of unknown. I was enjoying my research experience under Prof. Ormondroyd supervision with fruitful criticism of Dr Evan Hughes and Dr David Salmond and it was a great adventure and entertainment. It was like climbing on the mounting and seeing more thing from the height although climbing was sometimes rough. I never thought science can such fun. I would like thank General Dynamics UK and Ministry of Defence for their financial support of the project through DTC DIF Project 12.3.2.

Contents

Chapter 1

Introduction

1.1 Motivation

The problem of geolocation has received considerable attention over the past seven decades. One of the forces defining the pursuit of the research in this area was 'The Report and Order' issued by the U.S. Federal Communications Commission (FCC) in July 1996 that requires all wireless service providers, including cellular, broadband and wide-area licensees, to provide handset location information to Emergency 911 (E-911) public safety services. Another force driving the research in this area is the requirement for 'location aware' services for third generation mobile radio (3G) [1]. The basic function of a location system is to gather information about the position of a mobile station operating in a geographical area and to process that information to form a location estimate [2]. However, location services for mobile communications tend to exploit the features of a handset or base station's waveforms that allow precise time of arrival information which these geolocation systems use. Indeed, such geolocation is often carried out entirely by multiple base stations that, as part of the wireless interface, have information about the signal strength and timing from each and every mobile station in their respective services areas. These base-stations have the necessary network interconnectivity to exchange the required data from which a position fix of a mobile station is made possible. This approach requires a collaboration between mobile and base station for position estimation and can be viewed as cooperative geolocation. However, in many applications, such *a priori* information regarding the waveform is not available.

Geolocation of a wireless communications transmitter is of vital importance in military operations. It is required for tracking military personnel and other resources to enable effective co-ordination, command, and control. Radiolocation devices (nodes) may be embedded in handheld or wearable radios carried by warfighters, they may be mounted on vehicles/aircraft, or contained in unattended sensors distributed on the battlefield. Such applications may also utilise cooperative geolocation if the assets being tracked are 'friendly'.

In other situations, the transmission may represent enemy emissions, in which

case the geolocation method forms part of the Electronic Surveillance (ES) operation within the field of electronic warfare. The work in this thesis focusses largely on non-cooperative geolocation of radio frequency (RF) emitters.

Military wireless networks may be *ad-hoc* in nature: the ability to form a robust, dynamic communication network of soldiers, vehicles/aircraft, and sensors is highly desirable. Furthermore, the propagation environment may be harsh and varied (e.g., urban canyons, inside buildings, forest/mountain, etc.) One of the objectives of this research is to develop a robust and accurate geolocation system using wireless *ad-hoc* networks, which can be formed from sensors, mounted, for example, on mobile tactical unmanned aerial vehicles (UAV), operating in non-cooperative environments [3]. Some parts of this thesis can also be applied to the task of radar geolocation.

Geolocation is also required in wireless sensor network applications for calculating sensor positions in cases where sensors do not have their own GPS (Global Positioning System) devices [4]. At the same time, geolocation will play an important role in the emerging technology called 'cognitive radio', where the knowledge of the position of an RF emitter can be exploited for smart spectrum management in both civilian and military applications. There is a potential for the proposed emitter location techniques in this important new area.

1.2 Original Contributions

The purpose of this research is to develop suitable algorithms for fast and accurate geolocation of a RF emitter using passive sensors mounted on mobile platforms, for example, on Unmanned Aerial Vehicles. The algorithms should be robust in order to deal with non-line of sight propagation and the problem of multipath propagation in the 'urban canyon' environment. The scientific challenge is that, usually, the transformation from the measurement to the position estimate is non-linear, creating problems for traditional algorithms such as the least mean square estimator. The original contributions made to the field during the research are as follows:

- A Hough Transform (HT) based algorithm has been developed for emitter geolocation, thus providing a connection from signal processing algorithms for geolocation to an image processing algorithm, using a non-Bayesian estimator;
- The Hough Transform algorithm has been evaluated using the fusion of different type of measurements (angle of arrival, time difference of arrival and frequency difference of arrival), together with higher level fusion with terrain data;
- To reduce computational overhead, three variants of the Hough Transform have been developed for this application: the Randomized Hough Transform (RHT), the Multiresolution Hough Transform (MHT) and the Hybrid Hough Transform (HHT);
- The performance of the Hough Transform based algorithm and the particle filter have been compared and this has formed the basis for a comparison of non-Bayesian and Bayesian type estimators with the Cramer-Rao Lower Bound (CRLB), which is representative of the performance of classical estimators;
- The performance of algorithms has been evaluated on common scenario in presence of model mismatch - in a way where measurements noise assumed to be Gaussian by the algorithm, but in simulation has been generated according to Gaussian, Rayleigh or Uniform distributions;
- The model mismatch was explored further by changing the underlying assumption in algorithms that measurements error have Rayleigh distribution, while the simulated measurement noise was modelled using Gaussian, Rayleigh and Uniform distributions;
- A generalized estimator has been developed, where by changing a single parameter, α, the estimator changes from a Bayesian type to a non-Bayesian type. The analysis has been carried out on the results of this estimator;
- In addition, the fusion capability of the Hough Transform has been extended to the development of the weighted fusion algorithm, which can be used to self-weight the measurements from the sensors according to their GDOP;

- Based on the weighted Hough Transform, an agent-based data fusion algorithm for emitter geolocation has been proposed, thus moving the geolocation problem to a higher level of the fusion hierarchy;
- Agent-based data fusion has been applied to an even higher level of fusion between groups of agents, thus showing the possibility of using cluster level fusion based on the Hough Transform approach to geolocation.

1.2.1 List of publications

1. A. Mikhalev and R.F. Ormondroyd, Multi-Cluster Agent-Based Emitter Geolocation using Hough Transform Data Fusion. in Proc. The 11th International Conference on Information Fusion, July 2008, Cologne, Germany
2. A. Mikhalev and R.F. Ormondroyd, Passive Emitter Geolocation using Agent-based Data Fusion of AOA, TDOA and FDOA Measurements. in Proc. The 10th International Conference on Information Fusion, July 2007, Quebec, Canada
3. A. Mikhalev and R.F. Ormondroyd, Comparison of Hough Transform and Particle Filter Methods of Emitter Geolocation using Fusion of TDOA Data, in Proc. on 4th Workshop on Positioning, Navigation and Communication 2007, Hannover, Germany
4. A. Mikhalev and R.F. Ormondroyd, Comparison of Hough Transform and Particle Filter Methods of Emitter Geolocation using Fusion of TDOA Data, in Proc. on 22 International UAV Systems Conference , May 2007, Bristol, UK
5. A. Mikhalev and R.F. Ormondroyd, Emitter Geolocation using fusion of TDOA Data with a Particle Filter, in Student Papers. The International Conference on Information Sciences, Signal Processing and its Applications February 2007, **Best Student Paper Award**. Shardjah, UAE.
6. A. Mikhalev, None Line of Site Geolocation of emitters, in Proc. The 9th International Conference Intelligent Systems And Computer Sciences, November 2006, Moscow, Russia
7. A. Mikhalev and R.F. Ormondroyd, Fusion of Sensor Data for Source Localization using the Hough Transform, in Proc. The 9th International Conference on Information Fusion, paper266, July 2006. Florence, Italy.
8. A. Mikhalev and R.F. Ormondroyd, UAV-based Non-line-of-sight geolocation of emitter, in Proc. 21 International UAV Systems Conference, April 2006, 25.1-25.9, Bristol, UK
9. A. Mikhalev and R.F. Ormondroyd,Agent-based non-line of Site Geolocation of emitters, DTC DIF Conference, September, 2004, Shrivenham, UK

1.3 The problem definition

In order to proceed further it is important to explain the differences between handset location (mobile phone tracking), target tracking, localisation and emitter geolocation. These terms are often treated as being synonymous, whereas they are quite different and require different algorithms.

Localisation is the term used when all sensors and the target are stationary, the position of the sensors is assumed to be known and these sensors are not mobile.

Geolocation is the task of obtaining a position in the Cartesian coordinates (x, y) of the RF emitter by means of appropriate measurements, which can be extracted from the radio signal using specific signal processing and hardware (also known as sensors). In this task, the target (RF emitter) is assumed to be stationary, while the sensors can be stationary or mobile - when mounted on UAVs for example. The position of the sensors is assumed to be known accurately, using GPS or other positional techniques. If the geolocation algorithm does not exploit the motion of the sensor platforms the problem is reduced to a localisation problem.

On the other hand, **target tracking** assumes that the target is moving with a known or predictable trajectory. In general, the target trajectory can be defined in terms of the transitional matrix P and thus relies on the assumption that there is an underlying transitional process that relies on the measurements and the target motion, such as the Hidden Markov Chain or Markov chain [5]. Mobile handset location and tracking is a subset of target tracking in that the Base Stations are stationary (receivers) while the mobile handset are moving [6],[7][8]. It is commonly assumed that geolocation is a subset of the target tracking.

A major problem when attempting to geolocate a ground-based emitter using low mounted sensors, as is often the case in electronic surveillance and cellphone handset location, is that radio wave propagation is very complex, generally suffering from multipath propagation due to reflection at buildings and the ground as well as scattering from objects whose dimensions are of the order of the signal wavelength (for a detailed explanation see [9]). Often, the signal arriving at the sensors is non-line-of-sight with the emitter and in some environments this poor propagation may be worsened in so-called 'urban canyons' due to the presence of straight streets lined with high-rise buildings which act as 'waveguides' to the RF signal. This, and other effects such as shadowing are assumed to provide the wireless environment between the target emitter and the surveillance receiver.

However, in an attempt to ameliorate this severe problem, the sensors can be mounted on autonomous unmanned aerial vehicles (UAV). As a result these sensors are able to move and manoeuvre, allowing different types of measurements to be taken. By raising the height of the platforms, this can often improve the radio wave propagation environment from a non-line-of-sight scattering environment to free space propagation, thereby allowing the sensor platforms to geolocate over greater distances.

Another constraint of the scenario is that while the sensors mounted on the

mobile platform are passive, the target RF emitter is not collaborative, in order to avoid an early disclosure of geolocation activity and the position of the sensor platforms and this has an impact on the type of measurements that are possible. For example, time difference of arrival (TDOA) must be used rather than time of arrival (TOA) Similarly frequency difference of arrival (FDOA) measurements must be used instead of frequency of arrival. An important part of the work described in this thesis is the use of sensor fusion to enhance the emitter position accuracy by exploiting different type of measurements.

1.4 Fundamentals of emitter location

Algorithms for emitter location rely on the underlying methods of obtaining the position estimate by transforming measurements from the signal to a position estimate. One of the first researched methods is called triangulation. In the next section, triangulation will be described briefly and a recurring problem of emitter location will be highlighted - namely the non-linearity of the transformation. Later, hyperbolic location techniques will be described followed by a brief examination of classical estimator algorithms.

1.4.1 Triangulation

Triangulation is the method of obtaining the position of the target emitter in two or more coordinates within a known coordinate framework by measuring lines of bearing from sensors located on a baseline, as shown in figure 1.1. In the absence of measurement errors, the true emitter position corresponds to the intersection of these lines of bearing. For the purposes of precisely calculating the position enemy troops on the ground (two-dimensional plane) triangulation has been used since the 17th century, as seen in figure 1.2. This principle initiated work on RF emitter geolocation in earlier years and received significant attention from mobile service operators, once the requirement for location aware services grew.

According to [10] *triangulation* is a method applied to estimate position by calculating the most likely point for the target, given the intersection of two or more lines of bearings from sensors at known locations. For passive emitter location, the line of bearing represents the Angle Of Arrival (AOA) of the waveform of the RF emitter at each sensor. Triangulation can be implemented on all varieties of platforms including aircraft, ships and ground vehicles. As pictured in figure 1.1, the true Angle of Arrival, θ_i can be written as:

$$\theta_i = \tan^{-1}\left(\frac{y - y_i}{x - x_i}\right) \tag{1.1}$$

where (x, y) is the true position of the emitter, and (x_i, y_i) with $i = 1, 2$ are the known positions of the mobile sensor platform at two time instants (for the case of single platform location) or the fixed positions of the two separate platforms. If each

sensor platform is able to measure the true AOA between itself and the emitter, θ_1 and θ_2, the target position can be obtained from the intersection of the two lines of bearing to yield:

$$x = \frac{x_1 - x_2 \cdot \frac{\tan(\theta_1)}{\tan(\theta_2)} - y_1 \cdot \tan(\theta_1) + y_2 \cdot \tan(\theta_1)}{1 - \frac{\tan(\theta_1)}{\tan(\theta_2)}} \tag{1.2}$$

and

$$y = \frac{x_1 - x_2 \cdot \frac{\tan(\theta_1)}{\tan(\theta_2)} - y_1 \cdot \tan(\theta_1) + y_2 \cdot \tan(\theta_1)}{\tan(\theta_2) - \tan(\theta_1)} - \frac{x_2}{\tan(\theta_2)} + y_2 \tag{1.3}$$

In the absence of measurement noise this can be repeated for multiple lines of bearing, and all should intersect at the same point - the true emitter position. However, in the presence of measurement noise, the intersection of erroneous lines of bearing (shown as a dashed lines in figure 1.1) gives rise to an erroneous position estimate. In this case, more than two lines of bearing are unlikely to intersect at a single point and some form of statistical estimator must be used to provide a position estimate. Appropriate processing of multiple noisy measurements provides an improved estimate of the emitter position if the measurement errors are zero mean. In the next chapter, the overview of tradition estimators algorithms, such as the Maximum Likelihood estimator and the Kalman filter will be given, and their performance evaluated.

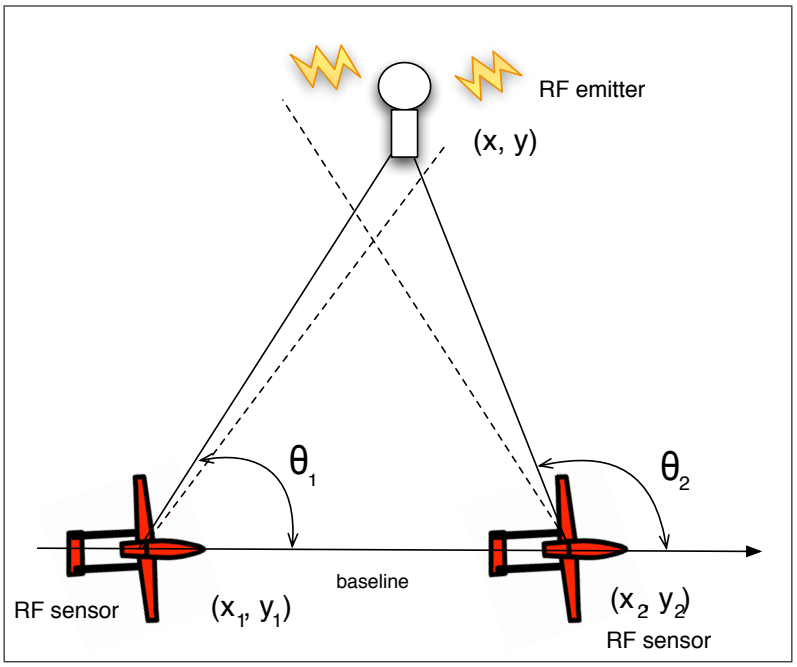

Figure 1.1: Triangulation using two AOA measurement

1.4.2 Hyperbolic location systems

Another technique that can be used for calculating the position of the RF emitter is based on processing the time of arrival (TOA)[11],[12],[13], or time-difference of

Figure 1.2: Use of triangulation instrument designed by Jost Bürgi, from Benjamin Bramin, Bericht zu M.Jobsten Burgi seligen geometricshen triangular Instruments, (Kassel, 1648)

arrival (TDOA) of the RF signal to each of the RF sensors. If the initial start time for the transmission is not known, then only the time-difference of arrival (TDOA) that the signal takes to arrive at the two sensors can be used, generally by correlating the signal received at each RF sensor using a 'sliding correlator'. This technique is often referred to as hyperbolic location as in [14], [15], [4],[16]. Hyperbolic location systems locate a transmitter by measuring the time of arrival of RF signal at three or more platforms. The measurements at the various stations are sent to a station that is designated as the master and does the processing. The arrival-time measurements at any two platforms are used to produce an arrival time difference that, in the absence of noise and interference, restricts the possible transmitter locations to lying on a hyperbola called the iso-delay curve where the time difference of arrival between the sensor platforms is the measured constant. The transmitter location is estimated from the intersections of two independently generated iso-delay hyperbolas which are determined from at least three sensor platforms for geolocation in 2-D Cartesian coordinates as shown in figure 1.3. However, in the presence of noise this method gives an error in the position estimation as the hyperbolas will not intersect at the true emitter position. In this case, multiple TDOA measurements are taken and the position of the emitter is estimated using a statistical estimator.

The hyperbolic equations for the TDOA method can be derived from the TOA method as follows: The measured time of arrival at the ith platform is:

$$t_i = t_0 + \frac{D_i}{c} + \epsilon_i \tag{1.4}$$

where c is the velocity of light, t_0 is the time the signal was transmitted, ϵ_i is the arrival time measurement error and D_i is the distance between the emitter and the platform given by:

$$D_i = \sqrt{(x_p - x_i)^2 + (y_p - y_i)^2} \tag{1.5}$$

The ith TDOA measurement between the $i$the platform and the $(i+1)$th platform is:

$$\tau = t_i - t_{i+1} = \frac{D_i - D_{i+1}}{c} + n_i, i = 1, 2, \ldots, M-1 \tag{1.6}$$

where $n_i = \epsilon_i - \epsilon_{i+1}$ is the measurement error due to the errors in measuring both times of arrival. It should be noted that $(M-1)$ TDOA measurements are generated from M TOA measurements.

As these equations are non-linear, solving them for (x, y) is not a trivial operation. Several algorithms have been proposed for this purpose having different complexities and accuracies as proposed in [15],[17],[18] and [19]. In a later section the mathematical model that is used by these algorithms, will be discussed. This will be followed by a survey of the algorithms that can be used for solving hyperbolic equations. A drawback of the TDOA method is that it requires a large bandwidth to transmit the signals to a central site [20] for TDOA processing. The provision of broadband wireless communications from UAVs to the central station is costly and limits the application of this method. The bandwidth of the link needs to be similar to the signal bandwidth of the emitter, since the accuracy of the timing measurements is inversely proportional to the signal bandwidth. A commercial and highly successful TDOA emitter geolocation system which is uses a mix of ground based and airborne sensor platform is the VERA E system, developed by the Czech company ERA [21].

If sufficient *a priori* information is provided in the signal, then the true time of arrival of the signal at each sensor can be obtained. This means that the emitter must lie on a circle of radius $r_1 = c\tau_{TOA1} = r_2 = c\tau_{TOA2}$ around sensor 1. The emitter position is the intersection of these range circles. This type of emitter location is often referred as trilateration since the range rings give the length of the sides of the triangle, rather than the bearing angles.

Frequency difference of arrival

Another technique, which can be used on its own, or frequently combined with the TDOA techniques, uses the measurement of the frequency difference of arrival (FDOA) at two remote sensors. The advantage of adding FDOA measurements is that they produce emitter location estimates whose error ellipse may lie in a different direction to the error ellipses of the other two methods. Consequently, it is possible to minimize the effect of geometric dilution of precision (GDOP) by suitable fusion of the different types of measurement data and this will be shown in later chapters. Assume that the FDOA measurement f_{d_i} between the two spatially separated receivers can be obtained, receiver 1 and receiver i using a Doppler receiver of bandwidth B. The individual Doppler shifts at r_1 and r_i are given by:

$$F_{r_1} = -\frac{f_0}{c} \frac{v_{x_{r_1}} (x - x_{r_1}) + v_{y_{r_1}} (y - y_{r_1})}{\sqrt{(x - x_{r_1})^2 + (y - y_{r_1})^2}} \tag{1.7}$$

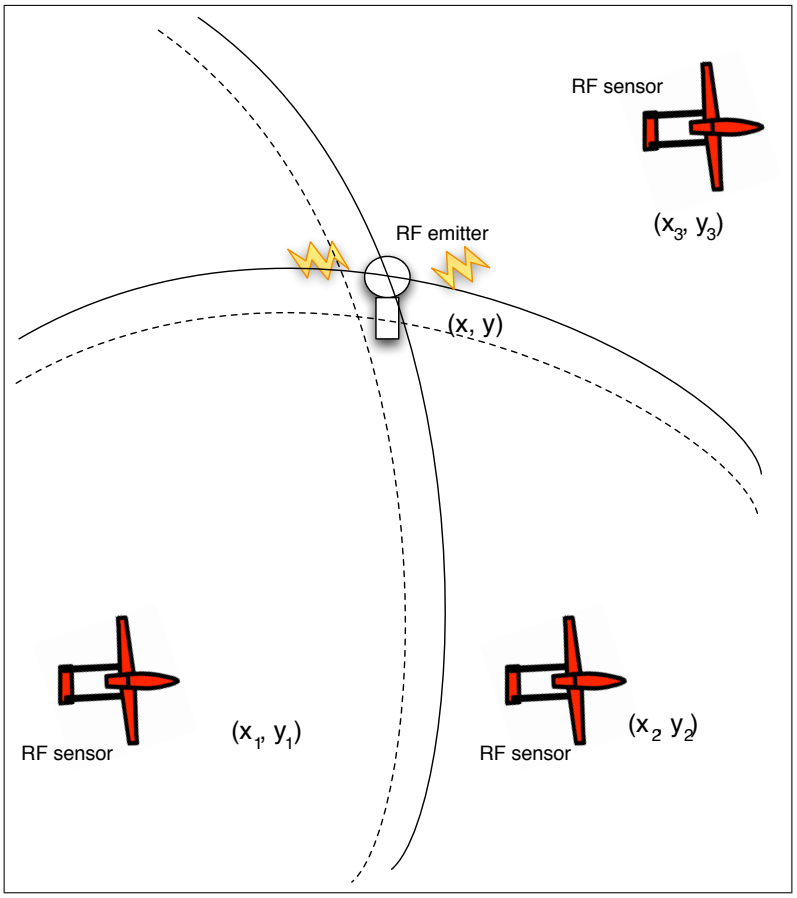

Figure 1.3: Illustration of geolocation using TDOA measurements

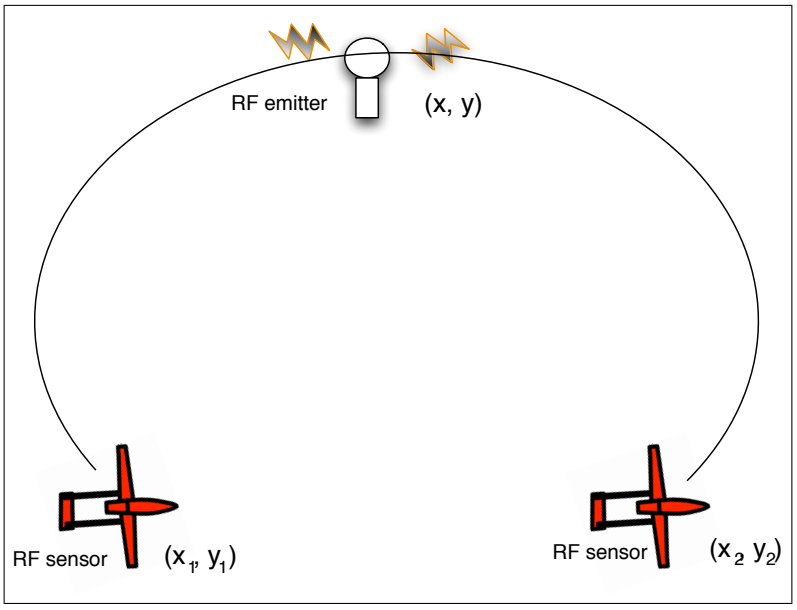

Figure 1.4: Illustration of geolocation using FDOA measurements

$$F_{r_i} = -\frac{f_0}{c}\frac{v_{x_{r_i}}\left(x - x_{r_i}\right) + v_{y_{r_i}}\left(y - y_{r_i}\right)}{\sqrt{\left(x - x_{r_i}\right)^2 + \left(y - y_{r_i}\right)^2}} \tag{1.8}$$

where (x, y) is the emitter position, (x_{r_i}, y_{r_i}) is the known position of the ith receiver at some time instant when the measurement is made, v_{x_i} and v_{y_i} are the components of the velocity of the platform in the x and y directions at the instant the measurement is made and f_0 is the frequency of the emitter signal of interest. The frequency difference $f_d = F_{r_i} - F_{r_1}$ provides an iso-Doppler curve as shown on figure 1.4. This curve corresponds to positions of the emitter that produce the same value of frequency difference of arrival. For error free FDOA measurements, the intersection of the two iso-Doppler curves (using three sensor platforms) provides the position of the emitter. When the measurements contain errors, a statistical estimator is used. In the next chapter, the use of classical estimators such as the least mean squares estimator to minimise the effect of measurement errors on the emitter position will be discussed.

Chapter 2

Overview of geolocation methods

In the previous chapter, three geolocation techniques: AOA, TDOA, FDOA were introduced as potential candidates for passive emitter geolocation. In this chapter, the use of an estimator algorithm to improve the emitter position estimate by optimally combining measurement data is presented. Two general types of estimator have been considered. The first is a batch estimator, where all measurements are taken prior to applying the estimator algorithm. The second is a sequential estimator, where the measurement data is collected and immediately applied to the estimation algorithm. This latter type of estimator offers the possibility of providing the sensor platform with a rough estimate of the emitter position after only few measurements have been obtained, which is then progressively improved (assuming algorithm convergence) as more measurements are supplied to the estimator. A number of batch estimator algorithms are examined including: the least mean square error estimator, a constrained least squares estimator and Brown's estimator. An iterative approach to position estimation based on Foy's method [22] (described in Appendix 9.2) is introduced and the methods are illustrated with the aid of simulation results that show the range error of the estimated emitter position and, using the root mean square error (RMSE) as a metric, the impact of the emitter/platform geometry on the accuracy of the estimate. Several sequential estimators are also examined, including the extended Kalman filter and the modified gain extended Kalman filter.

2.1 Batch Estimation

When measurements are made that contain errors, there are many ways of using multiple measurements to mitigate the effect of the errors and provide an improved estimate of the parameters of interest. In this section, details of the iterative least mean squares estimator (LMS) are presented. This algorithm is also known as the maximum likelihood estimator when the measurement errors are zero-mean Gaussian distributed. It is then shown how this estimator can be used to fuse the measurement data from a number of different geolocation techniques. The section begins with an overview of the least mean square estimator used for geolocation.

2.1.1 Least mean square estimation

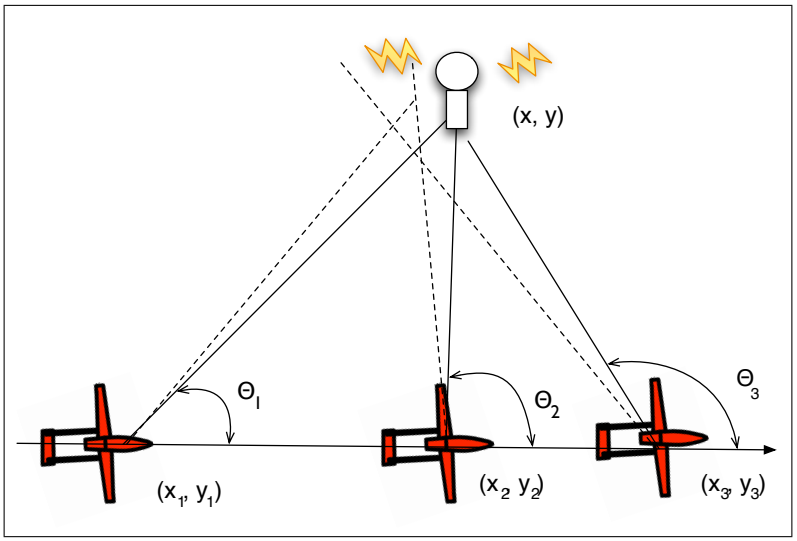

Figure 2.1: Geolocation using Angle of Arrival measurements

In this application, the least mean squares estimator is based on a Taylor series linearisation of the various non-linear emitter location equations for each of the techniques (i.e. AOA, TDOA, etc.) coupled to an iterative solution strategy to minimise the error due to the non-linearities. This method is able to fuse sensor data from the different geolocation measurement techniques mentioned above.

Mathematical Model for Mean Square Estimation

Assume that the 'state' of the emitter to be estimated is represented as an n dimensional vector, $\mathbf{x}$. The components of this vector are the position coordinates in two or three dimensions and it may also include the time of the emission. A set of M measurements, $m_i = 1, 2..., M$ is collected in order to estimate the state $\mathbf{x}$. The measurements can be made either at various times from a single moving platform (as in figure 2.1) or from M static platforms, or a combination of both. In the absence of random measurement errors, the actual measurement is related to the state of the emitter by a function, $f(x)$, that is assumed to be known. The function is defined by the measurement method being carried out at that time (e.g. AOA, TDOA etc.). However, in practice, the measurement is corrupted by additive noise; consequently the i^{th} measurement can be represented as:

$$m_i = fx + n_i, i = 1, 2..., M. \tag{2.1}$$

These M equations can be written as a single vector equation:

$$\mathbf{m} = \mathbf{f}(\mathbf{x}) + \mathbf{n} \tag{2.2}$$

The measurement error $\mathbf{n}$ is assumed to be a multivariate random vector with $M \times M$ positive definite covariance matrix

$$\mathbf{N} = \mathbf{E}[(\mathbf{n} - \mathbf{E}(\mathbf{n}))(\mathbf{n} - \mathbf{E}(\mathbf{n}))^T)] \tag{2.3}$$

where $E[\quad]$ represents the expected value of the random vector and the superscript T denotes the transpose operation. If $\mathbf{x}$ is regarded as an unknown but non-random vector and $\mathbf{n}$ is assumed to have a zero mean and Gaussian distribution, then the conditional density function of $\mathbf{m}$ given $\mathbf{x}$ is

$$p(\mathbf{x}|\mathbf{m}) = \frac{1}{(2\pi)^{\mathbf{N}/2}|\mathbf{N}|^{1/2}} \exp(-(1/2)[\mathbf{m} - f(\mathbf{x})]^T \mathbf{N}^{-1}[\mathbf{m} - f(\mathbf{x})]) \tag{2.4}$$

where $|\mathbf{N}|$ denotes determinant of $\mathbf{N}$ and the superscript -1 denotes the inverse operation. Because $\mathbf{N}$ is symmetric and positive definite, it's inverse exists. The maximum likelihood estimator [23] is that value of $\mathbf{x}$ that minimises the quadratic form

$$\mathbf{Q}(\mathbf{x}) = [\mathbf{m} - \mathbf{f}(\mathbf{x})]^T \mathbf{N}^{-1}[\mathbf{m} - \mathbf{f}(\mathbf{x})] \tag{2.5}$$

The minimisation of $\mathbf{Q}(\mathbf{x})$ is a reasonable criterion for determining an estimate even when the additive error cannot be assumed to be Gaussian. In this case, the resulting estimator is called a least squares estimator, and $\mathbf{N}^{-1}$ is regarded as a matrix of weighting coefficients. For the emitter geolocation problem described here, $f(\mathbf{x})$ is a nonlinear vector function representing either the triangulation equation given by equation (1.1), the hyperbolic equation given by (1.6) or FDOA emitter location described by equations (1.7) and (1.8). In order to simplify the problem, it is common to linearise $f(\mathbf{x})$ by expanding it in a Taylor series about a reference point specified by the vector $\mathbf{x_0}$ and retaining the first two terms;

$$\mathbf{f}(\mathbf{x}) \backsimeq \mathbf{f}(\mathbf{x_0}) + \mathbf{G}(\mathbf{x} - \mathbf{x_0}) \tag{2.6}$$

where $\mathbf{x}$ and $\mathbf{x_0}$ are $n \times 1$ column vectors and $\mathbf{G}$ is the $M \times n$ matrix of derivatives evaluated at $\mathbf{x_0}$:

$$\mathbf{G} = \begin{bmatrix} \left.\frac{\partial f_1}{\partial x_1}\right|_{x=x_0} & \cdots & \left.\frac{\partial f_1}{\partial x_n}\right|_{x=x_0} \\ \vdots & & \vdots \\ \left.\frac{\partial f_N}{\partial x_1}\right|_{x=x_0} & \cdots & \left.\frac{\partial f_N}{\partial x_n}\right|_{x=x_0} \end{bmatrix} \tag{2.7}$$

Each row of this matrix is the gradient vector of one of the components of $f(\mathbf{x})$. The vector $\mathbf{x_0}$ could be an estimate of the wanted emitter state, $\mathbf{x}$ determined from a previous iteration of the estimation procedure or based upon *a priori* information. It is assumed in the subsequent analysis that $\mathbf{x_0}$ is sufficiently close to $\mathbf{x}$ that (2.5) is an accurate approximation. Combining (2.6) and (2.5) gives

$$\mathbf{Q}(\mathbf{x}) = (\mathbf{r_1} - \mathbf{G}\mathbf{x})^T \mathbf{N}^{-1}(\mathbf{r_1} - \mathbf{G}\mathbf{x}) \tag{2.8}$$

where

$$\mathbf{r_1} = \mathbf{r} - \mathbf{f}(\mathbf{x_0}) + \mathbf{G}\mathbf{x_0} \tag{2.9}$$

To determine the necessary condition for the estimator, $\hat{\mathbf{x}}$, that minimises $\mathbf{Q}(\mathbf{x})$, now calculate the gradient of $\mathbf{Q}(\mathbf{x})$, defined by

$$\bigtriangledown_x \mathbf{Q}(\mathbf{x}) = \left[\frac{\partial Q}{\partial x_1}\frac{\partial Q}{\partial x_2}\cdots\frac{\partial Q}{\partial x_n}\right] \tag{2.10}$$

and then solve for $\mathbf{x}$ such that $\bigtriangledown_x \mathbf{Q}(\mathbf{x}) = \mathbf{0}$ where $\mathbf{0}$ is a null matrix. From its definition, $\mathbf{N}$ is a symmetric matrix; that is, $\mathbf{N}^T = \mathbf{N}$. Since $(\mathbf{N}^{-1})^T = (\mathbf{N}^T)^{-1}$, it follows that $(\mathbf{N}^{-1})^T = \mathbf{N}^{-1}$, which implies that $\mathbf{N}^{-1}$ is also symmetric. Therefore,

$$\bigtriangledown_x \mathbf{Q}(\mathbf{x})|_{x=\hat{x}_0} = 2\mathbf{G}^T\mathbf{N}^{-1}\mathbf{G}\hat{\mathbf{x}} - 2\mathbf{G}^T\mathbf{N}^{-1}\mathbf{r_1} = \mathbf{0} \tag{2.11}$$

There is an assumption that the matrix $\mathbf{G^T N^{-1} G}$ is nonsingular, but in practice, as $\mathbf{G}$ depends on the scenario, it has a problem of singularity. Thus the solution of (2.11) is

$$\hat{\mathbf{x}} = (\mathbf{G^T N^{-1} G})^{-1}\mathbf{G^T N^{-1}}\mathbf{r_1} = \mathbf{x_0} + (\mathbf{G^T N^{-1} G})^{-1}\mathbf{G^T N^{-1}}(\mathbf{r} - f(\mathbf{x_0})) \tag{2.12}$$

Substituting (2.2) into (2.12) and rearranging terms, the expression for $\hat{\mathbf{x}}$ can be written in the form

$$\hat{\mathbf{x}} = \mathbf{x} + (\mathbf{G}^T\mathbf{N}^{-1}\mathbf{G})^{-1}\mathbf{G}^T\mathbf{N}^{-1}[f(\mathbf{x}) - f(\mathbf{x_0}) - \mathbf{G}(\mathbf{x} - \mathbf{x_0}) + \mathbf{n}] \tag{2.13}$$

which shows how the estimator error is affected by the linearization error and the noise. The *bias* of the estimator $\hat{\mathbf{x}}$ is defined as $\mathbf{b} = E[\hat{\mathbf{x}}] - \mathbf{x}$. Using (2.13), the following is obtained

$$\mathbf{b} = (\mathbf{G^T N^{-1} G})^{-1}\mathbf{G^T N}^{-1}(f(\mathbf{x}) - f(\mathbf{x_0}) - \mathbf{G}(\mathbf{x} - \mathbf{x_0}) + \mathbf{E}[\mathbf{n}]) \tag{2.14}$$

If $f(\mathbf{x})$ is linear, then $\mathbf{E}[\mathbf{n}] = \mathbf{0}$ and the least squares estimator is unbiased. However, due to the non-linearity of the geolocation equation $\mathbf{E}[\mathbf{n}] \neq \mathbf{0}$ and the estimator is biased. The bias due to non-linearity of $f(\mathbf{x})$ can be estimated by application of equation (2.14). A very important metric of the estimator is the resulting positional error in the x and y directions. What is required to obtain this metric is a covariance matrix of $\hat{x}$, called $\mathbf{P}$. Equation (2.13) yields

$$\mathbf{P} = \mathbf{E}[(\hat{\mathbf{x}}] - E[\hat{\mathbf{x}}])(\hat{\mathbf{x}} - E[\hat{\mathbf{x}}])^T] = (\mathbf{G^T N^{-1} G})^{-1} \tag{2.15}$$

For the situation where $n = 2$ and the state $\mathbf{x}$ represents the coordinates, x and y, then $\mathbf{P}$ takes the form:

$$\mathbf{P} = \begin{bmatrix} \sigma_1^2 & \sigma_{12} \\ \sigma_{12} & \sigma_2^2 \end{bmatrix} \tag{2.16}$$

The diagonal elements σ_1^2 and σ_2^2 of $\mathbf{P}$ give the variances of the errors in the estimated components of $\mathbf{x}$. Generally, because of the effect of GDOP, $\sigma_1^2 \neq \sigma_2^2$ and the error in the x coordinate differs from that of y coordinate. If $\mathbf{n}$ is zero mean Gaussian, the maximum likelihood or least squares estimator for the linearized model is also the same as the minimum variance unbiased estimator. The measurement error vector $\mathbf{n}$ is assumed to encompass all the contributing errors, including uncertainties in the system or physical parameters, such as the station coordinates or the speed of propagation. The values of σ_1 and σ_2 are related to the dimensions of an 'error ellipse', describing the positional error of $\hat{\mathbf{x}}$ by these two statistical parameters. The parameter σ_{12} represents the rotation of the ellipse in the (x, y). This is discussed in next section.

Error ellipse of the estimate

The normalised dimensions of the error ellipse are given in terms of the quasi roots of the eigenvalues of, λ_1 and λ_2 of the covariance matrix $\mathbf{P}$. These eigenvalues are given by:

$$\lambda_1 = \frac{1}{2}\left[\sigma_1^2 + \sigma_2^2 + \sqrt{(\sigma_1^2 - \sigma_2^2)^2 + 4\sigma_{12}^2}\right] \tag{2.17}$$

$$\lambda_2 = \frac{1}{2}\left[\sigma_1^2 + \sigma_2^2 - \sqrt{(\sigma_1^2 + \sigma_2^2)^2 + 4\sigma_{12}^2}\right] \tag{2.18}$$

where only the positive square root is used. It is possible to scale this ellipse to reflect the probability of locating the emitter within the ellipse. The scale factor, k, is given by:

$$k = -2ln(1 - p_e) \tag{2.19}$$

where p_e is the probability of locating the emitter within the ellipse. The semimajor and semiminor lengths of the scaled error ellipse are given by $a = \sqrt{k\lambda_1}$ and $b = \sqrt{k\lambda_2}$ respectively. In equation (2.16), $\mathbf{P}$ contains an off-diagonal element, σ_{12}, as well as diagonal elements σ_1 and σ_2. This causes the ellipse to be *rotated* relative to the axes of the coordinate system. The angle of rotation of the major axis of the ellipse in relation to the x axis of the coordinate system is given by:

$$\theta = \frac{1}{2}\tan^{-1}\left(\frac{2\sigma_{12}}{\sigma_1^2 - \sigma_2^2}\right) - \frac{\pi}{4} \leq \theta \leq \frac{\pi}{4} \tag{2.20}$$

The diagram of the error ellipse relates its dimensions to the eigenvalues of the

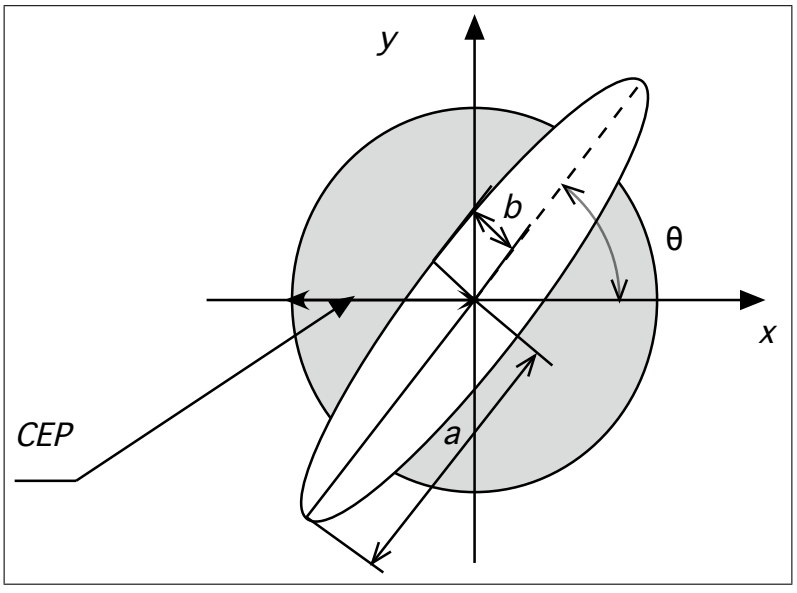

Figure 2.2: Illustration of error ellipse defined by the covariance matrix P (2.16) and CEP

covariance matrix. Setting $p_e = 10\%$, for example, in (2.19) will result in an ellipse whose dimensions enclose the 10% most likely position estimates of the target emitter.

2.1.2 Geometric dilution of precision (GDOP)

The geometric dilution of precision (GDOP) is defined as the ratio of the RMS position error to the RMS ranging error. It represents the factor by which the fundamental ranging error is magnified by the geometrical relationship between the emitter and each of the sensor platforms. However, the GDOP for each geolocation technique (i.e. AOA, TDOA, FDOA etc.) is different and some platform/emitter geometries that provide poor GDOP for one method of geolocation may well be acceptable for a different geolocation method. Consequently, combining different geolocation techniques in one algorithm through sensor level fusion will affect the overall GDOP for the combined geolocation methods. The mean-square position error of the estimate is given by:

$$\epsilon_r^2 = E\left[\sum_{i=1}^{n}(\hat{x}_i - x_i)\right] \tag{2.21}$$

Given that the covariance matrix of the estimate is given by (2.15), then

$$\epsilon_r^2 = tr(\mathbf{P}) + \sum_{i=1}^{n} b_i^2 \tag{2.22}$$

where $tr(\mathbf{P})$ is the trace of $\mathbf{P}$ and b_i is the ith component of the bias vector, $\mathbf{b} = \mathbf{E}[\hat{\mathbf{x}}] - \mathbf{x}$. The mean-square ranging error is dependent upon the geolocation method used. If a particular geolocation system has a mean-square ranging error σ_r^2, then the GDOP is:

$$GDOP = \frac{\sqrt{tr[\mathbf{P}]}}{\sigma_r} \tag{2.23}$$

2.1.3 Circular Error Probability

Clearly, for two dimensional Gaussian measurement errors, the error ellipse is a method of estimating the likely spread in the estimate of the emitter location. However, an alternative graphical method that is in common usage and which is easier to draw on maps is the circular error probable (CEP). This is a much cruder representation of the distribution of the errors. The CEP is defined as the radius of a circle that has its centre at the mean and contains 50% of the realizations of the random vector. If the target position estimator is unbiased, the CEP is a measure of the estimator uncertainty relative to the true transmitter position. The CEP is a measure of the uncertainty in the location estimator, $\hat{x}$ relative to its mean, $E(\hat{x})$. Of course, what it does not accurately represent is the two-dimensional distribution of the estimate. It can be shown [23] that the CEP is approximately related to the eigenvalues of the covariance matrix P by the appropriate use of the following equations:

$$CEP \approx 0.563\sqrt{\lambda_1} + 0614\sqrt{\lambda_2} \tag{2.24}$$

where $\lambda_1 \geq \lambda_2$ and $\gamma^2 = \lambda_2/\lambda_1$. This equation is accurate to 1% if $\gamma \geq 0.3$, it under estimates the CEP by less than 10% when $0.1 \leq \gamma \leq 0.3$ and it underestimates

the CEP by less than 20% for other conditions. In this latter condition, γ becomes so small that the eccentricity of the ellipse is very large and the use of a circle to represent an ellipse is probably inappropriate. An alternative form for CEP that is accurate to within 10% for all γ is:

$$CEP \approx 0.75\sqrt{\lambda_1 + \lambda_2} = 0.75\sqrt{\sigma_1 + \sigma_2} \tag{2.25}$$

The advantage of using the CEP is that it reduces the estimator metric to a single value and is thus widely used for comparison studies. In spite of the widespread use of CEP, extreme care is needed when using it to interpret some of the results because of the extreme eccentricity of some of the error ellipses for some geolocation methods such as AOA.

2.1.4 Fundamental performance bounds

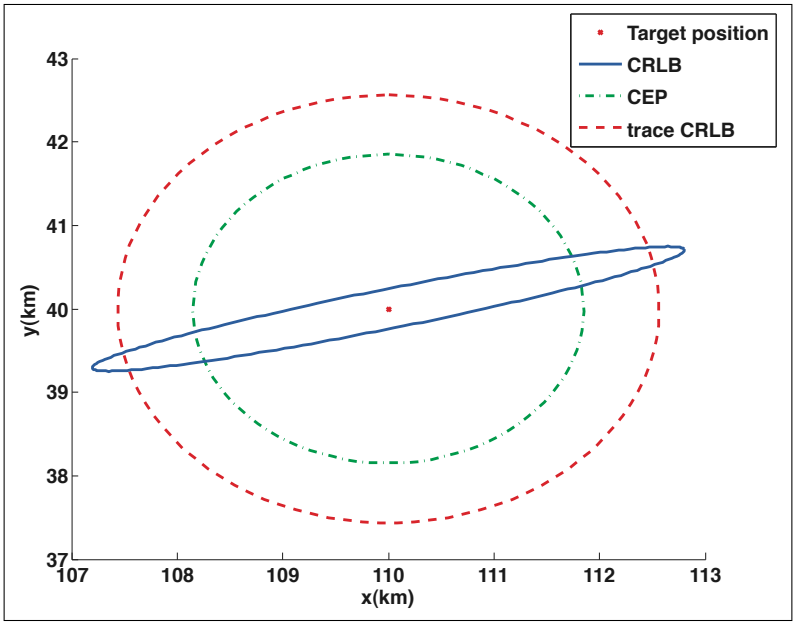

Figure 2.3: Illustration of the relationship between CRLB, defining error ellipse, CEP and trace of CRLB

The Fisher information matrix (FIM) as described in [24] provides a fundamental estimation limit for unbiased estimators which is referred to as the Cramer-Rao Lower Bound (CRLB) [25],[26]. This bound has been analyzed thoroughly in the literature, primarily for AOA, TOA and TDOA [27], [28] The 2×2 FIM $\mathbf{J}(p)$ is defined as

$$\mathbf{J}(p) = E\left(\nabla_p^T \ln p_E(\mathbf{m} - \mathbf{f}(\mathbf{p}))\nabla_p) \ln p_E(\mathbf{m} - \mathbf{f}(\mathbf{p}))\right) \tag{2.26}$$

$$\nabla_p \ln p_E(\mathbf{m} - \mathbf{f}(\mathbf{p})) = \frac{d \ln p_E(\mathbf{m} - \mathbf{f}(\mathbf{p}))}{dX} \frac{d \ln p_E(\mathbf{m} - \mathbf{f}(\mathbf{p}))}{dy} \tag{2.27}$$

where $\mathbf{x} = (x, y)$ is two diminutional position vector of the emitter and $p_E(\mathbf{m} - f(\mathbf{x}))$ is the likelihood given the error distribution. In the case of Gaussian measurement

errors $p_E(e) = \mathbf{N}(\mathbf{0}, \mathbf{N}(\mathbf{x}))$ the FIM equals

$$\mathbf{J}(\mathbf{x}) = \mathbf{Q}^T(\mathbf{x})\mathbf{N}(\mathbf{x})^{-1}\mathbf{Q}(\mathbf{x}) \tag{2.28}$$

$$\mathbf{Q}(\mathbf{x}) = \nabla_x(\mathbf{f}(\mathbf{x})) \tag{2.29}$$

where $\mathbf{f}(\mathbf{x})$ measurement function, for example for TDOA $\mathbf{f}(\mathbf{x}) = \mathbf{D_i} - \mathbf{D_1}$. In the general case, numerical methods are needed to evaluate the CRLB. The larger the gradient $\mathbf{Q}(\mathbf{x})$, or the smaller the measurement error, the more information is provided from the measurement and the smaller the potential estimation error. Information is additive, so if two measurements are independent, the corresponding information matrices can be added. This is easily seen from (2.28) for $\mathbf{Q^T} = (\mathbf{Q_1^T}, \mathbf{Q_2^T})$ and $\mathbf{N}$ being block diagonal, in which case it is possible to write $\mathbf{J} = \mathbf{J_1} + \mathbf{J_2}$. Plausible approximate scalar information measures are the trace of FIM or the smallest eigenvalue of FIM

$$\mathbf{J}_{tr}(p) \triangleq tr\mathbf{J}(p), \quad \mathbf{J}_{min} \triangleq \min eig\mathbf{J}(p) \tag{2.30}$$

The former information measure is additive as is FIM itself, while the latter is an underestimation of the information that is useful when reasoning about whether or not the available information is sufficient. It is worth noting that in the Gaussian case with a diagonal measurement error covariance matrix, the trace of the FIM is the squared gradient magnitude. The CRLB is given by

$$Cov(\hat{\mathbf{x}}) = E(\mathbf{x} - \hat{\mathbf{x}})(\mathbf{x} - \hat{\mathbf{x}})^T \geq \mathbf{J}^{-1}(\mathbf{x}) \tag{2.31}$$

where $\mathbf{x}$ denotes the true position and the $\hat{\mathbf{x}}$ estimated position. The CRLB holds for any unbiased estimate of $\hat{\mathbf{x}}$, in particular the ones based on minimizing criteria previously discussed. It is known that asymptotically, the ML estimate is $\hat{\mathbf{x}} \sim \mathbf{N}(\mathbf{x}, \mathbf{J}^{-1}(\mathbf{x}))$ [29] and thus reaches this bound. Yet, this may not hold for a finite amount of inaccurate data. The right-hand side of (2.31) gives an idea of how suitable a given sensor configuration is for positioning. However, it should always be kept in mind that this lower bound is quite conservative and relies on many assumptions. Figure 2.3 illustrates the relationship between CRLB error ellipse, the CEP circle and a circle defined by the trace of the CRLB matrix. In this work, CRLB derived in [30] is used for TDOA-only measurement:

$$tr(\mathbf{J}^{-1}) = (c\sigma_{TDOA})^2 tr\left[(\mathbf{G}\mathbf{G}^T)^{-1}\right] \tag{2.32}$$

where

$$\begin{aligned}
\mathbf{G} &= \nabla\mathbf{R_{ij}^T} = [\bar{\mathbf{g}}_{\mathbf{ij}}.....], \\
\bar{\mathbf{g}}_{\mathbf{ij}} &= \bar{\mathbf{g}}_{\mathbf{i}} - \bar{\mathbf{g}}_{\mathbf{j}}, \\
\bar{\mathbf{g}}_{\mathbf{i}} &= \underline{\nabla}\mathbf{R_i}(\mathbf{x}) = \frac{\mathbf{x} - \mathbf{x}_{\mathbf{r_i}}}{||\mathbf{x} - \mathbf{x}_{\mathbf{r_i}}||}
\end{aligned}$$

Here, $\mathbf{x}$ represents the emitter coordinates in vector form and $\mathbf{x}_{\mathbf{r_i}}$ represents the coordinate vector of the ith receiver. Clearly, $\bar{\mathbf{g}}_{\mathbf{i}}$ is a unit length vector with

$||\bar{\mathbf{g}}_\mathbf{i}|| = 1$. It points from receiver i to the emitter. $\mathbf{G}$ is the Jacobian matrix found in section 2.1.6. It clearly depends on: (i) the emitter position (ii) receiver position and (iii) the set of receiver pairs which are used for geolocation.

In practice, the root mean square error (RMSE) is perhaps of more importance. This can be interpreted as the achieved position error in meters. The CRLB implies the following bound:

$$RMSE = \sqrt{E[(x-\hat{x})^2 + (y-\hat{y})]} \geq \sqrt{trCov(\hat{\mathbf{x}})} \geq \sqrt{tr\mathbf{J}^{-1}(\mathbf{x_0})} \tag{2.33}$$

where (x, y) is the true target position and $(\hat{x}, \hat{y})$ is the estimated position. The first inequality becomes an inequality for unbiased estimates. The CEP defines a circular region of for RMSE. As mentioned before, the GDOP is related to the CRLB. Basically, the GDOP is the RMSE normalized by the measurement accuracy (see (2.31) for example). The relation between the GDOP and CRLB has been highlighted in [31]. Throughout this thesis the RMSE metric will be generally used, however CRLB and CEP will be also used, where appropriate.

2.1.5 Emitter location using the Maximum Likelihood Estimator with Angle of Arrival measurements only

Following introductory comments, it is assumed that the bearing measurements are space- and time-stamped by the platform, so it is irrelevant whether the M measurements are made by a $p \leq M$ stationary platforms or a single moving platform. Assuming that the platform positions are known accurately, the actual AOA from the platform to the target emitter given by:

$$\theta_{i_t} = \tan^{-1}\left(\frac{y - y_{p_i}}{x - x_{p_i}}\right) \tag{2.34}$$

where (x, y) position of the emitter and (x_{p_i}, y_{p_i}) is the position of the ith platform. However, each bearing measurement has a measurement error n_i associated with it, giving rise to a position error. Assume that M measurements are made and that the ith measurement has an associated error term, θ_i:

$$\theta_i = \theta_{i_t} + n_i \quad i = 1, 2, \ldots, M \tag{2.35}$$

where θ_{i_t} true AOA given by (2.34). Rewriting $f(\mathbf{x}) = \tan^{-1}\left(\frac{y-y_{p_i}}{x-x_{p_i}}\right)$ and representing M measurements of θ as a column vector $\mathbf{\Theta}$, allows (2.35) to be expressed in matrix form as:

$$\mathbf{\Theta} = \mathbf{f}(\mathbf{x}) + \mathbf{n} \tag{2.36}$$

Consequently, adopting the approach outlined in section 2.1.1, $\mathbf{f}(\mathbf{x})$ is linearized by a first-order Taylor series expansion evaluated about an initial estimate of the emitter location given by position vector $\mathbf{x_0}$:

$$\theta_i = \tan^{-1}\left(\frac{y_t - y_{p_i}}{x_t - x_{p_i}}\right) + \frac{\partial \tan^{-1}\left(\frac{y_t - y_{p_i}}{x_t - x_{p_i}}\right)}{\partial x}|_{x=x_0} + \frac{\partial \tan^{-1}\left(\frac{y_t - y_{p_i}}{x_t - x_{p_i}}\right)}{\partial y}|_{x=x_0} + n_i \tag{2.37}$$

or:

$$\mathbf{\Theta} = \mathbf{f}(\mathbf{x_0}) + \mathbf{G_{AOA}}(\mathbf{x} - \mathbf{x_0}) + \mathbf{n} \tag{2.38}$$

where the Jacobian is given by:

$$\mathbf{G_{AOA}} = \begin{bmatrix} -\frac{\sin\theta_{01}}{D_{01}} & \cdots & \frac{\cos\theta_{01}}{D_{01}} \\ \vdots & & \vdots \\ -\frac{\sin\theta_{0M}}{D_{0M}} & \cdots & \frac{\cos\theta_{0M}}{D_{0M}} \end{bmatrix} \tag{2.39}$$

where

$$\sin\theta_{0i} = \frac{y_0 - y_i}{D_{01}} \tag{2.40}$$

$$\cos\theta_{0i} = \frac{x_0 - x_i}{D_{01}} \tag{2.41}$$

$$D_{0i} = \sqrt{(x_0 - x_i)^2 + (y_0 + y_i)^2} \tag{2.42}$$

The maximum likelihood estimation is thus:

$$\hat{\mathbf{x}} = \mathbf{x_0} + (\mathbf{G_{AOA}^T N^{-1} G_{AOA}})^{-1} \mathbf{G_{AOA}^T N^{-1}} (\mathbf{\Theta} - \mathbf{f(x_0)}) \tag{2.43}$$

The solution to this equation requires that a rough estimate of the emitter position is made and this is used as $\mathbf{x_0}$. In order to demonstrate the performance of the Maximum likelihood estimator (MLE) for geolocation using AOA measurements the following scenario was set up:

- Two UAVs following the pre-defined flight paths as pictured by red circles in figure 2.4 with constant speed $v = 40m/s$
- It was assumed, that each platform can obtain one AOA measurement on each 10th second, which is correspond to one step in simulation, with a standard deviation of the AOA measurements $\sigma_\theta = 0.02$ radians
- Each UAV platform can obtain 55 measurements along the flight path
- MLE is used to fuse obtained measurements with an initial guess $x_0 = (x + 3, y + 3)$. Estimates of the emitter position is plotted as crosses in figure 2.5. The number of iterations for the MLE was limited to 100 and another stopping criteria was used $\|(\mathbf{G_{AOA}^T N^{-1} G_{AOA}})^{-1} \mathbf{G_{AOA}^T N^{-1}} (\mathbf{\Theta} - \mathbf{f(x_0)})\| \geq 2$
- This simulation was repeated for 50 times for the fixed scenario and the output of the MLE is plotted in figure 2.4, where each blues cross represents one of the 50 MLE position estimates.

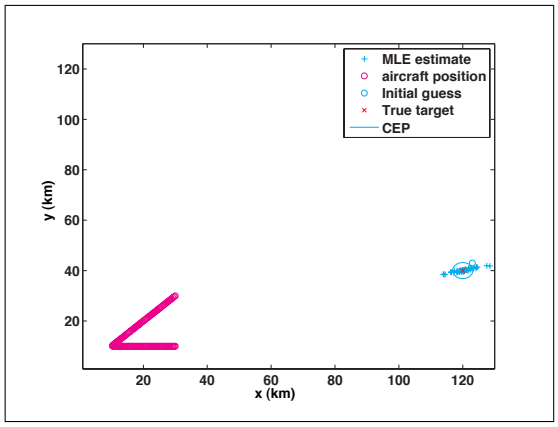

Figure 2.4: Scenario of multiplatform emitter geolocation using AOA measurements and MLE showing the flight paths of two UAV and the emitter of interest. Crosses show the estimated emitter position for 50 runs. Also shown is the CEP

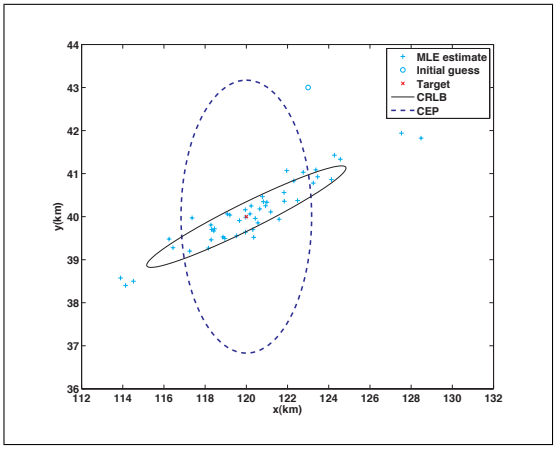

Figure 2.5: Results of the MLE for emitter geolocation using AOA measurements. Crosses show the estimated emitter position for each of 50 runs

Although the performance of the MLE for this particular scenario was good, it is important to recognize the fact that convergence of the MLE depends on the

scenario. In order to demonstrate the convergence problem of MLE, the target was placed on each point on the grid. The scenario as described above was repeated for 50 times for each target position and the output is shown in figure 2.6 in the form of the three dimensional plot, where the z-axis corresponds to the average RMS error for each target position. In this figure the maximum value of RMS error was

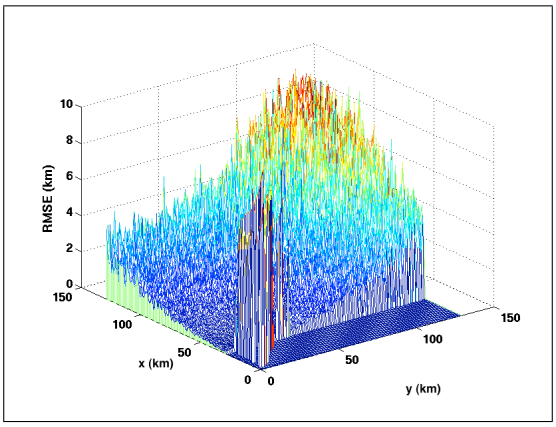

Figure 2.6: Three dimensional grid, demonstrating convergence and RMSE dependance on GDOP using AOA with MLE

capped at 10 km and the RMS error value was set to zero when the MLE would not converge. It will be noticed that the MLE estimator could not provide any estimate for the target positioned in the North West quadrant relative to the UAV flight paths. In order to illustrate the effect of the GDOP, the same scenario was repeated, but in this case the target positions were placed on the search space with an interval of 10 km, and the corresponding CRLB error ellipses are shown in figure 2.7. The error ellipse wasn't plotted when the MLE was not able converge, or when the trace of the ellipse is more than 20 km.

Figure 2.7 illustrates the bias introduced by the GDOP using triangulation: the spread in the position estimate depends on the distance and the angle relative to the platform. Zoomed parts of the figure 2.7 are plotted in figures 2.8, 2.9 and 2.10. It is clear that the best estimates (smaller error ellipses) for this scenario are located in the area in central part of figure 2.7, shown zoomed in figure 2.10.

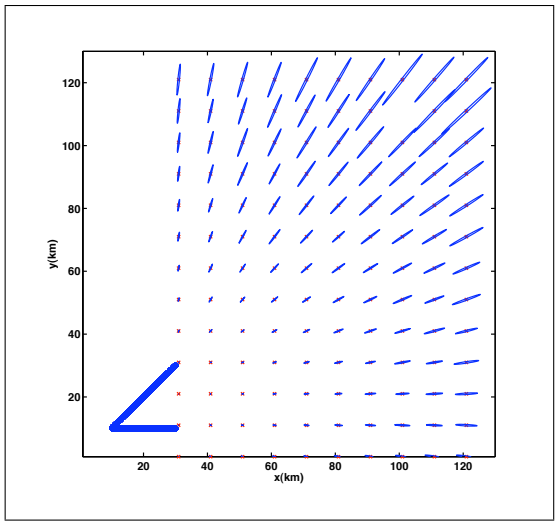

Figure 2.7: Illustration of GDOP. Ellipses defined by CRLB for MLE using AOA measurements only

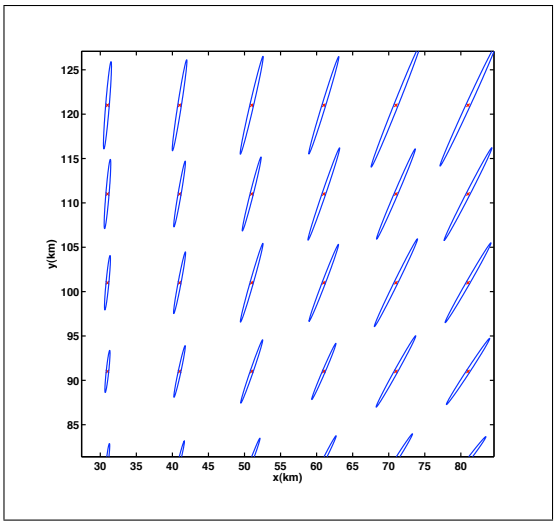

Figure 2.8: Zoomed CRLB ellipses for MLE using AOA measurements only, North from figure 2.7

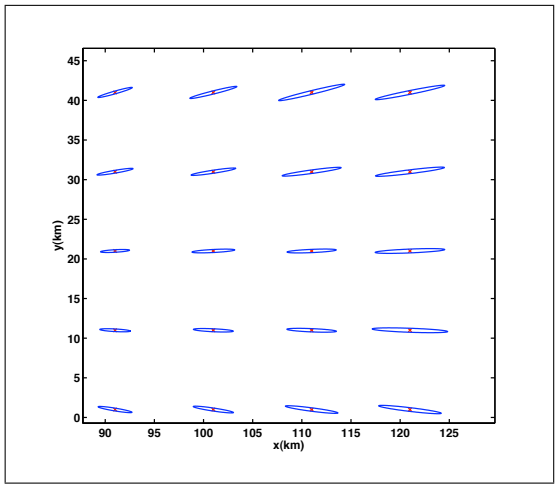

Figure 2.9: Zoomed CRLB ellipses for MLE using AOA measurements only, Eastern part of figure 2.7

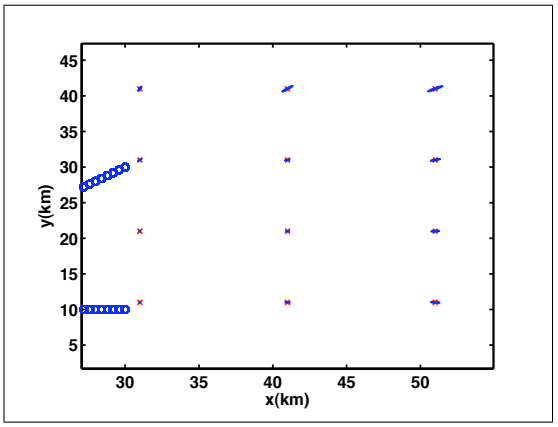

Figure 2.10: Zoomed CRLB ellipses for MLE using AOA measurements only, Central part of figure 2.7

2.1.6 Emitter location using time difference of arrival measurements (TDOA)

As described in section 1.4.2 the measured TOA at the ith platform is:

$$t_i = t_0 + \frac{D_i}{c} + e_i \tag{2.44}$$

where t_0 is the time the signal was transmitted,D_j/c represents the actual transmitted time of the RF signal to the ith receiver, D_i is the true distance between the emitter and the platform given by:

$$D_i = \sqrt{(x - x_i)^2 + (y - y_i)^2} \tag{2.45}$$

and e_i is the measurement error in the time of arrival. The measurements can be expressed in vector form as:

$$\mathbf{t} = \mathbf{t_0 1} + \frac{\mathbf{D}}{c} + \mathbf{e} \tag{2.46}$$

where $\mathbf{1}$ is a column vector of M ones. The i^th TDOA measurement between the $i$the platform and the $(i+1)$th platform is:

$$\tau_i = t_i - t_{i+1} = \frac{D_i - D_{i+1}}{c} + n_i, i = 1, 2, \ldots, M-1 \tag{2.47}$$

where $n_i = e_i - e_{i+1}$ is the measurement error due to the errors in measuring both times of arrival. It should be noted that $M-1$ TDOA measurements are generated from M TOA measurements. In order to formulated the problem along the lines of the vector representation of (2.36), it is necessary to account for the $M-1$ TDOA from M TOA measurements in order to ensure that there are M columns in the measurement matrix. This is accomplished using an $(M-1) \times M$ transformation matrix, $\mathbf{H}$.

$$\mathbf{H} = \begin{bmatrix} 1 & -1 & 0 & \cdots & 0 \\ 0 & 1 & -1 & \cdots & 0 \\ \vdots & \vdots & \vdots & \vdots & \vdots \\ 0 & 0 & \cdots & 1 & -1 \end{bmatrix} \tag{2.48}$$

such that

$$\mathbf{Ht} = \mathbf{HD/c} + \mathbf{He} \tag{2.49}$$

where the measurement vector $\tau \equiv \mathbf{Ht}$ and the non-linear function $\mathbf{f(x)} \equiv \mathbf{HD/c}$. The estimate of the emitter position, $\mathbf{x}$ is required which is contained in the M values of $D_i = \|\mathbf{x} - \mathbf{s_i}\|$, where $\mathbf{s_i}$ is the position vector of the ith measurement platform and $\|\quad\|$ is the Euclidian norm. Assume that the non-linear measurement equation is Taylor series expanded about the point $\mathbf{x_0}$ and that $D_{0i} = \|\mathbf{x_0} - \mathbf{s_i}\|$ is the distance of the ith platform to this point. Defining:

$$\mathbf{F} = \begin{bmatrix} (\mathbf{x_0} - \mathbf{s_1})^T / D_{01} \\ \vdots \\ (\mathbf{x_0} - \mathbf{s_M})^T / D_{0M} \end{bmatrix} \tag{2.50}$$

then the Jacobian for the TDOA method is:

$$\mathbf{G}_{TDOA} = \begin{bmatrix} \mathbf{1} & \dfrac{\mathbf{F}}{c} \end{bmatrix} \tag{2.51}$$

and

$$\mathbf{G}_{TDOA} = \mathbf{HF/c} \tag{2.52}$$

The corresponding maximum likelihood estimator for the TDOA geolocation method is thus:

$$\hat{\mathbf{x}} = \mathbf{x_0} + c\left(\mathbf{F^T H^T N_{TDOA}^{-1} HF}\right)^{-1} \mathbf{F^T H^T N_{TDOA}^{-1}}(\mathbf{Ht - HD_0}/c) \tag{2.53}$$

where $\mathbf{N_{TDOA}} = \mathbf{HNH^T}$ is the covariance matrix for the TDOA measurements obtained in terms of the original TOA measurement covariance matrix. The covariance matrix of the estimate, $\mathbf{P}$ is given by:

$$\mathbf{P} = c^2\left(\mathbf{F^T H^T N_{TDOA}^{-1} HF}\right)^{-1} \tag{2.54}$$

so

$$\mathbf{N}_{TDOA} = \begin{bmatrix} \sigma_{TDOA}^2 & 0 \\ 0 & \sigma_{TDOA}^2 \end{bmatrix} \tag{2.55}$$

Similar to AOA, the following scenario has been set up as pictured on figure 2.11.

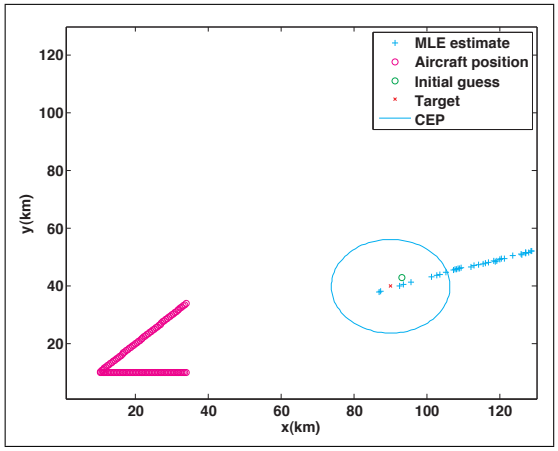

Figure 2.11: Scenario of multiplatform emitter geolocation using TDOA measurements and MLE showing the flight paths of two UAV and the emitter of interest. Crosses shows the estimated emitter position

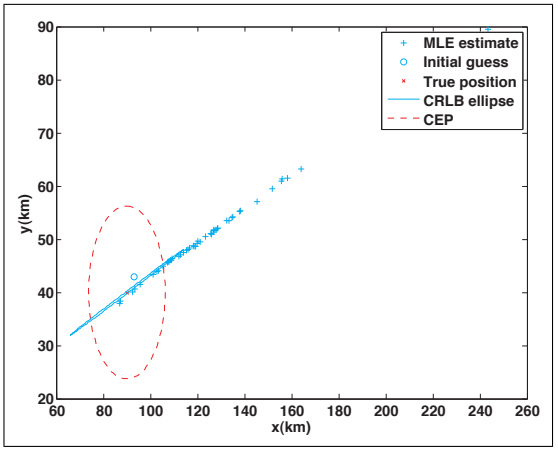

Figure 2.12: Results of the MLE estimates for emitter geolocation using TDOA measurements. Crosses indicate the estimated emitter position

In this scenario it was assumed that both UAVs can obtain time of arrival measurements from which TDOA measurement can be obtained. The standard deviation of the TDOA measurement was assumed $\sigma_{TDOA} = 7.4 \times 10^{-7}$ seconds. Each UAV was capable of obtaining 55 measurements along the flight path. The output of the MLE estimator for 50 simulation is shown in figure 2.12. It can be noted that the

error ellipse is much thiner for the case of TDOA geolocation, however the spread of the MLE estimates is much larger.

The convergence problem of the MLE algorithm for the case of TDOA emitter geolocation has been tested using the same approach as described before for the AOA scenario, where the target was placed on each point on the grid and the MLE estimator was run for 50 times, to obtain an average RMS error for the MLE, using 55 TDOA measurements for each target position. The output of these simulations is shown in figure 2.13 in the form of a three dimensional plot, where the z-axis corresponds to the average RMS error for each target position. In this figure, the maximum value of the RMS positional error was capped at 10 km and the RMS error value was set to zero when the MLE is not able to converge. It can be seen that using TDOA-only measurements from two mobile platforms, the MLE algorithm guarantees to converge in a smaller area. It will also be noted that the spread in the position estimates is different than the one for AOA. As an illustration, consider figure 2.14, where the CRLB error ellipses are plotted for each target, positioned on each point of the grid. Zoomed versions of this plot are shown in figures 2.15, 2.16 and 2.17 and illustrate, that the CRLB for TDOA-only measurements is much smaller, than for AOA, thus MLE provides more accurate estimates using TDOA measurements, rather than AOA-only measurements, but only in the area where MLE converge.

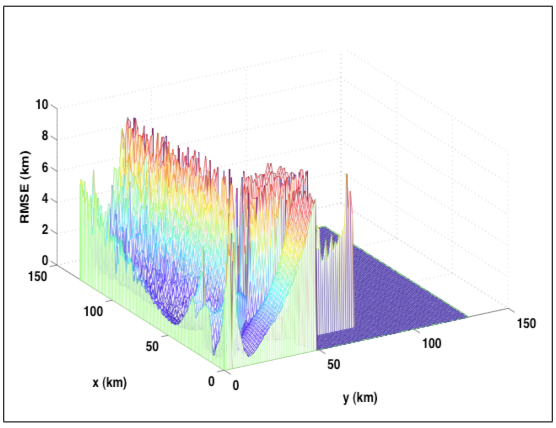

Figure 2.13: Three dimensional grid, demonstrating convergence and RMSE dependance on GDOP using MLE with TDOA measurements

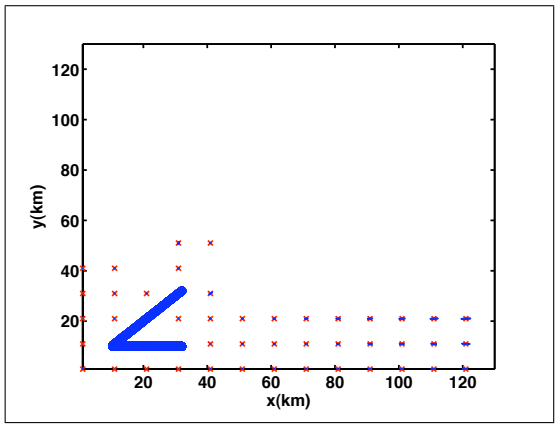

Figure 2.14: Illustration of GDOP. Ellipses defined by CRLB for MLE using TDOA measurements only

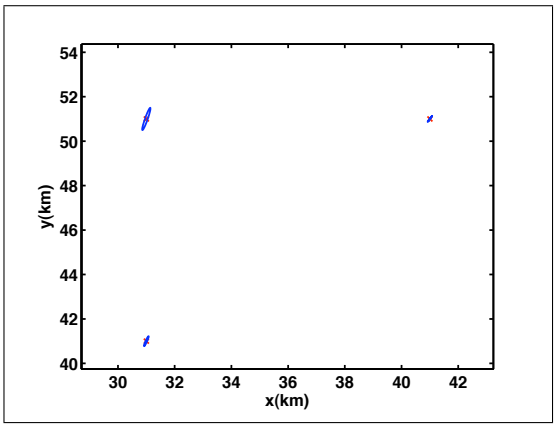

Figure 2.15: Zoomed CRLB ellipses for MLE using TDOA measurements, North part of figure 2.14

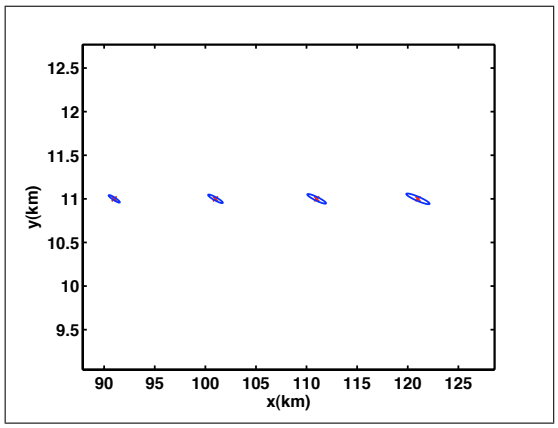

Figure 2.16: Zoomed CRLB ellipses for MLE using TDOA, East part of figure 2.14

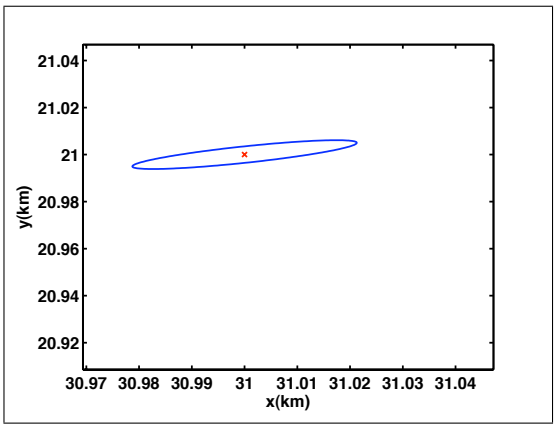

Figure 2.17: Zoomed CRLB ellipses for MLE using TDOA, Central part of figure 2.14

2.1.7 Geolocation fusing AOA and TDOA measurements using MLE

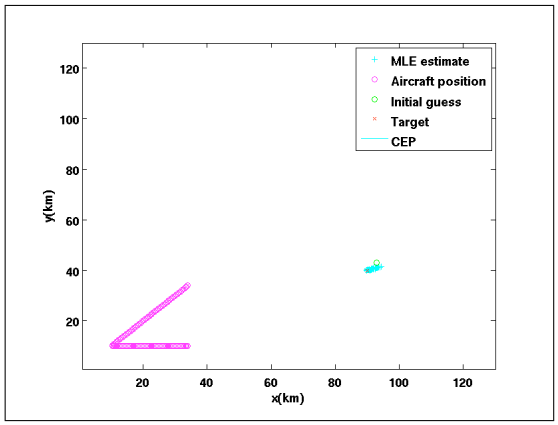

Figure 2.18: Scenario for geolocation fusing multiple AOA and TDOA measurements obtained by two mobile platforms denoted as circles

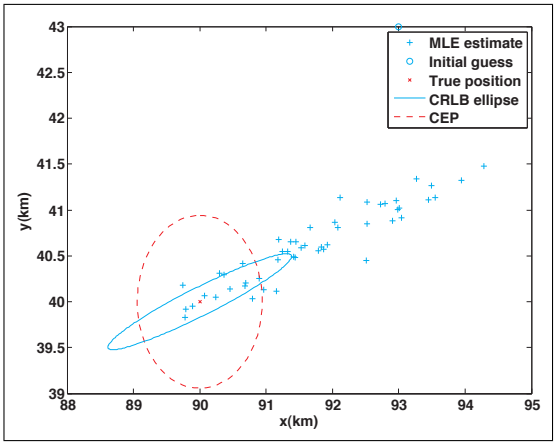

Figure 2.19: Result of the MLE algorithm fusing AOA and TDOA measurements from two platforms from the scenario 2.18. Crosses indicate MLE estimates

It is possible to use the maximum likelihood estimator to fuse different types of geolocation measurements. For example, to combine TDOA measurements with AOA measurements, it is possible to augment the vector $m - f(x)$ of (2.2) to include both the AOA and TDOA. Then combining TDOA (2.49) and AOA (2.36) yields:

$$\begin{bmatrix} \mathbf{Ht} \\ \mathbf{\Theta} \end{bmatrix} = \begin{bmatrix} \mathbf{HD/c} \\ \mathbf{f(x)} \end{bmatrix} + \begin{bmatrix} \mathbf{He} \\ \mathbf{n} \end{bmatrix} \tag{2.56}$$

Then the (2.12) becomes:

$$\hat{\mathbf{x}} = \mathbf{x_0} + (\mathbf{G^T_{fused}} \mathbf{N^{-1}_{fused}} \mathbf{G_{fused}})^{-1} \mathbf{G^T_{fused}} \mathbf{N^{-1}_{fused}} (\mathbf{m} - \mathbf{f(x_0)}) \tag{2.57}$$

where

$$\mathbf{N}_{fused} = \begin{bmatrix} \mathbf{N}_{TDOA} & 0 \\ 0 & \mathbf{N}_{AOA} \end{bmatrix} \tag{2.58}$$

In this case the combined Jacobian derived in [32] would be:

$$\mathbf{G}_{fused} = \begin{bmatrix} \mathbf{G}_{TDOA} \\ \mathbf{G}_{AOA} \end{bmatrix} = \begin{bmatrix} \frac{D_{02}(x_0 - x_1) - D_{01}(x_0 - x_2)}{cD_{01}D_{02}} & \frac{D_{02}(y_0 - y_1) - D_{01}(y_0 - y_2)}{cD_{01}D_{02}} \\ -\frac{sin(\theta_{01})}{D_{01}} & \frac{cos(\theta_{01})}{D_{01}} \\ -\frac{sin(\theta_{02})}{D_{02}} & \frac{cos(\theta_{02})}{D_{02}} \end{bmatrix} \tag{2.59}$$

for a two platforms scenario.

Figure 2.18 shows a simulation scenario for emitter location using combined TDOA and AOA measurements. In this figure, the flight paths of two aircraft, the target emitter and the estimated positions are shown. The standard deviation of

the angle measurements is $\sigma_\theta = 0.02$ radians and standard deviation of the TDOA measurements is $\sigma_{TDOA} = 7.4 \times 10^{-7}$ seconds were used, as in previous sections. The results of the fused MLE estimate are provided in figure 2.19. It can be seen that the spread of the estimates in case of the fused geolocation is smaller than for either TDOA or AOA alone. Another important point to make is that the fusion algorithm improved the convergence of the MLE compared to using TDOA-only measurements as shown in figure 2.20.

However the convergence of the MLE using fused measurements TDOA and AOA is still worse than using pair of AOA-only measurements, as can be seen in figures 2.6 and 2.7. Figure 2.21 illustrates the GDOP of the fused TDOA and AOA measurements, in this figure, the CRLB ellipses were plotted, assuming that the target was positioned on the vertices of a grid with a 10 km cell size. Only ellipses with a trace of the CRLB smaller than 20 km were plotted. Figures 2.22, 2.23, 2.24 are zoomed versions of figure 2.21. It is clear that the fusion of TDOA and AOA measurements increased the area, where the MLE algorithm converges and reduced the size of the ellipse.

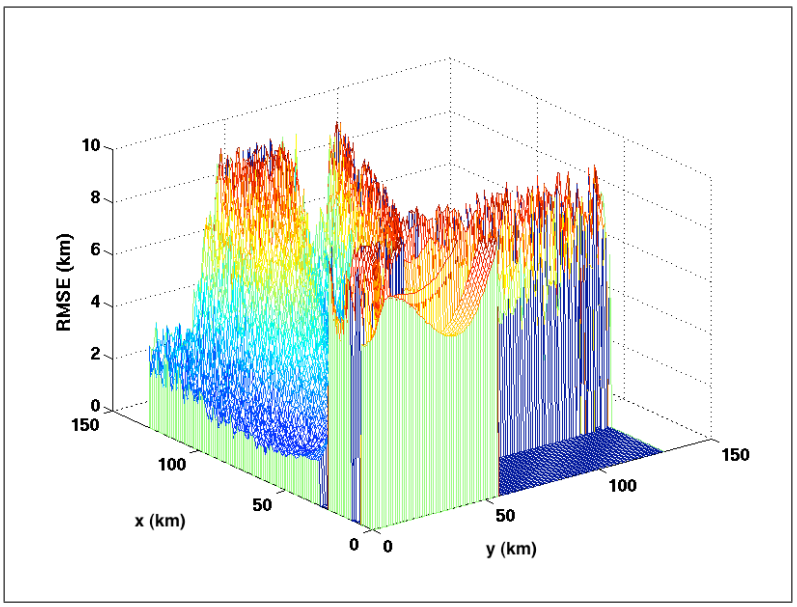

Figure 2.20: Three dimensional grid, demonstrating convergence and RMSE dependance on GDOP using TDOA and AOA measurements with MLE

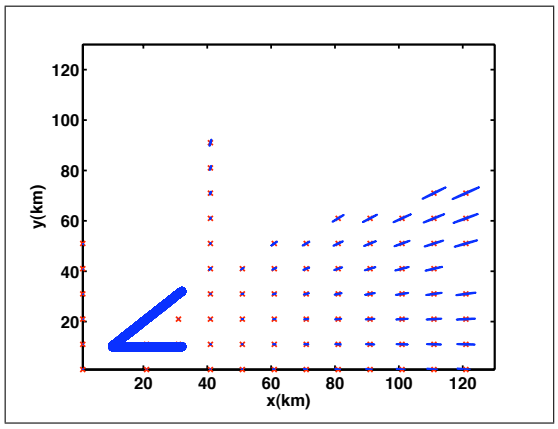

Figure 2.21: Illustration of GDOP. Ellipses defined by CRLB for MLE using fusion of TDOA and AOA measurements

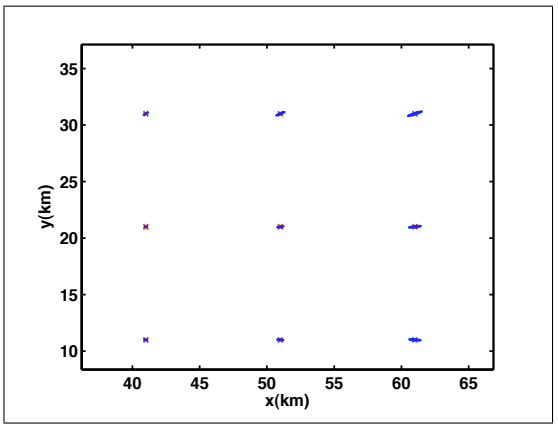

Figure 2.22: Zoomed CRLB ellipses for fused TDOA and AOA measurements using MLE, central part of figure 2.21

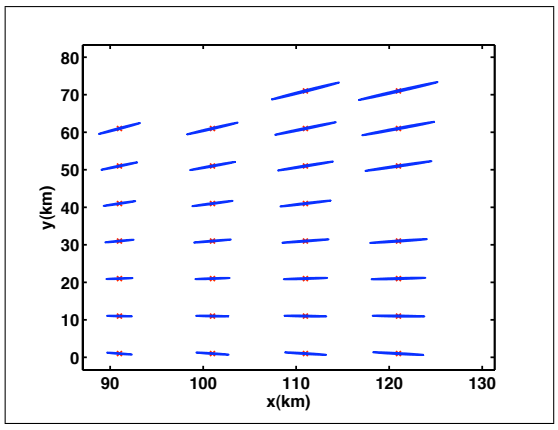

Figure 2.23: Zoomed CRLB ellipses for fused TDOA and AOA measurements using MLE, East part of figure 2.21

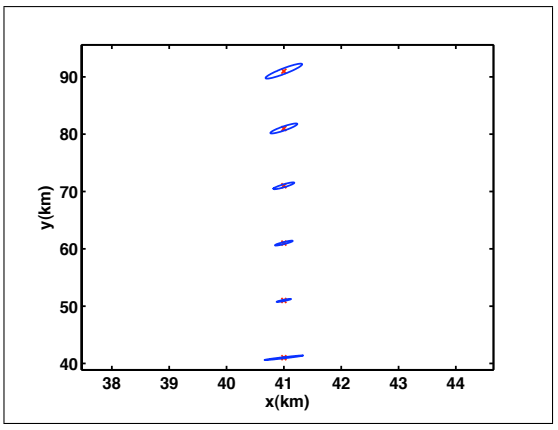

Figure 2.24: Zoomed CRLB ellipses for fused TDOA and AOA measurements using MLE, North part of figure 2.21

Fusion of multiple measurements using the MLE

In order to test the accuracy of all three geolocation methods using the MLE estimator as the fusing algorithm, the scenario shown in figure 2.4 has been modified by moving the target to position $(40, 12)$.

Also, it is in the interest of research to compare the performance of the each method as the number of measurements taken along the flight path is increased. Figure 2.26 shows the performance of the MLE algorithm as a function of the number of measurements taken, using a pair of AOA-only measurements, plotted together with the corresponding CRLB using the RMSE as a metric. When only AoA-measurements are used in scenario in figure 2.25 the changes in GDOP of the platforms after 40 measurements degrade the performance of the algorithm. It should be noted that target is close to the platforms and for AoA-only measurements overall performance of the algorithm is less than 1 km.

Figure 2.27 demonstrates the average RMSE error over 100 simulations for emitter geolocation using the MLE with TDOA-only measurements, taken by the same pair of platform, with corresponding CRLB. Figure 2.28 shows the average RMSE over 100 simulations of the combined estimates, using the MLE to fuse AOA and TDOA measurements in one batch estimate.

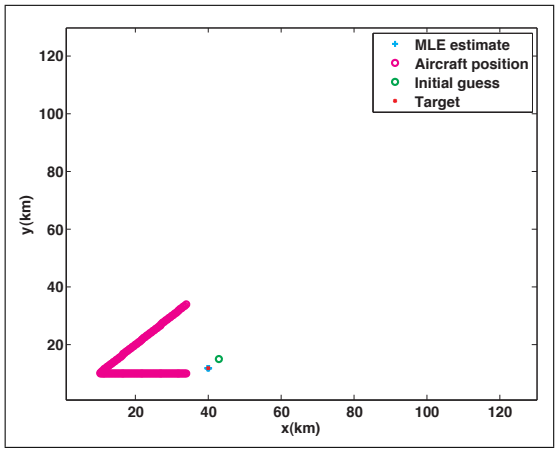

Figure 2.25: Scenario for comparison of the RMSE relative to a number of measurements taken, using AOA, TDOA and fused AOA and TDOA methods for geolocation

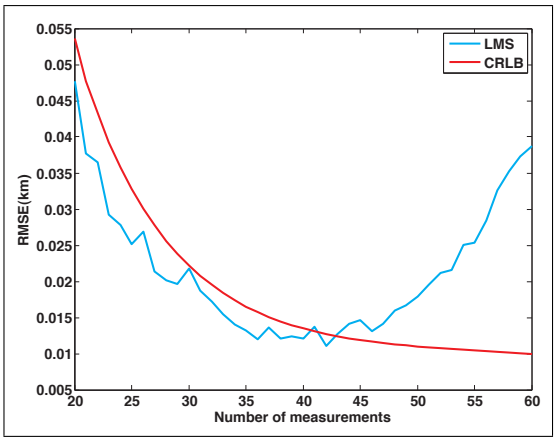

Figure 2.26: RMS error performance of the MLE for moving platform scenario from figure 2.25 as a function of number measurements (AOA-only) taken compared with corresponding CRLB

Close exploration of the figure 2.28 reveals that fusion AOA and TDOA measurement are not as beneficial as one might think.

The accuracy of geolocation is improved, compared with TDOA-only measurement. However, for this GDOP in this geolocation scenario, the estimates obtained by the fused measurements have lower accuracy, compared to AOA only measurements. It is important to realise that the scenario in figure 2.25 presents a challenge for TDOA-only geolocation, due to the small platform separation on initial states.

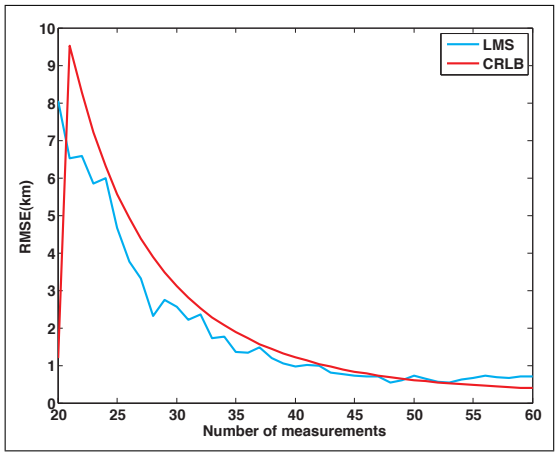

Figure 2.27: RMS error performance of the MLE for moving platform scenario from figure 2.25 as a function of number measurements (TDOA) taken compared with corresponding CRLB

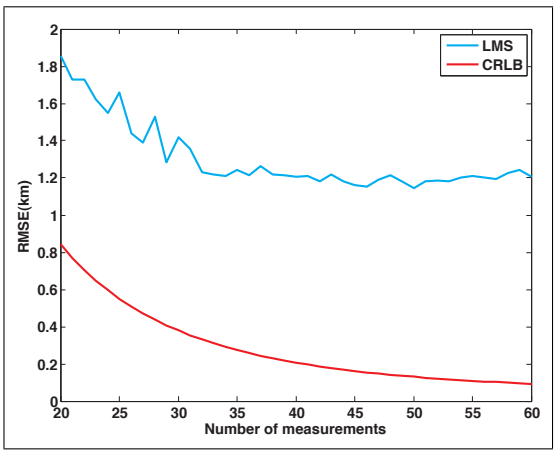

Figure 2.28: RMS error performance of the MLE for moving platform scenario from figure 2.25 as a function of number measurements (AOA and TDOA) taken compared with corresponding CRLB

Thus, using only AOA measurements is more beneficial in this particular case. Such behaviour of uncertainty when fusion of the different type of measurements lead to unexpected degradation of accuracy rather then using estimation using single type of measurements (for example AoA) is consistent, not only for MLE, but for other algorithms presented in this thesis. It has been suggested that this problem may be due to numerical problems when fusing data of different order (AOA - radians, TDOA - seconds) represented in one matrix N. It tends to suggest that the MLE estimator is more biased to one type of measurement than to another when fusing different type of measurements.

It is important to realise that GDOP is dependent on scenario and target position which is unknown *a priori*, thus it not possible to predict which of the type of measurements will lead to better estimate. The important point for use of the fusion of the different type of measurements using MLE that such fusion improves the convergence of the algorithm, however MLE may ignore some measurements if they contribute with likelihood value which is much smaller than other type of measurements. There is an attempt to address the problem of the fusion by introducing the weighting fusion for the estimator and such results presented in chapter 7.

2.1.8 Convergence to minimum

In it of the interest of research to explore the problem of convergence of the MLE algorithm. In the section 2.1.5 the stopping criteria was used

$$\|(\mathbf{G}_{\mathbf{AOA}}^{\mathbf{T}}\mathbf{N}^{-\mathbf{1}}\mathbf{G}_{\mathbf{AOA}})^{-1}\mathbf{G}_{\mathbf{AOA}}^{\mathbf{T}}\mathbf{N}^{-\mathbf{1}}(\boldsymbol{\Theta}-\mathbf{f}(\mathbf{x_0}))\| \geq 2 \tag{2.60}$$

This criteria is a mathematical equivalent of the distance, on which new estimate is moving and MLE will be stopped as soon as new estimate would not move to new

position[1].

In this section the impact of this stopping criteria on MLE will be demonstrated. In order to do this, the scenario in figure 2.29 was set up, where two platforms are moving with a speed 40 m/s and are capable of obtaining an AOA measurement on each 10th second, which correspond to one simulation step, with standard deviation of the measurement error $\sigma_\theta = 0.02$ radians. The true target location is $(90, 40)km$. The MLE algorithm, described above, was applied, without $\|(\mathbf{G_{AOA}^T N^{-1} G_{AOA}})^{-1}\mathbf{G_{AOA}^T N^{-1}}(\mathbf{\Theta} - \mathbf{f(x_0)})\|$ criteria.

In figure 2.30 the 'convergence path' is shown together with the corresponding CRLB ellipse. This figure demonstrates how the MLE improves the initial guess as the number of iterations increases. Figure 2.31 shows the RMS error on each iteration and the corresponding CRLB trace for this scenario (fixed). It can be noted that RMS error of MLE didn't change after 3th or 4th iteration, so repeating the MLE for another 95 iteration didn't improve the estimate. Also, it will be noted that, for this particular simulation, the MLE converges within CRLB the error ellipse as indicated by the final estimate shown in figure 2.30 and RMS error falls, less than the CRLB in figure 2.31. However, this is not always the case as can be seen in figures 2.32 and 2.33. These figures are obtained by repeating exactly the same simulation as plotted in figure 2.29. But the important point is that the MLE converged to this value during the first several iterations. This is known as convergence to a minimum [33]. This important observation demonstrates why MLE estimate doesn't necessarily improve with a increased number of iterations.

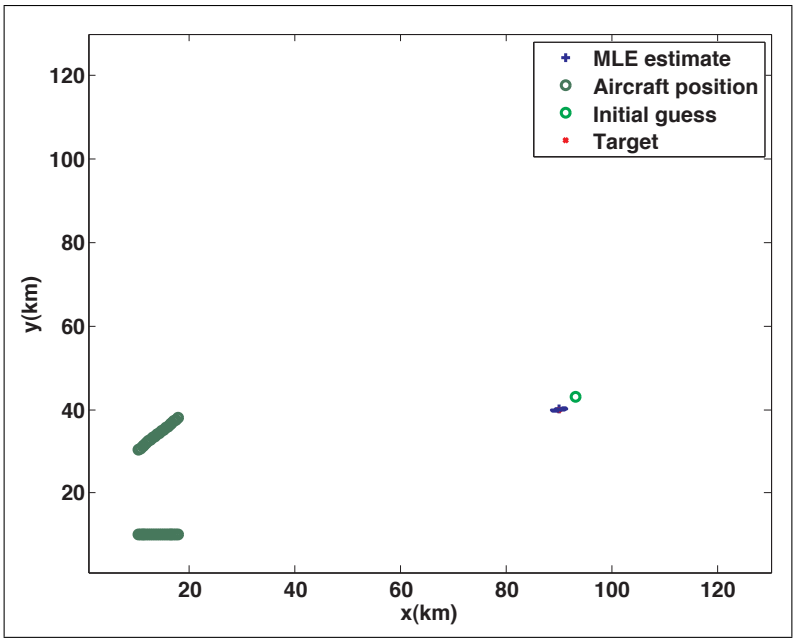

Figure 2.29: Scenario for demonstration convergence to minimum. Geolocation fusing AOA-only measurements from each platform using MLE

[1]See section 9.2.1 in Appendix for more details

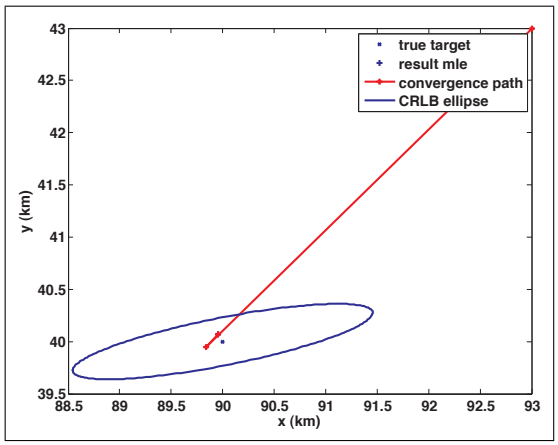

Figure 2.30: Convergence 'walk' of the MLE with 20 measurements without stopping criteria for a 100 iterations

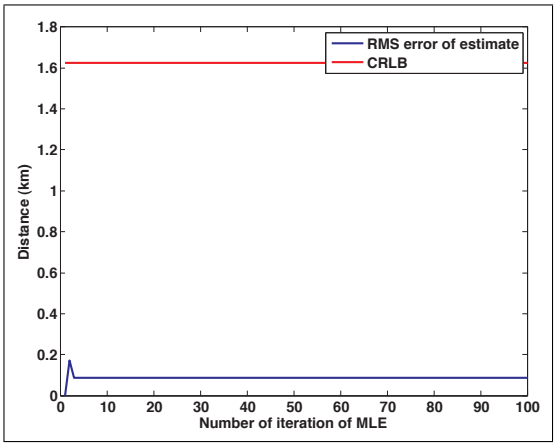

Figure 2.31: RMS error of the MLE with 20 measurements without stopping criteria for a 100 iterations

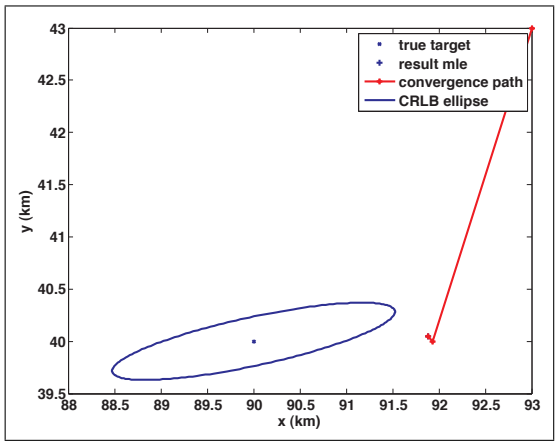

Figure 2.32: Convergence 'walk' of the MLE with 20 measurements without stopping criteria for a 100 iterations. Another run of the simulation in 2.29

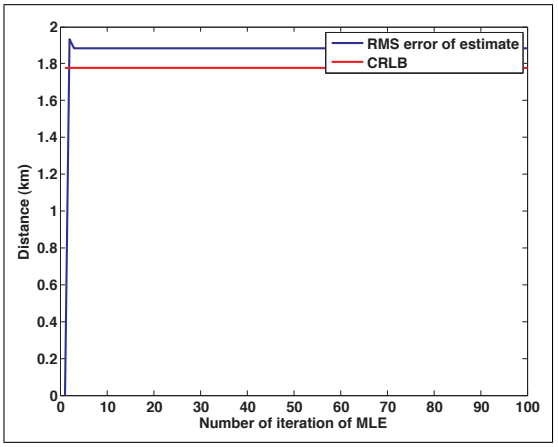

Figure 2.33: RMS error of the MLE with 20 measurements without stopping criteria for a 100 iterations. Another run of the simulation in 2.29

Impact of the stopping criteria

The simulation figure 2.29 was repeated with the previously mentioned stopping criteria (2.60) and the results are plotted in figures 2.34, 2.35 and for a twice as many measurements in figures 2.36, 2.37. It can be noted from this figures that the stopping criteria didn't allow MLE to iterate over more then 3 iterations, thus indicating the convergence to the minimum. Another observation is that additional measurements - twice as many (40), didn't required any additional iterations in order to be fused in MLE.

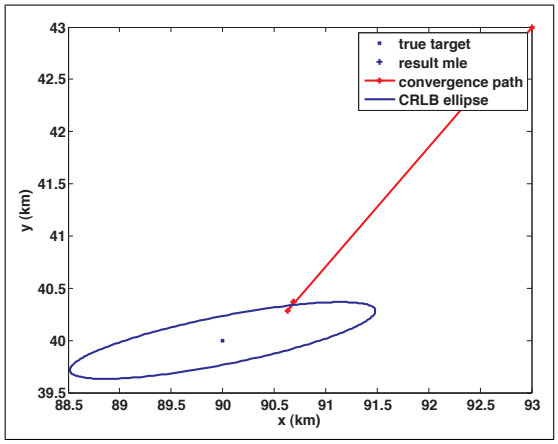

Figure 2.34: Convergence 'walk' of the MLE with 20 measurements taken *with* stopping criteria for a 100 iterations

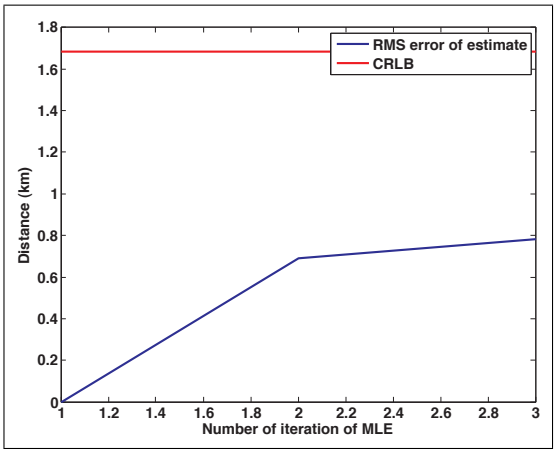

Figure 2.35: RMS error of the MLE with 20 measurements *with* stopping criteria for a 100 iterations

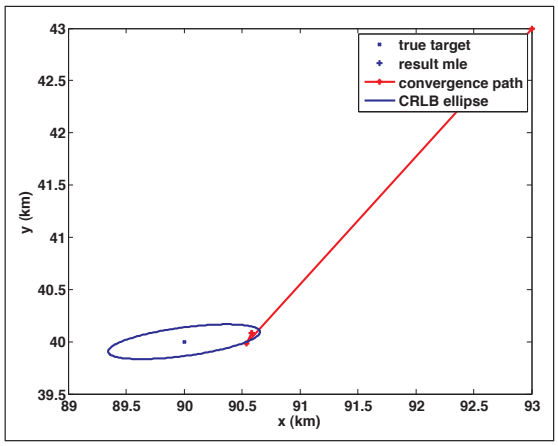

Figure 2.36: Convergence 'walk' of the MLE with 40 measurements taken *with* stopping criteria for a 100 iterations

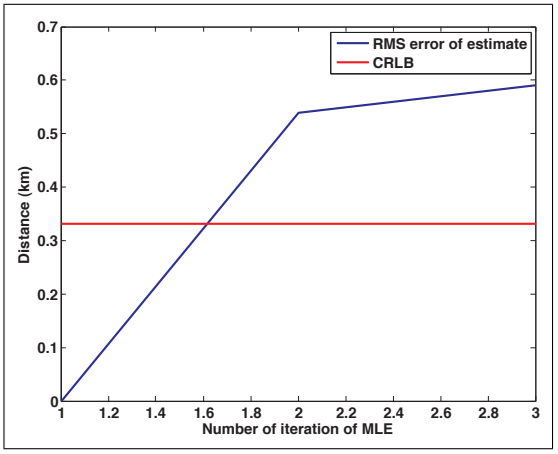

Figure 2.37: RMS error of the MLE with 40 measurements *with* stopping criteria for a 100 iterations

2.1.9 Conclusion

It has been shown that irrespective of the measurement method, the position error depends on the relative geometry of the transmitter location and the locations of the sensor platforms. This effect, known as geometric dilution of precision (GDOP), depends on the baseline between receivers and the nature of measurements. However, a strange effect has been discovered using a combined estimator. The theoretical RMS error is smaller, than the simulated one, when fusing measurements from multiple platforms and multiple parameters. It has been suggested that this problem may be due to numerical problems, when fusing data of different order (AOA - radians, TDOA - seconds) represented in one matrix $\mathbf{N}$. This problem has been highlighted and addressed in the next chapters.

One of the major disadvantages of the MLE is the problem of convergence. Although it is possible to predict the scenario for which MLE estimator would not converge, its inability to provide an estimate may be crucial in military and emergency applications. Another problem, namely the initial guess problem, an unreliable initial guess can increase a number of iterations for the MLE and even prevent the convergence.

Obtaining the initial guess by means of the appropriate transformation of the first measurement (or pair of measurements) indicates that the RF emitter geolocation depends on a sequence, in which measurements are processed. This may provide a poor performance in a situation where geolocation performed in non-line of sight environment, where the first measurement may wildly inaccurate. The following table summarises the advantages and disadvantages of the non-linear maximum likelihood estimator 2.1.9.

Advantages	Disadvantages
Multiple independent methods to a single station are averaged naturally	The method is iterative, requires an initial guess
Multiple measurements and mixed-mode measurements are combined properly, that is, with the correct geometric factors, and can be weighted according to their *a priori* accuracy	It is computationally complex compared to simple plotting of lines of position
The statistical spread of the solution can be found easily and naturally	Being a local correction, its convergence is not assured
Experience indicates that the initial position guess can be quite far off without preventing good convergence. Failure to converge can be detected	Fragile, altering the scenario (target position) can prevent algorithm convergence
Simulation is easy so the convergence can be easily tested	Difficult to fuse different types of measurements (numerical problem)
Computational complexity is less than Kalman filter	Problem of convergence

Table 2.1: Principal advantages and disadvantages of Maximum likelihood estimator

2.2 Sequential Estimators

Recursive estimators can be used to perform three different type of functions, depending upon the application:

- *Filtering:* estimate the state, $\mathbf{X}$, at time t, given samples of $\mathbf{Y}$ at times previous to, and including, t.
- *Prediction:* estimate $\mathbf{X}$ at some future time, $t + K$, given samples of $\mathbf{Y}$ at times previous to, and including, t.
- *Smoothing:* estimate $\mathbf{X}$ at time t, given samples of $\mathbf{Y}$ at times both before and after t

The Kalman filter [34] addresses the problem of estimating the state vector $\mathbf{X} \in \Re^n$ of a discrete time process that is governed by a linear stochastic difference equation:

$$\mathbf{X_k} = \mathbf{A}\mathbf{X_{k-1}} + \mathbf{B}\mathbf{U_k} + \omega_{\mathbf{k-1}} \tag{2.61}$$

with a measurement vector, $\mathbf{Z} \in \Re^m$ that is:

$$\mathbf{Z_k} = \mathbf{H}\mathbf{X_k} + \nu_{\mathbf{k}} \tag{2.62}$$

where $\mathbf{A}$ is an $n \times n$ matrix representing the process model relating the state vector, $\mathbf{X_k}$, at step k to the previous state vector, $\mathbf{X_{k-1}}$, in the absence of either a driving signal or process noise, $\mathbf{B}$ is an $n \times l$ matrix that relates the control input $\mathbf{U} \in \Re^l$ to the state vector $\mathbf{X_k}$, the measurement model, $\mathbf{H}$, is $m \times n$ matrix that relates the kth measurement, $\mathbf{Z_k}$, to the state vector, $\mathbf{X_k}$, and $\omega_{\mathbf{k}}$ and $\nu_{\mathbf{k}}$ are the process and measurement noise vectors respectively. The two types of noise are assumed to be uncorrelated, white, zero mean and with normal probability distributions:

$$p(\omega) \sim \mathbf{N}(0, \mathbf{Q}) \tag{2.63}$$

$$p(\nu) \sim \mathbf{N}(0, \mathbf{R}) \tag{2.64}$$

The process noise covariance, $\mathbf{Q}$, and the measurement noise covariance, $\mathbf{R}$, need not be time-invariant and in practice could change on each time step. Similarly, the process model, $\mathbf{A}$, and the measurement model, $\mathbf{H}$, could also change with each time step. For the two-dimensional geolocation problem, the state, $\mathbf{X_k}$, represents the estimate of the x and y coordinates of the RF emitter, $(\hat{x}_t, \hat{y}_t)$ after the kth measurement, $\mathbf{Z_k}$, has been included. Using the $k-1$ measurements, an *a priori* estimate of the state at step k is obtained. This predicted state is denoted $\mathbf{X_k^-}$. This estimate of the state is then refined when the kth measurement has been taken. The refined value of the state is the *a posteriori* state estimate $\hat{\mathbf{X}}_\mathbf{k}$. The *a priori* and *a posteriori* estimate errors are given by:

$$\mathbf{e_k^-} \equiv \mathbf{X_k} - \hat{\mathbf{X}}_\mathbf{k}^- \tag{2.65}$$

$$\mathbf{e_k} \equiv \mathbf{X_k} - \hat{\mathbf{X}} \tag{2.66}$$

The corresponding *a priori* and *a posteriori* estimate error covariances are, respectively:

$$\mathbf{P_k^-} = E\left[\mathbf{e_k^-}\mathbf{e_k^{-T}}\right] \tag{2.67}$$

$$\mathbf{P_k} = E\left[\mathbf{e_k}\mathbf{e_k^T}\right] \tag{2.68}$$

In the Kalman filter, the *a posteriori* state estimate $\hat{\mathbf{X}}_\mathbf{k}$ is obtained as a linear combination of the *a priori* estimate, $\mathbf{X_k^-}$ and a weighted difference between the actual kth measurement, $\mathbf{Z_k}$ and a prediction of the kth measurement, $\mathbf{H}\hat{\mathbf{X}}_\mathbf{k}^-$:

$$\hat{\mathbf{X}}_\mathbf{k} = \hat{\mathbf{X}}_\mathbf{k}^- + \mathbf{K}(\mathbf{Z_k} - \mathbf{H}\hat{\mathbf{X}}_\mathbf{k}^-) \tag{2.69}$$

The difference $(\mathbf{Z_k} - \mathbf{H}\hat{\mathbf{X}}_\mathbf{k}^-)$ is called the residual and it is a measure of the discrepancy between the predicted measurement, $\mathbf{H}\hat{\mathbf{X}}_\mathbf{k}^-$, and the actual measurement, $\mathbf{Z_k}$. The blending factor, $\mathbf{K}$, is an $n \times m$ matrix called the *Kalman gain* and the values of its elements are chosen to minimise the *a posteriori* error covariance matrix given by (2.68). The minimisation is carried out in the usual way by substituting (2.69) into (2.68), performing the required expectation, taking the derivative of the trace of the result with respect to K and then setting the result to zero, from which K can be solved.

The justification for (2.69) is rooted in the probability of the *a priori* estimate $\hat{\mathbf{X}}_\mathbf{k}^-$ being conditional on all prior measurements according to Bayes Rule. The Kalman filter maintains the first two moments of the state distribution:

$$E[\mathbf{X_k}] = \hat{\mathbf{X}}_\mathbf{k} \tag{2.70}$$

$$E[(\mathbf{X_k} - \hat{\mathbf{X}}_\mathbf{k})(\mathbf{X_k} - \hat{\mathbf{X}}_\mathbf{k})^\mathbf{T}] = \mathbf{P_k} \tag{2.71}$$

The *a posteriori* state estimate given by (2.69) reflects the first moment of the state distribution (assuming the noise distributions to be normally distributed) and the *a posteriori* estimate error covariance equation reflects the second moment. One form of $\mathbf{K}$ that minimises (2.68) is given by:

$$\mathbf{K_k} = \mathbf{P_k^-}\mathbf{H^T}\left(\mathbf{H}\mathbf{P_k^-}\mathbf{H^T} + \mathbf{R}\right)^{-1} \tag{2.72}$$

The equations of the Kalman filter fall into two groups: the *time update* equations and the *measurement update* equations. The time update equations project forward in time the current state and error covariance estimates to obtain the *a priori* estimates for the next time step. The measurement update equations provide feedback and incorporate a new measurement into the *a priori* estimate to provide the improved *a posteriori* estimate. The Kalman filter can be viewed as *predictor-corrector* algorithm for solving numerical problems. The filter time update equations are:

$$\hat{\mathbf{X}}_\mathbf{k}^- = \mathbf{A}\hat{\mathbf{X}}_{\mathbf{k-1}} + \mathbf{B}\mathbf{U_k} \tag{2.73}$$

$$\mathbf{P_k^-} = \mathbf{A}\mathbf{P_{k-1}}\mathbf{A^T} + \mathbf{Q} \tag{2.74}$$

These equations show how the both the state and covariance estimates are projected forward in time from $k-1$ to k. A and B are from (2.61) and Q is from (2.63). The first requirement during measurement update is to compute the Kalman gain, K_k according to (2.72). The next step is to make a measurement, Z_k and from this generate the *a posteriori* state estimate by incorporating the new measurement in (2.69). The final step is to obtain the *a posteriori* error covariance estimate using the following equation:

$$\mathbf{P_k} = (\mathbf{I} - \mathbf{K_k}\mathbf{H})\mathbf{P_k^-} \tag{2.75}$$

where $\mathbf{I}$ is the unit diagonal (identity) matrix. After each time and measurement update pair, the process is repeated with the previous *a posteriori* estimates used to project (or predict) the new *a priori* estimates in a recursive algorithm. In practice, the accuracy or even stability of the Kalman filter depend quite critically on the choices made for the initial estimate of the state vector, $\hat{\mathbf{X}}_\mathbf{0}$ and the error covariance $\mathbf{P_0}$.

Extended Kalman filter

The Kalman filter described in the previous section addresses the problem of estimating the state of a discrete-time process governed by a *linear* stochastic process. In many circumstances, including the case of passive geolocation, either the process equations defined by A or the measurement equations defined by H, or both, are non-linear. In this case the *extended Kalman filter* (EKF) is the form of Kalman filter that linearises the state and/or measurement equations about the current mean and covariance. It is this version of the Kalman filter that has tended to be applied to the problem of passive geolocation following the earlier work of Aidala [35].

For the case of the extended Kalman filter, assume that the state vector is governed by a non-linear stochastic differential equation:

$$\mathbf{X_k} = f(\mathbf{X_{k-1}}, \mathbf{U_k}, \omega_\mathbf{k-1}) \tag{2.76}$$

and that the state vector is related to the measurement vector by a set of non-linear measurement equations:

$$\mathbf{Z_k} = h(\mathbf{X_k}, \nu_\mathbf{k}) \tag{2.77}$$

where $\omega_\mathbf{k}$ and $\nu_\mathbf{k}$ represent the process and measurement noise respectively. In this case, the non-linear functions f relates the state vector at the previous time-stamp, $\mathbf{X_{k-1}}$, to the state at the current time step, $\mathbf{X_k}$ and the non-linear function h relates the current state vector $\mathbf{X_k}$ to the measurement, $\mathbf{Z_k}$ as before. A fundamental flow of the EKF is that the distributions of the various random variables are no longer normal after undergoing their respective non-linear transformations. The EKF is an *ad hoc* state estimator that only approximates the optimality of Bayes rule by linearisation. Linearising the process equation given by (2.76) yields:

$$\mathbf{X_k} \approx \tilde{\mathbf{X}}_\mathbf{k} + \mathbf{A}(\mathbf{X_{k-1}} - \hat{\mathbf{X}}_\mathbf{k-1}) + \mathbf{W}\omega_\mathbf{k-1} \tag{2.78}$$

whilst linearising the measurement equations gives:

$$Z_k \approx \tilde{Z}_k + H(X_k - \tilde{X}_k) + \mathbf{V}\nu_{\mathbf{k}} \tag{2.79}$$

where:

- $\mathbf{X_k}$ and $\mathbf{Z_k}$ are the actual state and measurement vectors
- $\tilde{\mathbf{X}}_\mathbf{k}$ and $\tilde{\mathbf{Z}}_\mathbf{k}$ are the approximate state and measurement vectors obtained by assuming zero process noise and measurement noise
- $\tilde{\mathbf{X}}$ is the *a posteriori* estimate of the state at step k
- the random variables, $\omega_\mathbf{k}$ and $\nu_\mathbf{k}$ represent the process and measurement noise vectors
- A is the Jacobian matrix of partial derivatives of f by X

$$\mathbf{A_{[i,j]}} = \frac{\partial f_{[i]}}{\partial \mathbf{X_{[j]}}}\left(\hat{\mathbf{X}}_{\mathbf{k-1}}, \mathbf{U_k}, 0\right) \tag{2.80}$$

- W is the Jacobian matrix of partial derivatives of f by ω

$$\mathbf{W_{[i,j]}} = \frac{\partial f_{[i]}}{\partial \omega_{[j]}}\left(\hat{\mathbf{X}}_{\mathbf{k-1}}, \mathbf{U_k}, 0\right) \tag{2.81}$$

- H is the Jacobian matrix of partial derivatives of h by $\mathbf{X}$

$$\mathbf{H_{[i,j]}} = \frac{\partial h_{[i]}}{\partial \mathbf{X_{[j]}}}\left(\hat{\mathbf{X}}_{\mathbf{k-1}}, 0\right) \tag{2.82}$$

- V is the Jacobian matrix of partial derivatives of h by X

$$\mathbf{V_{[i,j]}} = \frac{\partial h_{[i]}}{\partial \nu_{[j]}}\left(\hat{\mathbf{X}}_{\mathbf{k-1}}, 0\right) \tag{2.83}$$

where the time-step subscript k, has been dropped from $\mathbf{A}, \mathbf{W}, \mathbf{H}$ and $\mathbf{V}$ for simplicity of notation, even though in practice all the Jacobians will change at each time step. The complete set of equations for the EKF is now similar to those of the Kalman filter, in which the Jacobians need to be computed and replace $\mathbf{A}, \mathbf{H}, \mathbf{W}$ and $\mathbf{V}$ in (2.69)(2.68). The EKF time update equations can be written as:

$$\hat{\mathbf{X}}_\mathbf{k}^- = f(\hat{\mathbf{X}}_{\mathbf{k-1}}, \mathbf{U_k}, 0) \tag{2.84}$$

$$\mathbf{P_k^0} = \mathbf{A_k P_{k-1} A^T} + \mathbf{W_k Q_{k-1} W_k^T} \tag{2.85}$$

Similarly, the EKF measurement update equations are given by:

$$\mathbf{K_k} = \frac{\mathbf{P_k^- H_k^T}}{(\mathbf{H_k P_k^- H^T} + \mathbf{V_k R_k V_k^T})} \tag{2.86}$$

$$\hat{\mathbf{X}}_\mathbf{k} = \hat{\mathbf{X}}_\mathbf{k}^- + \mathbf{K_k}(\mathbf{Z_k} - h(\hat{\mathbf{X}}_\mathbf{k}, 0)) \tag{2.87}$$

$$\mathbf{P_k} = (\mathbf{I} - \mathbf{K_k H_k})\mathbf{P_k^-} \tag{2.88}$$

Iterated Extended Kalman filter

The estimate $\hat{\mathbf{X}}_\mathbf{k}$ can be improved by means of a local iteration of the new measurement [36]. In this method, the state vector, $\hat{\mathbf{X}}_\mathbf{k}$ and the Kalman Gain $\mathbf{K}$ are repeatedly calculated using the linearisation of $h(\hat{\mathbf{X}}_\mathbf{k})$ about the most recent estimate. The sequential structure of the Kalman filter it otherwise unchanged. The aim of the iterated EKF is to ensure that at each step k, the Taylor series expansion of the non-linear function is centered on the state estimate, so that the effect of the non linearity is minimised. The cost is the extra processing steps needed for each new measurement value. The algorithm of the iterated EKF is given by:

- Take new measurement, $\mathbf{Z}_\mathbf{k}$

$$\hat{\mathbf{X}}_{\mathbf{k_{i=0}}} = \hat{\mathbf{X}}_\mathbf{k}^- \tag{2.89}$$

  iterate for $i = 1, 2, \ldots$

$$\mathbf{H}(\hat{\mathbf{X}}_{\mathbf{k_i}}) = \frac{\partial h(\mathbf{X})}{\partial \mathbf{X}}|_{X=\hat{\mathbf{X}}_{\mathbf{k_i}}} \tag{2.90}$$

$$\mathbf{K_i} = \frac{\mathbf{P}_\mathbf{k}^- \mathbf{H}^\mathbf{T}(\hat{\mathbf{X}}_{\mathbf{k_i}})}{(\mathbf{H}(\hat{\mathbf{X}}_{\mathbf{k_i}})\mathbf{P}_\mathbf{k}^-(\mathbf{H}(\hat{\mathbf{X}}_{\mathbf{k_i}})^\mathbf{T} + \mathbf{R})} \tag{2.91}$$

$$\hat{\mathbf{X}}_{\mathbf{ki+1}} = \hat{\mathbf{X}}_\mathbf{k}^- + \mathbf{K_i}(\mathbf{Z_k} - h(\hat{\mathbf{X}}_{\mathbf{k_i}}) - \mathbf{H}(\hat{\mathbf{X}}_{\mathbf{k_i}})(\hat{\mathbf{X}}_\mathbf{k}^- - \hat{\mathbf{X}}_{\mathbf{k_i}})) \tag{2.92}$$

$$\mathbf{P_{ki+1}} = (\mathbf{I} - \mathbf{K_i}\mathbf{H}(\hat{\mathbf{X}}_{\mathbf{k_i}}))\mathbf{P}_\mathbf{k}^- \tag{2.93}$$

- end iteration, take next measurement $\mathbf{Z_{k+1}}$

2.2.1 Application of the EKF to geolocation

The non-linearity associated with the passive geolocation problem depends on the method of geolocation used (AOA, TDOA, FDOA). Consequently, the EKF convergence performance is dependent upon the geolocation method. A lot of papers have assumed 'bearing-only' geolocation. One of the most referenced is Spingarn's paper [36], where he compares the performance of the EKF and iterated EKF with the non-linear least-squares estimator when applied to the problem of 'bearing-only' passive position location. In his paper, he assumed that the sensor platform was moving and the target emitter was stationary resulting in the following linear process (state) equation:

$$\hat{\mathbf{X}}_\mathbf{k}^- = \mathbf{A}\hat{\mathbf{X}}_{\mathbf{k-1}} \tag{2.94}$$

$$\begin{bmatrix} \hat{x}_{t_k}^- \\ \hat{y}_{t_k}^- \end{bmatrix} = \begin{bmatrix} 1 & 0 \\ 0 & 1 \end{bmatrix} \begin{bmatrix} \hat{x}_{t_{k-1}} \\ \hat{y}_{t_{k-1}} \end{bmatrix} \tag{2.95}$$

where the state vector $\mathbf{X}$ represents by the emitter coordinates (x_t, y_t) and the state equations represented by $\mathbf{A}$ in (2.61) are simply update equations given by $\begin{bmatrix} 1 & 0 \\ 0 & 1 \end{bmatrix}$. B of (2.61) is zero and it is assumed that there is no process noise. $\hat{\mathbf{X}}_{\mathbf{k-1}}$ represents the smoothed position estimate of the emitter at time $k-1$ given $k-1$ measurements and $\hat{\mathbf{X}}_{\mathbf{k}}^{-}$ is the predicted position of the emitter at time k given $k-1$ measurements. Spingarn's measurement equation takes the form:

$$\mathbf{Z_k} = \mathbf{h}(\hat{\mathbf{X}}_{\mathbf{k}}) + \nu \tag{2.96}$$

where ν_k is the measurement noise sequence of variance σ_ν^2 (which assumed to be known) and the non-linear function for the bearings-only geolocation method is given by:

$$h(x_t, y_t) = \tan^{-1}\left(\frac{y_t - y_{p_k}}{x_t - x_{p_k}}\right) \tag{2.97}$$

where x_{p_k} and y_{p_k} are the x and y coordinates of the sensor platform at the kth time step. This is, of cause, identical to the measurement equation used for the least squares 'bearing-only' estimator given in 2.1.1.

The corresponding Jacobians are:

$$\frac{\partial \mathbf{h}(\mathbf{X})}{\partial \mathbf{X}}|_{\mathbf{X}=\hat{\mathbf{X}}_{\mathbf{k}}^{-}} = [\mathbf{H_{11}} \quad \mathbf{H_{12}}] \tag{2.98}$$

where

$$\mathbf{H_{11}} = \frac{\partial h}{\partial x_t}|_{x_t=\hat{x}_{t_k}^{-}} = \frac{-u}{1+u^2}\frac{1}{\hat{x}_{t_k}^{-} - x_{p_k}} \tag{2.99}$$

$$\mathbf{H_{12}} = \frac{\partial h}{\partial y_t}|_{y_t=\hat{y}_{t_k}^{-}} = \frac{1}{1+u^2}\frac{1}{\hat{x}_{t_k}^{-} - x_{p_k}} \tag{2.100}$$

and

$$u = \frac{\hat{y}_{t_k}^{-} - y_{p_k}}{\hat{x}_{t_k}^{-} - x_{p_k}} \tag{2.101}$$

Although it is assumed that there is no process noise for the case of linear process and non-linear measurement, the updated error covariance matrix for Spingarn's implementation of the EFK is given by (2.85), with $\mathbf{W} = \begin{bmatrix} 1 & 0 \\ 0 & 1 \end{bmatrix}$ and $\mathbf{Q} = \begin{bmatrix} 0 & 0 \\ 0 & q_{22} \end{bmatrix}$. In this case, the process noise term q_{22} is included but it is only a very small number and is used to prevent the $\mathbf{P}$ matrix from becoming singular. This is a common practice. In order to initialize the EKF, the *a priori* estimate of the state vector and the error covariance matrix must be obtained for time step $k = 0$:

$$\hat{\mathbf{X}}_{\mathbf{0}} = \begin{bmatrix} \hat{x}_{t_0} \\ \hat{y}_{t_0} \end{bmatrix} \tag{2.102}$$

$$\mathbf{P_0} = \begin{bmatrix} \sigma_x^2 & 0 \\ 0 & \sigma_y^2 \end{bmatrix} \tag{2.103}$$

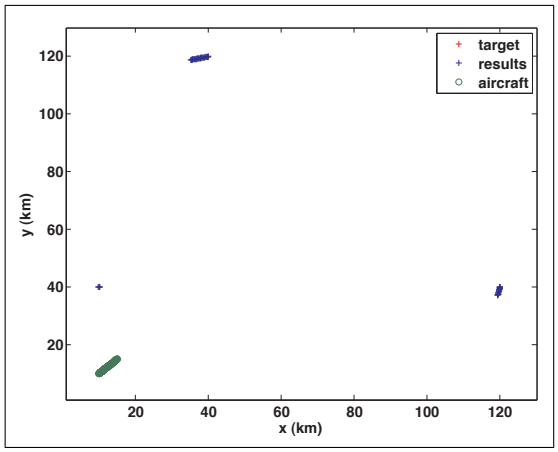

Figure 2.38: Simulation scenario from Spingarn's publication [36]. One aircraft capable to obtain AOA measurements. Geolocation using EKF

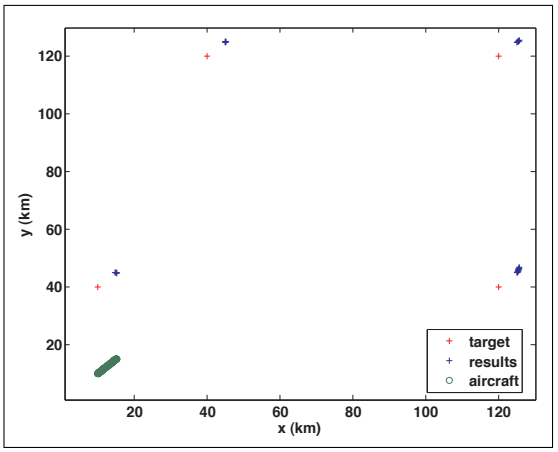

Figure 2.39: Simulation scenario from [36], where EKF doesn't converge. Scenario in figure 2.38 with initial guessed moved for 5 km

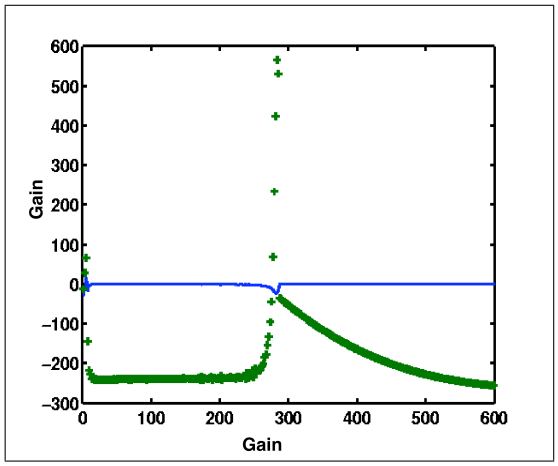

Figure 2.40: Kalman gain for geolocation using EKF for the scenario in figure 2.39

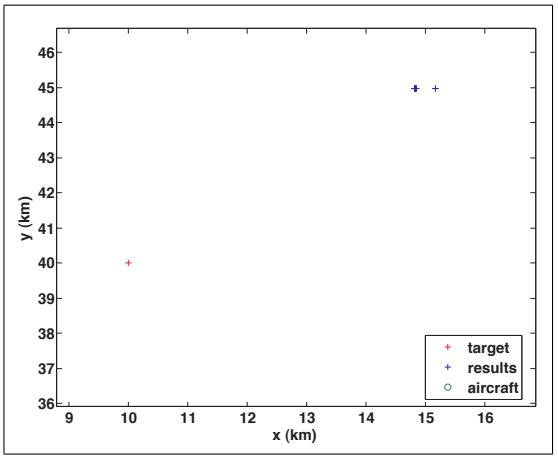

Figure 2.41: Zoomed results from EKF simulation, initial guess moved to 5 km off the true target position

Based on the Spingarn publication [36], an EKF algorithm was adapted to the geolocation problem and tested using a Matlab simulation. This method of sequential estimation has the advantage that emitter location estimates are obtained after the first two measurements. These are then progressively refined as subsequent measurements are incorporated. Figure 2.38 demonstrate a flight path of aircraft, taking AOA measurements on each step. The emitter (target) is placed in different quadrants in the positions $(10, 40)$km, $(120, 120)$km, $(120, 40)$ and $(40, 120)$km.

Estimates corresponding to each target position are plotted on the same figure as blue crosses. This estimates overlap true target position, indicating very small distance from true target position.

Whilst it is possible to replicate published results of simple geolocation algo-

rithms under the same conditions described in the forementioned publication as plotted on figure 2.38, generally the algorithms are not robust. As soon as an initial guess moves from a true target position for more than 2 km, the EKF cannot converge to the true target position and will ignore provided measurements as demonstrated in figure 2.39, where estimates obtained are always close to initial guess, but not to true target position. Figure 2.41 shows zoomed Kalman filter estimates around true target located $(10, 40)$km. It this case initial guess was moved to 5 km away from true target position, and Kalman gain plotted in figure 2.40 indicates that EFK doesn't converge in this case.

The reason for this appears to be the extreme non-linearity of the measurement equations that must be used to achieve geolocation. Two possible techniques that may solve the problem are:

- to use direction cosines in place of the Cartesian coordinate system currently being used;
- to use a coordinate transformation as proposed by Aidala and Hammel[35] for bearings only tracking of submarines.

In addition, other approaches, described in the next chapters, are being considered in which the EKF is replaced by other algorithms.

2.2.2 Conclusion

The Kalman filtering approach to geolocation proved to be overly dependent on the initial guess and therefore is not applicable for this research. Although maximum likelihood algorithm showed a good performance, there are number of disadvantages.

- Initial guess required, although it is not so sensitive as Kalman filter.
- When measurement error increases, number of iteration before algorithm can provide an estimate increases significantly
- It relies on approximation using Taylor series expansion
- Batch processing. This algorithm has to be processed after certain number of measurements has been completed.
- Centralized.
- Iterative.

In order to continue research for Non-Line-Of-Sight (NLOS) geolocation, a robust and effective algorithm has to be developed, which should satisfy the following criteria:

- be independent of an initial guess or should work without any *a priori* knowledge of estimated position
- non-iterative
- should be able to provide a rough estimate at any step

Chapter 3

Geolocation using Particle Filter

The particle filter has been widely used for target tracking [7] and other applications, such as state estimation, model estimation [37], mobile handset tracking in cellular networks [13],[38] and in-door localisation [39],[40].

Here, the use of the particle filter for the geolocation of radio emitters will be explored. Although this application appears to be similar to target tracking, there is a significant difference - in the case of geolocation the conditions of the target do not change with time, but the sensor positions do. The particle filter can be viewed as a sequential estimator according to the classification presented in section 2.2. This chapter will first introduce the concept of perfect Monte-Carlo sampling , then importance resampling and later sequential importance sampling leading to the particle filter. Then particle filter will be adapted to the problem of geolocation and then highlight some problems of application the particle filter, namely convergence particle degeneracy and random walk. In the later chapters, the particle filter will be applied to geolocation of radio frequency emitter in non-line-of-sight conditions.

3.1 Introduction to particle filter

Problem statement

According to [6] and it is traditional in signal processing that signals can be modelled as Markovian, nonlinear, non-Gaussian state space models. The unobserved signal (hidden states) $\{\mathbf{x}_t; t \in \mathbf{N}\}$, $\mathbf{x}_t \in \mathcal{X}$ is modelled as a *Markov process* of initial distribution $p(\mathbf{x_0})$ and transition equation $p(\mathbf{x_t}|\mathbf{x_{t-1}})$. The observations $\{\mathbf{y}_t; t \in \mathbf{N}^*\}$, $\mathbf{y_t} \in \mathcal{Y}$, are assumed to be conditionally independent given the process $\mathbf{x}_t; t \in \mathbf{N}$ and of marginal distribution $p(\mathbf{y}_t|\mathbf{x}_t)$. To sum up, the model is described by

$$p(\mathbf{x_0}) \tag{3.1}$$

$$p(\mathbf{x}_t|\mathbf{x_{t-1}}) \quad for\ t \geq 1 \tag{3.2}$$

$$p(\mathbf{y}_y|\mathbf{x_t}) \quad for\ t \geq 1. \tag{3.3}$$

where $\mathbf{x}_{0:t} \triangleq \{\mathbf{x_0} \ldots, \mathbf{x_t}\}$ and $\mathbf{y}_{1:t} \triangleq \{\mathbf{y_1} \ldots, \mathbf{y_t}\}$, denote respectively, the signal and the observation at the time t. The aim is to estimate recursively in time the *posterior distribution* $p(\mathbf{x_{0:t}}|\mathbf{y_{1:t}})$, its associated features (including the marginal distribution $p(\mathbf{x_t}|\mathbf{y_{1:t}})$, known as *filtering distribution*), and the expectations

$$I(f_t) = \mathbf{E}_{p(\mathbf{x}_{0:t}|\mathbf{y}_{1:t})}\left[f_t(\mathbf{x}_{0:t})\right] \triangleq \int f_t(\mathbf{x}_{0:t}) p(\mathbf{x}_{0:t}|\mathbf{y}_{1:t}) d\mathbf{x_{0:t}} \tag{3.4}$$

for some function of interest $f_t : \mathcal{X}^{(t+1)} \rightarrow \mathbf{R}^{n_{f_t}}$ integrable with respect to $p(\mathbf{x_{0:t}}|\mathbf{y_{1:t}})$. Example of appropriate functions include the conditional mean, in which case $f_t(\mathbf{x}_{0:t}) = \mathbf{x}_{0:t}$, or the conditional covariance of $\mathbf{x}_t$ where $f_t(\mathbf{x}_{0:t}) = \mathbf{x_t}\mathbf{x_t}^T - \mathbf{E}_{p(\mathbf{x_t}|\mathbf{y_{1:t}})}[\mathbf{x_t}]\mathbf{E}^T_{p(\mathbf{x_t}|\mathbf{y}_{1:t})}[\mathbf{x_t}]$ At any time t, the posterior distribution is given by *Bayes theorem*

$$p(\mathbf{x}_{0:t}|\mathbf{y}_{1:t}) = \frac{p(\mathbf{y}_{1:t}|\mathbf{x}_{0:t})p(\mathbf{x}_{0:t})}{\int p(\mathbf{y}_{1:t}|\mathbf{x}_{0:t}) d\mathbf{x_{0:t}}}. \tag{3.5}$$

It is possible to obtain straightforwardly a recursive formula for this joint distribution $p(\mathbf{x}_{0:t}|\mathbf{y}_{1:t})$,

$$p(\mathbf{x}_{0:t+1}|\mathbf{y}_{1:t+1}) = p(\mathbf{x}_{0:t}|\mathbf{y}_{1:t}) \frac{p(\mathbf{y}_{t+1}|\mathbf{x}_{t+1}) p(\mathbf{x}_{t+1}|\mathbf{x}_t)}{p(\mathbf{y}_{t+1}|\mathbf{y}_{1:t})} \tag{3.6}$$

The marginal distribution $p(\mathbf{x}_t|\mathbf{y}_{1:t})$ also satisfies the following recursion.

$$Prediction: \; p(\mathbf{x}_t|\mathbf{y}_{1:t-1}) = \int p(\mathbf{x}_t|\mathbf{x}_{t-1}) p(\mathbf{x}_{t-1}|\mathbf{y}_{1:t-1}) d\mathbf{x}_{t-1}; \tag{3.7}$$

$$Updating: \; p(\mathbf{x}_t|\mathbf{y}_{1:t}) = \frac{p(\mathbf{y}_t|\mathbf{x}_t) p(\mathbf{x}_t|\mathbf{y}_{1:t-1})}{\int p(\mathbf{y}_t|\mathbf{x}_t) p(\mathbf{x}_t|\mathbf{y}_{1:t-1}) d\mathbf{x}_t}. \tag{3.8}$$

These expressions and recursions are deceptively simple because one cannot typically compute the normalizing constant $p(\mathbf{y}_{1:t})$, the marginals of the posterior $p(\mathbf{x}_{0:t}|\mathbf{y}_{1:t})$, in particular $p(\mathbf{x}_t|\mathbf{y}_t)$, and $I(f_t)$ since they require the evaluation of complex high dimensional integrals. This is why, from the mid-1960, a great many papers and books have been devoted to obtaining approximations for this distributions, including, as described in previous chapter, the extended-Kalman filter [41] [42], the Gaussian sum filter [43] and grid-based methods [44]. The work in automatic control was done during the 60s and 70s based on Sequential Monte Carlo methods [45]. Most likely because of the modest computers available at the time, these last algorithms were overlooked and forgotten. In the late 1980s, the great increase of computational power made possible rapid advances in numerical integration methods for Bayesian filtering [46]. To address the problems described above, many scientific and engineering disciplines have recently devoted a considerable effort towards the study and development of *Monte Carlo*(MC) integration methods. These methods have the great advantage of not being subject to any linearity or Gaussian constraints on the model, and they also have appealing convergence properties.

In this section it will be shown that, when one has a large number of samples drawn from the required posterior distributions, it is not difficult to approximate the intractable integrals appearing in equations (3.6)-(3.8). It is, however, seldom possible to obtain samples from these distributions directly. One therefore has to

resort to alternative MC methods, such as importance resampling. By making this general MC techniques recursive, one obtains the *sequential importance sampling* (SIS) method. Unfortunately, it can easily be shown that SIS is guaranteed to fail as t increases. This problem can be summoned by including an additional selection step. The introduction of this key step in [37] led to the first operationally effective method.

Perfect Monte Carlo sampling

Assuming that it is possible to simulate N independent and identically distributed random samples, also named particles, $\{\mathbf{x}_{0:t}^{(i)};\ i = 1, \ldots, N\}$ according to $p(\mathbf{x_{0:t}}|\mathbf{y}_{1:t})$. An empirical estimate of this distribution is given by

$$P_N(d\mathbf{x_{0:t}}|\mathbf{y}_{0:t}) = \frac{1}{N}\sum_{i=1}^{N}\delta_{\mathbf{x}_{0:t}^{(i)}}(d\mathbf{x}_{0:t}) \tag{3.9}$$

where $\delta_{\mathbf{x}_{0:t}^{(i)}}(d\mathbf{x}_{0:t})$ denotes the delta-Dirac mass located in $\mathbf{x}_{0:t}^{(i)}$. One obtains the following estimate of $I(f_t)$

$$I_N(f_t) = \int f_t(\mathbf{x}_{0:t})P_N(d\mathbf{x}_{0:t}|\mathbf{y}_{1:t}) = \frac{1}{N}\sum_{i=1}^{N} f_t(\mathbf{x}_{0:t}^{(i)}). \tag{3.10}$$

This estimate is unbiased and, if the posteriori variance of $f_t(\mathbf{x}_{0:t})$ satisfies $\sigma_{f_t}^2 \triangleq \mathbf{E}_{p(\mathbf{x}_{0:t})|y_{1:t}}[f_t^2(\mathbf{x}_{0:t})] - I^2(f_t) \leq +\infty$, then the variance of $I_N(f_t)$ is equal to $var(I_N(f_t)) = \frac{\sigma_{f_t}^2}{N}$. Clearly, from the strong law of large numbers,

$$I_N(f_t) \xrightarrow[N\to+\infty]{a.s.} I(f_t), \tag{3.11}$$

where $\xrightarrow[N\to+\infty]{a.s.}$ denotes almost sure convergence. Moreover, if $\sigma_{f_t}^2 \leq +\infty$, then a central limit theorem holds

$$\sqrt{N}[I_N(f_t) - I(f_t)] \underset{N\to+\infty}{\Longrightarrow} \mathcal{N}(0, \sigma_{f_t}^2) \tag{3.12}$$

where $\underset{N\to+\infty}{\Longrightarrow}$ denotes convergence in distribution. The advantage of this perfect MC method as follows: from the set of random samples $\left\{\mathbf{x}_{0:t}^{(i)};\ i = 1, \ldots, N\right\}$, one can easily estimate any quantity $I(f_t)$ and the rate of convergence of this estimate is *independent of the dimension of the integrand*. In contrast, any deterministic numerical integration method has a rate of convergence that decreases as the dimension of the integrand increases. Unfortunately, it is usually impossible to sample efficiently from the posterior distribution $p(\mathbf{x}_{0:t}|\mathbf{y}_{1:t})$ at any time t, $p(\mathbf{x}_{0:t}|\mathbf{y}_{1:t})$ being multivariate, non-standard, and only known up to a proportionality constant. In applied statistics, Markov chain Monte Carlo (MCMC) are a popular approach to sampling from such complex probability distributions [47]. However, MCMC methods are iterative algorithms unsuited to recursive estimation problems, so, alternative methods were developed.

Importance sampling

An alternative classical solution consists of using the *importance resampling* method, for example [48]. An arbitrary so-called *importance sampling distribution* (also often referred to as the proposal distribution or the importance function) $\pi(\mathbf{x}_{0:t}|y_{1:t})$ can be introduced. Assuming that it is possible to evaluate $I(f_t)$, and provided that the support of $\pi(\mathbf{x}_{0:t}|y_{1:t})$ includes the support of $p(\mathbf{x}_{0:t}|y_{1:t})$, yields to the identity

$$I(f_t) = \frac{\int f_t(\mathbf{x}_{0:t}) w(\mathbf{x}_{0:t}) \pi(\mathbf{x}_{0:t}|\mathbf{y}_{1:t}) d\mathbf{x}_{0:t}}{\int w(\mathbf{x}_{0:t}) \pi(\mathbf{x}_{0:t}|y_{1:t}) d\mathbf{x}_{0:t}} \tag{3.13}$$

where $w(\mathbf{x}_{0:t})$ is known as the *importance weight*,

$$w(\mathbf{x}_{0:t}) = \frac{p(\mathbf{x}_{0:t}|y_{1:t})}{\pi(\mathbf{x}_{0:t}|y_{1:t})} \tag{3.14}$$

Consequently, if one can simulate N i.i.d. particles $\left\{\mathbf{x}_{0:t}^{(i)};\ i = 1, \ldots, N\right\}$ according to $\pi(\mathbf{x}_{0:t}|y_{1:t})$, a possible Monte Carlo estimate of $I(f_t)$ is

$$\hat{I}_N(f_t) = \frac{\frac{1}{N}\sum_{i=1}^{N} f_t(\mathbf{x}_{0:t}^{(i)}) w(\mathbf{x}_{0:t}^{(i)})}{\frac{1}{N}\sum_{j=1}^{N} w(\mathbf{x}_{0:t}^{(i)})} = \sum_{i=1}^{N} f_t(\mathbf{x}_{0:t}^{(i)}) \tilde{w}_t^{(i)} \tag{3.15}$$

where the *normalised importance weights* $\tilde{w}_t^{(i)}$ are given by

$$\tilde{w}_t^{(i)} = \frac{w_t^{(i)}}{\sum_{j=1}^{N} w_t^{(i)}} \tag{3.16}$$

For N is finite, $\hat{I}_N(f_t)$ is biased (ration of two estimates) but asymptotically, under weak assumptions, the strong law of large numbers applies, that is, $I_N(f_t) \xrightarrow[N\to+\infty]{a.s.} I(f_t)$. Under additional assumptions, a central limit theorem with a convergence rate still independent of the dimension of the integrand can be obtained [48]. It is clear that this integration method cab also be interpreted as a sampling method, where the posterior distribution $p(\mathbf{x}_{0:t}|\mathbf{y}_{1:t})$ is approximated by:

$$\hat{P}_N(d\mathbf{x}_{0:t}|\mathbf{y}_{1:t}) = \sum_{i=1}^{N} \tilde{w}_t^{(i)} \delta_{\mathbf{x}_{0:t}^{(i)}}(d\mathbf{x}_{0:t}) \tag{3.17}$$

and $\hat{I}_N(f_t)$ is nothing but the function $f_t(\mathbf{x}_{0:t})$ integrated with respect to the empirical measure $\hat{P}_N(d\mathbf{x}_{0:t}|\mathbf{y}_{1:t})$:

$$\hat{I}_N(f_t) = \int f_t(\mathbf{x}_{0:t}) \hat{P}_N(d\mathbf{x}_{0:t}|\mathbf{y}_{1:t}) \tag{3.18}$$

Importance sampling is a general Monte Carlo integration method. However, there is a problem with this method - one needs to get all the data $y_{1:t}$ before estimating $p(\mathbf{x}_{0:t}|\mathbf{y}_{1:t})$. In general, each time new data y_{t+1} become available, one needs to recompute the importance weights over the entire state sequence. The computational complexity of this operation increases with time. Next, the strategy to overcome this problem is presented.

Sequential Importance Sampling

The importance sampling method can be modified so that it becomes possible to compute an estimate $\hat{P}_N(d\mathbf{x}_{0:t}|\mathbf{y}_{1:t})$ of $p(\mathbf{x}_{0:t}|\mathbf{y}_{1:t})$ without modifying the past simulated trajectories $\left\{\mathbf{x}_{0:t}^{(i)};\ i=1,\ldots,N\right\}$. This means that the importance function $\pi(\mathbf{x}_{0:t}|y_{1:t})$ at time t admits as marginal distribution at time $t-1$ the importance function $\pi(\mathbf{x}_{0:t-1}|y_{1:t-1})$, that is

$$\pi(\mathbf{x}_{0:t}|\mathbf{y}_{1:t}) = \pi(\mathbf{x}_{0:t-1}|\mathbf{y}_{1:t-1})\pi(\mathbf{x}_{0:t-1}|\mathbf{y}_{1:t}) \tag{3.19}$$

Iterating, one obtains

$$\pi(\mathbf{x}_{0:t}|\mathbf{y}_{1:t}) = \pi(\mathbf{x}_0)\prod_{k=1}^{t}\pi(\mathbf{x}_k, \mathbf{x}_{0:k-1}|\mathbf{y}_{1:k}) \tag{3.20}$$

It is easy to see that the importance function allows to evaluate recursively in time the importance weights (3.16). Indeed, one has

$$\tilde{w}_t^{(i)} \propto \tilde{w}_{t-1}^{(i)}\frac{p(\mathbf{y}_{1:t}|\mathbf{x}_t^{(i)})p(\mathbf{x}_t^{(i)}|\mathbf{x}_{t-1}^{(i)})}{\pi(\mathbf{x}_{0:t}|\mathbf{x}_{0:t-1}, \mathbf{y}_{1:t})} \tag{3.21}$$

An important particular case for this framework arises when the prior distribution as importance distribution is adopted

$$\pi(\mathbf{x}_{0:t}|\mathbf{y}_{1:t}) = p(\mathbf{x}_{0:t}) = p(\mathbf{x}_0)\prod_{k=1}^{t}p(\mathbf{x}_k|\mathbf{x}_{k-1}) \tag{3.22}$$

In this case, the importance weights satisfy $\tilde{w}_t^{(i)} \propto \tilde{w}_{t-1}^{(i)}p(\mathbf{y}_t|\mathbf{x}_t^{(i)})$. In the next section the use of the prior distribution will be restricted to the case of importance resampling distribution, but it is important to keep in mind that the method is far more general than this. SIS is an attractive method, but it is only constrained version of importance resampling. Unfortunately, it is well known that importance resampling is usually inefficient in high-dimensional spaces [47], so as t increases, this problem will arise in SIS setting.

Particle filter

The problem encountered by the SIS method is that, as t increases, the distribution of the importance weights $\tilde{w}_t^{(i)}$ becomes more and more skewed. Practically, after the few steps only, only one particle has a non-zero importance weight. The algorithm, consequently, fails to represent the posterior distributions of interest adequately. To avoid this degeneracy, one needs to introduce an additional selection step.

The key idea of the particle (bootstrap) filter is to eliminate the particles having low importance weights $\tilde{w}_t^{(i)}$ [37]. Formally, the weighted empirical distribution $\hat{P}_N(d\mathbf{x}_{0:t}|\mathbf{y}_{1:t}) = \sum_{i=1}^{N}\tilde{w}_t^{(i)}\delta_{\mathbf{x}_{0:t}}(d\mathbf{x}_{0:t})$ is replaced by the unweighted measure:

$$\hat{P}_N(d\mathbf{x}_{0:t}|\mathbf{y}_{1:t}) = \frac{1}{N}\sum_{i=1}^{N}N_t^{(i)}\delta_{\mathbf{x}_{0:t}}(d\mathbf{x}_{0:t}) \tag{3.23}$$

where $N_t^(i)$ is the number of offspring associated to particle $\mathbf{x}_{0:t}$; It is an integer number such that $\sum_{i=1}^{N} N_t^{(i)} = N$. If $N_t^{(j)} = 0$, then the particle $\mathbf{x}_{0:t}^{(j)}$ dies. The $N_t^{(j)}$ are chosen such that $P_N(d\mathbf{x}_{0:t}|\mathbf{y}_{1:t})$ is close to $\hat{P}_N(d\mathbf{x}_{0:t}|\mathbf{y}_{1:t})$ in the sense that, for any function f_t,

$$\int f_t(\mathbf{x}_{0:t}) P_N(d\mathbf{x}_{0:t}|\mathbf{y}_{1:t}) \approx \int f_t(\mathbf{x}_{0:t}) \hat{P}_N(d\mathbf{x}_{0:t}|\mathbf{y}_{1:t}) \tag{3.24}$$

After the selection step, the surviving particles $\mathbf{x}_{0:t}^{(i)}$, that is the ones with $N_t^{(i)} \geq 0$, are thus approximately distributed according to $p(\mathbf{x}_{0:t}|\mathbf{y}_{1:t})$. There are many different ways to select the $N_i^{(i)}$, the most popular being the one introduced in [37]. Here, one obtains the surviving particles by sampling N times from the discrete distribution $\hat{P}(d\mathbf{x}_{0:t}|\mathbf{y}_{1:t})$; this is equivalent to sampling the number of offsprings $N_t^{(i)}$ according to a multinomial distribution of parameters $\tilde{w}_t^{(i)}$. Equation (3.24) is satisfied in the sense that one can check easily that, for any bounded function f_t with $\|f_t\| = \sup_{\mathbf{x}_{0:t}} |f_t \mathbf{x}_{0:t}|$, there exists C such that

$$\mathbf{E}\left[\left(\int f_t \mathbf{x}_{0:t} P_N(d\mathbf{x}_{0:t}|\mathbf{y}_{1:t}) - \int f_t(\mathbf{x}_{0:t}) \hat{P}_N(\mathbf{x}_{0:t}|\mathbf{y}_{1:t})\right)^2\right] \leq \frac{C\|f_t\|^2}{N} \tag{3.25}$$

Particle filter algorithm

Particle filter(PF) algorithm can be described in details as follows:

1. *Initialization, t=0*:
   - For $i = 1, ...N$, sample $x_0^{(t)} \backsim p(x_0)$ and set t=1.
2. *Importance sampling step*:
   - For $i = 1, ...N$, sample $\tilde{x}_t^{(i)} \backsim p(x_t|x_{t-1}^{(i)})$
   - Set $\tilde{x}_{0:t}^{(i)} = \left(x_{0:t-1}^{(i)}, \tilde{x}(i)_t\right)$
   - For $i = 1, \ldots N$, evaluate the importance weights
   $$\tilde{w}_t^{(i)} = p(y_t|\tilde{x}_t^{(i)}). \tag{3.26}$$
   - Normalise the importance weights.
3. *Selection step*
   - Resample with replacement N particles $\left(x_{0:t}^{(i)}; i = 1, \ldots, N\right)$ from the set $\left(\tilde{x}_{0:t}^{(i)}; i = 1, \ldots, N\right)$ according to importance weights
   - Set $t \leftarrow t + 1$ and go to step 2

Note that in equation (3.26), $\tilde{w}_{t-1}^{(i)}$ does not appear because the propagated particles $x_{0:t-1}^{(i)}$ have uniform weights after the resampling step at time $t - 1$. Also it is not

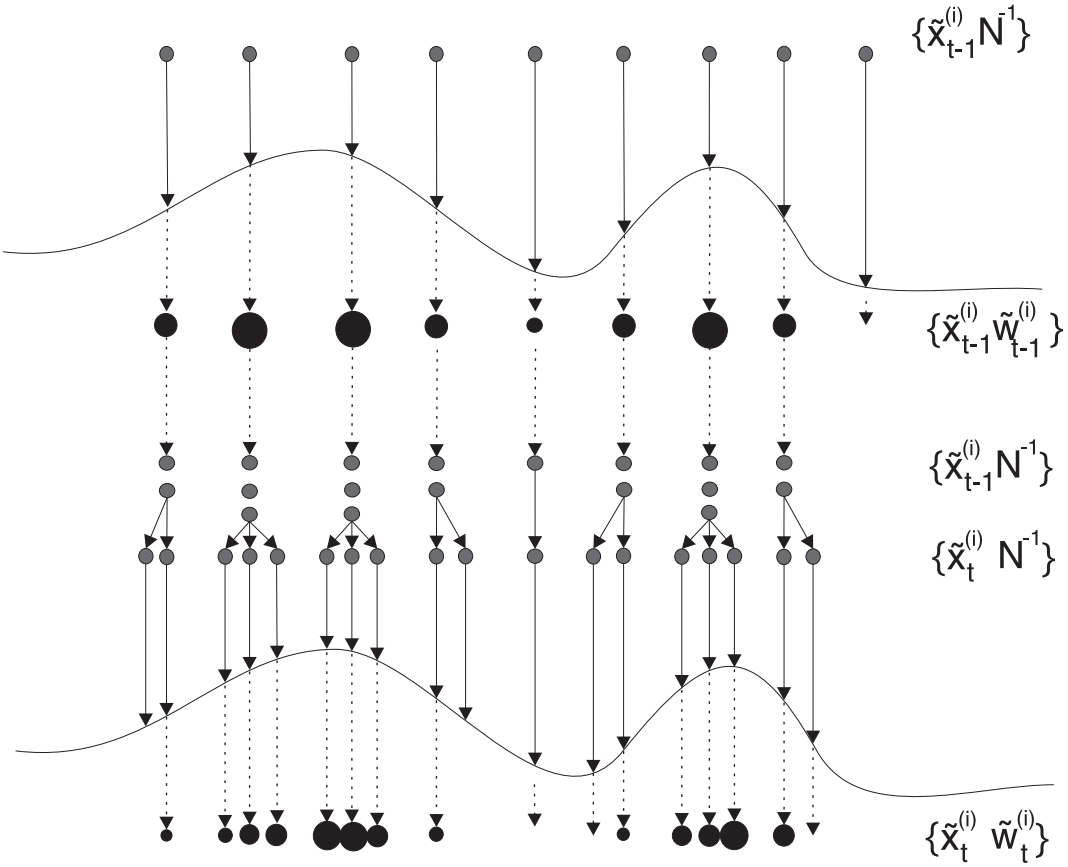

Figure 3.1: In this example, the particle filter starts at time $t-1$ with an unweighted measure $\tilde{x}^(i)_{t-1}, N^{-1}$, where $N = 1, .., 9$ particles. This provides an approximation of $p(x_{t-1}, |y_{1:t-2})$. For each particle the importance weights are computed using the information at time $t-1$. This results in the weighted measure $\tilde{x}^(i)_{t-1}, \tilde{w}^(i)_{t-1}$, which yields an approximation $p(x_{t-1}|y_{1:t-1})$. Subsequently, the resampling step selects only the fittest particles to obtain the unweighted measure $\tilde{x}^(i)_{t-1}, N^-1$, which is still an approximation of $p(x_{t-1}|y_{1:t-1})$. Finally, the sampling (prediction) step introduces variety, resulting in the measure $\tilde{x}^(i)_t, N^{-1}$, which is an approximation of $p(x_t|y_{y=1:t-1})$.

necessary to store the paths of the particles from 0 to time t if $p(x_t|y_{1:t})$ estimate is of the interest. A graphic representation of the algorithm is shown in figure 3.1 which is similar to one in [37]. The particle filter algorithm has several attractive properties. Firstly it is very quick and easy to implement. Secondly, it is to a large extend modular. That is, when changing the problem one need only change the expression for the importance distribution and the importance weight in the code. Thirdly, it can be straightforwardly implemented on a parallel computer. Finally, the resampling step is a black box routine that only requires as inputs the importance weights and indices (both being one dimensional quantities). This enables one to easily carry out sequential inference for very complex models.

3.2 Adaptation of the Particle filter for geolocation

In order to illustrate the application of the particle filter to the geolocation problem, the scenario shown in figure 3.2 was considered. In this scenario, the platform moves North according to a wavy path and is capable of obtaining one AOA measurement on each step, with a standard deviation of the measurement error $\sigma_\theta = 0.02$ radian. Wavy path was chosen due to the experience from MLE and impact of the GDOP on the estimator performance. It was observed that the worse performance for AoA measurements when target located in the direction of the motion of the platform as in figure 2.7, therefore wavy path was chosen as one which may provide better accuracy of the estimation.

The platform positions at each time step are denoted as green circles. The target is located at $(60, 50)$km. In order to apply the particle filter algorithm for geolocation using AOA measurements, the conditional probability $p(x, y|\theta_i)$, of the target being located at some point (x, y) within the search space given the measurement θ_i, has been used in a weighting process. This conditional probability for the AOA measurements has the form:

$$p(x, y|\theta_i) = \frac{\exp\left(-\frac{(\xi-\theta_i)^2}{2\sigma_{\theta_i}^2}\right)}{\sqrt{2\pi}\sigma_{\theta_i}} \tag{3.27}$$

where θ_i is the measured angle of arrival at the ith receiver and ξ is the calculated angle from the ith receiver at point (x_{r_i}, y_{r_i}) to the point (x, y) using an equation of the form given by (1.1). σ_{θ_i} defines the standard deviation of the AOA measurement error for that receiver. In order to implement the particle filter to estimate the state vector representing the emitter position, $\hat{x}$, using AOA measurements, the following algorithm was applied:

1. *Initialization, t=0*:
   - For $i = 1, ...N$, sample $x_0^{(t)} \backsim p(x_0)$ and set t=1.
2. *Importance sampling step*:
   - For $i = 1, ...N$, sample $\tilde{x}_t^{(i)} \backsim p(x_t|x_{t-1}^{(i)})$
   - Set $\tilde{x}_{0:t}^{(i)} = \left(x_{0:t-1}^{(i)}, \tilde{x}(i)_t\right)$
   - For $i = 1, \ldots N$, evaluate the importance weights
   $$\tilde{w}_t^{(i)} = p(y_t|\tilde{x}_t^{(i)}). \tag{3.28}$$
   - Normalise the importance weights.
3. *Selection step*

- Resample with replacement N particles $\left(x_{0:t}^{(i)}; i = 1, \ldots, N\right)$ from the set $\left(\tilde{x}_{0:t}^{(i)}; i = 1, \ldots, N\right)$ according to importance weights using multinomial resampling, described below
- Set $t \leftarrow t + 1$ and go to step 2

The sampling of the particles $\tilde{x}_t^{(i)} \backsim p(x_t|x_{t-1}^{(i)})$ performed as a sampling from a multivariate Gaussian distribution with a mean centred on the position, (x_p, y_p), of the survivor particle from the previous step of after initialisation. The resampled particle's positions are generated using:

$$\mathbf{x} = \mathbf{x}_p + N; \tag{3.29}$$

where $\mathbf{x}$ is the array of the particle position vectors, $\mathbf{N}$ is the array of zero-mean normally distributed random values with standard deviation $\sigma_{jitter} = 0.1569$ km (also known as *jitter* or *system noise*).

Multinomial Resampling

This is the simplest idea and widely used in bootstrap particle filter [49] that consist of drawing, conditionally upon σ-field generated by the generations of particles and weights up to time t, the new particles $\{\hat{\xi}^i\}_{1 \leq i \leq n}$ independently from the point mass distribution $\sum_{j=1}^{m} \omega_j \delta_{\xi_j}$. In practice, this is achieved by repeated uses of the inversion method:

1. Draw n independent uniforms $U_{1 \leq i \leq n}^i$ on the interval $(0, 1]$;
2. Set $I_i = D_\omega^{inv}(U^i)$ and $\hat{\xi}^i = \xi^{I^i}$, for $i = 1, \ldots n$, where D_ω^{inv} is the inverse of the cumulative distribution function associated with the normalised weights $\{\omega^i\}_{1 \leq i \leq m}$, that is, $D_\omega^{inv}(u) = i$ for $u \in \left(\sum_{j=1}^{i-1} \omega^j, \sum_{j=1}^{i} \omega^j\right]$.

This form of resampling is generally known as multinomial resampling since the duplication counts $N^1, \ldots, N^m$ are by definition distributed according to the multinomial distribution $Mult(n; \omega^1, \ldots, \omega^m)$.

After last measurement has been used in the particle filter, the two dimensional vector $\hat{x}$ obtained as a mean of the survived particles. It is also possible to generate or "perturb" particles not only using multivariate Gaussian distribution but also derive particle positions of the survived particles from two dimensional uniform distribution throughout search space. The rationale behind the use of such large distribution is to prevent convergence of the particles into one position and consequently degradation. The equation 3.29 simplified into $\mathbf{x} = \mathbf{x_p}$ where $\mathbf{x_p} \in 1 \ldots 130$ These two resampling methods has been tested for this implementation of the particle filter. Figure 3.6 shows the weighted particles after the Mth measurement using multivariate Gaussian resampling. In this figure (x, y) corresponds to the position of the particle and z-axis represents the weight. Next section presents the simulation and the results for emitter geolocation using the particle filter.

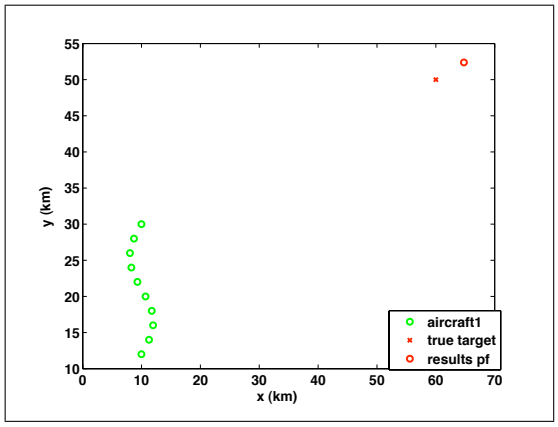

Figure 3.2: Illustration of geolocation using particle filter using AOA measurements

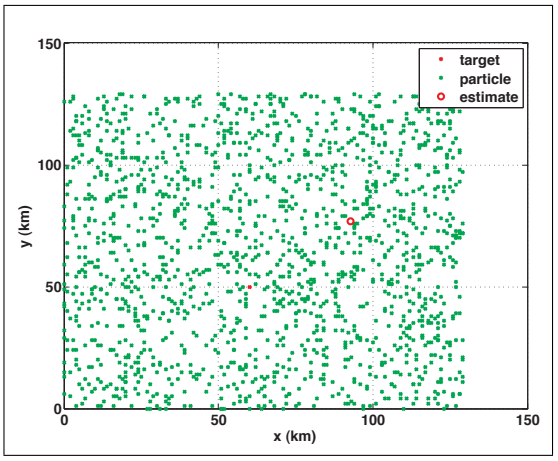

Figure 3.3: Initialisation step of the particle filter

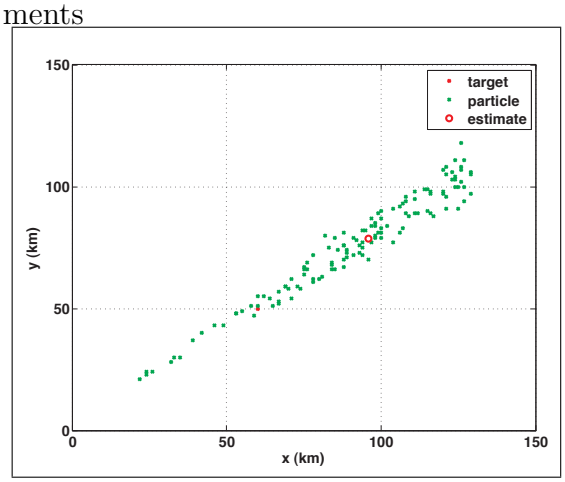

Figure 3.4: Illustration of the importance sampling step step for the scenario on figure 3.2

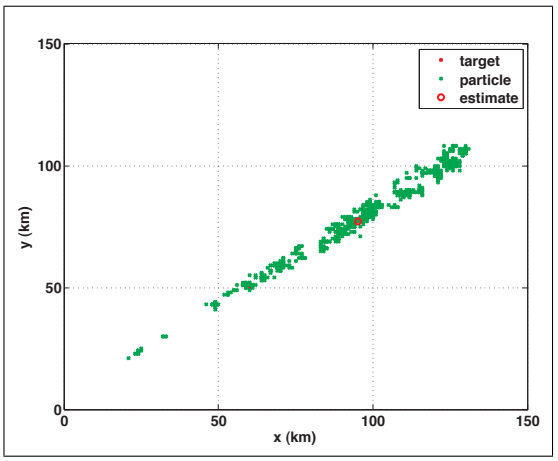

Figure 3.5: Illustration of the selection and resampling step in particle filter

3.2.1 Geolocation with particle filter fusing AOA measurements

In order to illustrate the performance of the particle filter, the scenario in figure 3.7 was simulated. In this scenario two platforms moving North with a speed 40 m/s and are capable of obtaining two AOA measurements, with standard deviation error $\sigma_{theta} = 0.02$ radians on each 10th second, corresponding to changes in a baseline between platforms 0.4 km on each simulation step. The emitter of interest is located at $(42, 100)$km. The particle filter algorithm was applied in order to obtain an estimate. The resulting average RMS error, calculated over 50 simulations for a different number of measurements are plotted in figure 3.8. It is clear that the

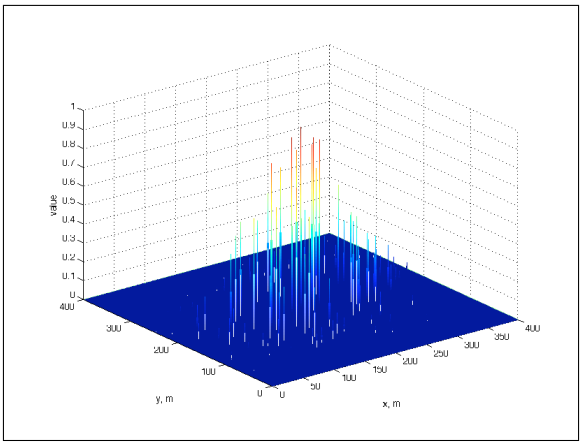

Figure 3.6: Illustration of the application of the particle filter to geolocation. Resampling step using multivariate Gaussian resampling

RMS error falls below 10 km for this simulation, but it doesn't improve with an increasing number of measurements as GDOP doesn't improved with time (baseline between platform remains constant). However, the CRLB for this scenario shows a very small value for the same number of measurements. Altering the scenario, as shown in figure 3.7, where the target has been changed to position $(90, 40)$km, demonstrates a significant improvement in RMS positional error as can be seen in figure 3.8. However, it raises a question whether it is possible to improve geolocation accuracy by using a different resampling method - uniform, instead of the Gaussian one used here.

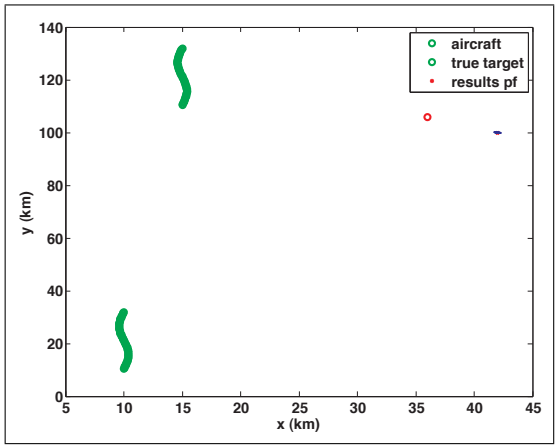

Figure 3.7: Scenario for geolocation using particle filter by fusion of AOA measurements from two platforms

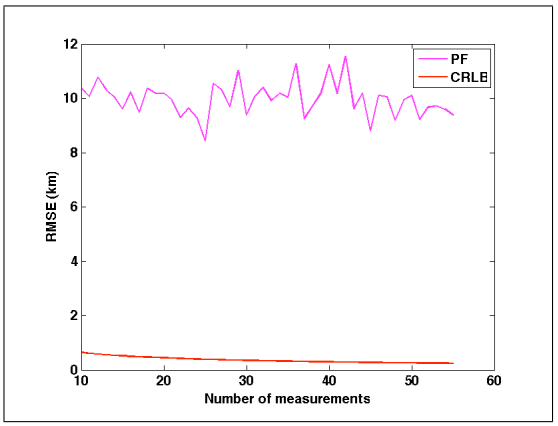

Figure 3.8: Average RMS error with corresponding CRLB of the simulation scenario in figure 3.7

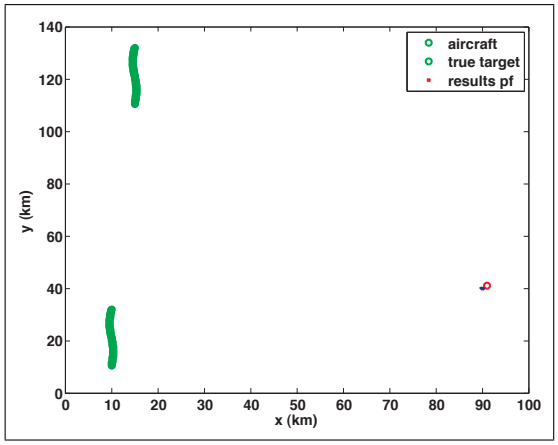

Figure 3.9: Scenario for geolocation using particle filter by fusion of the AOA measurements from two platforms

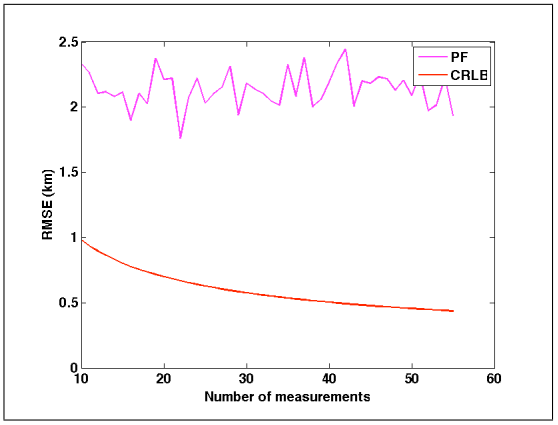

Figure 3.10: Average RMS error and corresponding CRLB value for scenario in figure 3.9

3.2.2 Impact of resampling method on geolocation accuracy

The purpose of this section is to test the impact of the resampling distribution on the geolocation accuracy. For this reason, the scenario shown in figure 3.11 was simulated. In this scenario two platforms moving North are capable of obtaining AOA measurement with standard deviation $\sigma_\theta = 0.02$ radians. The target is located at $(70, 63)$km. This simulation has a good GDOP due to the relative target position to the sensor platforms and their long baseline. Two resampling methods has been tested: multivariate Gaussian distribution, described earlier and uniform distribution, where the particles are derived randomly from two dimensional uniform distribution throughout the search space as it was for initialisation step on figure 3.3. In case of sampling particles from uniform distribution the equation performed as $\mathbf{x} = \mathbf{x_p} \in (1 \dots 130)$.

Average RMS error for different number of measurements are plotted in figure 3.12. In figure 3.12 it can seen that:

- Multivariate Gaussian distribution performs better for this scenario.
- RMS error of the particle filter estimate is larger, than corresponding CRLB.

Altering the target position, as shown in figure 3.13, where the target has been moved to $(90, 40)$km and exploring RMS error corresponding to this simulation in figure 3.14, it can be seen that although multivariate Gaussian resampling method performed better than the uniform resampling method, the accuracy of the particle filter doesn't depend on number of measurements in this scenario, although the CRLB, also plotted in figure 3.14, suggests otherwise. It is possible that such behaviour is due to the fact that at a arbitrary time step, t, there are only two states, the *prediction* state, simulated by a number of particles survived from a previous update and an *update* state introduced by a new pair of measurements. Correlation between these two states produces a new particle set, but it is clear that depending on the target position and thus GDOP, the particle filter occasionally fails to improve an estimate using extra measurements.

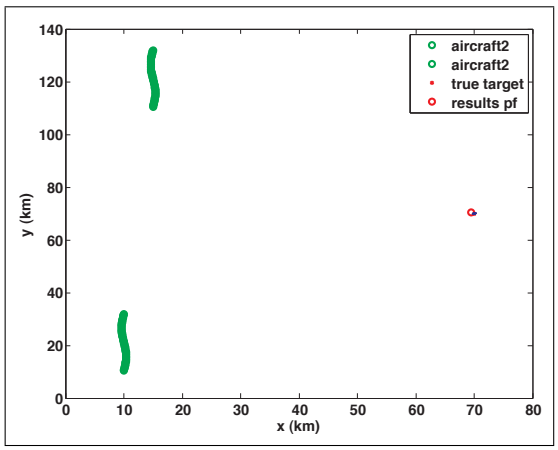

Figure 3.11: Scenario for geolocation using AOA measurements from two platform using particle filter with different resampling methods

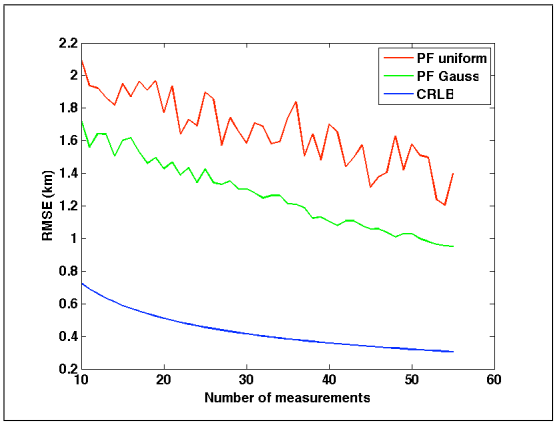

Figure 3.12: Average RMS error and corresponding CRLB value for the scenario in figure 3.11

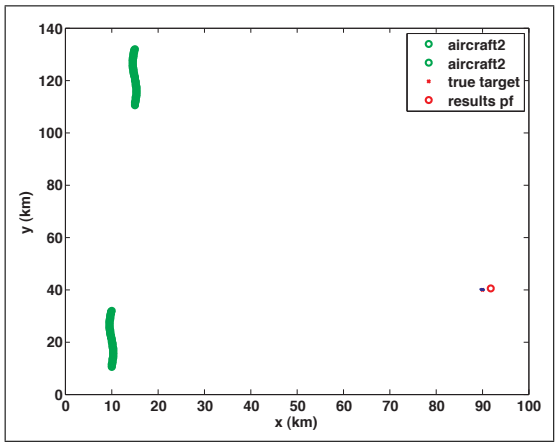

Figure 3.13: Scenario for geolocation using AOA measurements from two platform using particle filter with different resampling methods

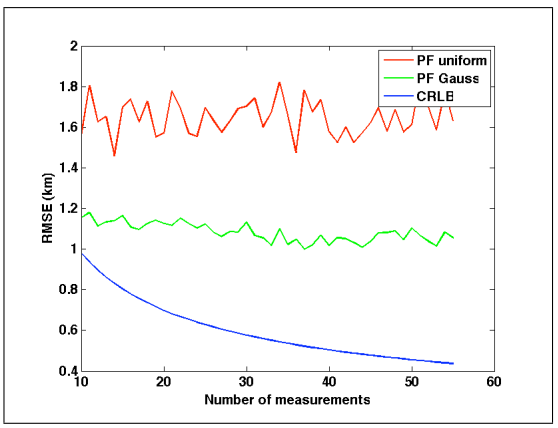

Figure 3.14: Average RMS error with corresponding CRLB for the scenario in figure 3.13

3.2.3 Geolocation using particle filter for TDOA measurements only

In this section, particle filter was applied to the problem of geolocation using TDOA-only measurements. The scenario in figure 3.15 was simulated, where two UAVs are capable of obtaining TDOA measurement on each step of their flight paths (denoted as green circles) notionally every 10 seconds along the flightpath. Standard deviation of the measurement error was considered to be $\sigma_{TDOA} = 7 \times 10^{-7}$ seconds, as before in MLE simulations. Note, that this scenario has a good geometry for GDOP for TDOA-measurements due to the fact that there is a long baseline between the two UAVs. The target position chosen was $(90, 40)$km. The average RMS error, calculated over 50 simulations are plotted in figure 3.16 for this scenario along with the corresponding CRLB. It is clear from figure 3.16 that the particle filter quickly obtains an estimate inside the circle defined by the CRLB, however it failed to improve as more measurements were taken along the flight paths.

In figure 3.15, the same simulation as before was repeated, but the target was moved to position $(100, 100)$km. The corresponding results for this simulation are presented in figure 3.18. It is clear that there is a shown similarity between the results in figure 3.16 and 3.18, however the estimate again failed to improve as the number of measurements to make the estimate increases. It should be noted that CRLB provide a conservative estimate and for small number of measurements it defines large circle, however as number of measurements increase it falls for very small value and it is clear that in this particular case CRLB provides lower bound for the case when number of measurements more than 40.

The scenario in figure 3.19 was altered in a way, that the target was moved to $(42, 100)$km. It is clear from the figure 3.21 that this scenario did not improve the fusion capabilities of the particle filter either. In the next section an attempt was made to improve the accuracy of the estimator using fusion of the different type of the measurements and in the later section, the poor accuracy of the particle filter with the chosen resampling method will be analysed.

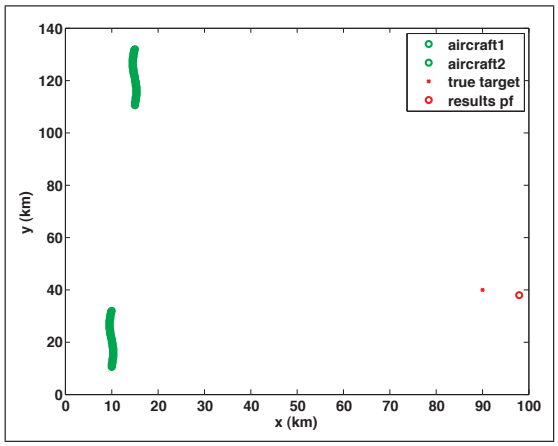

Figure 3.15: Scenario for geolocation using particle filter with TDOA-only measurements

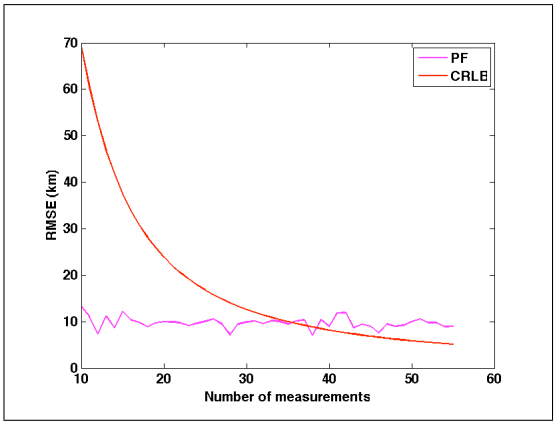

Figure 3.16: Results PF with TDOA-only measurements for the scenario in figure 3.15

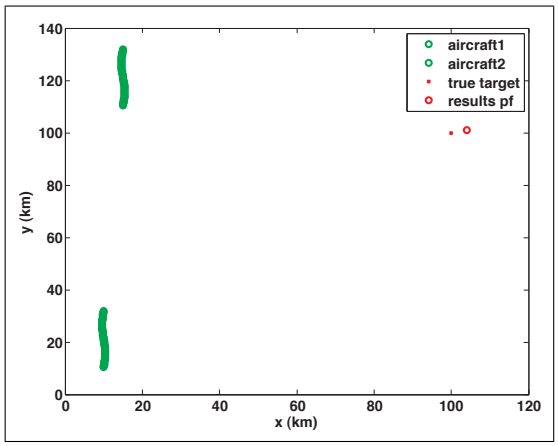

Figure 3.17: Scenario for geolocation using particle filter with TDOA-only measurements

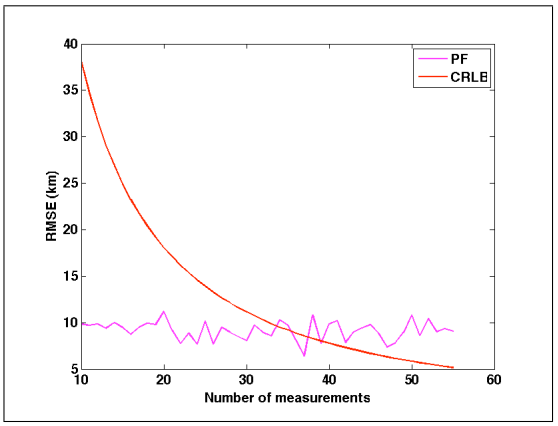

Figure 3.18: Results PF with TDOA-only measurements for the scenario in figure 3.17

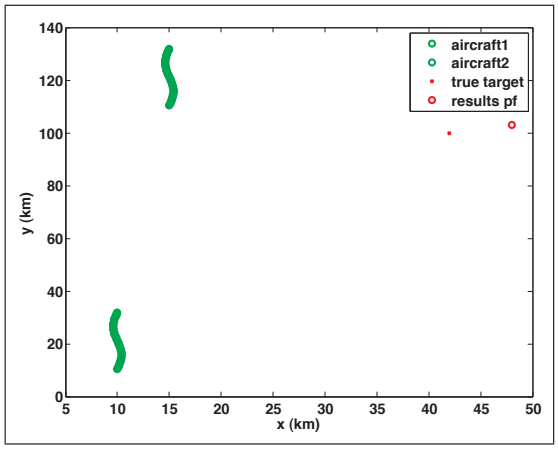

Figure 3.19: Scenario for geolocation using particle filter with TDOA-only measurements

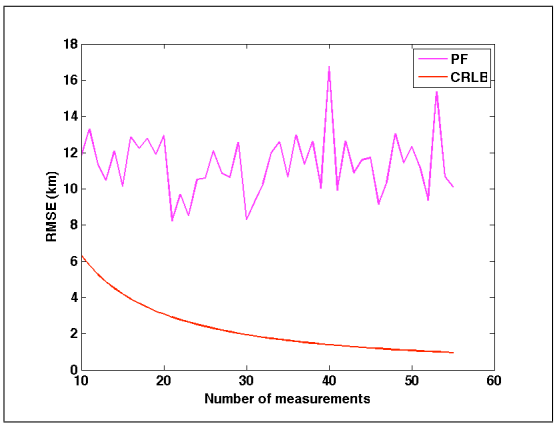

Figure 3.20: Resutls PF with TDOA-only measurements for the scenario on figure 3.19

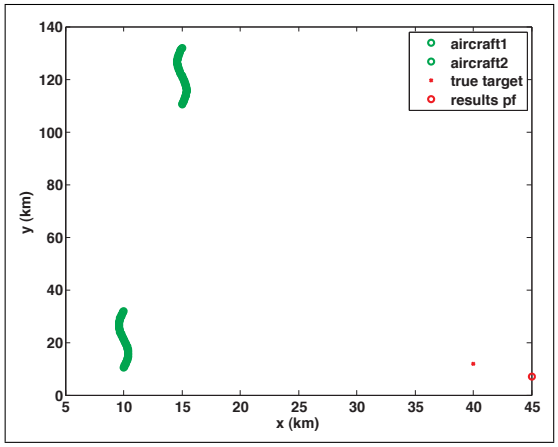

Figure 3.21: Scenario for geolocation using particle filter with TDOA-only measurements

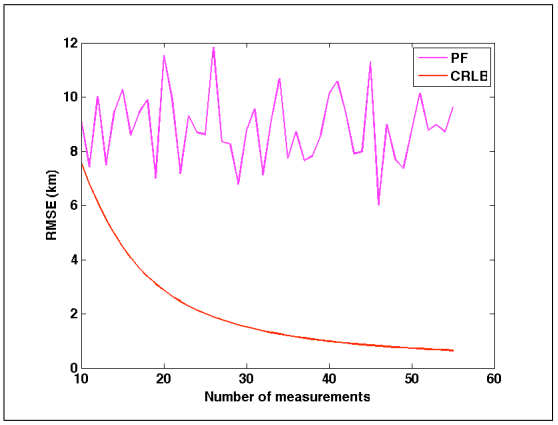

Figure 3.22: Results PF with TDOA-only measurements

3.2.4 Fusion of different types of measurements using particle filter

In order to test the performance of the particle filter at fusing different types of measurements, the scenario of figure 3.23 has been simulated. In this scenario, the two platforms are capable of obtaining one TDOA measurement with a standard deviation $\sigma_{TDOA} = 7.4 \times 10^{-7}$ seconds, and in addition, each platform is also capable of obtaining one AOA measurement with a standard deviation $\sigma_\theta = 0.02$ radians. The true target position is (40km,10km).

Figure 3.24 demonstrates the performance of the particle filter obtained in terms of the average RMS position error, as the number of measurements are accumulated. To obtain the RMS position error, each test was repeated 50 times and the corresponding RMS errors averaged. Comparing figures 3.24 and 3.22 it is clear that fusion of AOA and TDOA measurements significantly improved an estimate.

However, repeating this simulation with the target located at (40km,100km) as shown in figure 3.25 and (90km,40km) in figure 3.27 respectively, demonstrate that there is a consistent problem with the particle filter. It is clear from the results presented in figures 3.26 and 3.28, that the estimate doesn't improve with the number of measurements taken. In the next section this problem will be explored in details.

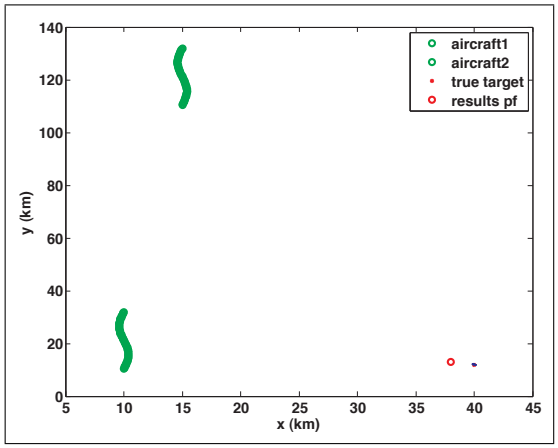

Figure 3.23: Scenario for geolocation using particle filter by fusion of two AOA and one TDOA measurement from two mobile platforms

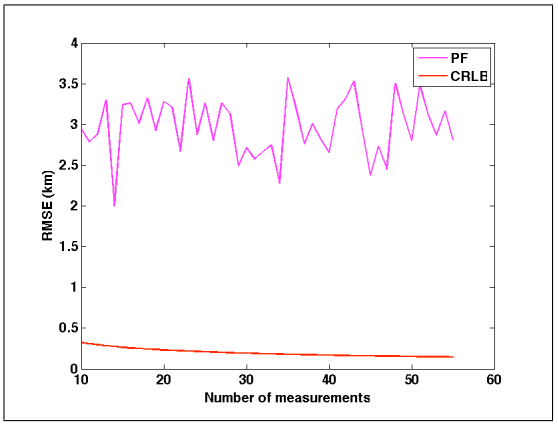

Figure 3.24: Average RMS error and corresponding CRLB value for the scenario in figure 3.23, fusion of two AOA and one TDOA measurement

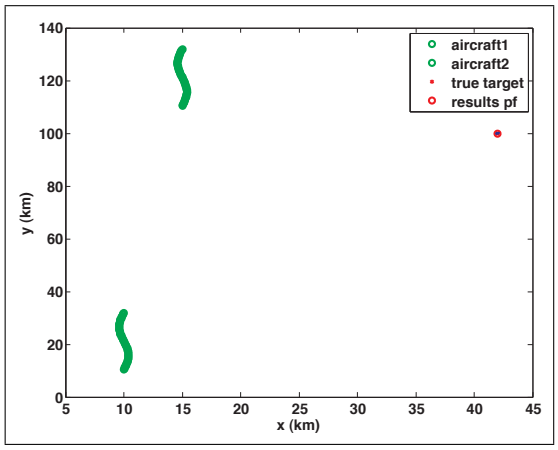

Figure 3.25: Scenario for geolocation using particle filter by fusion of two AOA and one TDOA measurement from two mobile platforms

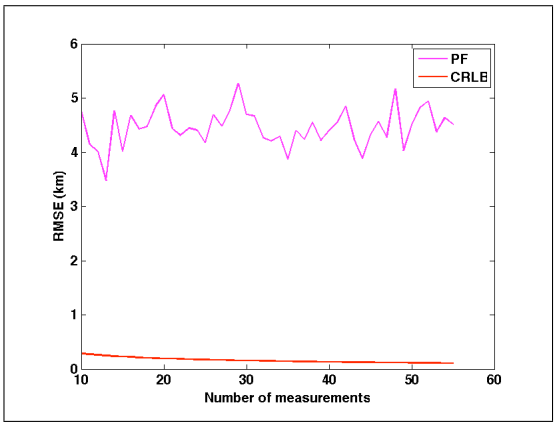

Figure 3.26: Average RMS error and corresponding CRLB value for the scenario in figure 3.25

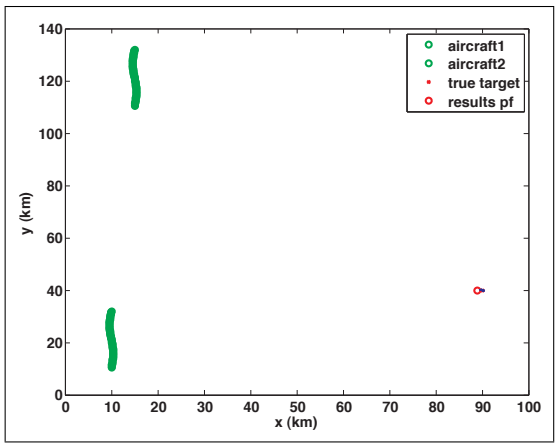

Figure 3.27: Scenario for geolocation using particle filter by fusion of two AOA and one TDOA measurement from two mobile platforms

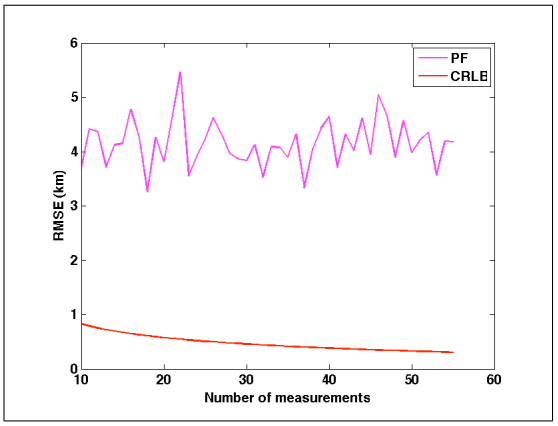

Figure 3.28: Average RMS error and corresponding CRLB value for the scenario in figure 3.27

3.2.5 Particle degradation

The aim of this section is to explore and to try to explain the behaviour of the particle filter algorithm, when additional measurements didn't improved an accuracy of the final estimate. In order to address this problem, the scenario in figure 3.29 was simulated. In this scenario two UAV are travelling North with speed 40 m/s, each capable to obtain AOA measurement on each 10th second, corresponding to one step of the simulation, with standard deviation of the measurement error $\sigma_\theta = 0.02$ radians.

Figures 3.30 and 3.31 present the 'convergence walk' of the particle filter algorithm together with the RMS error over a number of measurements. In this case, 10 measurements were used with resampling of the particle's positions after selection step from a two-dimensional Gaussian distribution with standard deviation $\sigma_{jitter} = 0.2218$.

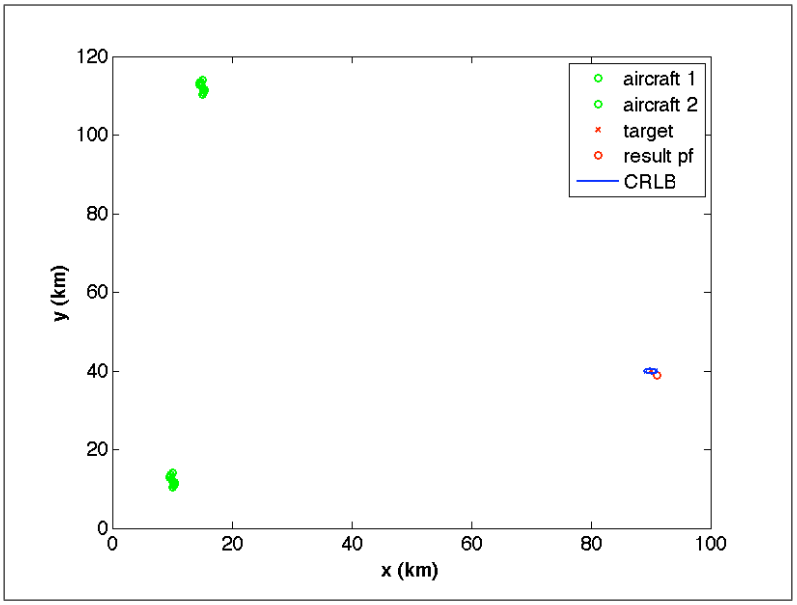

Figure 3.29: Scenario for geolocation using particle filter 10 measurements AOA measurements from each platform

This result demonstrates the problem of convergence to local point and particle degradation as result. It is possible to see that the estimator 'stuck' on 6th measurement and additional measurements are not able to overcome this problem, due to the small spread in new particles, generated during the resampling step. Repeating the same simulation for the same number of measurements only confirm the convergence problem, as can be noted from figures 3.32 and 3.33. Increasing the number of measurements to twenty didn't improve the estimate as can be seen from figures 3.34 and 3.35, where the results for twenty measurements are presented.

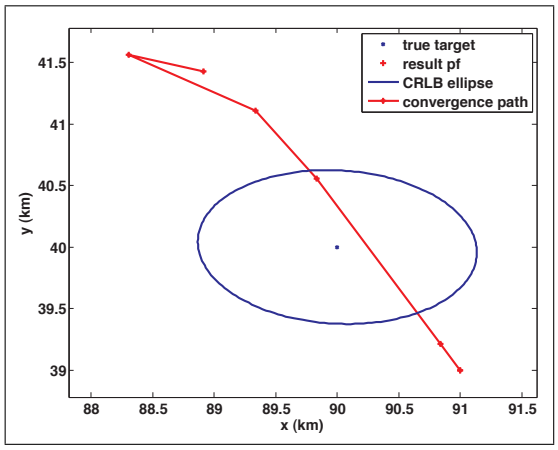

Figure 3.30: Particle filter convergence 'walk' with 10 measurements fused using small Gaussian resampling distribution spread

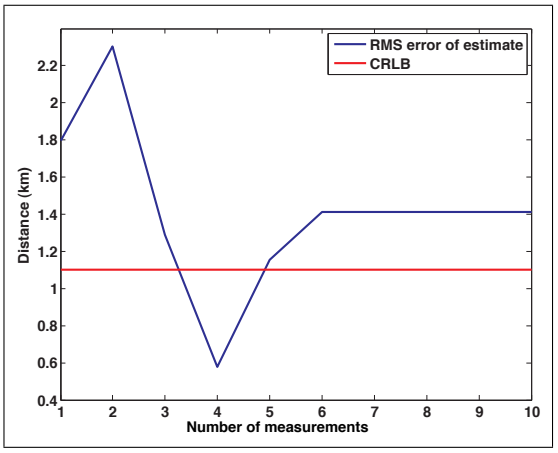

Figure 3.31: RMS error of the particle filter estimator with 10 measurements fused. Corresponds to convergence 'walk' in figure 3.30. Particles positions generated from Gaussian distribution with standard deviation $\sigma_{jitter} = 0.2218$

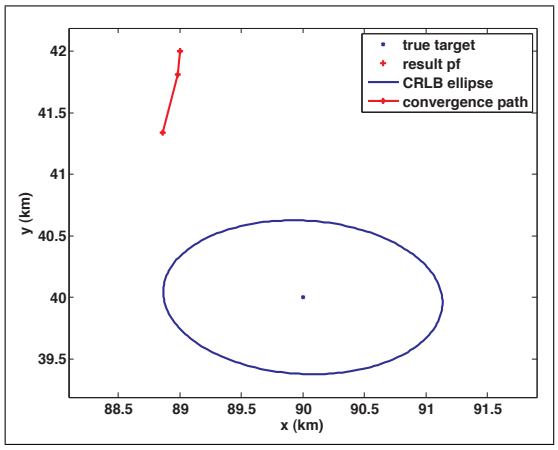

Figure 3.32: Particle filter convergence 'walk' with 10 measurements fused, using Gaussian distribution with $\sigma_{jitter} = 0.2218$ standard deviation for sampling particle's position. Second simulation

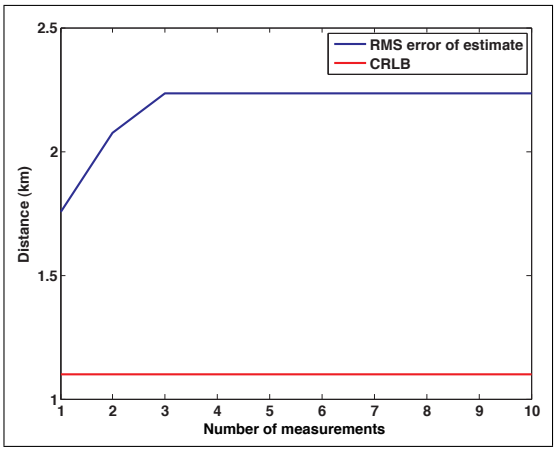

Figure 3.33: RMS error of the particle filter estimator with 10 measurements fused. Corresponds to convergence 'walk' in figure 3.32. Particles positions generated from Gaussian distribution with standard deviation $\sigma_{jitter} = 0.2218$. Second simulation

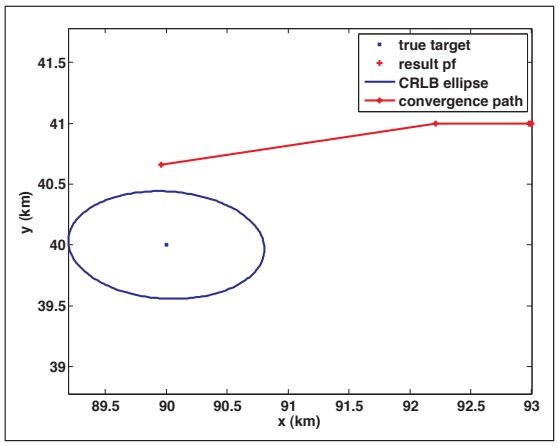

Figure 3.34: Particle filter convergence 'walk' with 20 AOA measurements fused. Particles positions generated from Gaussian distribution with standard deviation $\sigma_{jitter} = 0.2218$

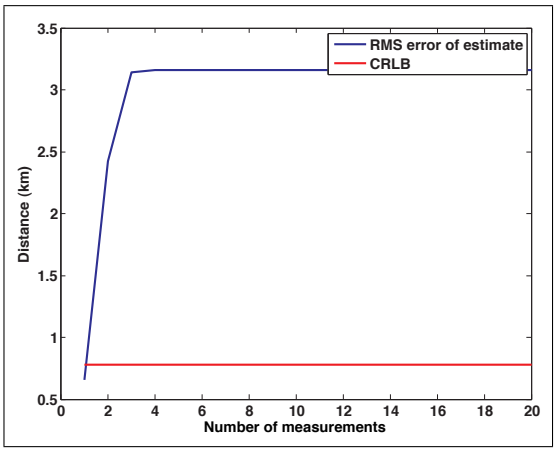

Figure 3.35: RMS error of the particle filter estimator with 20 measurements fused. Corresponds to convergence 'walk' in figure 3.34. Particles positions generated from Gaussian distribution with standard deviation $\sigma_{jitter} = 0.2218$

Increased resampling spread for the Gaussian distribution

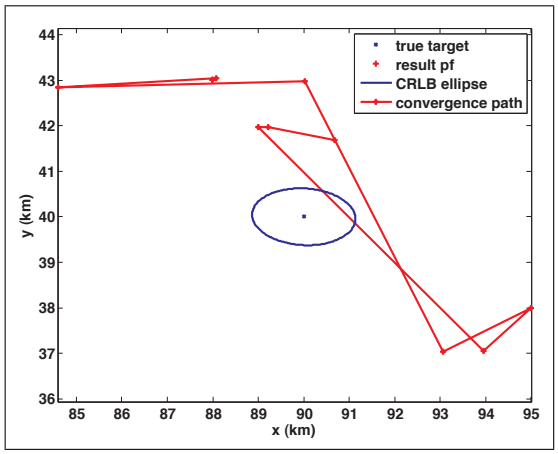

Figure 3.36: Particle filter convergence 'walk' with 10 measurements fused using Gaussian distribution $\sigma_{jitter} = 5.2218$ km to generate particle's positions

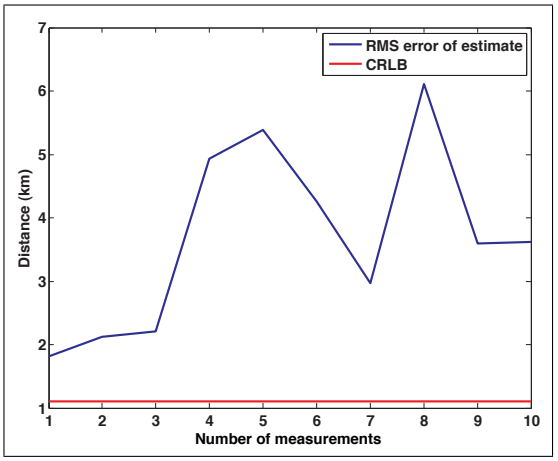

Figure 3.37: RMS error of the particle filter estimator with 10 measurements fused. Corresponds to convergence 'walk' in figure 3.36. Gaussian distribution $\sigma_{jitter} = 5.2218$ km used to generate particle's positions

The attempt was made to increase the spread of the multivariate Gaussian distribution from which the particle's positions are drawn on the resampling step. The resampling method was altered in a way that the size of the two dimensional Gaussian distribution was artificially increased in a way that the new particle's positions will be regenerated from a two dimensional distribution with standard deviation $\sigma_{jitter} = 5.2218$ km radius. This gives a larger spread to a particle, after the resampling step, therefore this can prevent convergence to one point on the grid and particle degradation as the result.

The results of this simulations are shown in figures 3.36,3.37 and for 20 measurements in figures 3.38, 3.39, where the simulation in figure 3.29 was repeated with a new resampling method described above. It is clear that particle filter algorithm doesn't converge to one point, however it doesn't converge closer to the true target position. From figure 3.37 that the RMS (distance) of the estimate increases with time, although new measurements were added to particle filter on each step. Increasing the number of measurements to twenty didn't help in this case, as the "random walk" drove the estimate further and further on each step, as demonstrated in figures 3.38 and 3.39.

Again it is noticeable from figure 3.39 that additional measurements didn't provide an improved estimate.

It is clear how increasing the spread in the multivariate Gaussian distribution during resampling step can help to overcome the problem of convergence to local minima, however there is a danger of initiating so-called 'random walk' [50] where the estimate of the particle filter will walk further from true target position independently of precision of added measurements.

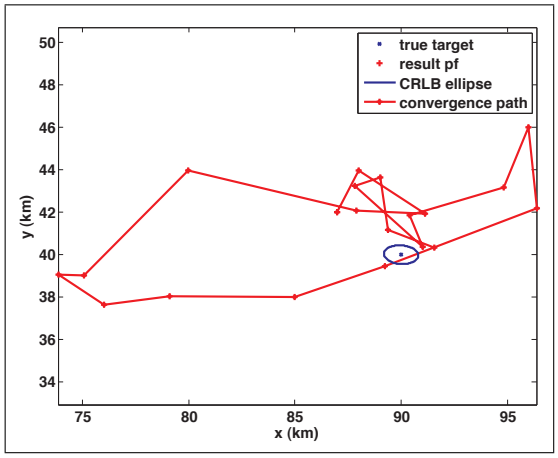

Figure 3.38: Particle filter convergence 'walk' with 20 measurements, fused using large Gaussian resampling distribution spread

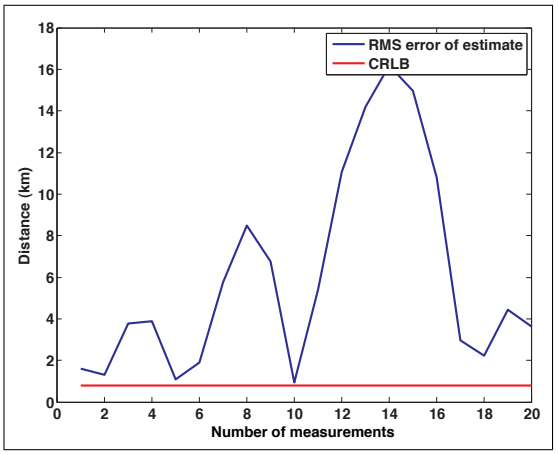

Figure 3.39: RMS error of the particle filter estimator with 20 measurements fused. Corresponds to convergence 'walk' in figure 3.38. Large Gaussian resampling distribution spread used

3.2.6 Conclusions

In this chapter particle filter was introduced and applied for geolocation problem using different type of measurements AOA and TDOA and fusion of both types of measurements. Particle filter doesn't require an initial guess as MLE or Kalman filter, but instead rely on prior distribution, and it doesn't require a linearised Jacobian for estimation. However, although particle filter doesn't have a problem of convergence as MLE, there is a problem highlighted, namely the choice of the σ_{jitter} standard deviation of the system noise is important, which can lead to particles degradation, or to the condition when particles "explode" over all search space. Some improvement of the stability and accuracy of the particle filter will be demonstrated in chapter 5. In the next chapter novel algorithm based on Hough Transform will be presented and then compared with particle filter on one common scenario.

Chapter 4

Hough Transform Based estimator

4.1 Hough Transform approach to geolocation

4.1.1 Introduction

In order to find a better solution to the emitter geolocation problem in terms specified in 2.2.2, a robust and accurate algorithm of geolocation is needed, which is suitable for dealing with the multipath non-line-of-site problem. The Hough Transform, a robust clustering and fusion algorithm for state estimation (according to [51]) has been used in image processing for line and arbitrary shape detection for a number of years. Some researchers, such as Alexiev [52], have proposed it for multi-sensor data fusion in target tracking for the elimination of ghost detections. Others [53],[54], in robotics have proposed it for map matching and self positioning (location) of robots. There is a related Radon Transform, which is more general integral version of the Hough Transform. Hough Transform is viewed by some researchers as discrete version of the Hough Transform. The comprehensive description of the differences of the Hough and Radon transform can be found in [55]. Our research shows that this algorithm can be adapted to the process of geolocation and displays good performance for this task.

4.1.2 Original Hough Transform

The Hough Transform (HT) was patented in 1962 [56] as a mathematical transformation that could map points from an input space, referred to as the feature space (FS) into curves in a special parameter space (PS). It is particularly well known for straight line detection. The method is based on the fact that all points from a straight line positioned in the FS can be mapped in a single point in the PS. Many applications in image recognition use the HT for the detection of different types of image features - straight lines, circles, ellipses, etc. [57].

The Hough Transform can be introduced using the traditional example of line

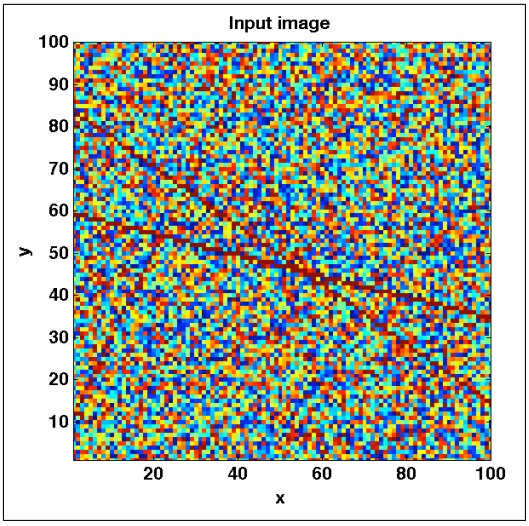

Figure 4.1: Input image for Hough Transform with three lines and the noise

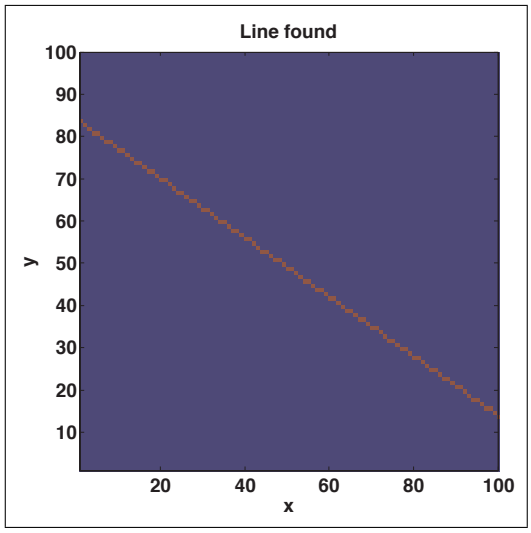

Figure 4.2: Line found in image 4.1, using Hough Transform

detection in a noisy image. Consider the image in figure 4.1. This noisy image contains three lines in order to illustrate the properties of the HT to detect these lines. The 'normal' HT mapping equation [58] is used:

$$r = x\cos(\theta) + y\sin(\theta) \tag{4.1}$$

The algorithm maps each point (x, y) from FS to a curve in the PS (r, θ). For each value of the discrete parameter θ in (4.1) the corresponding values of parameter r are calculated. If several points in FS lie on a straight line the corresponding curves are intersected by a single point in PS. A simple 'voting' algorithm is used to locate this point and this is represented by:

$$A(r, \theta) = \sum_{\theta=1}^{360} r(x, y|\theta) \tag{4.2}$$

The parameterized space for this example is plotted in figures 4.3 and 4.4. The peak of the votes in figure 4.3 occur at values of the accumulator whose corresponding template includes the most points that are lying on the line. It will be noted that the PS in this example has three peaks. This is due to the fact that the image of figure 4.1 has three lines. In this example, the algorithm returns only one line as it was looking for one corresponding to the peak in PS space. The parameters (r, θ) corresponding to peak 1 in the PS can be used to represent the equation of a straight line using the parametric equation:

$$y = \tan\theta \cdot x + r \tag{4.3}$$

and this is used to draw the straight line corresponding to the largest peak in figure 4.3, which is shown in figure 4.2. The problem of RF emitter geolocation can be adapted in terms of HT as a search not for a line, but for a point on a grid (x, y).

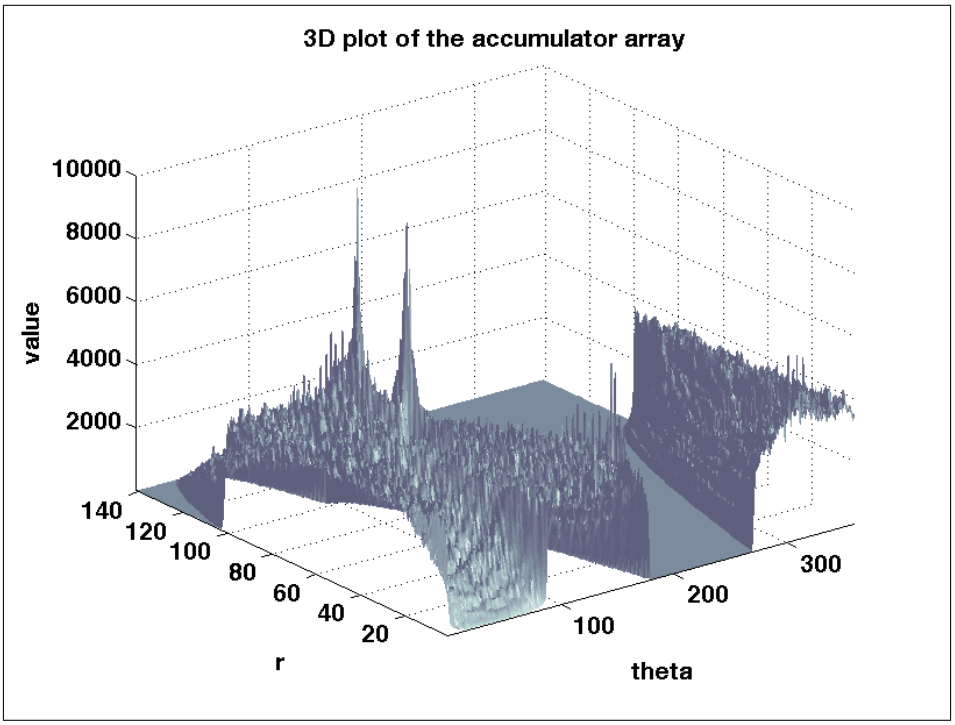

Figure 4.3: Three dimensional plot of Accumulator array for traditional Hough Transform

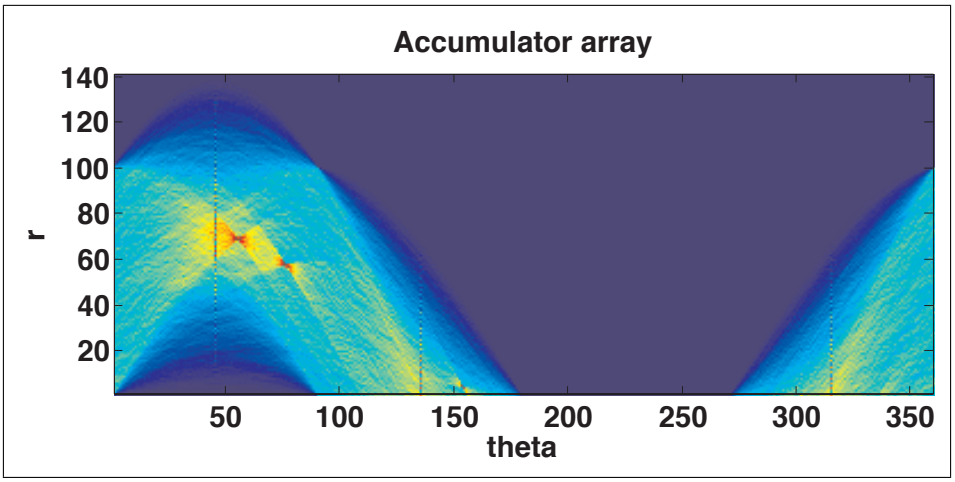

Figure 4.4: Two dimensional accumulator array for traditional Hough Transform

4.2 Adaptation of the Generalized Hough Transform for Geolocation

In order to adapt the Hough Transform to the RF emitter geolocation problem, let our sets of hypotheses exist in some coordinate framework (an N-dimensional array). An event can occur within this coordinate system and can indicate with its conditional probabilities a set of hypotheses whose parameters are fixed relative to the event. The conditional probability table of the event can then also be considered as an N-dimensional array centered on the event, where N is the dimensionality of the hypothesis space. This array is called the *voting array* for the event. It contains the values of the normalized conditional probabilities and so each event will simply add its own voting array into the accumulator representing the hypothesis space. For example, in the case of line detection, described above, the hypothesis was that points in feature space lay on a straight line. The voting array determines the most likely line that the points lay on.

Imagine that the hypothesis space is a particular point located in two dimensions. In this case, the hypothesis space is then a 2D array of numbers representing the conditional probability of the event. In the geolocation application, the events that are of interest are the observations (i.e. the measurements of the parameters of the source). Associated with each measurement is a probability that the source is located at a particular point (x, y) within the search space. This is equivalent to assigning the event to a particular part of the hypothesis space. The conditional probability voting array can be obtained for each measurement by placing the source into each position in turn and calculating the conditional probability and adding these values to the voting array. This approach is described for different measurement techniques in the following sections.

4.2.1 Angle of arrival measurements

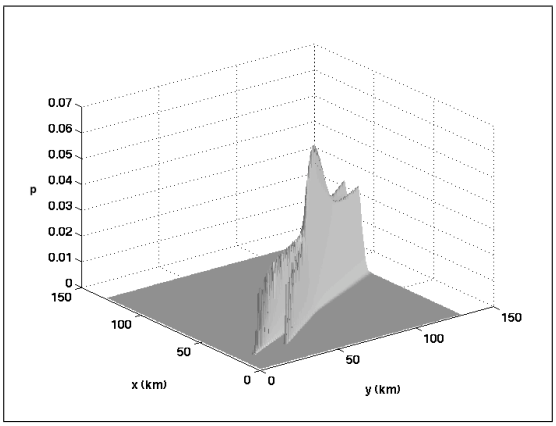

Figure 4.5: An example of three-dimensional parameterised space for AOA-only measurements

Consider a 2D scenario with M receivers (that may be mobile) and one stationary

radio source. Assume that the receivers can obtain the Angle of Arrival (AOA) of the source emission using an RF interferometer or an antenna array and also assume that the measurement errors in the AOA are Gaussian (although other distributions can be accommodated easily). The voting function can be defined in terms of the likelihood, $p(x, y|\theta_i)$, of the target being located at some point (x, y) within the search space given the measurement θ_i. This conditional probability for the AOA measurements has the form:

$$p(x, y|\theta_i) = \frac{\exp\left(-\frac{(\xi-\theta_i)^2}{2\sigma_{\theta_i}^2}\right)}{\sqrt{2\pi}\sigma_{\theta_i}} \tag{4.4}$$

where θ_i is the measured angle of arrival at the ith receiver and ξ is the calculated angle from the ith receiver at point (x_{r_i}, y_{r_i}) to the point (x, y) using an equation of the form given by (1.1). σ_{θ_i} defines the standard deviation of the AOA measurement error for that receiver. Clearly, the emitter position (x, y) is unknown and so $p(x, y|\theta)$ is evaluated for all values x and y in the search space.

Although the point (x, y) could lie anywhere within the search space, in practice, the search space is split into a regular grid and (x, y) is constrained to lie at one of the grid points and (4.4) is evaluated at each of these grid points. Assuming that multiple measurements are made at each receiver, in the usual way, the pdf is evaluated for each measurement for all receivers. In this method, the pdfs due to each measurement are accumulated as follows:

$$A_{AOA}(x, y) = \frac{1}{M}\sum_{m=1}^{M} p(x, y|\theta_m) \tag{4.5}$$

where M represents the total number of measurements made. This accumulated pdf now represents the voting array for the Hough Transform.

As an example, consider two stationary receivers located at (20km,10km) and (20km,30km) respectively and the emitter of interest is located at (60km,80km). At each receiver, a single AOA measurement was taken and the standard deviation of each measurement due to the effect of receiver noise was taken as $\sigma_\theta = 0.02$ radians. The corresponding Hough Transform space for these AOA measurements is shown in figure 4.5. Note how the Hough Transform shows the likely lines of bearing and the peak occurs where the likely lines of bearing intersect. The maximum of the Hough Transform space corresponds to the most likely position of the source.

Now, consider a geolocation scenario in figure 4.6. In this scenario, one platform moving North according to a wavy path and another moves East, with a target located at $(60, 70)$. Platforms speed is 40m/s and the the standard deviation of the measurement error $\sigma_\theta = 0.02$ radians. Figure 4.7 demonstrates the ability of the Hough Transform to geolocate using AOA measurements from one platform only (marked as UAV1 on figure 4.6). In this figure, the average RMS error calculated over 50 simulations. The CRLB corresponding on this scenario is also plotted on figure 4.7. It can be also noted, that the accuracy of geolocation using AOA measurements from one platform is relatively poor compared to RMS error when fusion

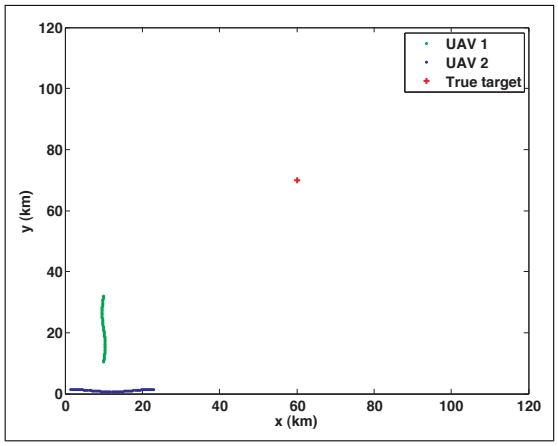

Figure 4.6: Scenario for geolocation fusing pair of AOA measurements from each platform using HT

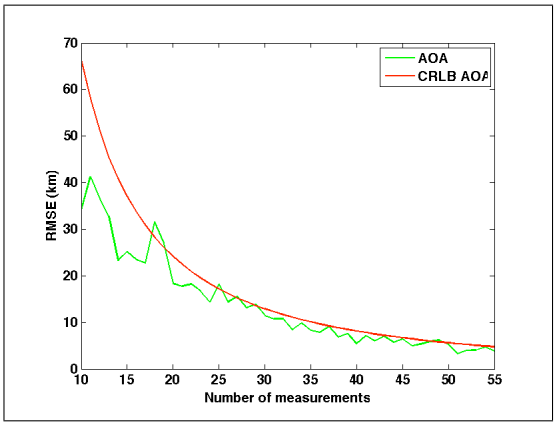

Figure 4.7: Average RMS errror for geolocation using AOA measurements from one platform only

of each AOA measurement from both platforms performed. Figure 4.8 demonstrates the performance of this fusion. In this case fused estimate obtained by summing likelihoods of the AOA measurements from both platform in one parameterised space. It is clear, how additional AOA measurements improve geolocation accuracy: in this case the RMS error of figure 4.8 half of the RMS error for figure 4.7 for the same scenario.

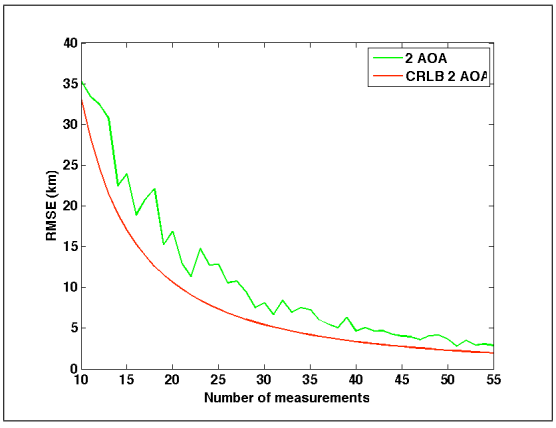

Figure 4.8: Average RMS error fusing two AOA measurements from platform using GHT for the scenario in figure 4.6

4.2.2 Time difference of arrival measurements

The following illustrates the method for the case of geolocation using the time difference of arrival (TDOA) method. Assume that it is possible to obtain the TDOA between two spatially separated receivers (using signal cross correlation or other delay estimation technique, for example). Referring all TDOAs to the first receiver, which is assumed to be the first to receive the transmitted signal, let the index $i = 2, 3, ..., M$ unless otherwise specified, (x, y) be the source location and (x_{r_i}, y_{r_i}) be the known location of the ith receiver. The range of the source to the ith receiver is:

$$R_i = \sqrt{(x_{r_i} - x)^2 + (y_{r_i} - y)^2} \tag{4.6}$$

and the range difference between receiver i and receiver 1 is:

$$\begin{aligned} c\tau_{i,1} &= R_i - R_1 \\ &= \sqrt{(x_{r_i} - x)^2 + (y_{r_i} - y)^2} \\ &\quad -\sqrt{(x_{r_1} - x)^2 + (y_{r_1} - y)^2} \end{aligned} \tag{4.7}$$

where, $\tau_{i,1}$ is the measured TDOA between the ith receiver and receiver 1 and c is the velocity of light.

The likelihood of the source location for this case is given by:

$$p(x, y|\tau_{i,1}) = \frac{\exp\left(\frac{R_{i,1}^2 - c^2\tau_{i,1}^2}{2\sigma_r^2}\right)}{\sqrt{2\pi}\sigma_r} \tag{4.8}$$

where $R_{i,1}$ is the difference between the range of a particular point on the grid to receiver 1 and the range from the same grid point to receiver i, σ_r is the range error for this measurement. As for the AOA method, $R_{i,1}$ is obtained for each point on the search space grid from the known receiver positions, and $p(x, y|\tau_{i,1})$ is calculated at the point, given the measurement $\tau_{i,1}$. This gives the probability of finding the emitter due to that single measurement. The range error is dependent upon the error in the time difference of arrival measurement, σ_{TDOA}, *and* the geometric dilution of precision (GDOP). According to [19] the range error for a single TDOA measurement is given by:

$$\sigma_r = \frac{c\sigma_{TDOA}}{2\sin(\frac{\Theta}{2})} \tag{4.9}$$

where the numerator represents the timing measurement error and the denominator is the GDOP. Θ is the angle subtended between the two lines of position from receiver 1 to the source and receiver i to the source, respectively. There are a number of different theoretical approximations for σ_{TDOA} depending upon the assumptions made regarding the SNR of the received signal [10]. For good SNR conditions it is common to assume that the standard deviation of the timing error is given by:

$$\sigma_{TDOA} \approx \frac{1}{W\sqrt{\text{SNR}}} \tag{4.10}$$

where W is the noise bandwidth of the receiver, whereas for low SNR the achievable timing error is often given by [59]:

$$\sigma_{TDOA} \geq \sqrt{\frac{3}{8\pi^2 T}} \frac{1}{\text{SNR}} \frac{1}{\sqrt{f_2^3 - f_1^3}} \tag{4.11}$$

where T is the integration time used in the receiver and $W = f_2 - f_1$. Using, for the sake of example, the high SNR case given by (4.10), the range error becomes:

$$\sigma_r = \frac{c}{2W sin(\frac{\Theta}{2})\sqrt{\text{SNR}}} \tag{4.12}$$

Using the conditional pdf (4.8), the voting array can be built, as per the earlier case for the AOA measurements (4.5) using:

$$A_{TDOA}(x, y) = \frac{1}{L} \sum_{l=1}^{L} p(x, y|\tau_{l,1}) \tag{4.13}$$

where L represents the number of TDOA measurements taken from the M receivers.

As an example, consider the case of geolocation using three stationary receivers. These are located at: (20km, 10km), (20km, 75km), (60km, 10km). The emitter of interest is located at (40km, 40km). In the simulation, it is assumed that the bandwidth of the received signal is $W = 1$ MHz and the $SNR = +3dB$, leading to a value for $\sigma_{TDOA} = 7 \times 10^{-7}$ seconds using (4.10). Only two TDOA measurements are taken - between receiver 1 and receiver 2 and receiver 1 and receiver 3. The resulting Hough Transform space due purely to the provided TDOA information is shown in figure 4.10. Note how the Hough Transform appears to plot the two most likely iso-delay curves for the two TDOA measurements and the emitter position is the intersection of these two curves. Again, the dominant peak in the Hough Transform space denotes the likely source position. By taking many measurements, the effect of the noise on accumulated pdf is reduced and the peak representing the emitter position is substantially sharpened. It is possible to geolocate using TDOA only

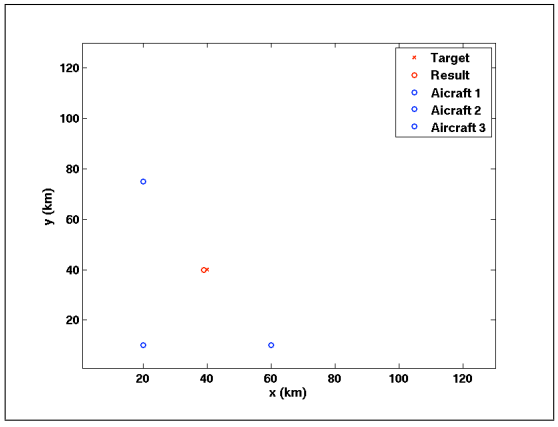

Figure 4.9: Scenario for geolocation using TDOA-only measurements

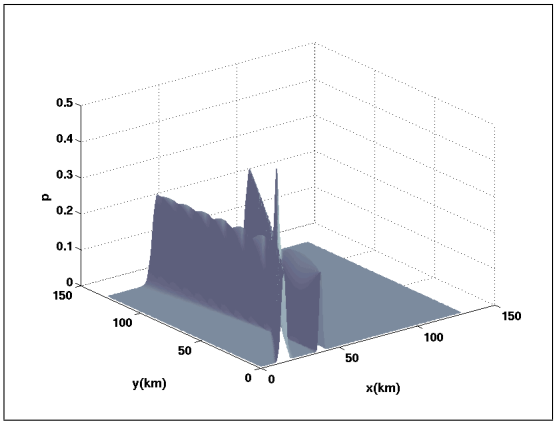

Figure 4.10: HT 3d parameterized space for one pair of TDOA measurements

measurements between pairs of mobile platform. Consider the scenario in figure 4.11. In this scenario two platforms moving North are capable of obtaining one TDOA measurement on each step, with $\sigma_{TDOA} = 7 \times 10^{-7}$ seconds. The resulting average RMS error is plotted in figure 4.12 together with corresponding CRLB, for comparison. As before, average RMS obtained over 50 simulations for different number of measurements. It can be seen that for this particular scenario, the CRLB predicts much worse performance for the estimator than the average RMS of the HT estimator. The green line below CRLB indicates that all estimates were inside of the circle, defined by the trace of the CRLB, as in figure 2.3. It should be noted that this scenario have a good GDOP due to the directions of the motion of the platforms and location of the target. Also, due to the fact that Hough Transform is grided algorithm and target located on the grid, the RMS errors in position estimates are limited to steps starting from $\approx$ 1.4 km, thus can be closer to the true target by being on the closer grid cell.

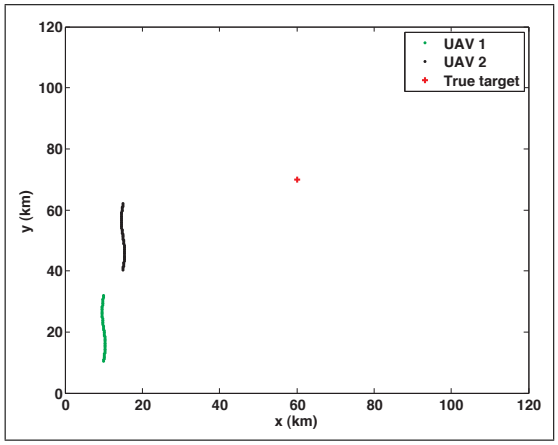

Figure 4.11: Scenario for geolocation with TDOA-only measurements using Hough Transform

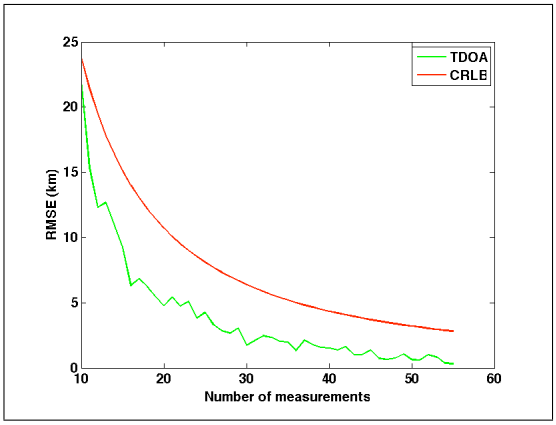

Figure 4.12: Average RMS error for geolocation using HT with TDOA-only measurements for the scenario in figure 4.11

4.2.3 Fusion of AOA with TDOA Measurements

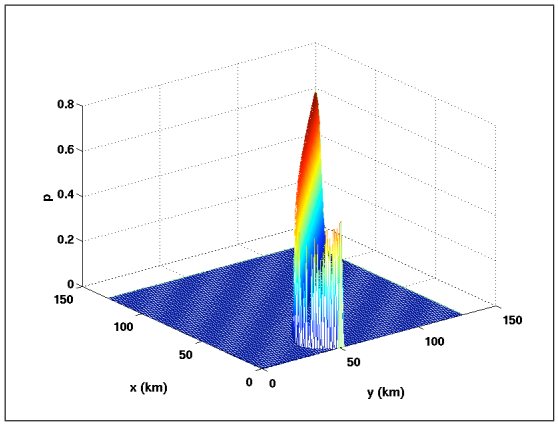

Figure 4.13: 3D parameterised space for one TDOA measurement

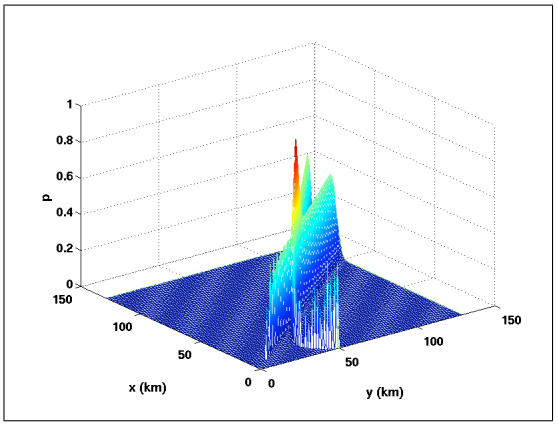

Figure 4.14: An example of 3D parameterised space fusing one AOA and one TDOA measurements

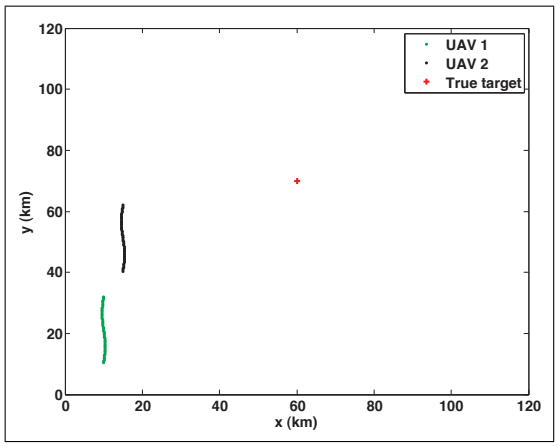

Figure 4.15: Scenario for geolocation using HT, fusion of TDOA and one AOA measurement

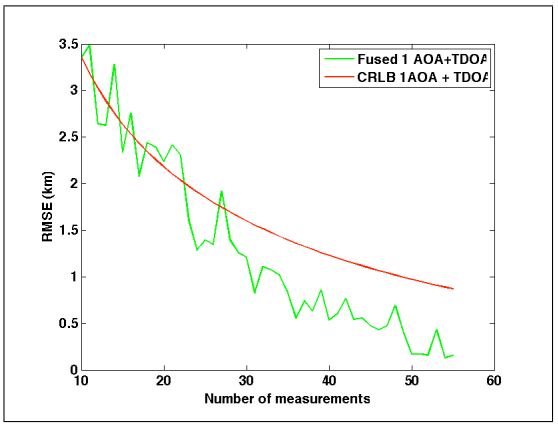

Figure 4.16: Average RMS error, geolocation using HT, fusing TDOA and AOA measurements

Because the sensor data for either AOA or TDOA measurements has been transformed into conditional probabilities and are now in a unified parameterized space, irrespective of the type of measurement, it is possible to merge the TDOA sensor data with the AOA sensor data very easily.

$$A(x,y) = \frac{1}{M}\sum_{m=1}^{M} p(x,y|\theta_m) + \frac{1}{L}\sum_{l=1}^{L} p(x,y|\tau_{l,1}) \tag{4.14}$$

The results of fusing the two TDOA measurements, described in the previous section and plotted in figure 4.13, with one AOA measurement, are shown in figure 4.14. The strong single peak in the Hough transform space, coincides with the maximum likelihood of the emitter position.

Figure 4.15, shows the scenario as in figure 4.12 for TDOA-only measurements, but with addition that one UAV (marked as UAV2) is capable to obtain additional AOA measurement and pair of UAV is capable to obtain one TDOA measurement. The purpose of this modification is to check fusion of AOA and TDOA measurements. The standard deviation of the TDOA measurement error in this simulation is set at $\sigma_{TDOA} = 7 \times 10^{-7}$ seconds and the standard deviation of the AOA error is set at a value of 0.02 radians. It is clear how the additional AOA data has provided further information to improve the accuracy of localizing the target position as shown in figure 4.16. Additional AOA measurements forced average RMS error to fall below 3.5 km on initial 10 measurements, compared to 25 km using TDOA-only measurements as shown in figure 4.12.

Frequency difference of arrival

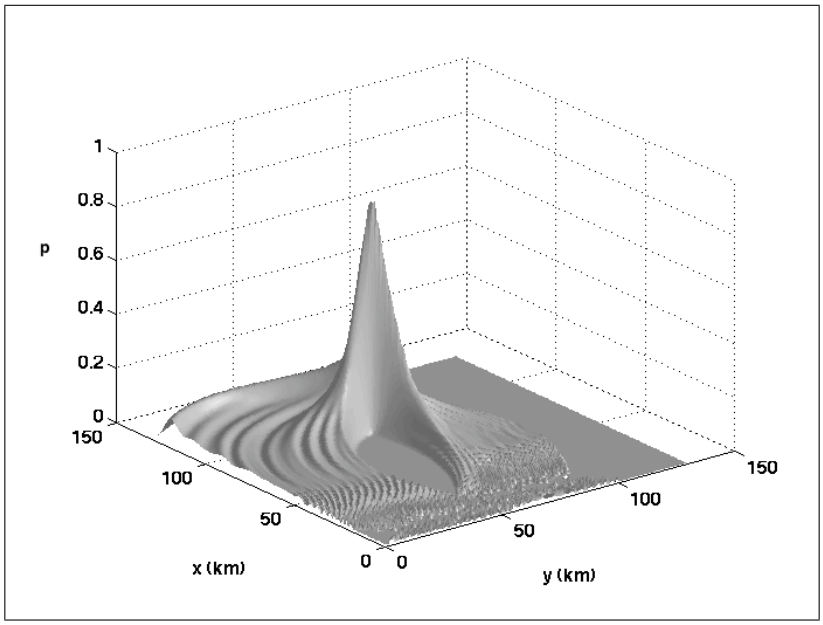

Figure 4.17: Hough Transform space for FDOA-only measurements

In the previous section, the Generalized Hough Transform was used for TDOA and AOA measurements. In this section, this approach will be extended to using frequency difference of arrival measurements. The advantage of adding FDOA measurements is that they produce emitter location estimates whose error ellipse may lie in a different direction to the error ellipses of the other two methods. Consequently, it is possible to minimize the effect of geometric dilution of precision (GDOP) by suitable fusion of the different types of measurement data. The following illustrates the Hough Transform method for the case of emitter geolocation using frequency difference of arrival (FDOA). Assume that the FDOA measurement f_{d_i} between the two spatially separated receivers can be obtained, using a Doppler receiver of bandwidth B. The individual Doppler shifts at receiver 1 and receiver i are given by:

$$F_{r_1} = -\frac{f_0}{c}\frac{v_{x_{r_1}}(x - x_{r_1}) + v_{y_{r_1}}(y - y_{r_1})}{\sqrt{(x - x_{r_1})^2 + (y - y_{r_1})^2}} \tag{4.15}$$

$$F_{r_i} = -\frac{f_0}{c}\frac{v_{x_{r_i}}(x - x_{r_i}) + v_{y_{r_i}}(y - y_{r_i})}{\sqrt{(x - x_{r_i})^2 + (y - y_{r_i})^2}} \tag{4.16}$$

where (x, y) is a point on the search space grid representing a possible emitter position, (x_{r_i}, y_{r_i}) is the known position of the ith receiver at some time instant when the measurement is made, v_{x_i} and v_{y_i} are the components of the velocity of the platform in the x and y directions at the instant the measurement is made and f_0 is the carrier frequency of emitter signal of interest. The pdf of the emitter location

for this case is given by:

$$p\left(x,y|f_{d_i}\right) = \frac{\exp\left(-\frac{(F_{r_i}-F_{r_1}-f_{d_i})^2}{\sigma_{f_d}^2}\right)}{\sqrt{2\pi}\sigma_{f_d}} \tag{4.17}$$

The resulting accumulator array for N measurements is given by:

$$A_{FDOA}(x,y) = \frac{1}{N}\sum_{m=1}^{N} p\left(x,y|f_{d_i}\right) \tag{4.18}$$

Figure 4.17 shows the ability of two moving platforms to geolocate an emitter. In this case, the two platforms were moving generally North at 40 m/s according to a wavy path, as described in figure 4.18; where $\sigma_{f_d} = 12$mHz is taken from [10] as a Cramer-Rao lower bound value for $B = 25$kHz with an integration time $T = 1$s and $SNR = +3$dB. The measurements assumed to be taken each 10th second. Figure 4.17 represents the accumulation of 10 FDOA measurements. Note, how the Hough Transform is able to accommodate the different receiver positions during the set of measurements because it operates in a unified parameterised space. In figure 4.19

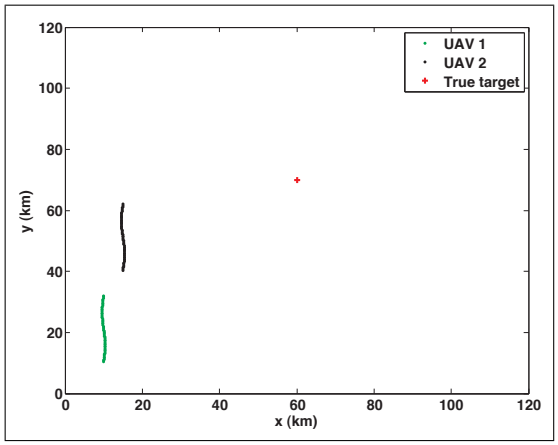

Figure 4.18: Scenario for geolocation with HT, using FDOA-only measurements

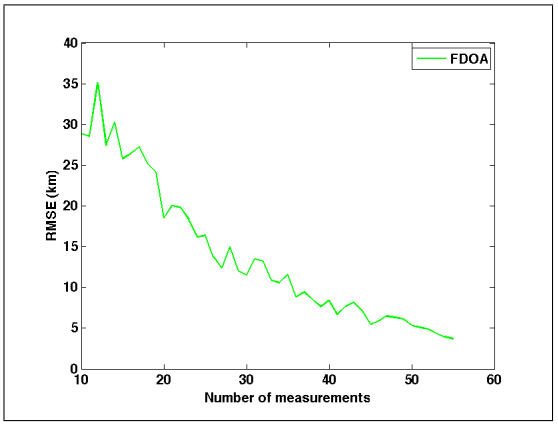

Figure 4.19: Effect of number of measurements on the average RMS positional error, showing effect of fusion different number of measurements. FDOA-only measurements used for the scenario in figure 4.18

average RMS error is noticeable high, starting from 35 km for 10 measurements. This is due to the fact that F_{r_1} and F_{r_i} depend on the speed vectors (direction of the movement) $(v_{x_{r_1}}, v_{y_{r_1}})$ and $(v_{x_{r_1}}, v_{y_{r_i}})$ respectively, but both platforms moving in the same direction as in TDOA-only scenario on figure 4.11. In the next section the advantage of fusion of all three different type of measurements will be demonstrated.

4.2.4 Fusion of AOA and TDOA with FDOA Measurements

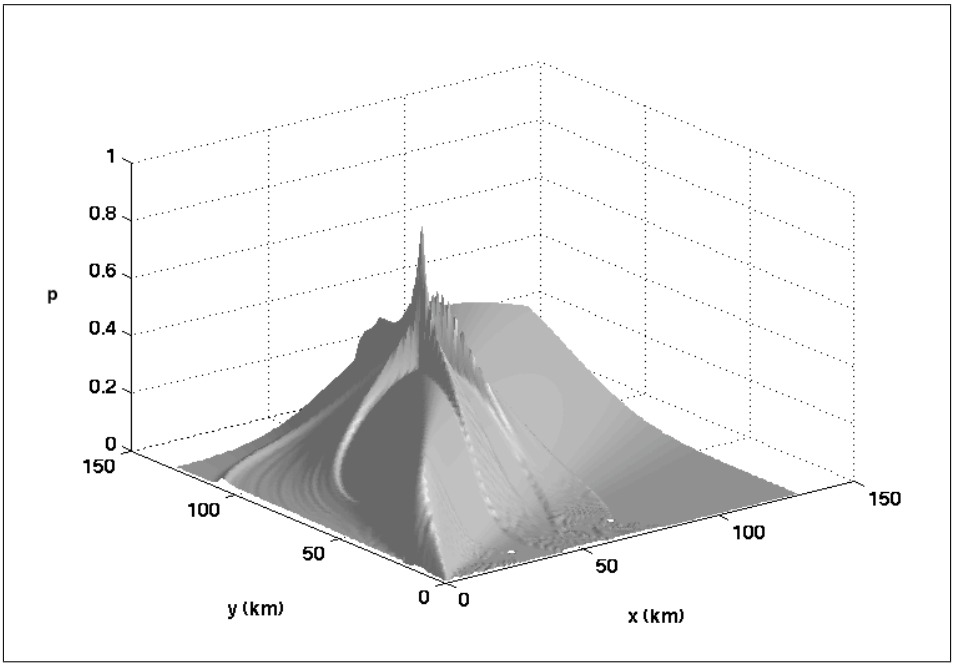

Figure 4.20: Hough Transform space for fusion of AOA, TDOA and FDOA measurements

Because the sensor data has been transformed into conditional probabilities and are now in a unified parameterized space, irrespective of the type of measurement, it is possible to merge the FDOA sensor data with TDOA and AOA sensor data as in (4.14), using (4.18), (4.13) and (4.5):

$$\begin{aligned} A(x,y) &= \frac{1}{L}\sum_{l=1}^{L} p(x,y|\tau_{l,1}) + \\ &\quad \frac{1}{M}\sum_{m=1}^{M} p(x,y|\theta_m) + \\ &\quad \frac{1}{N}\sum_{m=1}^{N} p(x,y|f_{d_i}) \end{aligned} \tag{4.19}$$

Figure 4.20 shows the ability of three moving platforms to geolocate an emitter according to the scenario shown in figure 4.21. In this case, the two platforms moving North at 40 m/s according to a wavy path are able to take TDOA and FDOA measurements, whereas the platform moving East at 40 m/s is able to take AOA measurements only. The standard deviation of the TDOA measurement error in this simulation is set at 7×10^{-7}s and the standard deviation of the AOA error was set at a realistic value of 0.02 radians and the standard deviation of the FDOA measurement was set at 12mHz. This set of results shows how it is possible to fuse three different measurement types using the Hough Transform. To obtain figure 4.20 a total of ten TDOA and FDOA measurements were taken along with ten

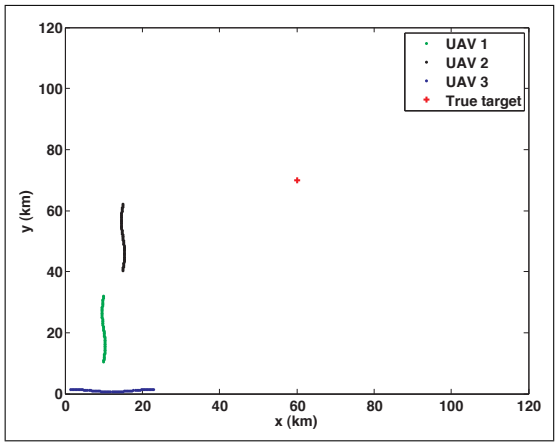

Figure 4.21: Scenario for fusion of AOA, TDOA and FDOA within HT

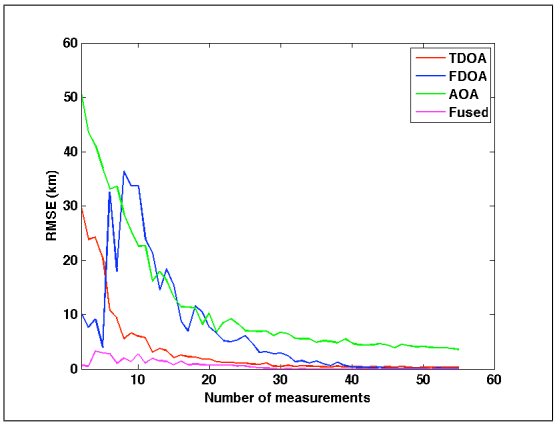

Figure 4.22: Effect of number of measurements on the average RMS positional error, showing effect of fusion different type measurements for the scenario in figure 4.21

AOA measurements. Figure 4.22 demonstrates the results of fusion all three types of measurements, using the RMS positional error as the metric. This figure shows quite clearly how fusion improves the positional accuracy of emitter location with an additional FDOA measurements. In chapter 7 it will be shown how the geolocation accuracy can be improved by weighting the contributions to the accumulator array from the AOA, TDOA and FDOA measurements in (4.14).

4.2.5 Fusion of sensor data with terrain data

The new HT method is also very convenient for adding terrain data. In this case, the terrain data is first processed to give a first order likelihood that the emitter can be located at a particular map reference on the basis of *a priori* knowledge. This terrain-based likelihood map is then transformed into the Hough transform space where it is merged with the Hough transforms for the TDOA data and the AOA data. For example, in figure 4.23 the likelihood that our target is *not* likely at a particular point on the map is shown as the darkened areas. This area may be a maritime area for a land-based target, thus it is assumed that the target cannot be located in the water. Alternatively it may be known to be a naval target, where the marked area is land. The influence of this additional information on the Hough Transform space, and hence the likelihood of location the emitter is shown in figure 4.24. In this figure the Hough Transform for TDOA-only measurements was altered by map-aided information. This can be written as

$$A_{fused}(x, y) = A(x, y|\tau) + A_{terrain} \tag{4.20}$$

where $A(x, y|\tau)$ is the HT for TDOA only measurements as pictured in figure 4.10 and $A_{terrain}$ is the transformed map data obtained as a emitter likelihood - *a priori* information. In this modified parameterized space the peak of the likelihood will

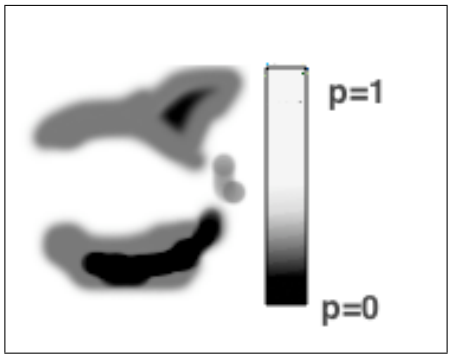

Figure 4.23: Illustration of map data showing regions where the emitter is unlikely to be (increasing level of grey)

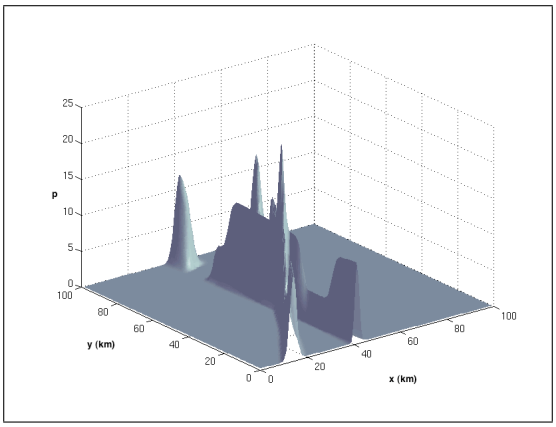

Figure 4.24: Fusion of TDOA data with map data

always be located within the possible conditions of target location, even if the noisy measurements will point into the wrong region masked by *a priory* information. It should be theoretically possible to add different *a priori* information with different levels of confidence. This simple property may be used for target geolocation in mixed environments like coastal areas. There is an ongoing work to use particle filter for tracking with map-aided systems [60].

4.2.6 Conclusion

A new geolocation algorithm based on the Hough Transform has been presented. It has the following advantages over traditional estimator algorithms: (i) the algorithm does not require an initial guess of the emitter position, (ii) it is easy to fuse data from different sensors, (iii) terrain data can be incorporated with the sensor data, (iv) the method can have a flexible error model (e.g. the error model may be Gaussian or other distribution), (v) it is robust. The results have shown that this new approach provides average RMS errors that are close to the CRLB. Some results presented in this section have raised many questions about the applicability Cramer-Rao lower bound to the geolocation problem, and also about the proper method of calculation of the CRLB for a given scenario. Although there are a number of papers about the

use of CRLB in sensor localisation and geolocation they are based on Foy's paper [22] "Position-Location Solutions by Taylor-Series Estimation" and it seems as if the use of this approximation is not sufficiently due to non-linearity of the geolocation problem. Moreover, CRLB defined in terms of the variance (mean) and although incorporates geometry of the location as an ellipse may not be able to reflect the true performance of the estimators in geolocation. As it was demonstrated before it defines the circle out of error ellipse defined by Fisher information matrix as show in figure 2.3. But CRLB is becoming lower bound as number of measurements increase.

4.3 Geolocation in fading and NLOS conditions

4.3.1 Signal and channel model

Introduction

In order to test the performance of the algorithm in non-line of sight environments, it is necessary to model the signal and channel of interest. The scenario was chosen, where a number of small tactical UAVs are trying to geolocate an RF emitter in a 'hilly' terrain. The RF emitter can be a mobile handset or a rapidly deployable base station. In this section, literature overview of the multipath propagation model and the non-line-of-sight problem will be given, followed by a detailed description of the simulated channel and finally simulations scenario and results will be presented.

Multipath Propagation

Multipath propagation occurs due to the reception of multiple delayed copies of the same signal due to multiple reflections from the ground, building and other scatters. These multiple signals can combine constructively or destructively at the antenna in the receiver and this results in what is known as fading [61], [62], where the amplitude of received signal can fluctuate by 20 or 30 dB in both spatial and temporal domain and the phase of the receiver and the phase of the received carrier can vary randomly. This fluctuation in signal level can seriously affect the accuracy of measuring AOAs, TOAs and TDOAs. In AOA estimation, the multipath environment might cause the AOA of the received paths to be different from the true AOA due to reflection and scattering. In location algorithms that use AOA estimates to locate the sender, using the AOA estimates that correspond to the multipath AOAs (not the true AOA) will induce an error in the sender location estimate. Time-based location systems such as TDOA most often use correlation techniques to obtain TDOA and these estimates are affected by the presence of multipath [61], which smears the time of arrival of the signal (the time-delay spread). If one arriving multipath ray has more power than other such rays, the estimated delay using conventional delay estimators will be biased towards the strong multipath ray which may be far from the true delay estimate. Thus, for location algorithms that utilise delay estimates to locate the emitter, an error will be induced into the estimate of the wanted emitter location. The effect of multipath on code acquisition (for TOA estimation) is discussed in [63],[64], and on delay locked loops (DLLs) in [65] where the multipath component is seen to bias the tracking of the DLL. Methods that provide better resolution for estimating TOA in multipaths include subspace techniques [66] and adaptive techniques [67].

For time-based location systems, the extra propagation distance of the non-line-of-sight (NLOS) path directly corresponds to a positive added error to the true range between the sender and receiver. This kind of error occurs when the direct path between the sender and the mobile emitter is blocked, for instance by a building, and

a constant positive bias is added to the measurements due to the extra path length of the scattered signal. A typical ranging error introduced by NLOS propagation has been measured in the Global System for Mobile communications (GSM) system which indicates that the NLOS spatial error can average between 500-700 meters [68]. For direction finding location systems, the angle from which the signal arrives at the receiver is not in the true direction to the emitter. The measured angle will be the one corresponding to reflections from scatterers that surround the RF emitter. NLOS analyse derived in [69] and [28]. There are also several methods to mitigate the NLOS error for TOA signal for mobile networks proposed in [70]. Several simulations described in the literature have found that the position error in the location estimators increases linearly with the increase in the NLOS errors [71]. One of the most common approaches to battle this problem consists of exploiting the fact that the variance of the TOA measurements is significantly increased in NLOS scenarios ([72] and [71]). These algorithms try to detect the NLOS-receivers by comparing the estimated variance of the measurements with an *a priori* known variance. This last variance cannot normally be provided because it depends on environmental conditions (rural, urban or suburban). Another approach is to use a fixed scatter model to obtain an improved TOA estimate from a set of TOA measurements corrupted by multipath errors [73]. Although these approaches can ameliorate the effect of the multipath, they cannot detect constant NLOS errors in short observation windows. Finally, another approach consists of exploiting the redundant information present in the measurements to detect and drop the NLOS errors. The most relevant contribution in this direction was presented in [74] where the problem was formulated in terms of hypotheses, where each hypothesis corresponded to a set of receivers considered under NLOS scenarios. The algorithm presented was based on a weighted combination of the partial position estimates associated to each hypothesis. Unfortunately, this combination presents poor performance if the NLOS error presented in the TOA measurement is high.

Transmitted signal of interest

At the outset, it was assumed that the signal of interest was a GSM cellular radio transmitter [75] that was either a mobile handset or a rapidly deployable base station. Accordingly, this type of signal was modelled in Matlab as a Gaussian minimum shift keyed signal (GMSK) with a data rate of 271kb/s. The signal waveform has the form:

$$s(t) = A\cos\left(2\pi f_c t + a(t)\int_0^t f_d(t)\,dt\right) \tag{4.21}$$

where, A is the carrier amplitude, f_c is the carrier frequency (typically 900MHz or 1800MHz), $a(t)$ represents the binary data stream after it has been passed through a Gaussian filter with a time-bandwidth product, $BT = 0.3$. In the usual way, this signal was modelled as a complex-valued baseband equivalent model. The notional carrier frequency used to define the channel parameters was chosen to be 1800MHz.

A standard 0.577ms GSM timeslot containing 156.25 data bits was generated for

each user. A full eight user GSM time frame of 4.615ms duration was continuously generated in which data was randomly generated for each user. Although the GSM standard has a fixed training pattern within the middle of each time slot, these were not used by the receivers in the UAVs to obtain timing as this would have implied some form of cooperative emitter geolocation. Instead the preferred method was to cross-correlate the signal at each UAV over the entire wanted user's time slot to obtain the relative time of arrival difference between those pair of platforms. The reason for performing a full multi-user simulation is that timing errors due to the different ranges of each UAV platform from the emitter of interest ensure signals from users in adjacent time-slots may fall within the correlation window used to obtain the time difference of arrival. This partially decorrelates the signal of interest and is a potential source of timing error. However by performing correlations of the signal between receivers on each UAVs this problem can be mitigated. Consequently, this is an important feature to include in the model.

Channel Model

At the outset, it was assumed that tactical UAVs would be used to geolocate the wanted, stationary emitter. It was further assumed that the environment in which the UAVs flew ensured that there was no single direct line-of-sight path between each UAV and the transmitter of interest (due to localised scattering of the signal near the emitter). Consequently, it was assumed that propagation between the handset and the UAVs suffered from multipath propagation in which each echo suffered from Rayleigh fading at a rate dictated by the Doppler spread due to the motion of the UAVs.

A Cooperation in the field of Scientific and Technical Research 207 (COST 207) propagation channel model was used to represent the received signal at each UAV [76][77]. This is a standard channel propagation model for GSM signals as recommended by the International Telecommunication Union (ITU. In this model, it is assumed that the channel impulse response may be represented by:

$$h(t,\tau) = \sum_{l=0}^{L_p} c_l \exp^{j\phi_l t}\, \delta\left(t - \tau_l(t)\right) \tag{4.22}$$

where L_p is the number of multipath components (including the direct path if one exists), $c_l(t)$ is a random time-varying path-loss coefficient for the l_{th} path which has Rayleigh statistics, $\phi_l(t)$ is a random time-varying phase shift associated with the l^{th} path which has a uniform distribution in the range $(0, 2\pi)$ and τ_l is the time-varying time-delay associated with the lth path due to the length of that path. All these parameters are time varying due to the change in environment as the UAV receiver platforms move. Consequently, the rate at which these parameters change is determined by the speed of the receivers. The parameters of the impulse response given by (4.22) can often be represented by generic channel environments, such as the 'urban', 'suburban' or 'hilly' channel models, in which the number of paths is fixed, along with its delay profile and the mean path loss for each path, as defined by the

'standard' for that model. These different models have been developed in response to many years of experimental propagation studies in a wide variety of geographic areas. In this work, a COST 207 'hilly' model was used, as an example for the possible applications of the selected scenario, for which the stationary characteristics of the impulse response of (4.22) are represented by figure 4.25 below, where the mean path loss values, $\overline{c_i}$, are relative to the direct component, $\overline{c_0}$. The hilly model provides particular challenges due to very long delay spread out to 17μseconds which is due to the time taken for the signal to reflect of distant hills which are typically $3-4$ km away. COST 207 'hilly' model has a strong line-of-sight component and in order to simulate non-line-of-sight this component was removed, as shown in figure 4.26

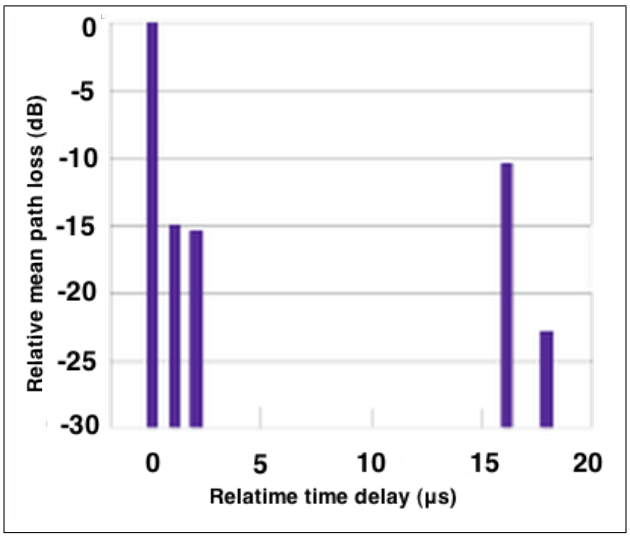

Figure 4.25: Impulse response for the COST 207 'Hilly' channel model

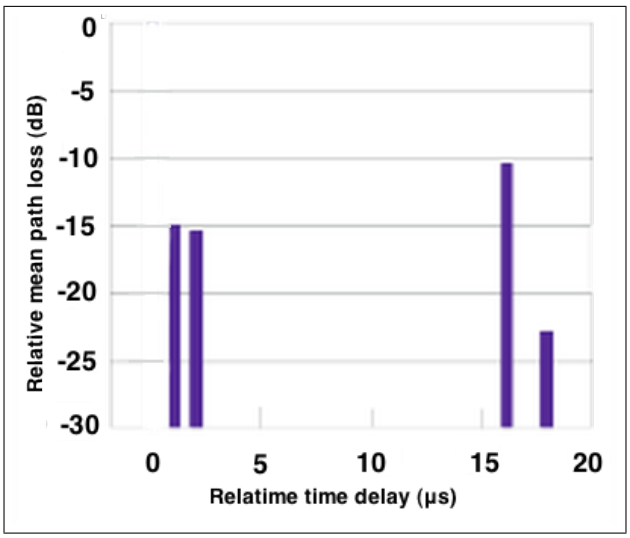

Figure 4.26: Impulse response for the COST 207 'Hilly' channel model, simulating NLOS conditions, LOS component removed

The actual mean path loss of the direct component of the received signal is assumed to be given by one of two forms, depending used to represent model of the propagation. For low-flying UAVs, where there is high probability of the signal at the UAV receiver containing both a direct ray and a reflected signal from the ground, a 'plane-earth' propagation model was used where the mean path loss is given by:

$$L_{pe} = \frac{(h_t h_r)^2}{d^4} \tag{4.23}$$

where h_t and h_r are the transmitter and receiver heights respectively and d is the range between the transmitter and receiver. For the case of high flying UAVs, where there is a line-of-sight component to the received signal, the path losses were modeled by a free space propagation loss model of the form:

$$L_{free} = \frac{(4\pi d)^2}{\lambda^2} \tag{4.24}$$

where λ is the wavelength of the transmitted signal, d is the range between the transmitter and receiver. The decision whether to use the plane-earth or free space propagation equations is determined by the degree of 'clearance' that exists for the signal of interest. This clearance is given in terms of the Fresnel zone clearance shown in figure 4.27. In this work, it is assumed that the path has adequate clearance if the first Fresnel zone clears any obstacles along the flight path. Other clearance criteria are possible such as '$0.7R_1$', but the clearance used here is quite conservative. In figure 4.27, UAV1 has a clear line of sight path for the transmitter of interest. Furthermore, the first Fresnel zone 'clears' the building by the small margin, indicating that there will be no diffraction effects. For this situation, free-space propagation is assumed, with Rician random perturbations to account for localised scattering along the path of interest. For the case of UAV2, the direct line of sight path clears the obstruction but the first Fresnel zone does not clear the obstruction, indicating either strong diffraction losses or scattering. In this case we assume that the propagation model is LOS but with a scattered component that is Rician distributed and which includes diffraction losses for the direct path. For the case of UAV3, it is assumed that the signal arrives at the UAV receiver *via* non-line of sight scattering and a plane-earth Rayleigh model is assumed for this case. This is the model used most often in this work in order to simulate NLOS components.

In this scattering model, each of the L paths is assumed to be faded, due to local scattering, with a Rayleigh distribution. This provides a random component to the coefficient $c_l(t)$ which in figure 4.28, is given by $\tilde{c}_i(t)$. Figure 4.28 shows how the multipath channel is modelled as a transversal filter, in which τ_{di} represents the relative path delay between the $(i\text{-}1)^{th}$ path and the i^{th} path. The mean path loss coefficient $\bar{c}_i$ is obtained from figure 4.3.1 and each path loss coefficient, $\tilde{c}_i\,(t)$ is independently generated from a Rayleigh distributed coefficient generator. However, in this Matlab model, since the data is complex valued baseband data, $\tilde{c}_i$ is also complex valued and it is generated by random selection from two independent Gaussian distributions, one for the real component of the signal, the other for the imaginary term.

$$\tilde{c}_i = \tilde{c}_{R_i} + j\tilde{c}_{I_i} \tag{4.25}$$

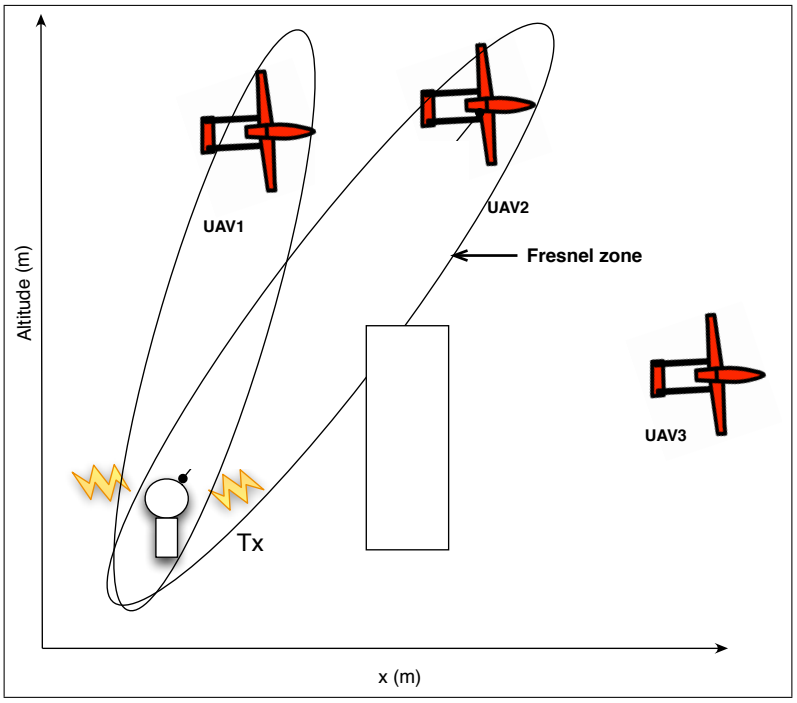

Figure 4.27: Fresnel zone clearance

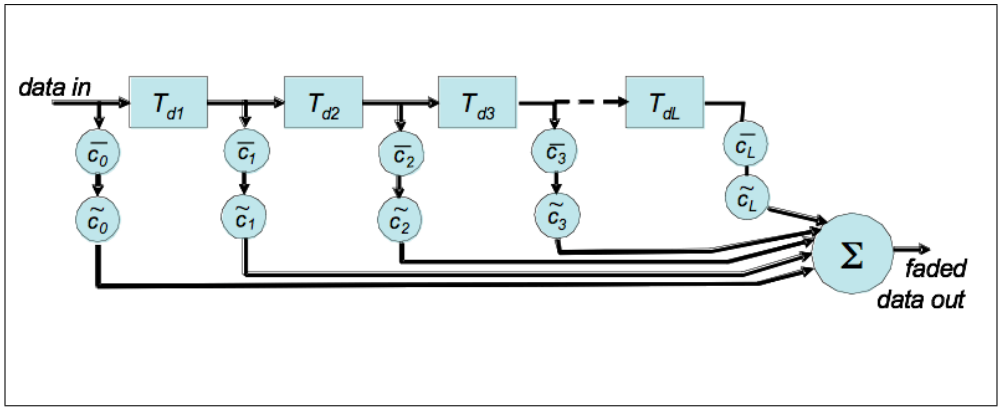

Figure 4.28: Schematic of the channel model, based on a transversal filter.

The time variation of these coefficients is set by the Doppler velocity of the UAV receiver platforms and this is achieved by filtering the samples of the Rayleigh distributed path coefficient, $\tilde{c}_i(n)$ with an appropriate digital realisation of a 'Doppler filter'. This filter represents the spectral characteristics of the Doppler spread that occurs when a signal has been scattered and received over the full 360 $^\circ$ azimuth, provided by a moving omni-directional receiving antenna. A common digital representation of the Doppler filter is to convolve the Rayleigh distributed path coefficients with the impulse response of the Doppler spread function.

Figure 4.25 shows a schematic diagram of how the time varying channel coefficients for the i^{th} path are generated for complex valued data.

In this simulation, the maximum frequency of the Doppler filter is set at accord-

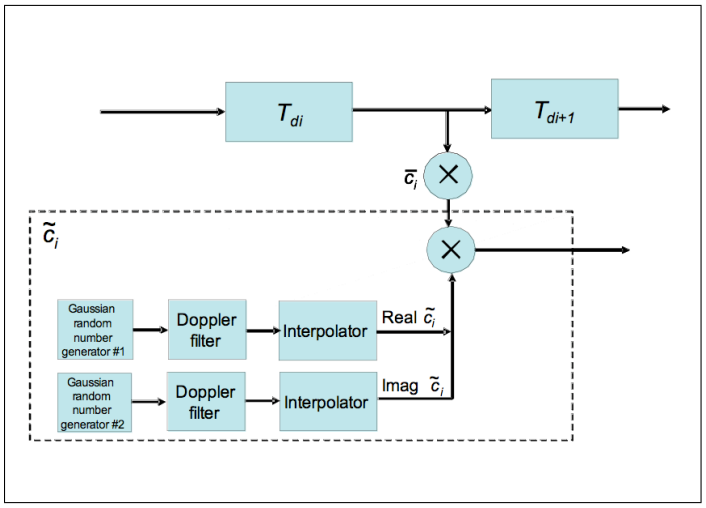

Figure 4.29: Schematic showing how the time-varying channel coefficients are generated

ing to:

$$f_{D_1} = -\frac{f_0}{c}\frac{v_{x_{r_1}}\left(x - x_{r_1}\right) + v_{y_{r_1}}\left(y - y_{r_1}\right)}{\sqrt{\left(x - x_{r_1}\right)^2 + \left(y - y_{r_1}\right)^2}} \tag{4.26}$$

as in section 1.4.2, although it is common in GSM mobile phone simulations to simulate it with $v_{\max} f/c$, where v_{max} is the maximum velocity. The received signal is the convolution of the transmitted signal with the channel impulse response:

$$r\left(t\right) = \int_0^{T_s} h\left(t,\tau\right) s\left(t-\tau\right) d\tau + n\left(t\right) \tag{4.27}$$

where T_s is the total delay spread of the impulse response and $n\left(t\right)$ is complex-valued additive noise provided by the channel[1].

One of the key aspects of this propagation model is that the overall propagation loss is used to compute the instantaneous signal level of the emitter of interest at the various UAV receivers as this plays an important part in determining the error in the timing measurements needed to geolocate the emitter.

4.3.2 Receiver Model

In the context of the geolocation problem addressed here, the UAVs are not required to intercept the GSM signal, merely to act as a remote antenna system which is able to time-stamp the received signal and to append the precise location of the UAV at the time the signal was received. It is assumed that this is accomplished using GPS navigation and timing. Accordingly, the receiver used in each UAV is

[1]It is a complex valued process because the signal is modelled as complex valued baseband signal

assumed to have a bandwidth that accepts the GSM signal without adding further distortion. Its bandwidth is defined by a root-raised cosine filter. The equivalent noise bandwidth of the filter was set to $W = 200$kHz. The receiver model includes the effect of additive Gaussian noise and for this was a typical value of the receiver noise temperature $T_s = 1300$K, the antenna noise temperature $T_a = 290$K yielding an equivalent noise temperature for the receiver of $T_e = T_s + T_a = 1590$K. From this the variance of the receiver noise signal is:

$$N_{se} = kT_eW = 4.4 \times 10^{-15} \quad W \tag{4.28}$$

The carrier power to noise ratio at the receiver is given by:

$$SNR = 10 \log_{10} (P_r/N_{se}) \tag{4.29}$$

where P_r is the received power given by:

$$P_r = P_e L_{total} \tag{4.30}$$

where P_e is the effective isotropic radiated power of the transmitter, and the path loss, L_{total}, is total sum of all path losses. When a good path is assumed L_{total} will include the free-space path loss term and when plane-earth propagation exists, plane-earth loss is used in L_{total}. SNR is an important factor to include in the model due to the fact that the accuracy of the estimation of AOA, TDOA and FDOA directly depends on it. For example, there are a number of different theoretical approximations for σ_{TDOA} depending upon the assumptions made regarding the SNR of the received signal [10]. For good SNR conditions it is common to assume that the standard deviation of the timing error is given by:

$$\sigma_{TDOA} \approx \frac{1}{W\sqrt{\text{SNR}}} \tag{4.31}$$

where W is the noise bandwidth of the receiver, whereas for low SNR the achievable timing error is often given by [59]:

$$\sigma_{TDOA} \geq \sqrt{\frac{3}{8\pi^2 T}} \frac{1}{\text{SNR}} \frac{1}{\sqrt{f_2^3 - f_1^3}} \tag{4.32}$$

where T is the integration time used in the receiver and $W = f_2 - f_1$. Whereas the effect of SNR on the standard deviation of a AOA measurements is given by [23]:

$$\sigma_\theta^2 \geq \left(\frac{c}{2\pi f_0 d \cos(\theta)} \right)^2 \left(\frac{1}{SNR} \right) \tag{4.33}$$

where f_0 is the carrier frequency of the received signal, d is the maximum separation between antenna elements of interferometer antennas, and θ is the true bearing angle. There is a known problem with AOA measurements in multipath/NLOS environment that in addition to σ_θ^2 multipath can add multipath error in the range $(0, 2\pi)$ thus rendering AOA measurements unreliable. This limits the application of the AOA measurements to RF emitter geolocation problem in NLOS environment. In this simulation it was also difficult to obtain reliable FDOA measurements due to the relatively slow UAV speed and high fading. Consequently, the research has concentrated on the application of TDOA measurements to RF emitter geolocation in NLOS environment.

4.3.3 TDOA Measurements

The measurement of the TDOA between two UAV platforms is obtained by correlating the signal received at each of the platforms[2]. The cross-correlation between a sampled signal $x(n)$ and a sampled signal $y(n)$ at a lag of m samples is given by:

$$R_{xy}(m) = E\{x(n+m)y^*(n)\} = E\{x(n)y^*(n-m)\} \tag{4.34}$$

where where $x(n)$ and $y(n)$ are jointly stationary random sampled processes,$-\infty < n < \infty$, and E is the expectation. This is carried out for all useful values of m that cover the expected time difference of arrival of the signal. Figure 4.30 shows the output of the cross-correlation function (CCF) of the received GSM signal one of which is delayed relative to the other due to the path length difference. The x-axis of 4.30 represent time-delay in terms of number of samples (Fast Fourier transform bins). Bin number 13596 represent the CCF with the signal with no delay ($\tau = 0$). Time sampling rate for the signal $t_s = 1 \times 10^{-7}$ seconds. It is possible to obtain the value $\tau_{i,1}$ time-delay between two signals by obtaining maximum, than calculating the off-set in bins of the CCF t_{bins} of this maximum bin out of $\tau = 0$ and then multiplying it by sampling rate t_s:

$$\tau_{i,1} = t_{bins} t_s \tag{4.35}$$

Although 4.30 seems to have a sharp peak, zooming into it as in figure 4.31 demonstrates that it consists of multiple peaks, thus maximum in this cross-correlation function can shift due to the fading conditions.

Implicit in this method is that a data link exists between each platform and a control centre, where the TDOA and emitter position are computed. It is assumed that the bandwidth of the data links is sufficient so as not to distort the waveforms prior to correlation. It is also assumed that the UAV platforms time-stamp the signals prior to them being sent along the data links so that differential link delays can be compensated for. A time-stamping precision of $\sigma_T = 5ns$ is assumed, which is known to be achievable by GPS. It is possible to include the *a priori* knowledge about the model into the geolocation algorithm by altering the σ_{TDOA}. In this case

$$\sigma_{TDOA} = \sigma_T + \sigma_{multipath} \tag{4.36}$$

where $\sigma_{multipath}$ average multipath delay, selected empirically based on a fading channel model.

Simulation Scenario and Results

Using the channel model described in section 4.3.1 a performance of the Hough Transform algorithm was tested in NLOS conditions. Figure 4.32 shows a typical

[2]It is assumed that each UAV is able to exchange the raw signal that it has received via a broadband RF link to allow this correlation to take place. This segment of raw signal will be space and time stamped.

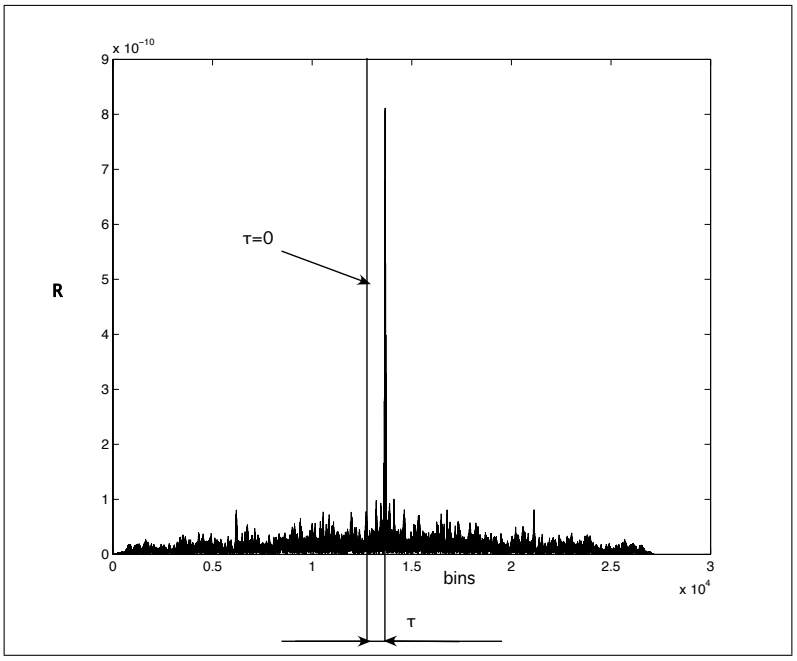

Figure 4.30: Output of the cross-correlation of the two GSM signals

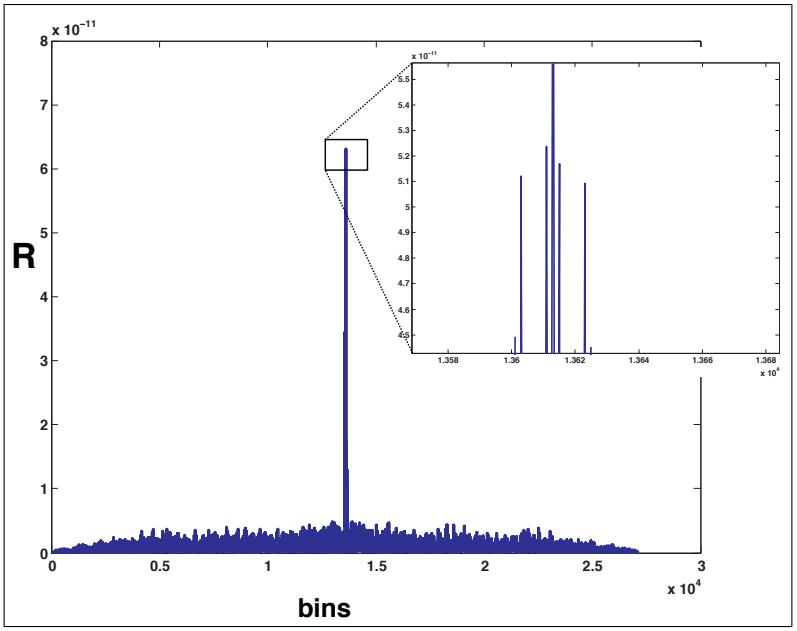

Figure 4.31: Output of the cross-correlation of the two GSM signals with zoomed peak

scenario in which three UAVs are used to geolocate a single handset, denoted as a cross at $(2664m, 3157m)$. The three UAVs, denoted as circles, can have arbitrary flight paths and are shown here with wavy paths for two platforms and a straight path for the other. The speed of the platforms is $40m/s$ and $\sigma_{TDOA} = 5ns$. It is necessary to use three UAV because two platforms are not enough to provide an estimate in NLOS conditions. Direct application of the Hough Transform algorithm leads to the following results: figure 4.33 shows the effect on the RMS position

error of increasing the number of TDOA measurements taken by the platform along their respective flight paths. It is assumed that the position of the UAV is precisely known during the estimation of the TDOA between pairs of platforms and does not contribute to the RMS position error.

Figures 4.34 and 4.35 demonstrate the effect of number of measurements on geolocation accuracy in line-of-sight COST 207 'hilly-terrain' and additive white gaussian noise channels (AWGN) respectively. It can be noted, that that the average RMS error for COST 207 model with line-of-sight component in figure 4.34 indistinguishable from 4.35. This is due to the fact that the method of obtaining TDOA measurement chosen (cross-correlation) is capable to suppress the impact of fading on the value of TDOA measurement and because of this additional suppression the simulations were able to produce identical results as difference in the channel models were suppressed by cross correlation. But it is clear, that the NLOS component has made an impact on accuracy of TDOA measurements and thus on average RMS geolocation error in figure 4.33, where average RMS error falls below 25 meters only after 20 measurements, while in figure 4.34 falls below 10 meters most of the time.

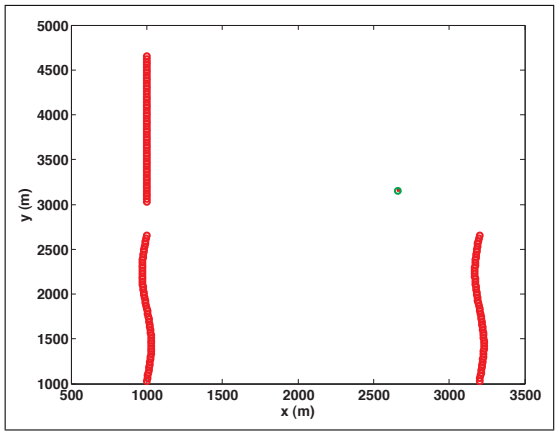

Figure 4.32: Scenario for geolocation using multiple UAV with COST 207 channel model, showing flight paths of three UAV platforms and emitter. The green circle shows the estimated emitter position

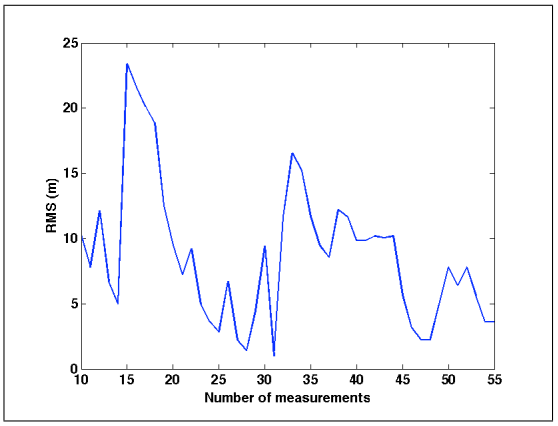

Figure 4.33: Average RMS positional error of the emitter (meters) against number of measurements, used to provide an estimate with NLOS model simulated by COST 207 'hilly-terrain' parameters. Average RMS error was calculated over 50 simulations

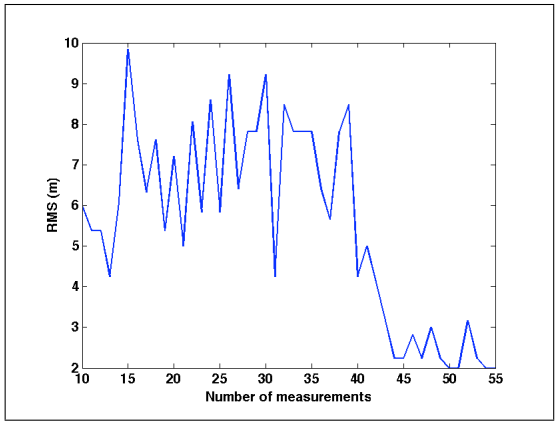

Figure 4.34: Average RMS positional error of the emitter (meters) against number of measurements, used to provide an estimate with LOS fading model simulated by COST 207 'hilly-terrain' parameters. Average RMS error was calculated over 50 simulations

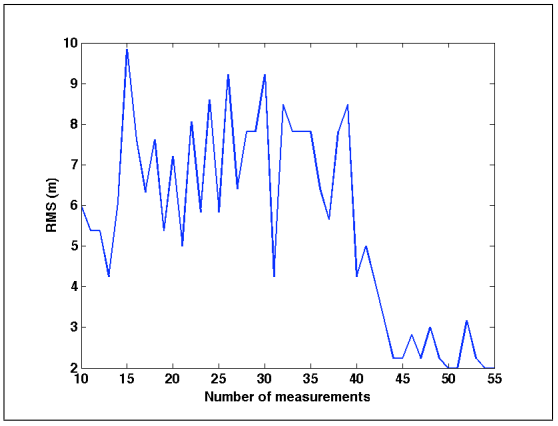

Figure 4.35: Average RMS positional error of the emitter (meters) against number of measurements, used to provide an estimate with additive white gaussian noise channel model. Average RMS error was calculated over 50 simulations

Figure 4.36 shows 2D representation of the HT space for the scenario 4.32. Figure 4.37 shows zoomed parameterised space in the vicinity of the emitter. It was as-

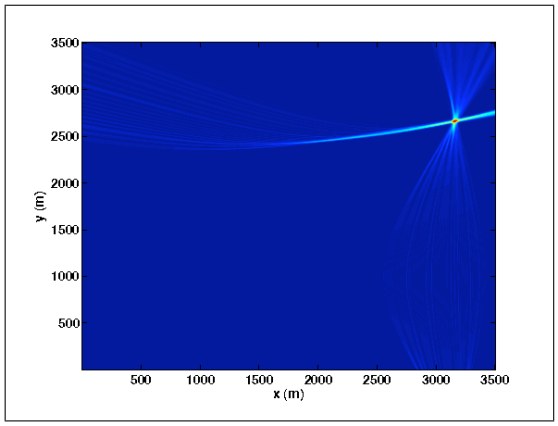

Figure 4.36: Illustration of the 2D parameterised space for geolocation scenario in figure 4.32 using NLOS COST207 model

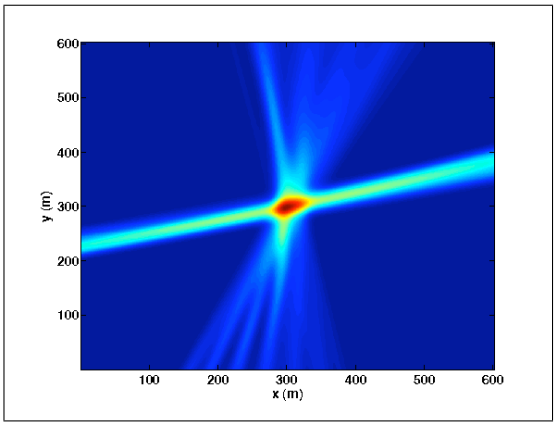

Figure 4.37: Zoomed illustration of the 2D parameterised space for geolocation scenario in figure 4.32 using NLOS COST207 model

sumed that there is a model mismatch between likelihood used in Hough Transform as NLOS channel model introduces additional delay as can be seen on figure 4.26, therefore it is possible to 'tune' the HT algorithm by using equation 4.36, improving geolocation accuracy by using *a priori* knowledge about the NLOS conditions. Assuming $\sigma_{TDOA} = 50ns$ and reapplying HT algorithm to the same scenario leads to the results presented in figure 4.38. It is clear that by collecting a minimum five sets of TDOA measurements between three UAV platform causes the RMS position to fall to values that are less than 10m and the value of the average RMS error less variable, compared to initial results in figure 4.33. Figures 4.39 and 4.40 shows the

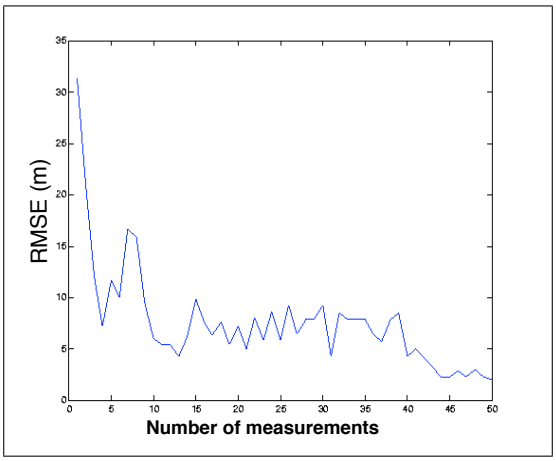

Figure 4.38: Average RMS positional error of the emitter (meters) against number of measurements, used to provide an estimate with NLOS model simulated by COST 207 'hilly-terrain' parameters. Average RMS error was calculated over 50 simulations

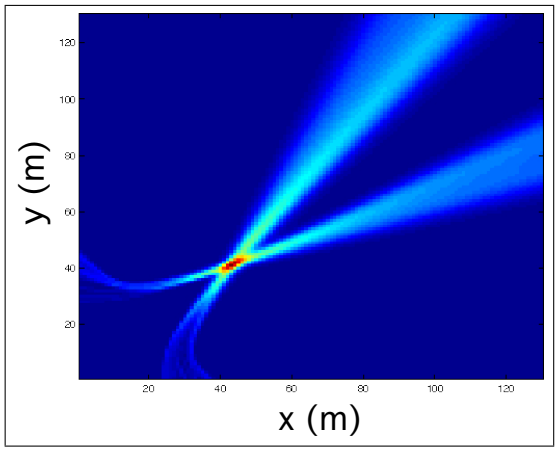

Figure 4.39: 2D Hough Transform space for geolocation using COST 207 channel model, illustrating the impact of the fading on HT

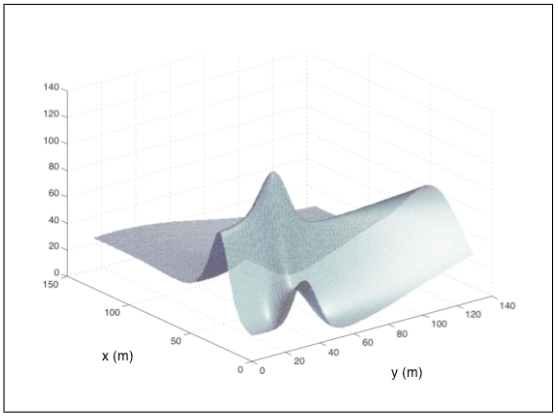

Figure 4.40: Three dimensional accumulator plot of HT space for TDOA-only measurements for the scenario given by 4.32. In this case the area shown is limited to a $150m \times 150m$ around the true emitter position

Hough Transform space, where 20 TDOA measurements from the moving platforms were fused, as per the scenario of figure 4.32. This figures does not show the entire search space but only a small area of $(150m \times 150m)$ in the vicinity of the target emitter with standard deviation of the measurement error $\sigma_{TDOA} = 50ns$. The peak of the HT space indicates the estimated emitter position, which is shown as the green circle in figure 4.32. It can be noticed comparing two dimensional representation of the parameterised space in figures 4.37 and 4.39 that 'smoother' curves lead to an improved results in the case of NLOS conditions, due to their ability to incorporate TDOA measurements altered by NLOS component.

Conclusion

In this section the Hough Transform was applied to the problem of geolocation in NLOS conditions. The simulations have shown how relatively few sets of TDOA measurements are needed to obtain acceptable RMS position errors using Hough Transform, even in NLOS conditions. Having established the methods utility for emitter location, the further work is focussed on reducing the computational overhead of the method using established techniques such as the Multi-resolution Hough Transform and Randomized Hough Transform, described in the next section.

4.3.4 Computational Complexity Reduction of the Hough Transform

The computational complexity of the Hough transform depends on the grid size and is of the order $(n \times m)$ where n and m are the grid dimensions. However, it is possible to perform a real-time Hough transform using real-time content-addressable memory [78] or to use optimized Hough Transform algorithms, such as the Randomized Generalized Hough Transform (RHT) [79]. It is also possible to reduce the computational load by 'divide and conquer' optimization, by dividing the parameterized space into overlapping 'tiles' that provides a multi-resolution Hough transform (MHT) [80], and this approach has been used here. In this method, the parameterized space is first divided into a coarse grid and the likelihood function is evaluated for this grid. The maximum for this coarse grid is then obtained and this is used to refine the search space to a finer resolution tile containing the maximum. For this new search space, the grid size is refined to provide a much higher resolution. Clearly, this method can be iterated several times, achieving progressively higher spatial resolution at each stage. For example, if the original parameterized space had an $n \times n$ grid, the computational complexity of calculating the likelihood is $O(n^2)$ for the standard Hough transform. However, for the multi-resolution Hough Transform, let the number of grid points for the first iteration be scaled down by a factor of p. In this case, the order of complexity for the first iteration is $O\left(\frac{n\times n}{p}\right)$, whilst the order of complexity for the second iteration $O\left(\frac{n\times n}{p}\right)$. Consequently, for just two iterations, the overall order of complexity is $O\left(\left(\frac{n\times n}{p}\right)+\left(\frac{n\times n}{p}\right)\right)$ for the same overall resolution. An example of the use of the multi-resolution Hough

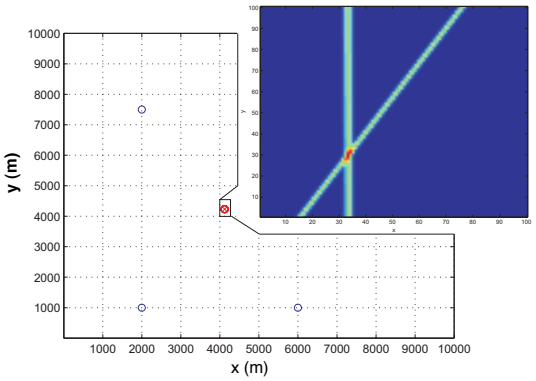

Figure 4.41: An example of the use of the Multi-resolution HT for emitter location using TDOA measurements

transform method is shown in figure 4.41. In this case, the source is located at (4.13km, 4.13km) (marked with a cross) within a search space of (10km, 10km) and the platforms are located at (1km, 2km), (1km, 6km) and (2km, 7.5km) (marked with circles). The number of grid points used for the first iteration was 100×100 (i.e 10,000 'tiles' with a separation between grid points of 0.1km). For the second iteration, an area equivalent to one tile centered on the grid with the maximum

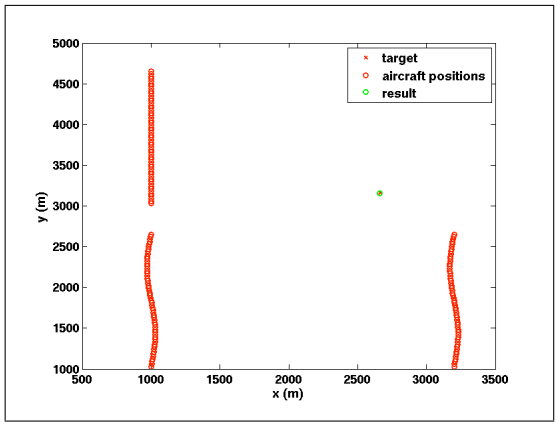

Figure 4.42: Scenario for geolocation using Multiresolution Hough Transform fusing TDOA measurements with COST 207 NLOS channel model

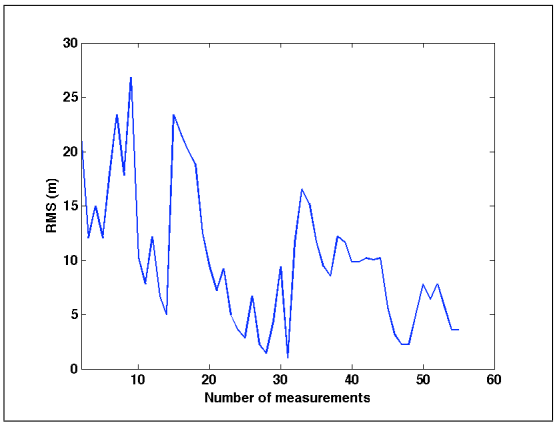

Figure 4.43: Average RMS error, for geolocation using multi-resolution Hough Transform for the scenario on figure 4.42 with COST 207 NLOS channel model

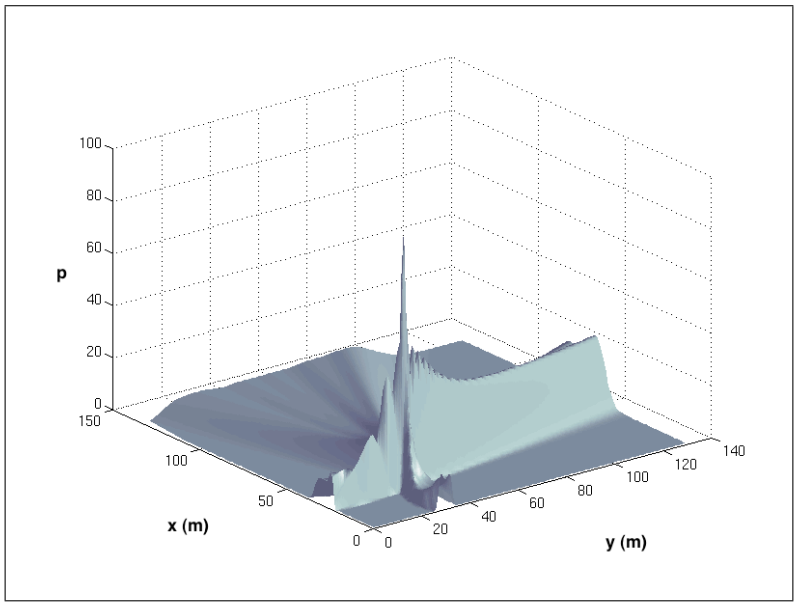

Figure 4.44: 3D parameterised space for MHT on second iteration in the vicinity of the emitter, illustrating one 'tile'

in the accumulator was used, and this tile was split into 100×100 grid points (corresponding to a separation between grid points of 1m).

Consider a scenario for geolocation pictured in figure 4.42. In this scenario three UAV are trying to geolocate an emitter in NLOS conditions described earlier in this chapter using TDOA measurements. Average RMS error, calculated over 50 simulations for this scenario, is shown in figure 4.43. The example of the parameterised space of MHT on a second step (fine resolution grid) is shown in figure 4.44. As in the previous examples of parameterised space for the HT, one can see the strong peak, indicating an estimated emitter position. It is clear that on a fine resolution grid size, the parameterised space for the MHT and HT indistinguishable

from one another. It can be concluded that the performance of the Multiresolution Hough Transform is quite close to the performance of the Hough Transform in COST 207 NLOS conditions, but this approach to optimization is known to have a specific problem, when the emitter of interest is located on the edge of the 'tiles'. In this case zooming doesn't improve the estimate and the obtained estimate will always have an error, proportional to the size of the tile. The target position on figure 4.42 and tile size are selected in a way, that it will always be inside a tile. It is possible to use other techniques, such as the Randomized Hough Transform, where the search space is not evaluated at a fixed point on the grid, but only at the points, selected randomly.The RHT approach to grid evaluation helps to overcome the problem of edges of the tiles, but at the expense of the accuracy of the estimation. For the shown scenario in the figure 4.42 an attempt was made to implement the Randomized Hough Transform by evaluating the likelihood of the emitter position only on the points of the grid, which are randomly generated from the uniform distribution. Figure 4.45 represents the accuracy of the RHT depending on the number of measurements for a RHT evaluated on a $350 \times 350 = 122500$ grid points, whereas figure 4.46 demonstrate results for RHT using twice as many grid points $700 \times 700 = 490000$. Exploring the figures 4.45 and 4.46 one can only conclude that the accuracy of the RHT is randomized, thus leading to unpredictable results.

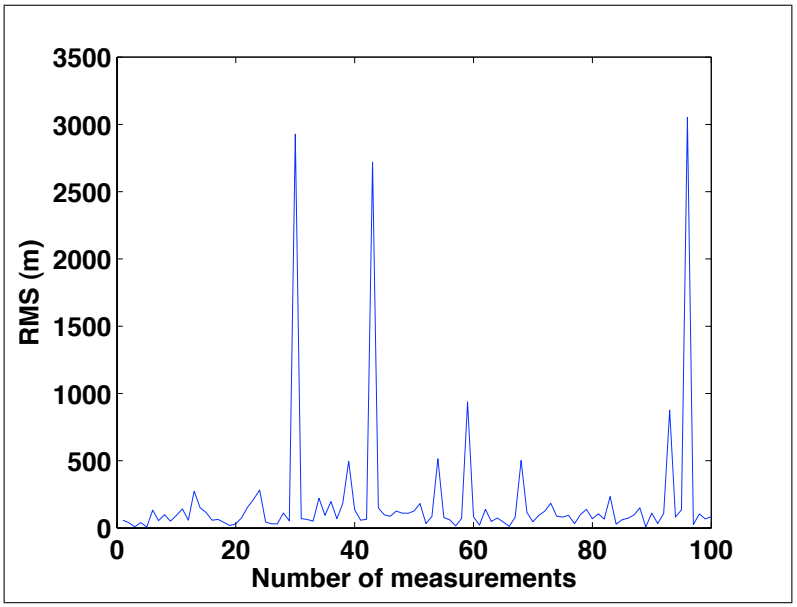

Figure 4.45: Randomized Hough Transform evaluated over 350×350 grid samples for the scenario shown in figure 4.42

The idea of using the random points on the grid as in Randomized Hough Transform is similar to the resampling method for the particle filter. In the next chapter the optimized versions of the Hough Transform and particle filter will be compared for a similarscenario and the differences and similarities between particle filter and RHT will be highlighted. Before comparing the performance of the optimized versions of the Hough Transform with the Particle Filter, it is in the interest of research to test the particle filter performance in NLOS conditions.

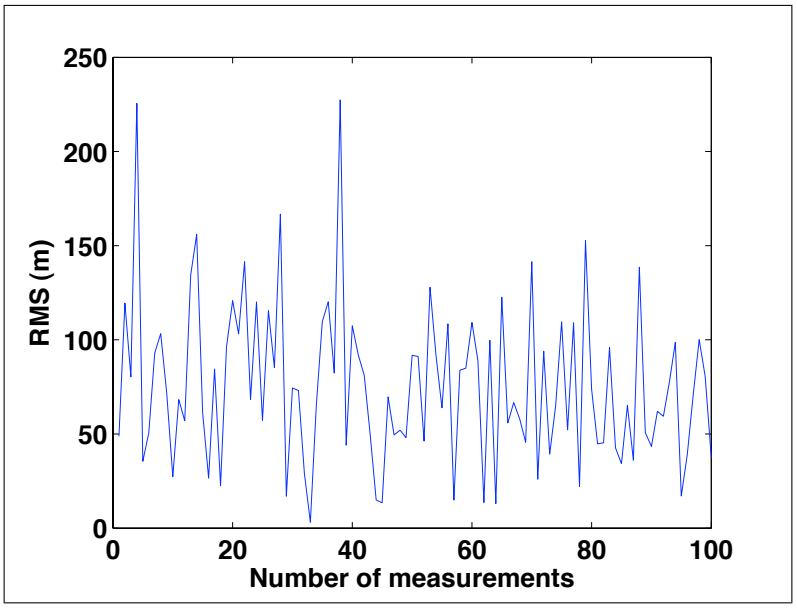

Figure 4.46: Randomized Hough Transform evaluated over 700 × 700 grid samples for the scenario shown in figure 4.42

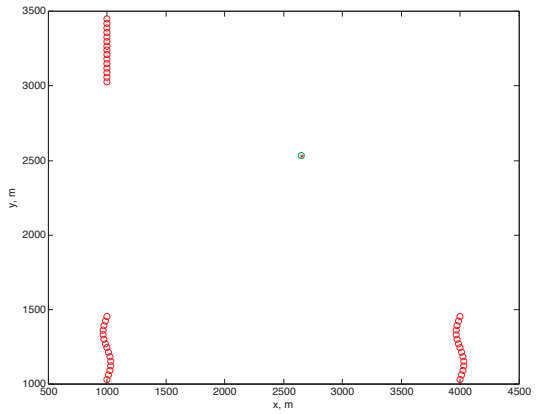

Figure 4.47: Scenario of multi-platform emitter geolocation showing the flight paths of 3 UAV platforms and the emitter of interest. The green circle shows the estimated emitter position

4.4 Geolocation in NLOS conditions using Particle filter

In this section, the particle filter described in chapter 3, was applied to the problem of emitter geolocation in an NLOS environment, using the channel and signal model described earlier in this chapter.

Figure 4.47 shows a typical scenario in which three UAVs are used to geolocate a single handset, denoted as a cross at (2664m, 3157m). The three UAVs, denoted as circles, can have arbitrary flight paths and are shown here with wavy paths for two platforms and a straight path for the other platform. The speed of the platforms is

40m/s.

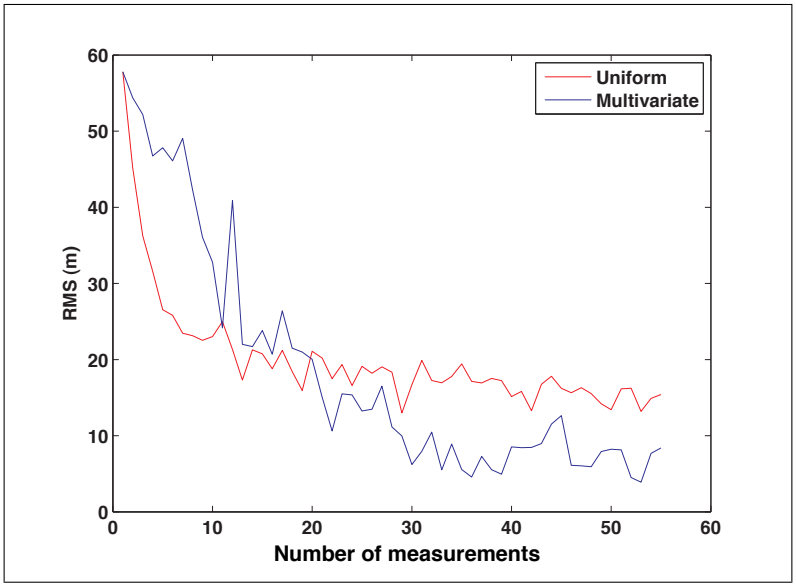

Figure 4.48: Average RMS positional error obtained over 50 simulations for different numbers of measurements with uniform and Gaussian resampling

Figure 4.48 shows the performance of the particle filter in the multipath conditions described earlier in section 4.3.1. The y-axis shows an average root mean square error calculated over 50 simulation, the x-axis represent the number of measurements taken. Figure 4.48 shows the effect on the RMS position error of increasing the number of TDOA measurements taken by the platforms along their respective flight paths. It is assumed that the position of the UAV is precisely known during the estimation of the TDOA between pairs of platforms and does not contribute to the RMS position error. From the results presented in figure 4.48 it is clear that the PF algorithm is capable of geolocating an emitter in the NLOS environment, described in section 4.3.1. Exploring figures 4.48 and 4.33 or 4.48 and 4.38 it is clear that in NLOS conditions the particle filter performed slightly worse than the Hough Transform, in terms of RMS error over the same number of measurements in NLOS conditions, especially, when uniform resampling is used. The accuracy of the estimation raised a question whether the particle filter performed worse than the HT due to the NLOS problem or due to some fundamental limit of the application of the particle filter to geolocation. Also, the initial accuracy of the PF algorithm with uniform resampling (when there were only a few measurements) raised a question about the best resampling distribution for emitter geolocation using a particle filter. This question remains unanswered, however in section 6.2 an attempt was made to bring some light into it.

4.5 Conclusion

In this chapter, a novel method of geolocation based on Hough Transform was presented. This method allows an easy fusion of the different type of the measurements and also fusion with terrain data. It also doesn't have a convergence problem and the emitter estimate can be obtained at any point in time – it doesn't require minimum number of measurements. HT method was applied to a problem of geolocation using a complex model of the signal and NLOS channel, and although computationally intensive, the algorithm was capable to geolocate the RF emitter in such difficult conditions. The particle filter, described earlier in section 3, has been applied to the problem of geolocation in NLOS conditions and also was capable to geolocate the emitter with reasonable accuracy - within 20 meters.

Several ways to optimize the performance of the Hough Transform were proposed: the Multiresolution Hough Transform and the Randomized Hough Transform. There is a similarity between the Randomized Hough Transform and the particle filter. In some senses the RHT can be viewed as one of the steps of the particle filter, with one *major* difference: that the HT variants use sum instead of the product of the probabilities. Comparison of the Generalised Hough transform and Particle Filter with Maximum Likelihood Estimator presented in Chapter 2 is impractical due to the problem with convergence of the MLE estimator: it would be possible to choose the scenario where MLE convergence, however changes in target position will render estimator unreliable as it was highlighted before in Section 2.1.6.

In the next chapter the particle filter, the Hough Transform and the RHT will be compared on a simpler geolocation scenario, and new variant of the Hough Transform, inspired by the particle filter, called the Hybrid Hough Transform will be introduced.

Chapter 5

Comparison of Hough Transform and Particle Filter

5.1 Introduction

In this chapter, in order to reduce the computational workload and retain the accuracy of the Generalized Hough Transform, two modifications of the Generalized Hough Transform were tested: the Randomized Hough Transform (RHT) and the Hybrid Hough Transform (HHT). And then the GHT variants were compared and tested with particle filter in section 5.2.

The essence of this chapter is to compare whether the non-Bayesian approach of the Generalized Hough Transform and its variants, can outperform the particle filter in terms of RMS positional error and computational efficiency.

5.1.1 Use of the Hough Transform and its Variants for Emitter Geolocation

Adaptation of the Generalized Hough Transform

The main description of the Hough Transform was done in section 4.1. From this chapter onwards, Hough Transform will be referenced as Generalized Hough Transform (GHT), in order to distinguish it from it's variants. A brief review of the Generalized Hough Transform for geolocation independent of the type of the measurements:

1. A fixed grid representing the parameters (x, y) that need to be estimated is created

2. At each point on the grid, the likelihood of the estimate being (x, y) given the measurement β, $p(x, y|\beta)$, is evaluated and accumulated in an array, A as in (4.5) where β_l is the lth measurement of a total L.

3. The estimate is taken as the grid position corresponding to the peak accumulated likelihood

Using the conditional pdf (4.8), the voting array (accumulator) for the Hough Transform can be built using (4.13).

The Randomized Hough Transform

Whereas the Generalized Hough Transform considers *every* point on the grid of possible emitter locations, the Randomized Hough Transform examines a smaller subset of these points chosen statisitically. Our implementation of the Randomized Hough Transform is as follows.

1. A number of samples representing points on the grid of the parameterized space are generated randomly with a uniform distribution
2. At each selected point on the grid, the likelihood corresponding to each TDOA measurement is evaluated and stored in an array as in (4.13)
3. The estimated emitter position is taken as the grid position corresponding to the peak accumulated likelihood.

Because the likelihoods are evaluated at fewer grid positions than for the Generalized Hough Transform the computational time and storage requirements are reduced. However, because the effective grid spacing is increased (albeit in a statistical way), the accuracy of the method can be compromised.

When viewed in this way, it will be immediately apparent that there are parallels between the Randomized Hough Transform and the particle filter. However, it is worthy of comment that whereas the particle filter uses a Bayesian approach, the Randomized Hough Transform is non-Bayesian, as indicated by (4.13).

The particle filter algorithm using Gaussian multivariate resampling as described in chapter 3 will be used for the comparison in this chapter.

The Hybrid Hough Transform

In this section, the use of a further variant of the Hough Transform is proposed, named the Hybrid Hough Transform. It is inspired by the particle filter algorithm and the multi-resolution Hough Transform [80]. The performance of this algorithm will be shown in Section 5.2 to be much better than either the particle filter or the Randomized Hough Transform, on which it is based. The Hybrid Hough Transform algorithm is as follows. The first three steps are identical to those of the Randomized Hough Transform.

1. A number of samples representing points on the grid of the parameterized space are generated randomly with a uniform distribution

2. At each selected point on the grid, the likelihood corresponding to each TDOA measurement is evaluated and stored in an array, as in (4.13)

3. The grid position (x, y) of the parameterized space corresponding to the peak accumulated likelihood is obtained

4. A fixed grid Generalized Hough Transform is performed around (x, y) using a fixed tile size (for example 10×10 points in our case)

5. The estimate corresponds to the maximum of the updated parameterized space, as shown in figure 5.1

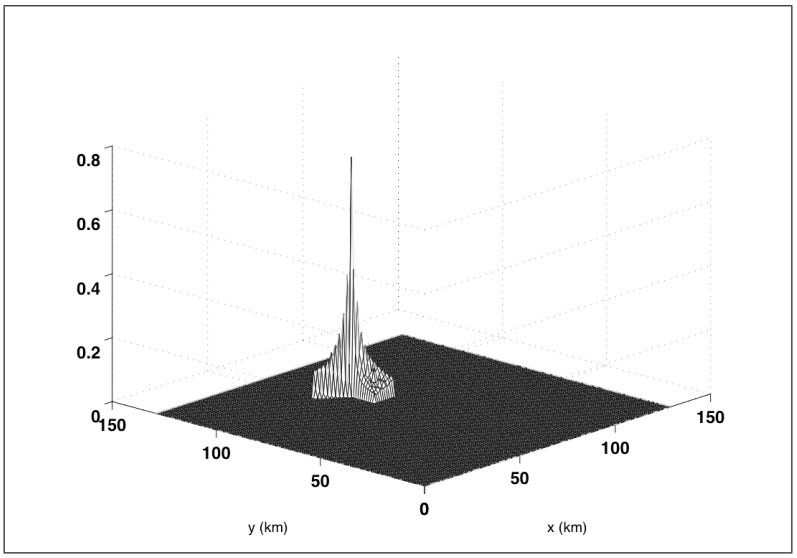

Figure 5.1: Parameterized space of the Hybrid Hough Transform

5.2 Simulation Scenario and Results

Figure 5.2 shows a simplified scenario in which two UAVs are used to geolocate a single transmitter, denoted as a circle at (93km, 40km). The two UAVs can have arbitrary flight paths, shown here with wavy paths. A new measurement is taken at each point on the path. The speed of the platforms is 40 m/s.

Figure 5.3 shows the RMS error performance of: (i) the Generalized Hough Transform, (ii) the Randomized Hough Transform and (iii) the particle filter from section 3 as a function of the number of measurements taken. In this figure, the x axis represents the number of measurements taken and the y axis is the average value of the RMS emitter position error over 500 simulation runs for a given number of measurements. For this particular set of simulations the number of particles for the Randomized Hough Transform and particle filter were the same, $N = 8450$. This corresponded to half the number of grid points used in the Generalized Hough Transform.

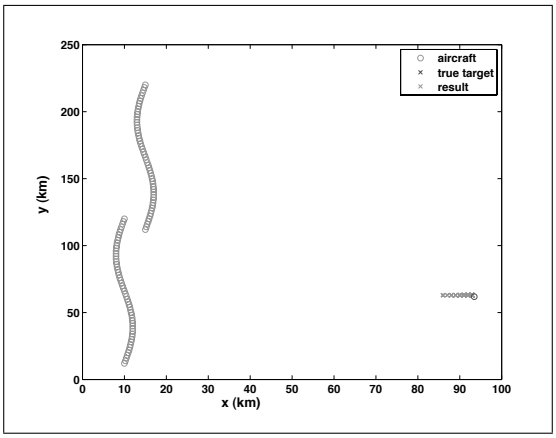

Figure 5.2: Scenario of multiplatform emitter geolocation showing the flight paths of 2 UAV platforms and the emitter of interest. The crosses show the estimated emitter position using PF algorithm

As expected, the RMS error tends to fall as the number of measurements taken increases. It should be noted that the RMS error for the Generalized Hough Transform and the particle filter are very close up to approximately 30 measurements, even though the particle filter evaluates the position likelihood at half the number of grid points than the Generalized Hough Transform. However, the average computational time for the three methods, as shown in figure 5.4, shows quite clearly that the Generalized Hough Transform has a much lower computational overhead than the particle filter. Although the error performance of the Randomized Hough Transform is worse than for the Generalized Hough Transform, it offers the lowest computational overhead. Note that above 30 measurements, the error performance of the particle filter starts to diverge slightly, which is not observed in the Hough Transform methods. In figure 5.5, the number of particles was adjusted so that the

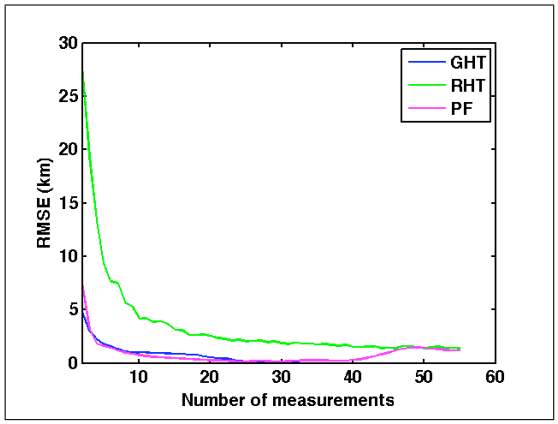

Figure 5.3: Average RMS positional error obtained over 500 simulations for different number of measurements. For the Randomized Hough Transform and the PF, the number of particles ($N = 8450$) was 50% of the total number of grid points

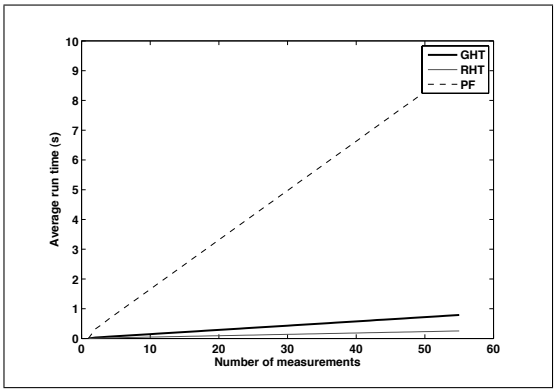

Figure 5.4: Average computation time over 500 simulations for different numbers of measurements for the different estimators

RMS error performance of the particle filter, the Generalized Hough Transform and the Randomized Hough Transform were approximately the same. In this case, the number of particles used for the particle filter was 20% of the number of grid points used for the Generalized Hough Transform and the Randomized Hough Transform used 75% of the grid points. Figure 5.6 shows that the computational overhead for the particle filter is still substantially more than for the Randomized Hough Transform. In considering these results, it should be noted that the magnitude of the

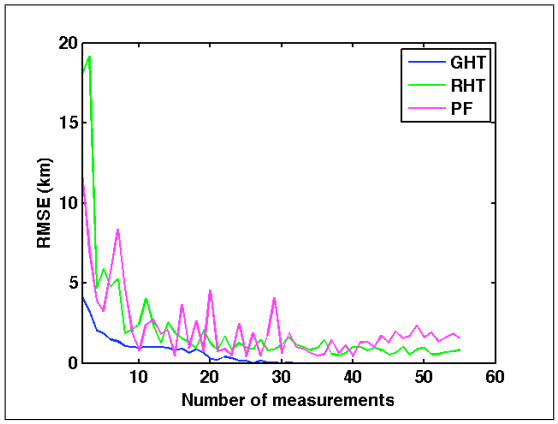

Figure 5.5: Average RMS positional error obtained over 20 simulations for different number of measurements. For the particle filter $N = 3380$ (corresponding to 20% of the grid) and for the Randomized Hough Transform $N = 12675$ (corresponding to 75% of the total number of grid points)

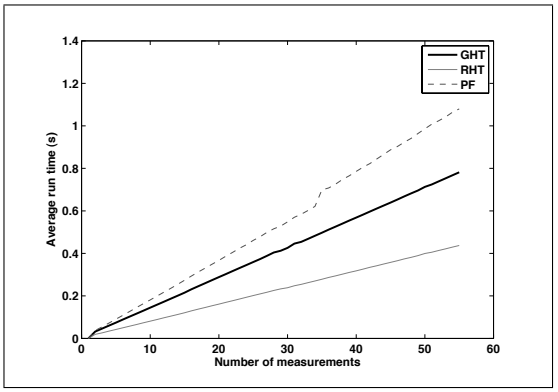

Figure 5.6: Average computation time over 20 simulations for different numbers of measurements for the different estimators

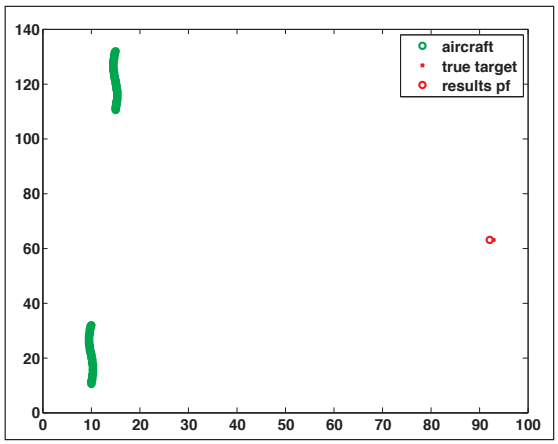

Figure 5.7: Scenario for comparison of GHT, RHT and PF algorithms using TDOA measurements only

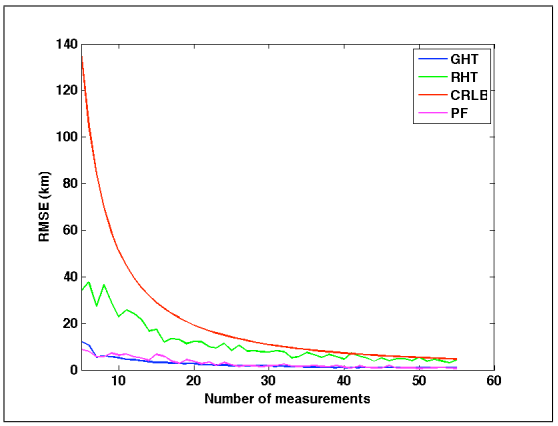

Figure 5.8: Average RMS error of the simulation scenario on figure 5.7

RMS position accuracy depends quite critically on the relative position of the emitter to the platforms because of the effect of GDOP and different platform/target

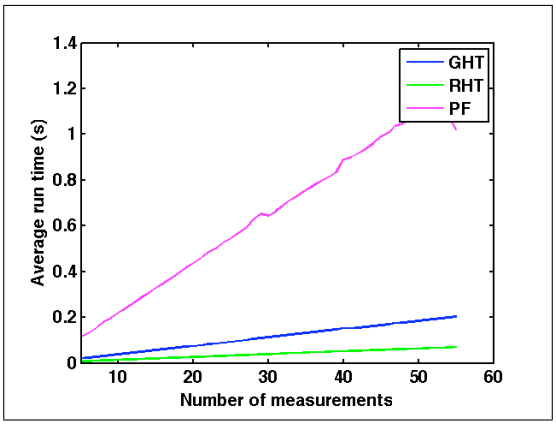

Figure 5.9: Average run time for each algorithm, for the scenario on figure 5.7

scenarios may produce better or worse RMS error, depending on the GDOP. This is demonstrated in figure 5.7 with corresponding average RMSE and average run time shown in figures 5.8 and 5.9 respectively, were target was moved to (92km,62km). On this particular scenario GDOP for estimation using TDOA measurements was perfect and thus all estimators performed within circle defined by CRLB, the behaviour always desired by rarely encounted in practice. Changing the scenario and moving target will provide a different results in terms of RMS accuracy of the estimators and CRLB. It should be noted that GHT is grided algorithm and although CRLB can decrease to the numbers smaller than 1 km over large number of measurements, GHT algorithm can't provide estimate with such precision if target happens to be off the grid. The comparison of the particle filter and GHT with target off the grid will be explored in details in the next section.

But the trends across the three types of estimator remain the same - particle filter has high computational overhead due to resampling on each step, whereas RHT can be considered as one step of the particle filter in terms of complexity. The foregoing has shown that the Randomized Hough Transform has a low computational overhead, but this is at the expense of accuracy. In contrast, the Generalized Hough Transform has a high accuracy, but with a corresponding high computational overhead. Repeating the simulation in figure 5.2 using Hybrid Hough transform for comparison, instead of the particle filter leads to the results plotted in figures 5.10 and 5.11. The Hybrid Hough Transform provides the reduced computational overhead of the Randomized Hough Transform with the accuracy of the Generalized Hough Transform and this is clearly shown in figure 5.10, which compares the average RMS positional accuracy of the three Hough Transform methods and figure 5.11, which shows the average computation time for the three Hough Transform variants.

The results show that the computational overhead of the Hybrid Hough Transform is slightly higher then Randomized Hough Transform but accuracy of the algorithm is almost indistinguishable from the Generalized Hough Transform.

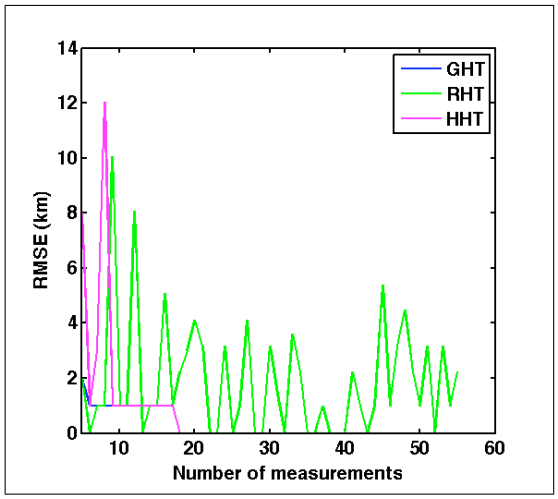

Figure 5.10: Average RMS error over 500 simulations, Hybrid Hough transform using fixed grid 10×10 sizes

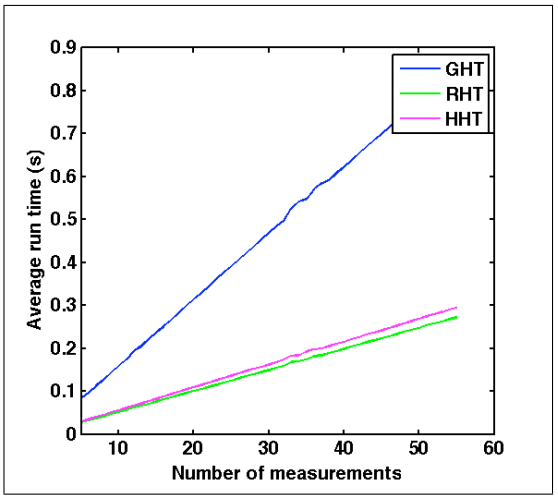

Figure 5.11: Average time obtained over 500 simulations for different numbers of measurements for the same scenario. Hybrid Hough transform using 10×10 fixed grid

5.2.1 Bayesian Randomized Estimator

It is possible to construct a Bayesian estimator using a similar approach to the Randomized Hough Transform in which the accumulation of likelihoods by arithmetic addition is replaced by taking the product. Such an estimator has been implemented here for comparison with the Hough transform estimators. In this implementation of the Bayesian Randomized estimator, no resampling is carried out on each measurement update cycle. This must be contrasted with the particle filter, where resampling is an important part of the algorithm to prevent degeneracy. The consequence of this on the performance of the Bayesian Randomized estimator will be examined in this section. An example of degeneracy is shown in figure 5.12, which shows the parameterized space after 55 measurements have been used. The comparison of

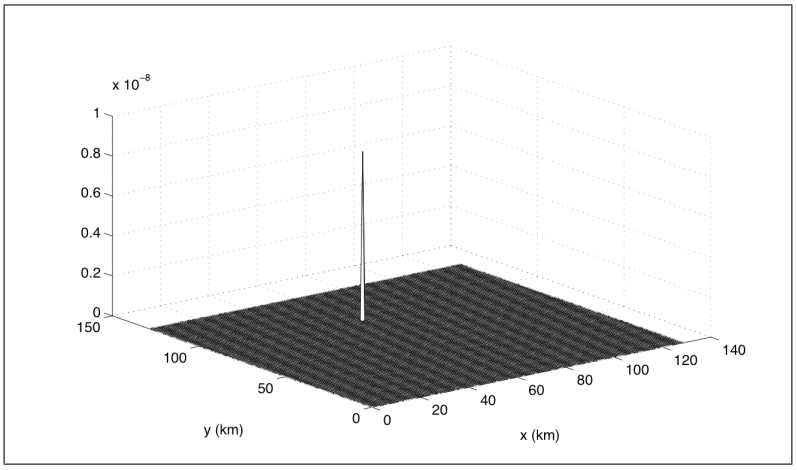

Figure 5.12: Parameterized space of the Bayesian Randomized estimator after 55 measurements, showing degeneracy

results are presented in figure 5.13. As can be seen, the average RMS positional error performance of the Randomized Hough Transform and the Bayesian estimator are identical to about 20 measurements. The performance of the two algorithms in terms of computation time are shown in figure 5.14 and again, the computational overhead is identical. However, it is clear from figure 5.13 that the average RMS positional error of the Bayesian Randomized estimator starts to diverge with an increasing number of measurements, whereas the Randomized Hough Transform and the Generalized Hough Transform continue to converge. Although not shown here, other results for larger numbers of measurements confirm that the RMS error performance of the Bayesian Randomized estimator diverges for this emitter location scenario.

One of the advantages of the Hough Transform approach to dealing with the accumulation of the likelihoods is that it does not require reinitialization of the parameterized space on each measurement update cycle. Hence it can be used as both a sequential and a batch estimator at the same time.

In the same way that the Randomized Hough Transform was modified to form the Hybrid Hough Transform, an attempt was made to improve the accuracy of the

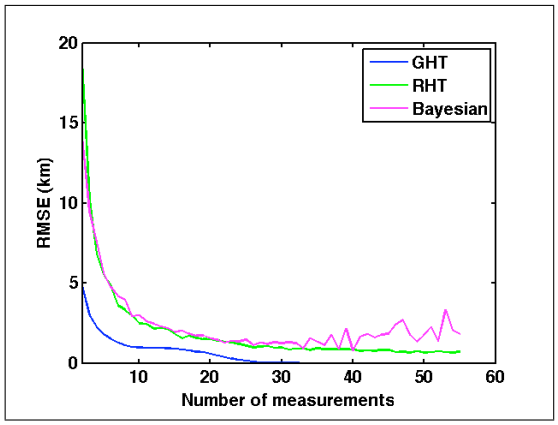

Figure 5.13: Average RMS positional error over 500 simulations for the Randomized Hough Transform and the Bayesian estimator using the same number of particles (75% of the grid size used for the GHT)

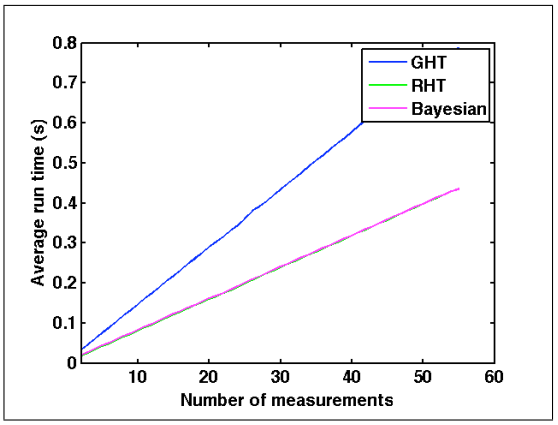

Figure 5.14: Average computational time over 500 simulation runs run for the Generalized Hough Transform, Randomized Hough Transform and the Bayesian Randomized estimator

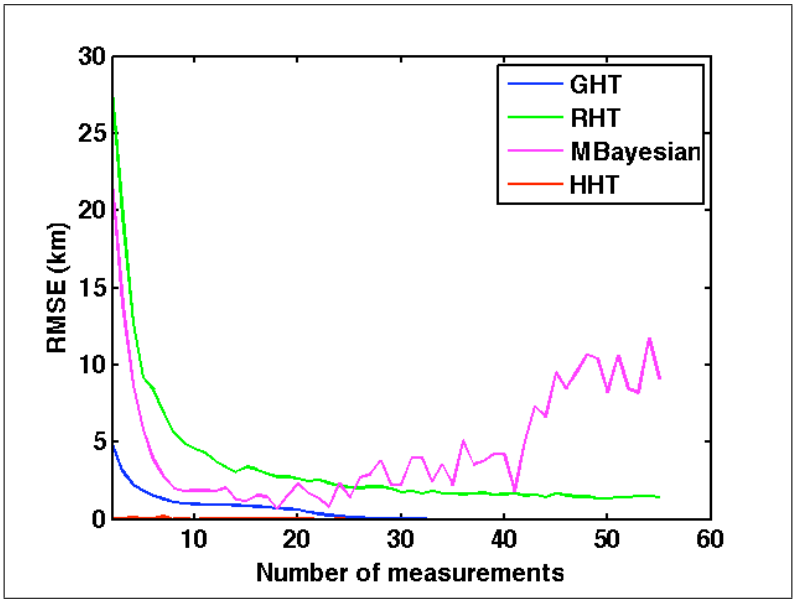

Figure 5.15: Average RMS positional error obtained over 500 simulations for a different number of measurements for the Generalized Hough Transform, Randomized Hough Transform, modified Bayesian Randomized estimator and the Hybrid Hough Transform

Bayesian Randomized estimator using a similar hybrid approach whereby a fixed grid search was incorporated with the Bayesian Randomized estimator. Figure 5.15 compares the performance of this modified Bayesian estimator with the three Hough Transform variants. It is clear from this result that this approach does not lead to improved results.

It is also possible to implement uniform resampling and reinitialization of the

parameterized space before updating it with each measurement. However it will lead to an algorithm that is very close to a particle filter, the performance of which has already been presented earlier. In the next section the comparison of the particle filter and Hough Transform variants will be presented on one common, but difficult for geolocation scenario, and then methods for improving algorithms performance will be discussed.

5.3 Comparison of the particle filter and Hough transform variants on common scenario

It is important to compare previously presented algorithms in this thesis algorithms on one scenario. For this purpose the following simulation has been generated: figure 5.16 pictures the flight path and target location for all algorithms. Number of measurements from 2 till 110, each measurement obtained once aircraft passes 0.4 km. Target located on $(70.5, 60.5)$km. Flight paths for the UAV were generated according to:

$$x(t) = x_0 + v \sin\theta(\Delta t) \tag{5.1}$$

$$y(t) = y_0 + v\Delta t \tag{5.2}$$

where (x_0, y_0) is $(10, 10)$km the initial position of the first aircraft and $(10, 40)$km for the second aircraft. $\theta(\Delta t) \in (0, 2\pi)$ is the angle changing on each time step up with step $\Delta\theta = 2\pi/N_m$. Where N_m - duration in simulation, which is equivalent to number of measurements taken during the simulation. $v = 0.4$ km is progression of the UAV in space during Δt.

Measurement noise assumed to be zero mean Gaussian noise with standard deviation $\sigma_{AOA} = 0.02$ radians for Angle of Arrival measurements and $\sigma_{time} = 7.4 \times 10^{-7}$ seconds for

This simulation presents challenge for TDOA-only based estimation as in this particular case GDOP of TDOA doesn't improve with the time because the aircraft manoeuvre synchronously and TDOA baseline - distance between aircrafts remains constant during simulation. This scenario is nearly worst case for the geolocation of the emitter due to the poor GDOP, but the one which can be en-counted in practice. In this chapter we will start from exploring different algorithm performances on a fixed scenario generated once with fixed number of measurements and those measurement's error assumed to be Gaussian and measurements, corrupted by measurement's noise were generated only once; then the comparison of the performance of the algorithms has been performed on this one set of measurements and one type of noise (Gaussian). Algorithms are programmed in such a way that number of points of Particle filter $N = 16900$ is equal to number of grid points for Generalised Hough Transform and also Randomized and Hybrid Hough Transform.

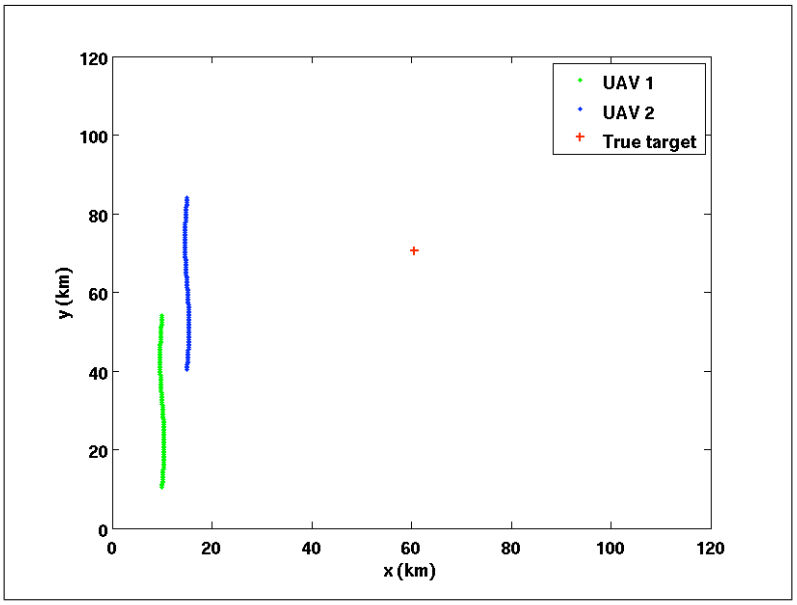

Figure 5.16: Comparison scenario

Particle filter algorithm

Quick overview of the particle filter algorithm from chapter 3 which is later going to be modified to increase accuracy:

1. *Initialization, t=0*:
   - For $i = 1, ...N$, sample $x_0^{(t)} \backsim p(x_0)$ and set t=1.
2. *Importance sampling step*:
   - For $i = 1, ...N$, sample $\tilde{x}_t^{(i)} \backsim p(x_t|x_{t-1}^{(i)})$
   - Set $\tilde{x}_{0:t}^{(i)} = \left(x_{0:t-1}^{(i)}, \tilde{x}(i)_t\right)$
   - For $i = 1, \ldots N$, evaluate the importance weights
   $$\tilde{w}_t^{(i)} = p(y_t|\tilde{x}_t^{(i)}). \tag{5.3}$$
   - Normalise the importance weights.
3. *Selection step*
   - Resample with replacement N particles $\left(x_{0:t}^{(i)}; i = 1, \ldots, N\right)$ from the set $\left(\tilde{x}_{0:t}^{(i)}; i = 1, \ldots, N\right)$ according to importance weights using multinomial resampling, described below
   - Set $t \leftarrow t + 1$ and go to step 2

The sampling of the particles $\tilde{x}_t^{(i)} \backsim p(x_t|x_{t-1}^{(i)})$ performed as a sampling from a multivariate Gaussian distribution with a mean centered on the position, (x_p, y_p), of the survivor particle from the previous step of after initialisation. The resampled particles are generated using:

$$\mathbf{x} = \mathbf{x}_p + N; \tag{5.4}$$

where $\mathbf{x}$ is the array of the particle position vectors, $\mathbf{N}$ is the array of zero-mean normally distributed random values with standard deviation $\sigma_{jitter} = 0.1569$ km (also known as *jitter* or *system noise*).

Multinomial Resampling

This is the simplest idea and widely used in bootstrap particle filter [49] that consist of drawing, conditionally upon σ-field generated by the generations of particles and weights up to time t, the new particles $\{\hat{\xi}^i\}_{1\leq i\leq n}$ independently from the point mass distribution $\sum_{j=1}^{m} \omega_j \delta_{\xi_j}$. In practice, this is achieved by repeated uses of the inversion method:

1. Draw n independent uniforms $U_{1\leq i\leq n}^i$ on the interval $(0, 1]$;
2. Set $I_i = D_\omega^{inv}(U^i)$ and $\hat{\xi}^i = \xi^{I^i}$, for $i = 1, \ldots n$, where D_ω^{inv} is the inverse of the cumulative distribution function associated with the normalised weights $\{\omega^i\}_{1\leq i\leq m}$, that is, $D_\omega^{inv}(u) = i$ for $u \in \left(\sum_{j=1}^{i-1} \omega^j, \sum_{j=1}^{i} \omega^j\right]$.

This form of resampling is generally known as multinomial resampling since the duplication counts $N^1, \ldots, N^m$ are by definition distributed according to the multinomial distribution $Mult(n; \omega^1, \ldots, \omega^m)$.

5.3.1 Ungrided Randomized and Hybrid Hough Transform

In order to make Randomised Hough Transform practically comparable with PF, generation of the initial distribution for Randomized Hough Transform was changes to ungrid-based float type values, generated uniformly within search space, which is similar to initialisation step for the particle filter. Number of particles for RHT $N = 16900$. Other steps of the Randomized Hough Transform remained unchanged and as presented in previous chapter.

The following changes were made for Hybrid Hough Transform:

- Number of particles $N = 16800$ generated from uniform distribution as in RHT and PF.
- Evaluation of the likelihood performed as in RHT
- Smaller grid with center on particle with maximum likelihood formed such as:

- Lower left corner of the "small" grid calculated as $x_{min} = \hat{x}_{rnd} - (4.5\sigma_r)$ $y_{min} = \hat{y}_{rnd} - (4.5\sigma_r)$ where $\hat{x}_{rnd}$ and $\hat{y}_{rnd}$ are (x, y) estimates of the target obtained on the previous step and $\sigma_r = \frac{\sigma_{timeC}}{\sqrt{(2)}}$
- Upper right corner of the grid calculated as $x_{max} = \hat{x}_{rnd} + (4.5\sigma_r)$ $y_{max} = \hat{y}_{rnd} + (4.5\sigma_r)$ respectively
- Likelihood evaluated over each point of the minor grid with step size equal σ_r

Such changes allowed HHT to become ungrided and have exactly the same total number of particles (on both steps) as PF $N = 16900$. Generalized Hough Transform remains unchanged as presented in previous chapters with size of the grid $(130, 130)$, which is equivalent resolution down to 1 km.

5.3.2 Geolocation using TDOA only measurements

This section presents simulation results for TDOA measurements with corresponding CRLB. It can be clearly seen on figure 5.17 that CRLB for this particular scenario and TDOA only measurements present flat line, which doesn't change with number of measurements. It also can be seen that most algorithms presented in previous chapters are able to perform close to CRLB bound after 60 measurements, with the exception of the PF filter, which on the present scenario and type of measurements demonstrated rather poor performance. It should be noted that target location is $(60.5, 70.5)$ km, thus traditional Generalized Hough Transform is unable to located target precisely, due to the grid resolution up to 1 km.

Figure 5.18 depicts same information as 5.17, but in terms of logarithmic RMS error against number of measurements. As it was said earlier, geolocation using TDOA-only measurements is the most challenging in this scenario as estimate doesn't improve with time, as demonstrated by CRLB distance. It can be seen that all algorithms performed equally in terms of accuracy, achieving level of available information. Figure 5.18 allow to see zoomed changes in estimates, which may not be visible on figure 5.17. Figure 5.19 clearly shows the difference in algorithms running time, where particle filter with same number of particles as number of points in GHT grid estimates much slower than any of Hough Transform variants.

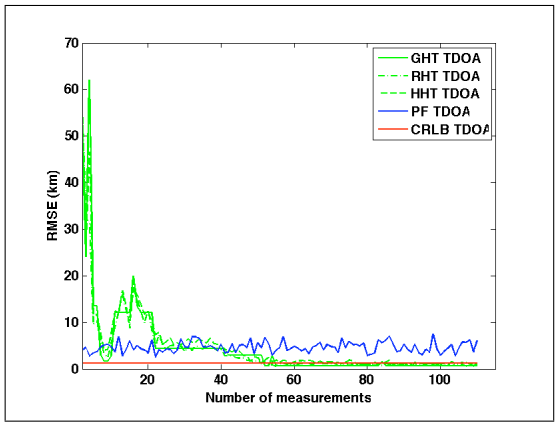

Figure 5.17: RMS error over number of measurements using TDOA only

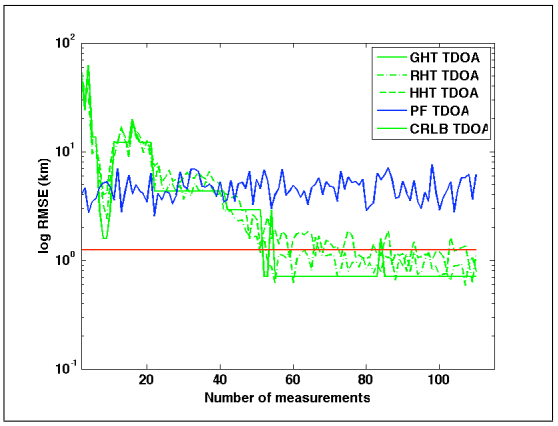

Figure 5.18: Logarithmic plot of the RMS error over number of measurements using TDOA only

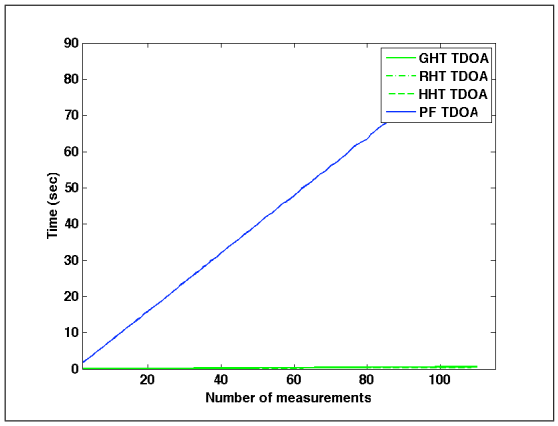

Figure 5.19: Runing time of the each algorithm for TDOA only measurements

5.3.3 Geolocation using AOA only measurements

This section presents the results of using same algorithms for geolocation using AOA-only measurements from first platform, which flight path marked as green circles on 5.16. As before 5.20 and 5.21 depict RMS error against number of measurements and 5.22 shows time. GDOP for this type of estimation is slightly better in the terms that it is improving over time, however as it was demonstrated before, single AOA estimation produces very long ellipse, hence the accuracy of the single AOA estimation is fairly poor. In order to compare the performance of the algorithms, it is nessesary to test their performance using the fusion of the 2 AOA measurements with TDOA measurement.

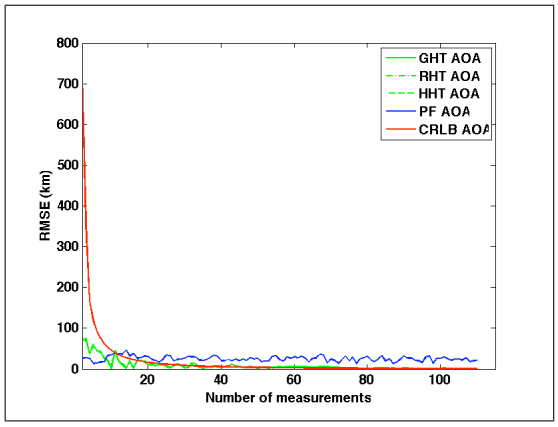

Figure 5.20: RMS error over number of measurements for one AOA only

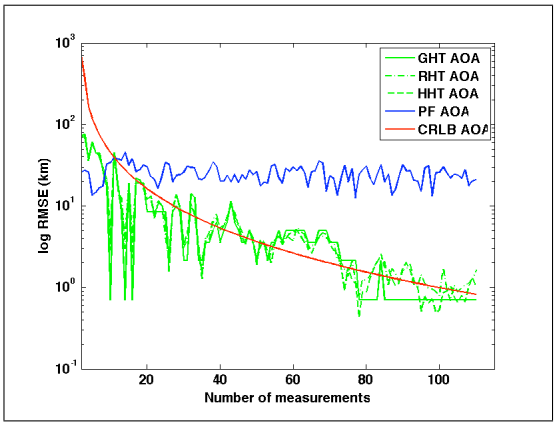

Figure 5.21: Logarithmic plot of the RMS error over number of measurements for one AOA only measurement

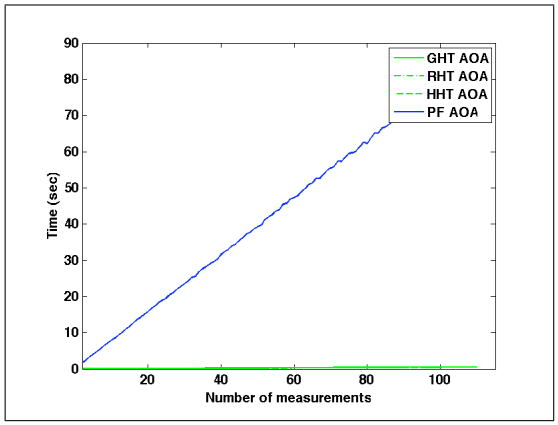

Figure 5.22: Comparison of the calculation time for AOA only

5.3.4 Geolocation using combined two AOA and TDOA measurements

This section presents the results of the geolocation using combined AOA and TDOA measurements from both aircrafts. Figures 5.23 and 5.24 shows the performance of the algorithms in terms of RMS against number of measurements. It should be noted again that all participating algorithms using same set of data. In figure 5.23 CRLB gradually became smaller, despite of the fact that TDOA-only measurements doesn't improve geolocation with number of measurements, combination of both 2AOA and TDOA improves with increasing number of measurements.

The performance of all presented algorithms comparable, with Hough Transform variants estimating with precision down to one km, while particle filter, geolocating target within 1.4 km, demonstrate unstable behaviour. Note that GHT can't locate target close than nearest grid point, thus 0.7 km is the best possible estimate for GHT. Figures 5.26 and 5.27 are zoomed versions of the figures 5.23 and 5.24 respectively. On figure 5.28 presented the comparison of the calculation time for Hough Transform variants, which is indistinguishable line on figure 5.25.

It should be noted that all algorithms use exactly same number of particles and equivalent number of grid points. Observing the results on figures 5.23 and 5.26 it is possible to conclude that for this particular scenario, particle filter performed reasonably accurately in terms of RMS error, but slower than Hough Transform variants. Obviously, GHT precision limited to grid, however Hybrid Hough Transform in it's ungrided form performed best in terms of accuracy and calculation time. It should be noted that performance of the particle filter in this conditions doesn't improve with number of measurements and this behaviour is consistent, even in case of another set of measurements for the same scenario.

It is usually assumed that performance of the particle filter can be improved by altering values of system noise (jitter). However, results of the simulation presented in figure 5.29, where RMS error of the particle filter calculated as average of 12 simulations for each number of measurements for different values of system noise. It is clear that choosing right value of σ_r is challenging (also demonstrated in chapter 3) and additional means of improving particle filter shall be considered. Next step is to improve particle filter algorithm with known technique called Metropolis-Hastings step.

5.4 Improving particle filter

5.4.1 Modified Particle Filter with Metropolis-Hastings step

Metropolis-Hastings step

As stated in [6] chapter 7, there can be a problem of degeneracy in particle filter when the target distribution $p(x_{1:t}|y_{(1:t)})$ in the particle filter does not overlap significantly

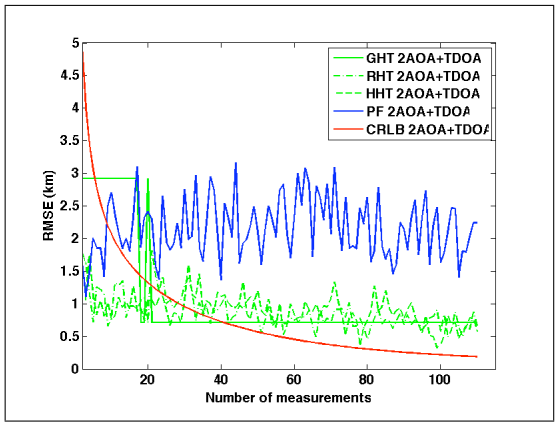

Figure 5.23: RMS error against number of measurements for 2AOA and TDOA

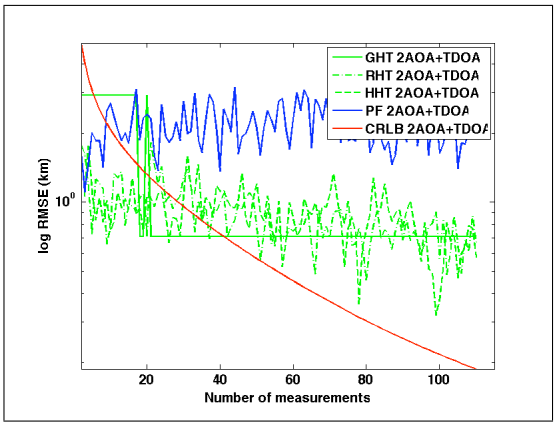

Figure 5.24: Logarithmic plot of the RMS error over number of measurements for 2 AOA and TDOA measurements

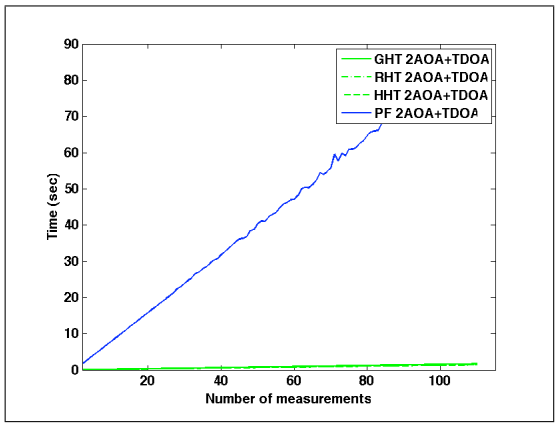

Figure 5.25: Calculation comparison time for 2 AOA and TDOA measurements

with the prediction distribution $p(x_{1:t}, y_{1:t-1})$. One way to overcome the deficiency is to incorporate Markov chain moves into the scheme. Since we wish particles to be drawn from $p(x_{1:t}|y_{1:t})$ it seems reasonable to design Markov chain transition kernel $T(x_{1:t}, \partial x'_{1:t})$ having $p(x_{1:t}|y_{1:t})$. In practice Metropolis-Hastings step can be described as:

- Sample the proposal candidate $\theta_t^{*(i)} \backsim p(\theta_t|\theta_{t-1}^{(i)})$
- If $v \backsim U_{[0,1]} \leq \min\left\{1, \frac{p(\mathbf{y}_t|\mathbf{x}_t, \theta_t^{*(i)})}{p(\mathbf{y}_t|\mathbf{x}_t, \tilde{\theta}_t^{*(i)})}\right\}$
  - then accept move: $\theta_{0:t}^{(i)} = \left(\tilde{\theta}_{(0:t-1)}^{(i)}, \theta_t^{*(i)}\right)$
  - else reject move: $\theta_{0:t}^{(i)} = \tilde{\theta}_{0:t}^{(i)}$

Particle filter algorithm modified to include additional Metropolis-Hastings step implemented as follows:

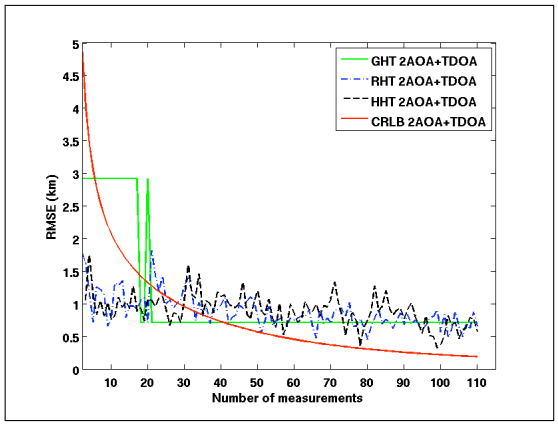

Figure 5.26: RMS error over number of measurements for 2AOA and TDOA. Hough Transform variants only

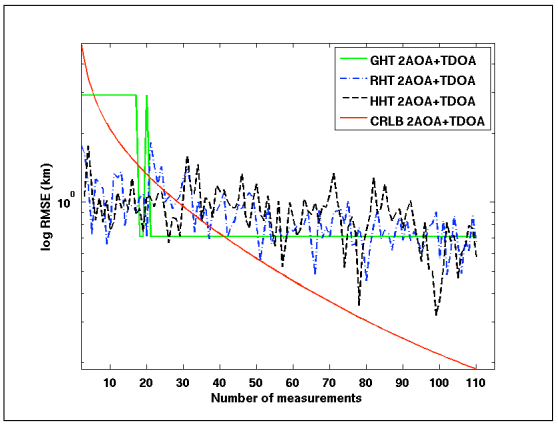

Figure 5.27: Logarithmic plot of the RMS error over number of measurements for 2AOA and TDOA measurements. Hough Transform variants only

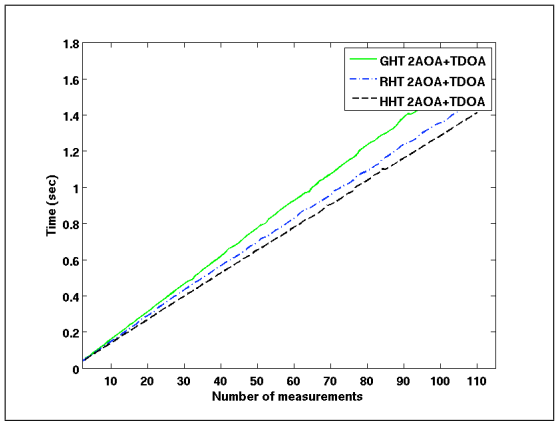

Figure 5.28: Comparison time of the calculation for 2 AOA and TDOA measurements, Hough Transform variants only

1. *Initialization, t=0*:
   - For $i = 1, ...N$, sample $x_0^{(t)} \backsim p(x_0)$ and set t=1.
2. *Importance sampling step*:
   - For $i = 1, ...N$, sample $\tilde{x}_t^{(i)} \backsim p(x_t|x_{t-1}^{(i)})$
   - Set $\tilde{x}_{0:t}^{(i)} = \left(x_{0:t-1}^{(i)}, \tilde{x}(i)_t\right)$
   - For $i = 1, \ldots N$, evaluate the importance weights

$$\tilde{w}_t^{(i)} = p(y_t|\tilde{x}_t^{(i)}). \tag{5.5}$$

   - Normalise the importance weights.
3. *Selection step*

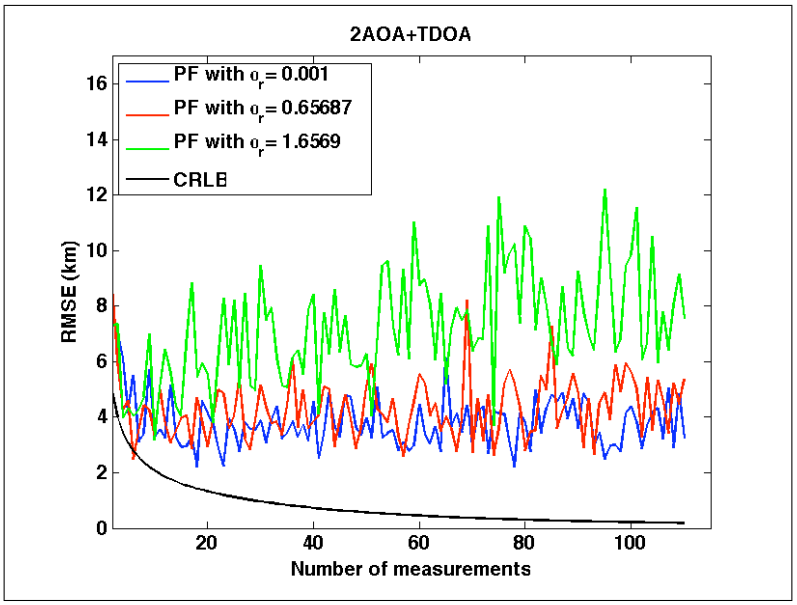

Figure 5.29: RMS error for particle filter using 2AOA and TDOA measurement with changing values of σ_r (system noise or jitter). Number of particles $N = 16900$.

- Resample with replacement N particles $\left(x_{0:t}^{(i)}; i = 1, \ldots, N\right)$ from the set $\left(\tilde{x}_{0:t}^{(i)}; i = 1, \ldots, N\right)$ according to importance weights using multinomial resampling, described above

4. *Metropolis Hastings step*

5. Set $t \leftarrow t + 1$ and go to step 2

5.4.2 Particle filter with Metropolis-Hastings step

Using particle filter with Metropolis-Hastings step it was possible greatly improve accuracy of the particle filter as can be noted on 5.30 and 5.31. Particle filter with Metropolis-Hastings step, marked as PF with MH on a figure, quickly converges to the value below CRLB, but as CRLB became smaller with each number of measurements it became close to the Cramer-Rao lower bound. Figure 5.32 demonstrates that such accuracy improvement came at expense of the calculation time.

5.4.3 PF with Metropolis-Hastings step and different values for standard deviation

It has been suggested that standard deviations for "jitter"(system noise on step 2) and for proposal distribution in Metropolis-Hastings step should be different. Simulation was performed with changed values for these distribution σ:$\sigma_{jitter} = 1 \times 10^{-4}$km and $\sigma_{MH} = 2.2185$km. However results, presented in figures 5.33 and 5.34 didn't indicate any improvement in performance.

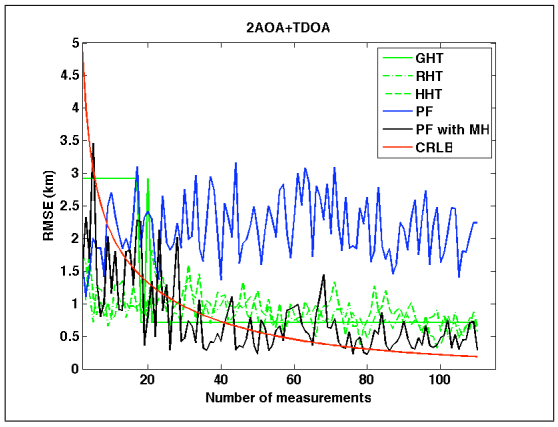

Figure 5.30: RMS error for PF with MH step

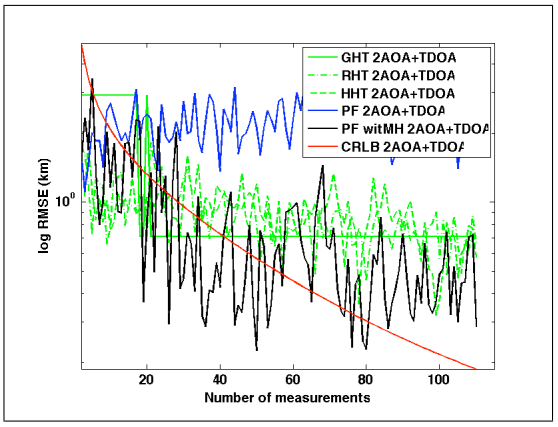

Figure 5.31: Log RMS error for 2 AOA+ TDOA measurements for PF with MH step

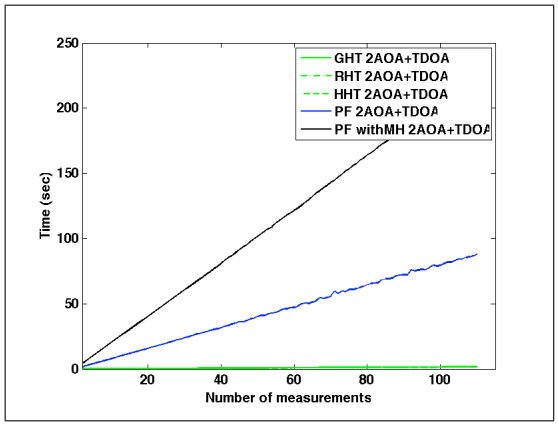

Figure 5.32: Calculation time for 2 AOA and TDOA measurements for PF with MH

5.4.4 Discussion

The addition of the Metropolis-Hastings step significantly improve the performance of the particle filter in terms of RMS error: after just few measurements particle filter converges to the fairly small value, outperforming CRLB on initial state, however later converges to a floor, the limit of precision with available information. However such precision resulted in slowing down particle filter. Changing different values for "jitter" of the particles, choosing different measurement noise and system noise didn't improve the performance of the particle filter in this particular scenario. Thus far particle filter algorithm has been compared with Hough Transform variants on one scenario and same number of particles and grid points. Then particle filter was modified to include Metropolis-Hastings step, which resulted in improved accuracy of the particle filter estimates, but slow down the calculation time. In the next section we will change number of particle for particle filter and particle filter with Metropolis-Hastings step so their calculation time will be comparable with HT

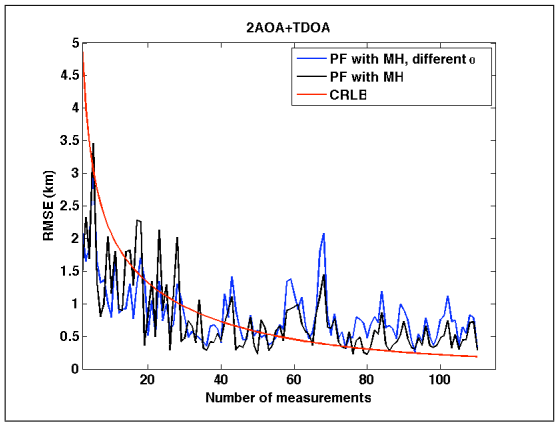

Figure 5.33: RMS error for PF with MH step and same PF with MH with different σ:σ_{jitter} = 1×10^{-4}km and σ_{MH} = 2.2185km

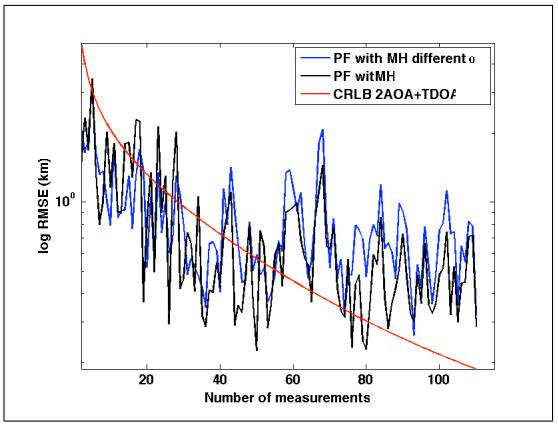

Figure 5.34: Log RMS error for 2 AOA+ TDOA measurements for PF with MH step and same PF with MH with different σ:σ_{jitter} = 1×10^{-4}km and σ_{MH} = 2.2185km

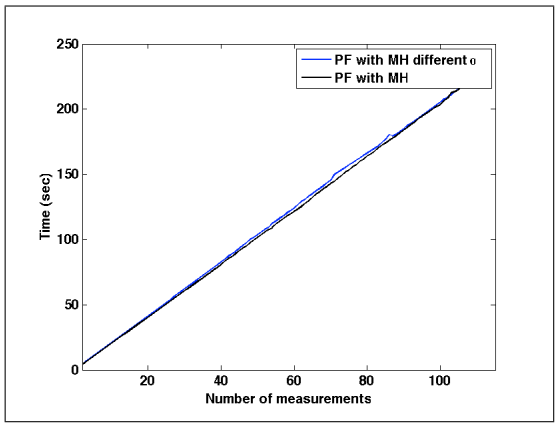

Figure 5.35: Calculation time for 2 AOA and TDOA measurements for PF with MH step and same PF with MH with different σ:σ_{jitter} = 1×10^{-4}km and σ_{MH} = 2.2185km

variants.

5.5 Particle filters with calculation time comparable with HT variants

The aim of this section is to change number of particles in particle filter and particle filter with Metropolis-Hastings step in a way that their computation time will be matching or close to the computation time of the Generalized Hough Transform - to make all performing algorithms comparable in time. Although by changing number

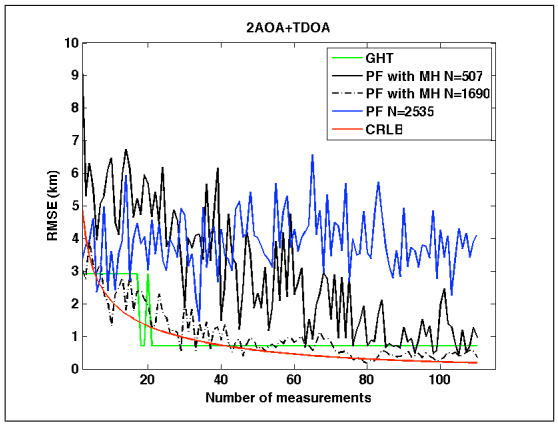

Figure 5.36: RMS error for PF with MH step, PF with different N and GHT

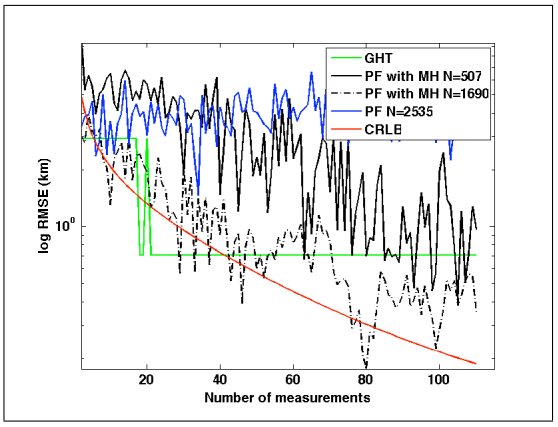

Figure 5.37: Log RMS error for 2 AOA+ TDOA measurements for PF with MH step and PF with different number of particles N

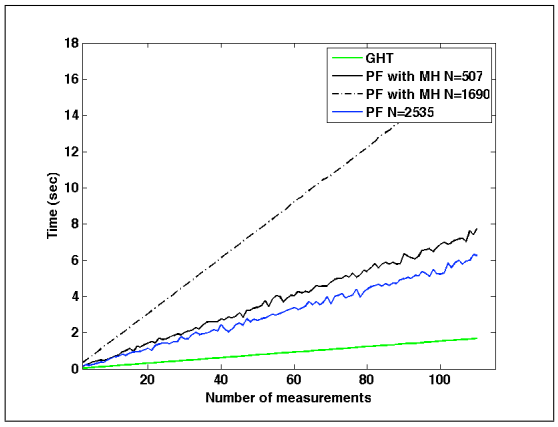

Figure 5.38: Calculation time for 2 AOA and TDOA measurements for PF with MH step and PF with different number of particles

of particles $N = 169$ (1/100 of the GHT grid) for particle filter with MH step produce comparable performance time with GHT (slowest out of Hough Transform variants), it resulted in unreliable estimates. Increasing N to 250 didn't improve estimate, hence it was necessary to increase $N = 507$. Traditional particle filter (bootstrap) where allowed to use $N = 2535$ particles, as it correspond to comparable computation time of the particle filter with Metropolis-Hastings step $N = 507$. The results of the evaluation of these algorithms presented in figure 5.36 and 5.37, while their calculation time in 5.38. Particle filter with Metropolis-Hastings step and $N = 1690$ (1/10 of GHT grid) is pictured as example of the particle filter with good accuracy. There are a number of publications on particle filter and sequential importance resampling estimation [81] and [82] and book [83] which specifically insist on resetting weights after importance resampling. The Selection step in this case implemented:

- *Selection step*
  - Resample with replacement N particles $\left(x_{0:t}^{(i)}; i = 1, \ldots, N\right)$ from the set $\left(\tilde{x}_{0:t}^{(i)}; i = 1, \ldots, N\right)$ according to importance weights using multinomial resampling, described above
  - Reset particle weight $w_t^{(i)} = 1/N$
  - Set $t \leftarrow t + 1$ and go to step 2

As re-sampling converts the weight values into spatial density, all the weights must now have a uniform distribution. Such step greatly improves particle filter performance as can be seen on figure 5.39 for the same scenario 5.16 and type of measurements. Figure 5.39 shows that particle filter marked as "PF(w)" performs reaching CRLB and tracking it very closely.

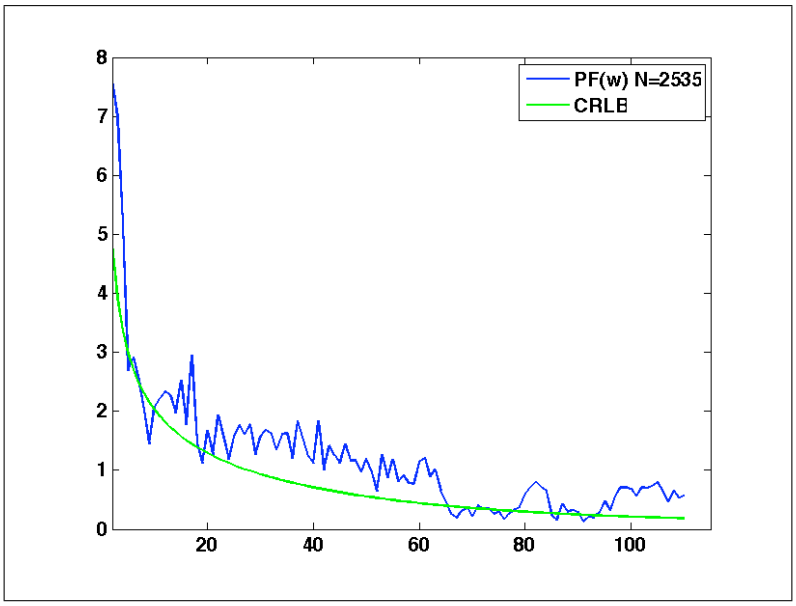

Figure 5.39: Particle Filter with weights reset after resampling and corresponding CRLB

It is clear from these figures that particle filters with small number of samples and comparable performance with GHT provide slightly worse results than GHT, while increasing number of particles proved much more reliable estimator, but at expense of the calculation time. One of the ways to demonstrate this trade-off between accuracy and computation time is to plot points extracted from Pareto surface. Figures 5.40 show RMS error against computation time and 5.41 shows same for Hough Transform variants only, for a number of measurements fixed on 78 measurements. This number of measurements were chosen as the point where each of the algorithms appears to have reached a steady-state performance, but the particle filter times are not too extreme.

Figure 5.40 demonstrates that out of particle filter algorithms best precision demonstrated by particle filters with Metropolis-Hastings step $N = 1690$ and particle filter with reset weights PF(w) with $N = 2535$, while bootstrap with $N = 2535$

demonstrated the best calculation time. Generalized Hough Transform and particle filter with reset weights PF(w) with $N = 2535$ are both optimal solutions. Particle filter with Metropolis-Hastings step demonstrated how the small increase in the performance from the particle Filter with Metropolis step comes at a great processing cost. Therefore Generalized Hough Transform is the fastest compared solution while particle filter with reset weights PF(w) is more precise due to the relative grid size and target position.

Generalized Hough Transform while being slowest from HT variants has demonstrated good accuracy and calculation time on this scenario. Figure 5.41 shows the comparable time and performance trade of for Hough Transform variants and in this figure it is clear that Hybrid Hough Transform is an overall optimal solution. It

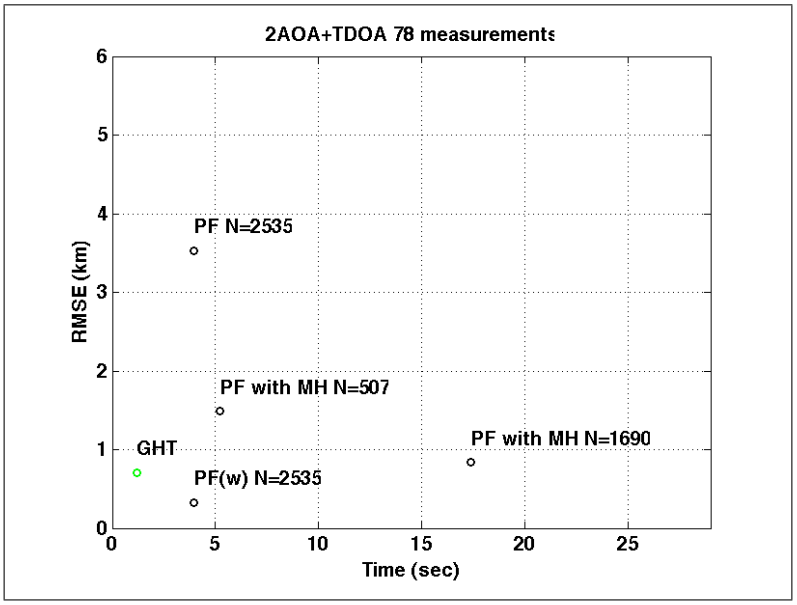

Figure 5.40: RMS error for PF and GHT with fixed number of measurements

was presented in this section that it is possible to build robust particle filter based estimator by adding Metrpolis-Hastings step and the results of the performance such algorithm has been presented. The calculation time of the particle filter can be improve by choosing the lower number of particles. It was also demonstrated that performance of the particle filter can be comparable to GHT, however for this particular scenario it was not possible to demonstrate particle filter which will outperform GHT in terms of calculation time.

One would argue that some of the results and unstable behaviour of the algorithms can be due to some artefact in the generated measurements and the robustness of the algorithms should be tested by regenerated scenario with new noisy measurements randomly corrupted by Gaussian noise and RMS error should be averaged over the number of simulation. Such simulation was performed and average was calculated over 100 simulations for the same fixed number of measurements 78. Figures 5.42 and 5.43 present same mean of the RMS error over 100 simulation in a same way as before, for particle filters with GHT and Hough Transform variants. Figure 5.46 shows the clustering of the GHT can be where the estimates

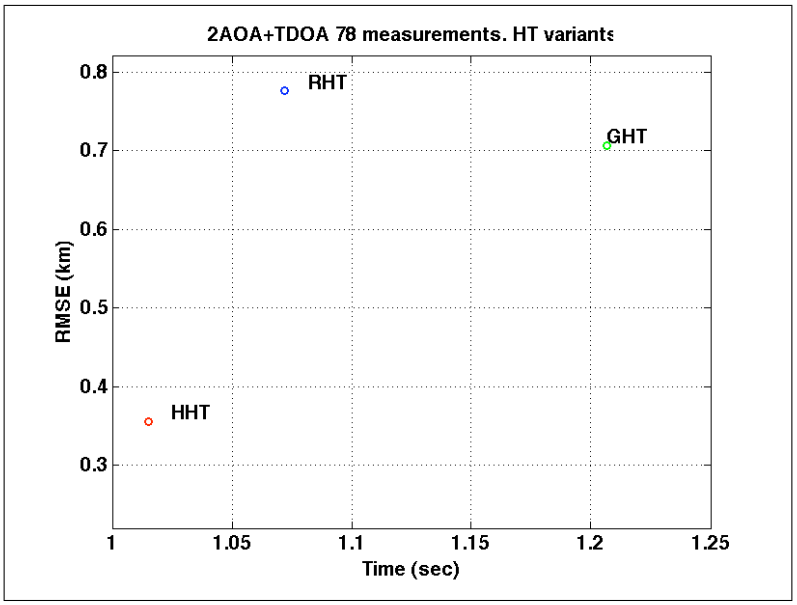

Figure 5.41: HT variants with fixed number of measurements

clusters presented as 4 points on a grid with error ellipse defined by covariance matrix over estimates with center of the ellipse being on the mean of the estimates. Figure 5.44 depicts error ellipses of PF algorithms, GHT and error ellipse which is used to calculate CRLB and it is marked as CRLB for reference. All error ellipses from the algorithm output plotted as defined by covariance matrix calculated using corresponding algorithms estimates, with center on the mean of these estimates.

Figure 5.45 shows the estimates of the particle filter with error ellipse as defined by covariance matrix calculated using these estimates. It is clear that the mean of the particle filter estimates is close to the true target location, however large spread in estimated position produced very long error ellipse. Figure 5.47 demonstate the impact of the Metropolis-Hastings step on the particle filter estimates. The ellipse is smaller than simple particle filter, however this ellipse is now rotated due to the skewness introduced by the particles accepted from uniform distribution during Metropolis-Hastings step. This skewness is not noticeable in figure 5.48 as number of particles sufficient to improve estimate by simulating better *a priori* distribution.

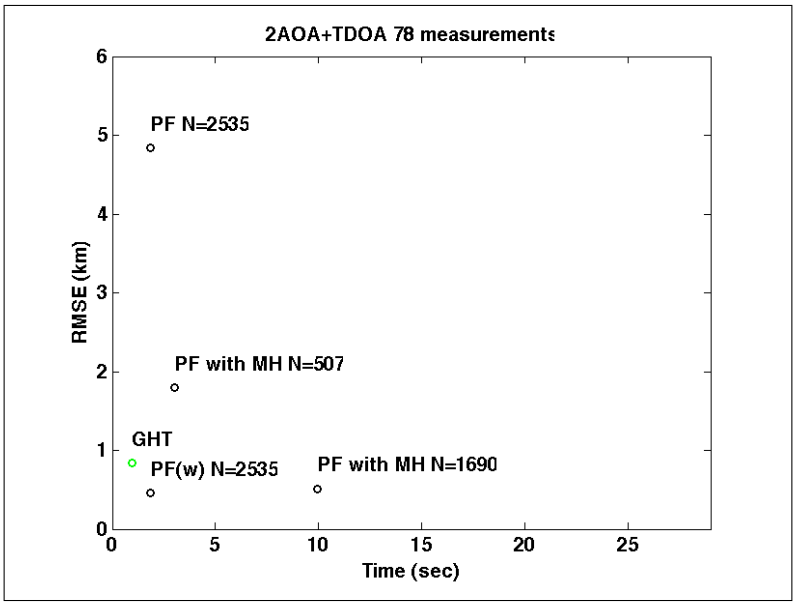

Figure 5.42: RMS error (mean over 100 simulations) for PF and GHT with fixed number of measurements

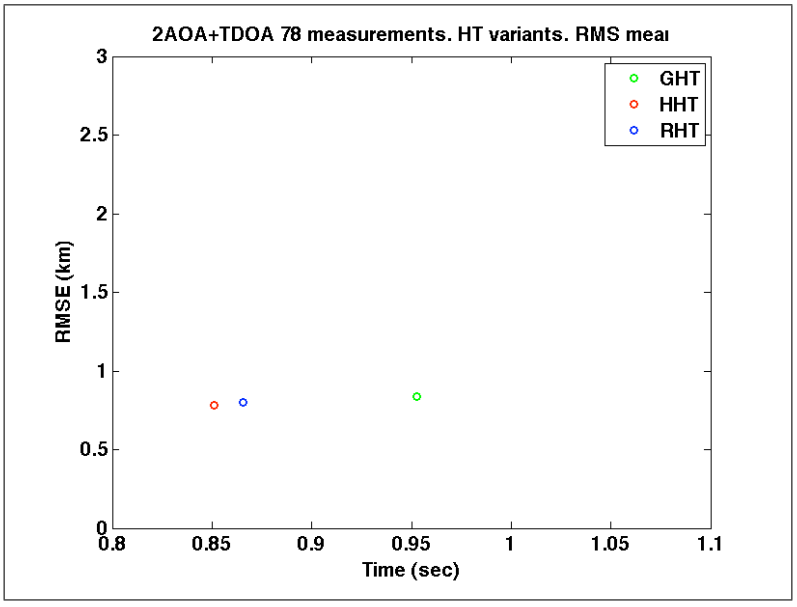

Figure 5.43: RMS error (mean over 100 simulation) for HT variants with fixed number of measurements

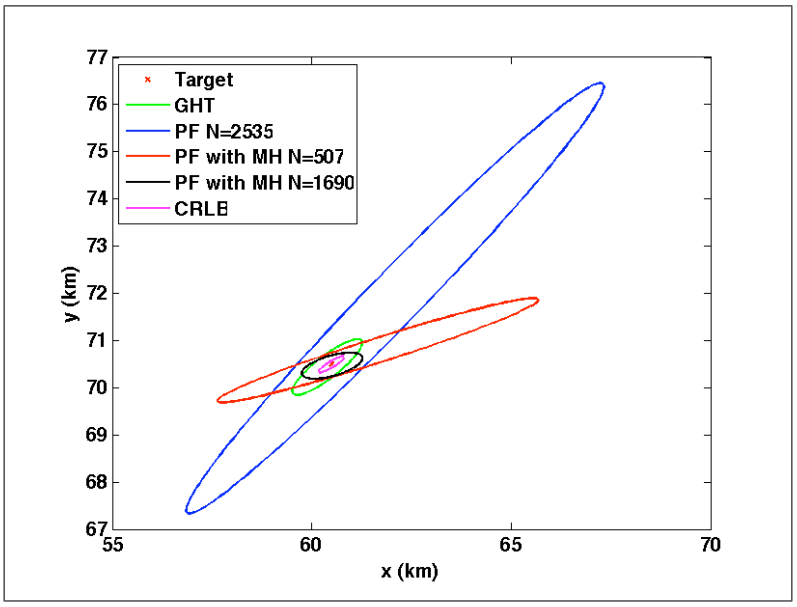

Figure 5.44: Error ellipses corresponding to covariance matrixes calculated over 100 estimates for each algorithm with mean centred on a mean of 100 estimates

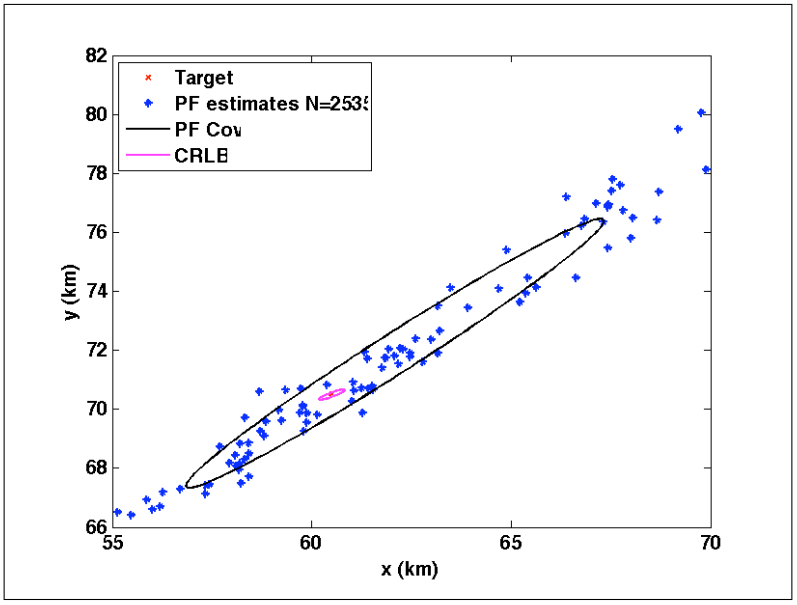

Figure 5.45: Estimates from the particle filter with error ellipse defined by the covariance matrix

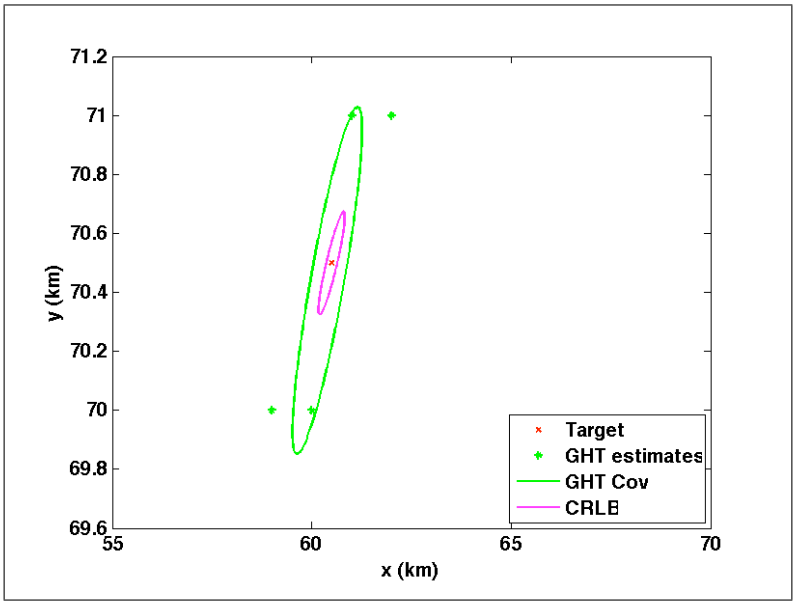

Figure 5.46: GHT estimates and error ellipse

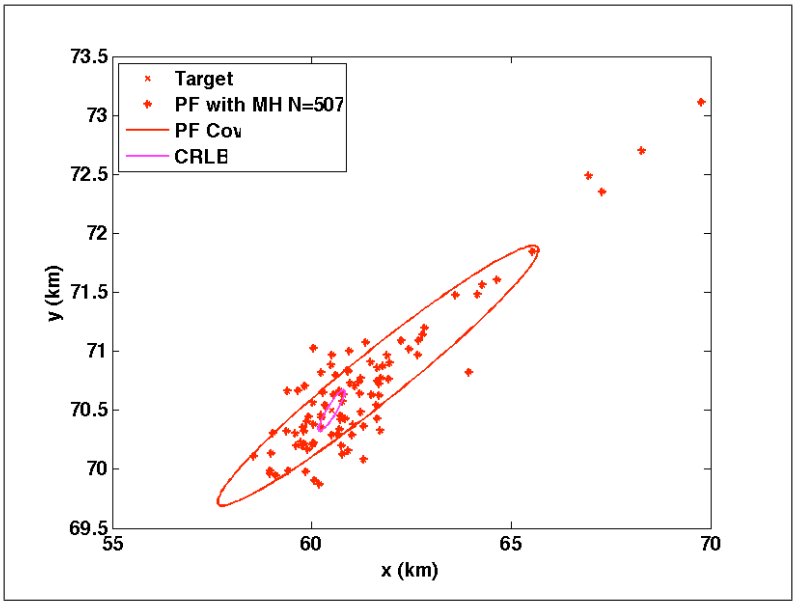

Figure 5.47: Particle filter with Metropolis-Hastings step $N = 507$ estimates and ellipse defined by the covariance matrix

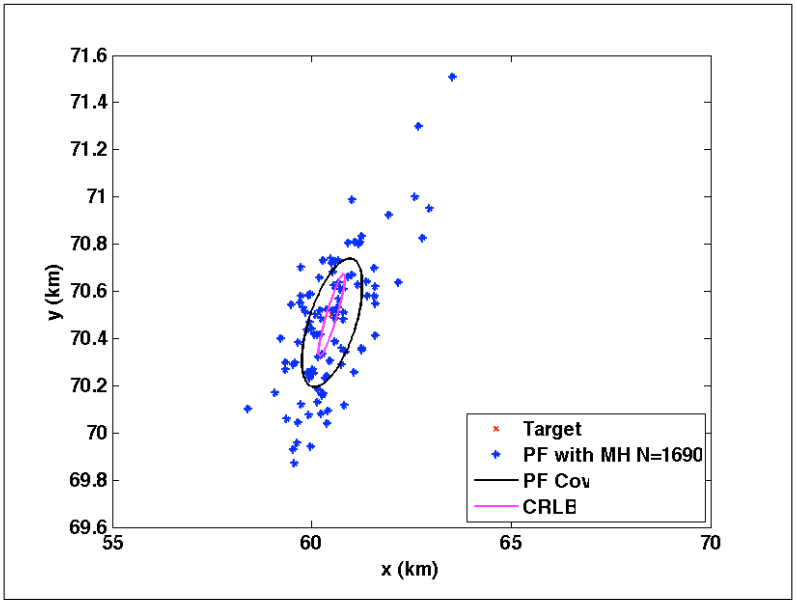

Figure 5.48: Particle filter with Metropolis-Hastings step $N = 1690$ estimates and ellipse defined by the covariance matrix

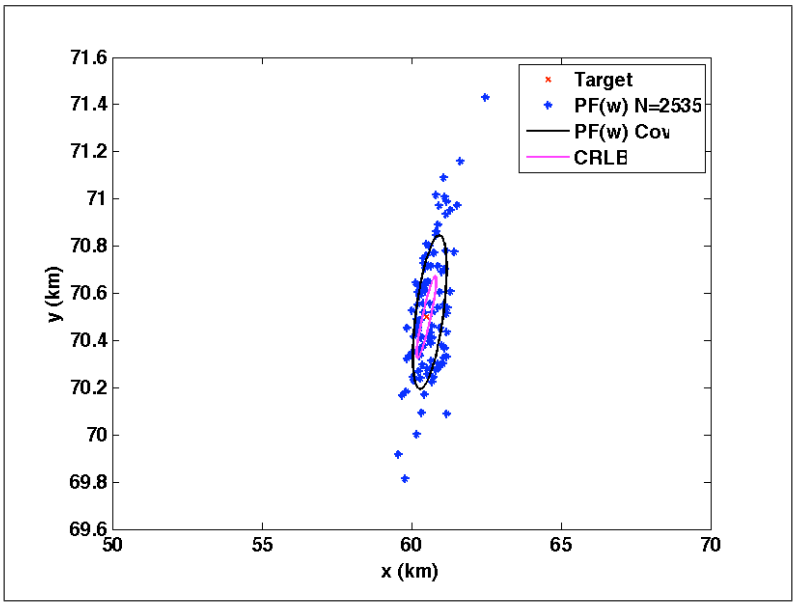

Figure 5.49: Particle filter with weights reset after resampling $N = 2535$, estimates and ellipse defined by the covariance matrix

5.5.1 Conculsion

This section showed that it is possible to implement particle filter with good accuracy by additional Metropolis-Hastings step and by resetting weights to uniform after re-sampling. The performance of this new particle filter algorithm was compared with Generalized Hough Transform, Randomized Hough Transform and Hybrid Hough Transform. Trade-off for particle filter based algorithm between accuracy and calculation time was demonstrated on single scenario with fixed noise measurements and then extended to the case where measurements were regenerated with zero-mean Gaussian noise on each simulation. The presenting algorithm were compared in terms of estimation accuracy and computation time. In the next section algorithms will be tested against model mismatch scenario, where measurement noise has been changed from Gaussian to Uniform and Rayleigh.

5.6 Model Mismatch

Simulation scenario was changed in a way that Gaussian measurement noise was replaced by Uniform and Raleigh distribution with parameter 0.5 distributed measurement noise. The target position was changed to $(60, 70)$km, in order to see whether any of the algorithms will be able to converge precisely to target location. Note, that during these simulations both algorithms were using same set of data rather than sharing model. Results of the particle filter are shown in figure 5.50. GHT is only marginally worse - it took longer to converge to true target location, but it located target precisely 5.51.

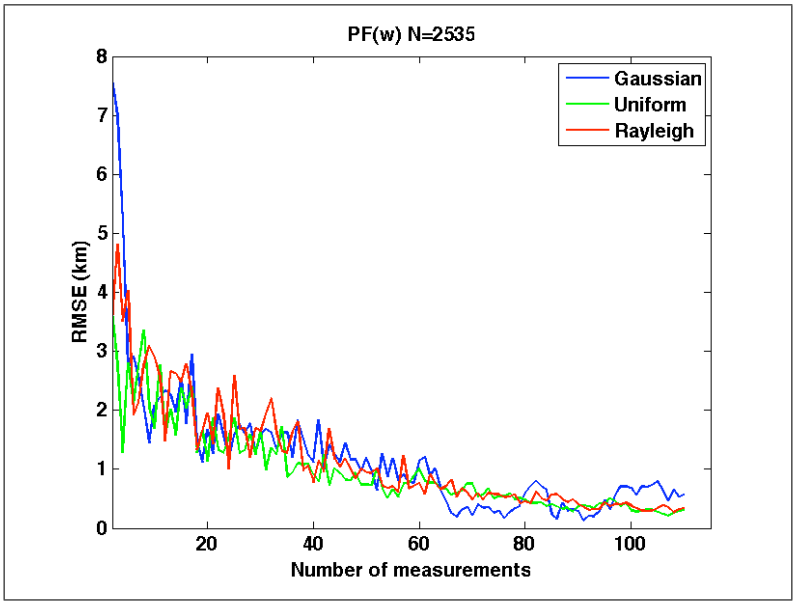

Figure 5.50: RMS error for PF with weights reset for different measurement error models

5.6.1 Using Rayleigh probability

In previous section model mismatch test was performed in a way that all algorithms assumed that measurement error is Gaussian, thus Gaussian likelihood function was used as weighting in particle filter and Hough Transform algorithms, but actual measurements in simulation were generated using different distributions: Gaussian, Rayleigh and Uniform.

In this section we propose to change the underlying assumption about the model and use Rayleigh defined pdf as weighting in particle filter and Hough Transform.

Applying Rayleigh pdf for TDOA let $\zeta = (R_{i,1} - c\tau_{i,1})$, then:

$$p(x, y|\tau_{i,1}) = \zeta \frac{\exp\left(\frac{\zeta^2}{2\sigma_r^2}\right)}{\sigma_r^2} \tag{5.6}$$

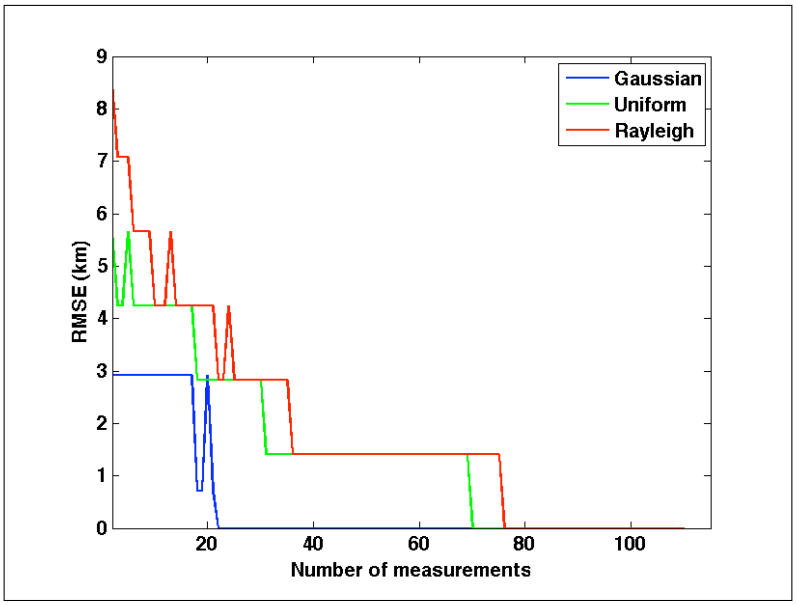

Figure 5.51: RMS error for Generalized Hough Transform for different measurement error models

for all $\zeta > 0$ or $p(x, y|\tau_{i,1}) = 0$ otherwise. Where R_i range of the source to the ith receiver is:

$$R_i = \sqrt{(x_{r_i} - x)^2 + (y_{r_i} - y)^2} \tag{5.7}$$

and the range difference between receiver i and receiver 1 is:

$$\begin{aligned} c\tau_{i,1} &= R_i - R_1 \\ &= \sqrt{(x_{r_i} - x)^2 + (y_{r_i} - y)^2} \\ &\quad -\sqrt{(x_{r_1} - x)^2 + (y_{r_1} - y)^2} \end{aligned} \tag{5.8}$$

where, $\tau_{i,1}$ is the measured TDOA between the ith receiver and receiver 1 and c is the velocity of light.

Similarly, for AOA measurements $\zeta_\theta = (\xi - \theta_i)$:

$$p(x, y|\theta_i) = \zeta_\theta \frac{\exp\left(\frac{\zeta_\theta^2}{2\sigma_\theta^2}\right)}{\sigma_\theta^2} \tag{5.9}$$

where θ_i is the measured angle of arrival at the ith receiver and ξ is the calculated angle from the ith receiver at point (x_{r_i}, y_{r_i}) to the point (x, y) using an equation of the form given by (1.1). σ_{θ_i} defines the standard deviation of the AOA measurement error for that receiver.

Figures 5.52 and 5.53 demonstrate the performance of the particle filter with Metropolis Hastings step with number of particles $N = 507$ and $N = 1690$ respectively, in presence of different type of noise with Rayleigh pdf as weighting function.

Figure 5.54 present the results of the Generalized Hough Transform for the different type of noise with Rayleigh pdf as likelihood function.

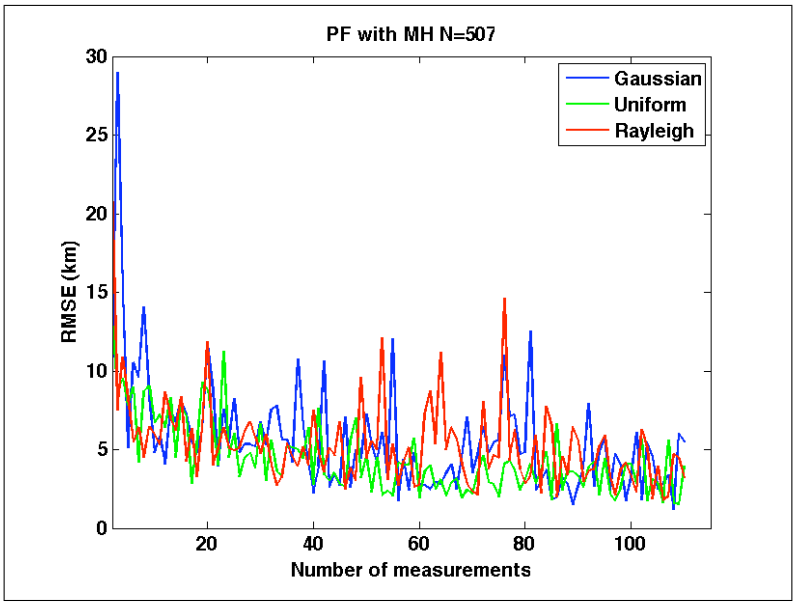

Figure 5.52: Particle filter with Metropolis Hastings step $N = 507$ number of particles. Likelihood calculated according to Rayleigh distribution

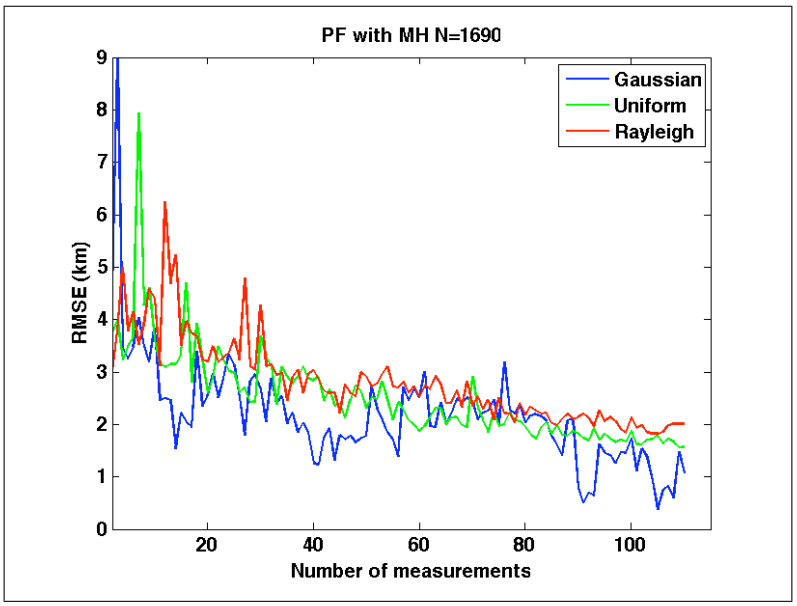

Figure 5.53: Particle filter with Metropolis Hastings step $N = 1690$ number of particles. Likelihood calculated according to Rayleigh distribution

In this section the performance of the particle filter with Metropolis Hastings step and GHT has been compared on different model mismatch simulations:

1. Measurement error assumed to be Gaussian and thus Gaussian pdf used as likelihood/weighting function in the model in the algorithm, while measurement noise was generated using additive Gaussian, Rayleigh and Uniform distributions.

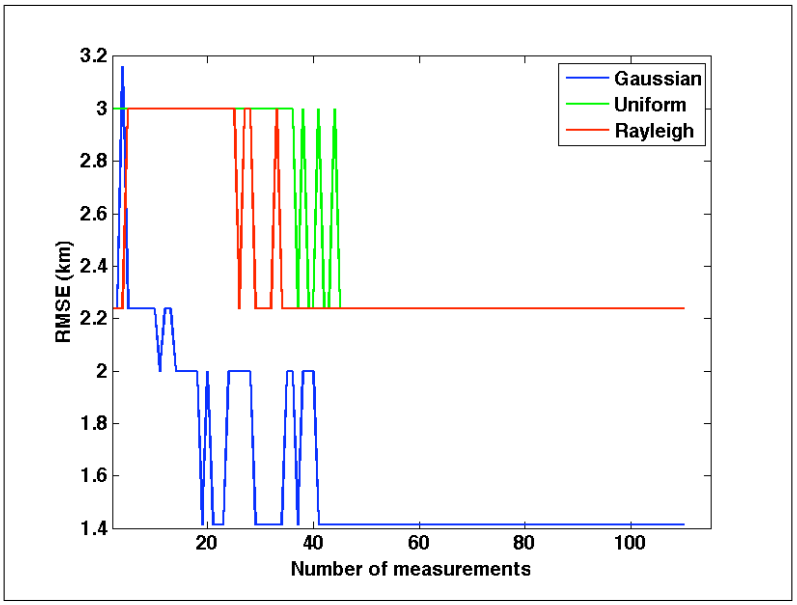

Figure 5.54: Generalized Hough Transform. Likelihood calculated according to Rayleigh distribution

2. Measurement error assumed to be Rayleigh, hence Rayleigh pdf used as likelihood/weighting function in the model in the algorithm, while measurement noise was generate using Gaussian, Rayleigh and Uniform distributions.

Changing the assumptions that the measurement's errors are not Gaussian, but Rayleigh, as in the second case, didn't improved the performance of the particle filter algorithm and it's sustainability to the different types of measurement noise. In the same case using Rayleigh likelihood in Hough Transform worsened the performance of HT in presence of Rayleigh and Uniform measurements noise. The case for this slightly worsened estimate, apart from size of the grid may be the problem of additions peaks in the parameterised space of the Hough Transform: due to long tail of Rayleigh distribution - some tails intersect and add to the value of the likelihood in Hough Transform, thus producing multiple peaks around real target position. Hough Transform algorithm with Gaussian likelihood provided good performance in presence of model mismatch, therefore the optimal algorithm for geolocation would be Hough Transform variants with assumption of the Gaussian model.

Simulation of the measurements for the scenario 5.16 was changed in a way where 33% of the AOA measurements were altered by random phase $\theta_{fading} \in (0 \ldots \pi/3)$. in practice such alteration of the AOA measurements occur due to fading of the radio signal. Results of the simulations averaged over 12 simulations are presented in figure 5.55 5.56 with particle filter with reset weights and assumption of that underlying distribution is Rayleigh in figure 5.57 It is possible to geolocate target in presence of model mismatch using Bayesian approach and particle filter; and it is also possible to locate target using Non-Bayesian approach and Hough Transform, with any kind of model mismatch and any kind of likelihood. Using Rayleigh likelihood in the model marginally improved the performance of the particle filter in presence of AOA

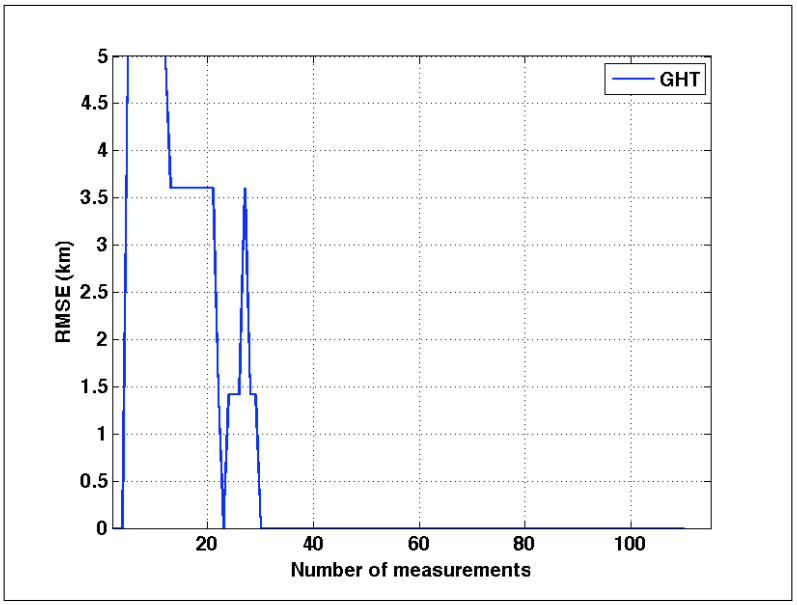

Figure 5.55: GHT with faded AOA measurements, geolocation using fused 2 AOA and TDOA measurements

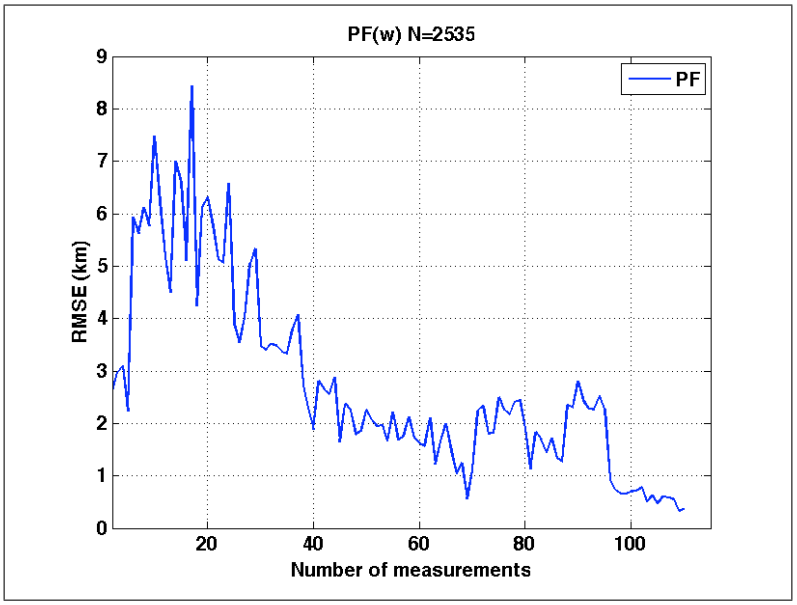

Figure 5.56: PF with weights reset and faded AOA measurements, geolocation using fused 2 AOA and TDOA measurements

measurements with fading, as can be noticed in figure 5.57, but overall performance of the particle filter algorithm and Hough Transform algorithm has been comparable in terms of accuracy and robustness in terms of dealing with model mismatch.

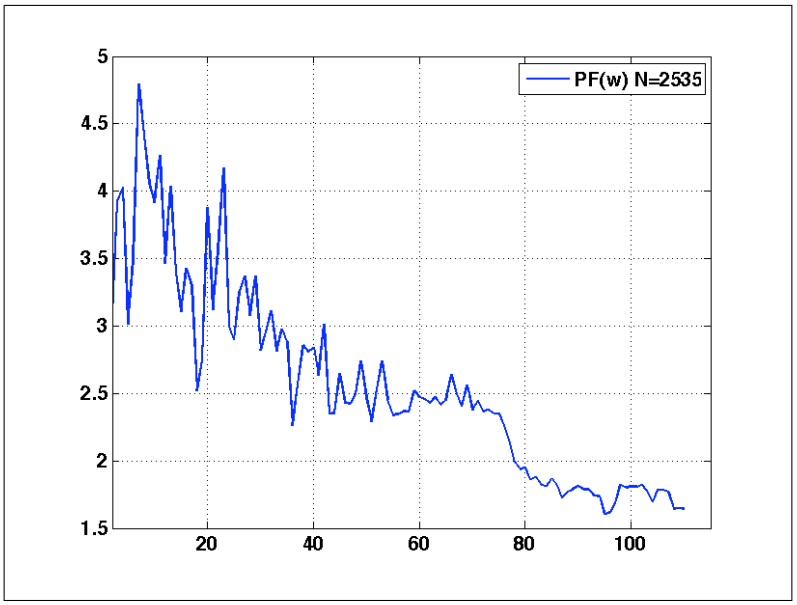

Figure 5.57: PF with Raylegh likelihood faded AOA measurements, geolocation using fused 2 AOA and TDOA measurements

5.7 Conclusion

In this chapter, five different geolocation algorithms have been compared. Three of these are based on the Hough Transform, one on the particle filter and one on the Bayesian Randomized estimator. After performing the comparisons under identical conditions, it was found that whilst all five estimators were able to geolocate the target successfully, there were important trade-offs between the positional accuracy of the estimate and the computational overhead such that the choice of the estimator may depend entirely on the application rather than whether one estimator is more 'accurate' than another.

In attempting to reduce the computational overhead of the Generalized Hough Transform, the performance of the Randomized Hough Transform was obtained. Whilst it is seen that the RMS positional error of the Randomized Hough Transform is not as good as the Generalized Hough Transform, the reduction in computational overhead is substantial. The Hybrid Hough transform, provides an excellent compromise that results in an RMS error performance that is indistinguishable from the Generalized Hough Transform for a computational overhead that is marginally worse that the Randomized Hough Transform.

It was identified that there are many structural similarities between the Randomized Hough Transform and the particle filter, except that the latter uses a Bayesian approach and the former is non-Bayesian.

Also in this chapter the performance of the algorithm has been compared on single scenario and single set of data and evaluated in terms of algorithms accuracy and computational time. The particle filter algorithm has been extended by Metropolis-Hastings step and performance of the algorithm presented. Optimal

points of the Pareto surface were extracted and presented for fixed number of measurements and trade-off between algorithms complexity and accuracy demonstrated. The robustness of the presented algorithms has been tested by regenerating simulation scenario for 100 times using random measurements noise, but same scenario and the results confirmed initial comparison positions of the optimal points from Pareto surface. Generalized Hough Transform have a major disadvantage as it is grid based method, so it would not be possible to locate target precisely if it is not on the grid as in above performed experiment. Particle filter on the other hand is not grid based method, but the one required resampling, thus it would be possible to locate target precisely with additional computational effort. Modification of the Hough Transform algorithm as Hybrid Hough Transform algorithm in a way so it would not be gridded, allow overcome grid-based limits of GHT and keep computation time low. Overall performance of the particle filter algorithm and Hough Transform algorithm has been directly comparable in terms of accuracy and robustness in terms of dealing with model mismatch. There was no advantage in these terms of one over another.

Chapter 6

Generalized estimator

6.1 Introduction

In this chapter, a generalized approach to an estimator is developed in a novel way that illustrates how the Hough Transform estimator and the ideal Bayesian Estimator described in the previous chapters are linked *via* a single parameter α. For each value of α a new estimator is generated with its own RMS error characteristics and it is through the variance of the mean RMS positional error with α that the generalized estimator is examined in details.

It is commonly assumed that the optimum estimator is based on the Bayesian estimator, such as the Kalman filter. For linear problems, the Kalman filter is an optimal Bayesian estimator for Gaussian noise. However, it is clear from the previous chapters that the Hough Transform can be used as an estimator that is non-Bayesian. In this chapter, the connection of a non-Bayesian estimator with a Bayesian-type is developed and exploited in more detail. This is achieved by developing a generalized estimator. The aim of the generalised estimator is to demonstrate the relationship between the Bayesian and Hough Transform approach.

6.2 Generalized Estimator

According to [84] the Bayesian theorem attributed to Bayes (1744-1809), tells how to revise the probability of events in the light of new data. It is important to point out that this theorem is consistent with the probability theory and is widely accepted by scientific community. There is disagreement however regarding whether the theorem should be applied to subjective notions of probabilities (the Bayesian approach) or whether it should only be applied to frequentist notions (the frequentist approach) [85]. Consider the case of the two measurements z_1 and z_2, conditionally independent given the quantity to be estimated x (in geolocation x is a position vector of the target), the generalised estimator function might be:

$$p_{mix}(x|z1, z2) = \alpha \left(p(z_1|x) + p(z_2|x)\right) + (1 - 2\alpha) \left(p(z_1|x)p(z_2|x)p(x)\right) \tag{6.1}$$

In this case, where $\alpha = 0$, the $p_{mix}(x|z1, z2)$ will reduce to Bayes rule (up to normalising constant) and to Hough Transform approach for $\alpha = 05$.

6.3 Simulation of generalised estimator

As a way of illustrating the effect of changing the estimator function from Bayesian to Hough by means of the parameter α, consider an illustrative scenario, with two stationary receivers capable of obtaining Angle-of-Arrival measurements of the signal from a stationary emitter. The scenario is plotted on figure 6.1, where the receivers are denoted as blue circles and the emitter (target) as a red cross. Each receiver provides one measurement corrupted by Gaussian measurement noise with a standard deviation of 0.02 radians. This scenario is used in order to demonstrate the overall behaviour of the generalised estimate. Quantitate results will be presented further, using common scenario 5.16. For a particular value of α, a parameterized space is formed, using (6.1) instead of the traditional Hough Transform function. Parameterised space was initialised evenly with $\epsilon = 2.2204 \times 10^{-16}$. In figure 6.2

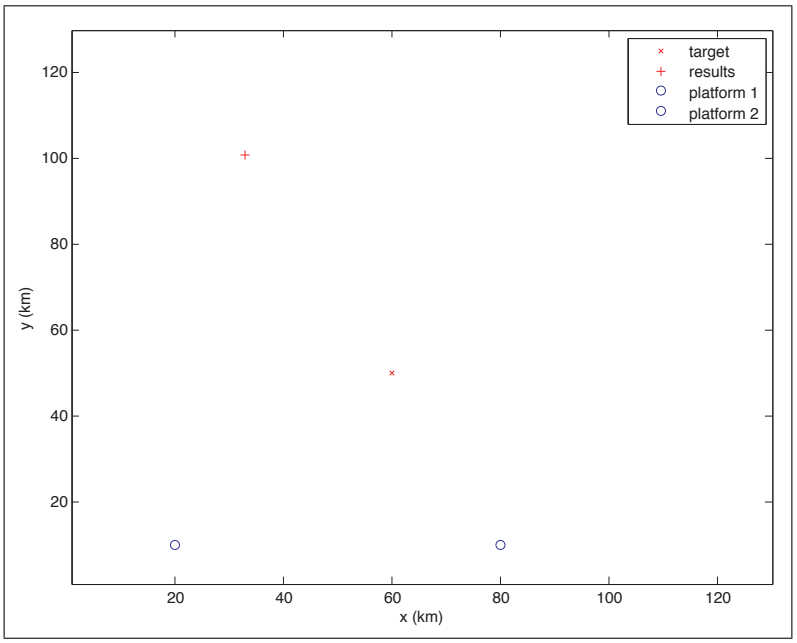

Figure 6.1: Simple scenario in order to test the generalized estimator (α function)

with $\alpha = 0$ the 3D accumulated likelihood function represents that of the Bayesian estimator, whereas figure 6.3 shows the situation for $\alpha = 0.5$ corresponding to the Hough Transform. Examining the surface plot with $\alpha = 0.6$ and $\alpha = 0.9$, as shown in figures 6.4 and 6.5, it is noticeable that this distribution has a 'dip' (which is the subtraction of $p(z_1|x)p(z_2|x)$) and the minimum of this function will provide a position estimate, instead of a peak as in figures 6.2 and 6.3. Hence, for values of $\alpha \geq 0.6$ it would make sense to look for a minimum in the parameterized space instead of a maximum. The simulation was performed with a step size of $\alpha = 0.01$ and the results were plotted in figure 6.6, showing the average RMS error calculated

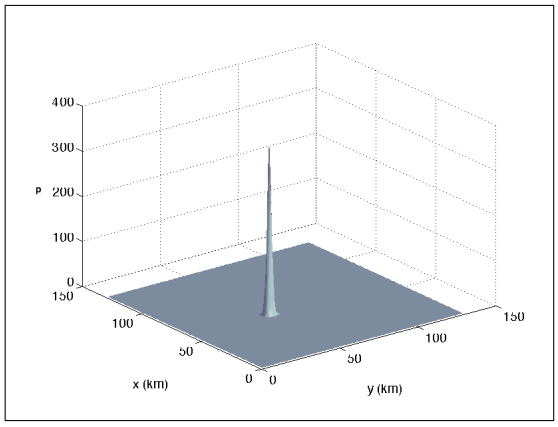

Figure 6.2: 3D parameterized space with $\alpha = 0$, Bayesian like, initialised with probability distribution over the first measurement

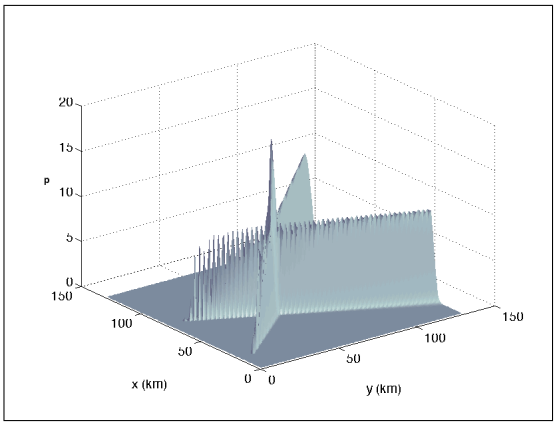

Figure 6.3: 3D parameterized space with $\alpha = 0.5$, Hough Transform

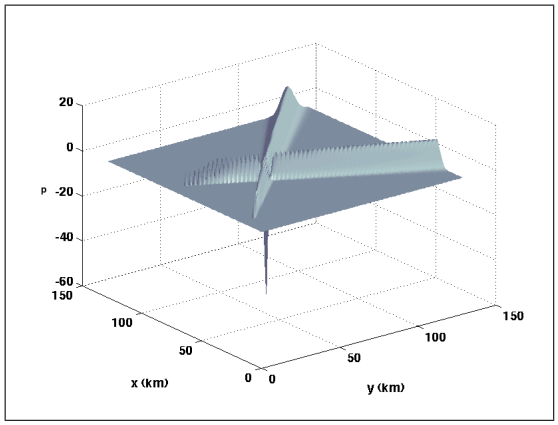

Figure 6.4: 3D parameterized space with $\alpha = 0.6$, 'Dipped' Hough Transform

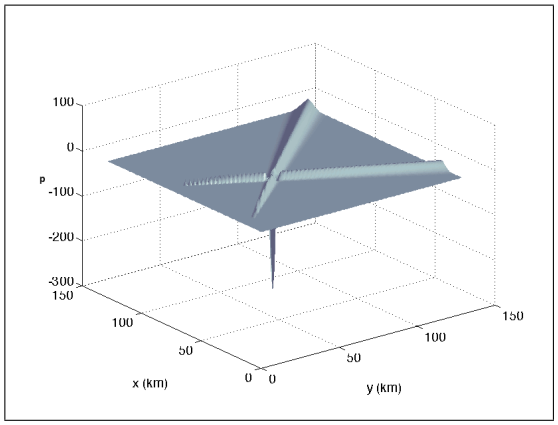

Figure 6.5: 3D parameterized space with $\alpha = 0.9$, 'Dipped' Hough Transform

over 50 simulations. As was mentioned before, the RMS error of the minimum of the function in the parameterized space was also calculated and the average RMS plotted in figure 6.6, marked as 'RMS MIN'.

In order to analyse this data, the standard deviation of the RMS error of the estimates using maximum of the parameterised space was calculated and plotted as shown in figure 6.7. Figure 6.7 shows that Bayesian estimator have smallest standard deviation out of all function and it can be logically concluded comparing figures 6.2 and 6.14-6.3. The paremeterised space with $\alpha = 0$ have very thin and sharp peak thus the standard deviation, while outlining "raised plato" in function with $\alpha = 0.1 \ldots 0.5$ will impact on the standard deviation of the estimates.

To compare the performance of these functions, another metric was introduced. Assuming that it is possible to threshold the parameterized space on the levels 50%, 75% and 95% of maximum. Moreover, it is possible to use the size of this contour, calculated as a sum of the total number of points under the contour, as

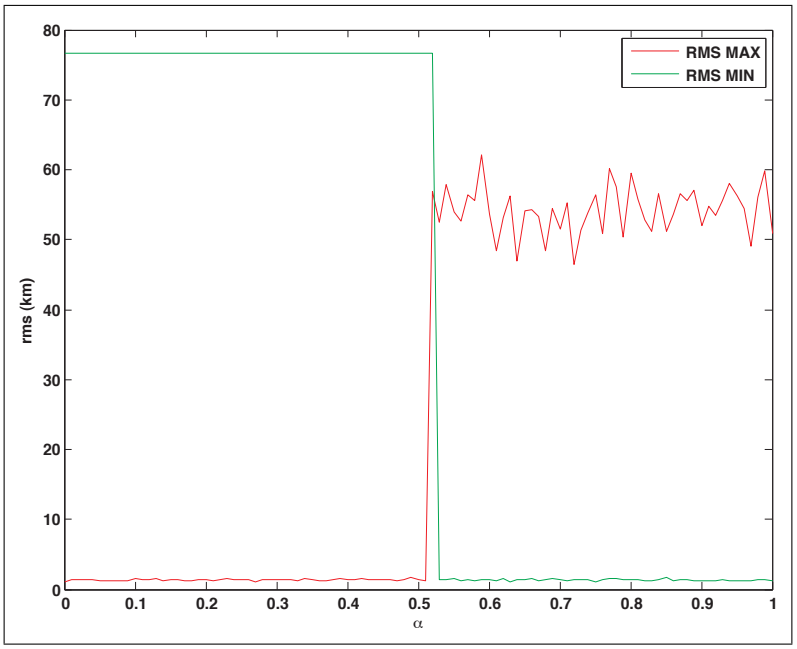

Figure 6.6: Average RMS error over 50 simulation with two AOA measurements, with the likelihood of the probability of the first measurement used as initial conditions, for the scenario in figure 6.1

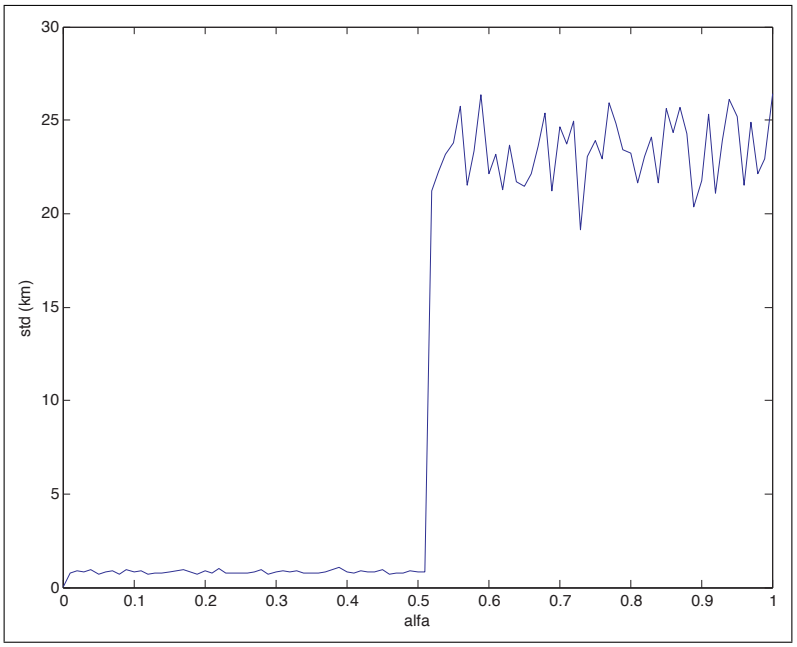

Figure 6.7: Average standard deviation of the RMS error using maximum of the parameterised space calculated over 50 simulations for the scenario in figure 6.1

a weight for these functions. The average value of the weights were obtained over by 50 simulations and plotted in figure 6.8. The weights characterize the accuracy of locating the emitter when using these functions in parameterized space on the selected threshold and this property might be used as a measure of the goodness of GDOP for the particular scenario for a particular geolocation method and estimator.

In some sense, these weights are an inverse equivalent of the Tukey and Mosteller robustness measurement for the distributions and thus it is an additional measure the robustness of the functions for the case of the emitter geolocation. According to Mosteller [86] and [84] two types of robustness were defined, where robustness is a lack of susceptibility to the effects of non-normality:

- Robustness of validity means that the confidence intervals for the population location have a 95% chance of covering the population location regardless of what the underlying distribution is.
- Robustness of efficiency refers to a high effectiveness in the face of non-normal tails.

The proposed weights are similar measure, covering the population location under 50%, 25% and 5% confidence interval in terms of the [86]. Figure 6.8 demonstrates that this weights and thus measure of robustness exists only for the values of $\alpha > 0.45$. The usefulness of this method of weighting for data fusion will be exploited in detail in chapter 7, but in this chapter it is important to point out that the weights with 50% threshold exists only for Hough Transform and 'dipped' Hough Transform. It also should be noted that for $\alpha \in [0 \ldots 0.4]$ "weight" is very small value - close to one, this suggest that distribution have very sharp peak, thus small spread in estimation and consequently higher confidence.

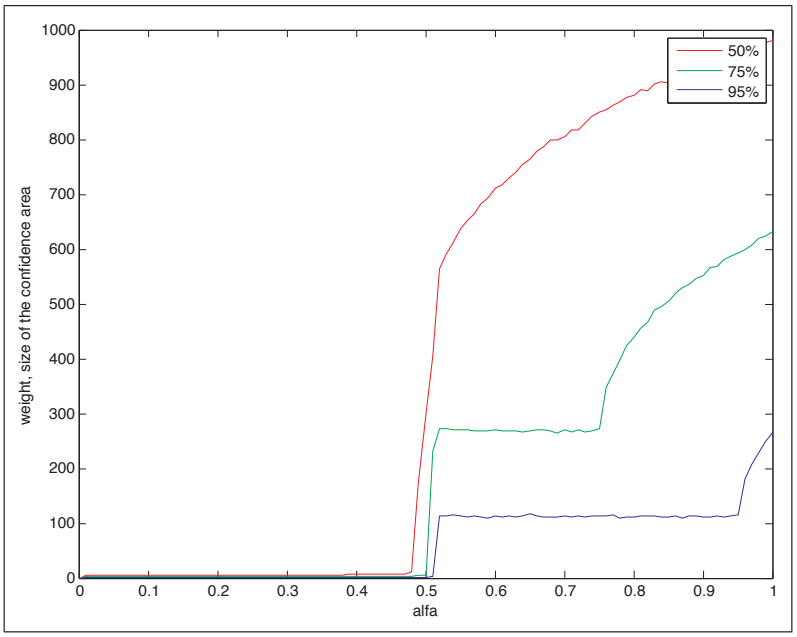

Figure 6.8: Average value of the weights calculated over 50 simulations for the scenario in figure 6.1

6.3.1 Near Hough Transform estimation with $\alpha \in [0.4 \ldots 0.6]$

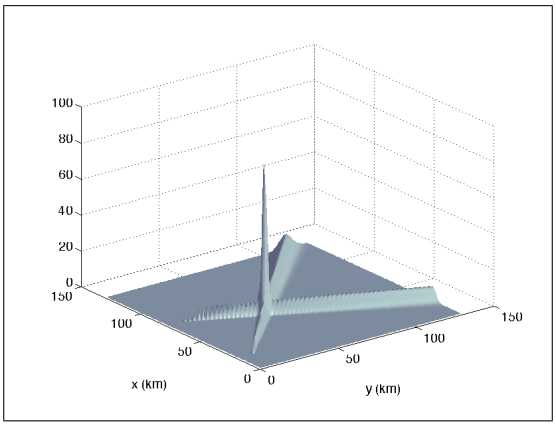

Figure 6.9: Example of 3D parameterized space with $\alpha = 0.4$, similar to Gaussian mixture

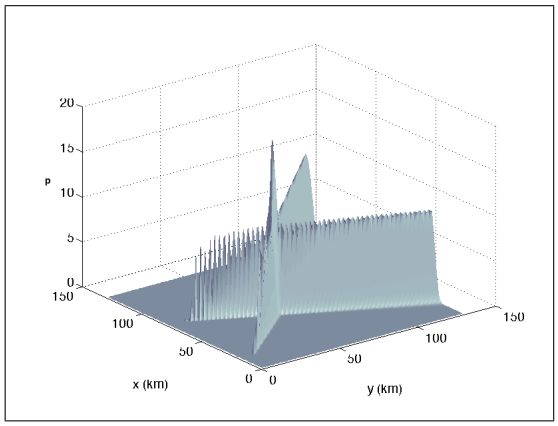

Figure 6.10: 3D parameterized space with $\alpha = 0.5$, Hough Transform

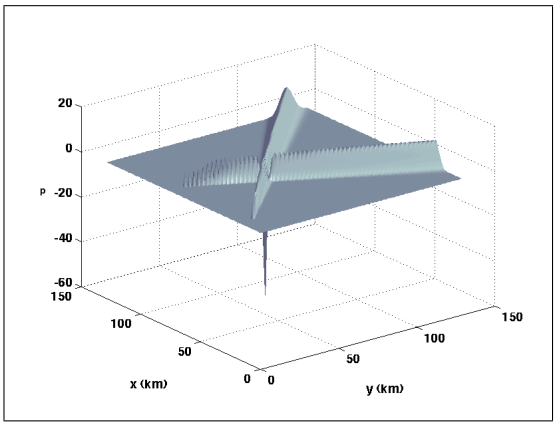

Figure 6.11: 3D parameterized space with $\alpha = 0.6$, 'Dipped' Hough Transform

We now look closely as the area where $\alpha = 0.5$, which is the equivalent of the Hough Transform estimator. The average RMS error over 50 simulations and the weights described earlier are plotted in figures 6.12 and 6.13 for the same scenario as before, plotted in figure 6.1.

From these figures, it is possible to conclude that when $\alpha >= 0.51$ the distribution in parameterized space goes from 'peaky', to uniform plate in which it is impossible to estimate the emitter position. It then forms a 'dip', where after $\alpha = 0.545$ a global minimum can provide an estimate of the position, as shown in 6.12. Another interesting fact is that the weight with a confidence area of 50% exists only after $\alpha = 0.49$ to $\alpha = 0.51$, thus when $\alpha = 0.5$ the Hough Transform can provide an 'estimate' of the 50% confidence area and this factor will be used in data fusion.

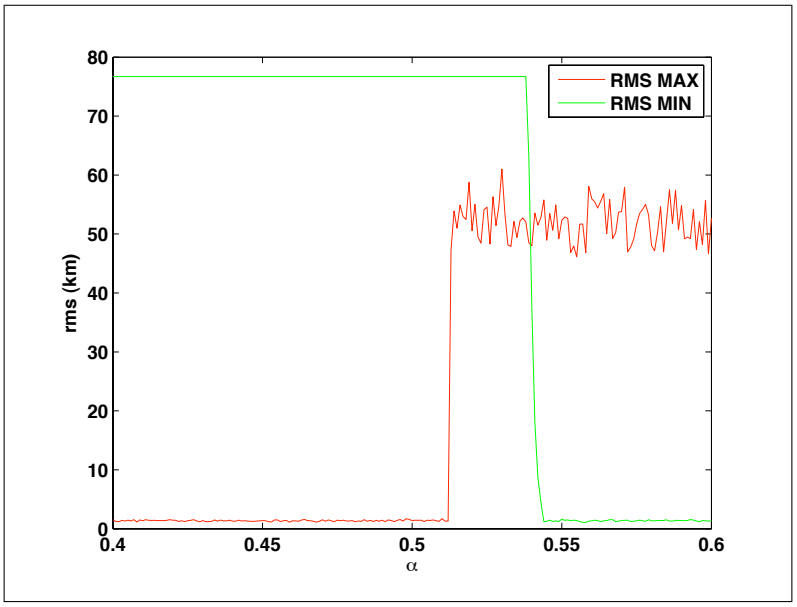

Figure 6.12: RMS error over 50 simulations, Hough Transform for the case when $\alpha = 0.5$, step size $\alpha = 0.001$

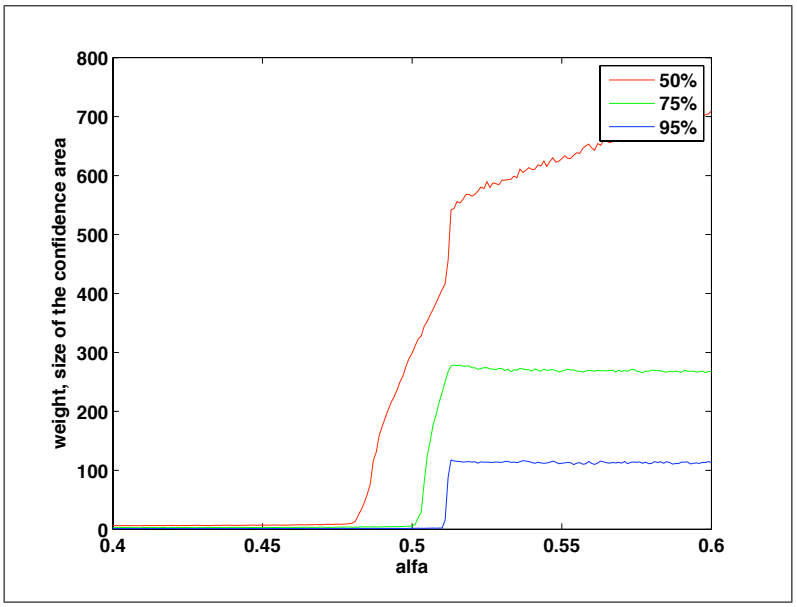

Figure 6.13: Average weights, with Hough Transform when $\alpha = 0.5$ and step size 0.001

6.3.2 Bayesian or near Bayesian estimation

There are multiple application of Gaussian Mixture [87], including particle filters [88] and sigma point particle filter [89]. It may be possible to define connection between generalised estimator with small values of α and Gaussian mixture.

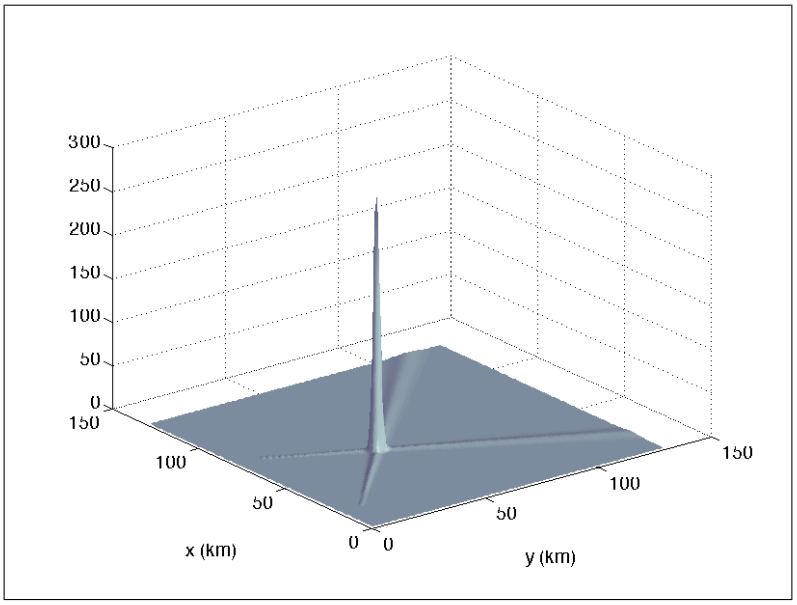

Figure 6.14: Example of 3D parameterized space with $\alpha = 0.01$, Gaussian mixture

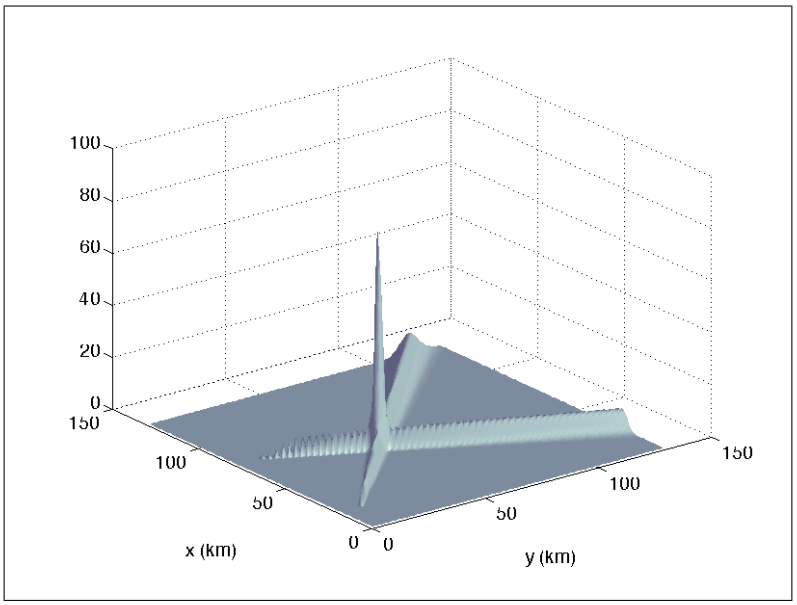

Figure 6.15: Example of 3D parameterized space with $\alpha = 0.4$, still similar to Gaussian mixture

According to [90], a Gaussian mixture or contaminated Gaussian model can be described as:

$$f(x) = (1 - \epsilon) f_n(x) + \epsilon f_c(x) \tag{6.2}$$

where $f_n(x)$ is the nominal Gaussian density with variance σ_n^2, ϵ is a small positive constant determining the percentage of contamination, and $f_c(x)$ is the contaminating Gaussian density with a large relative variance, such that $\sigma_c^2 >> \sigma_n^2$. Writing (6.1) using $\alpha = 0.001$ yields:

$$p_{mix}(x|z1, z2) = 0.001\,(p(z_1|x) + p(z_2|x)) + (0.998)\,(p(z_1|x)p(z_2|x)p(x)) \tag{6.3}$$

Now, equation (6.3) can be rewritten in a way where $f_n(x) = p(z_1|x)p(z_2|x)p(x)$ (standard Bayesian) and $f_c(x) = p(z_1|x) + p(z_2|x)$ the equation (6.3) can be defined as a Gaussian mixture:

$$f(x) = 0.998 f_n(x) + 0.001 f_c(x) \tag{6.4}$$

Figure 6.14 shows the parameterized space for the value of alpha $\alpha = 0.01$ similar to Gaussian mixture and in figure 6.15 for $\alpha = 0.4$ it can be seen that it is still similar to Gaussian mixture.

6.4 Data fusion using the generalised estimator and model mismatch

The aim of this section is to test the Generalised Estimator on the scenario presented in figure 5.16 and to discover whether there is a value of alpha, different from $\alpha = 0.5$ which can provide reliable estimates in presence of model mismatch, when the measurements noise modelled as Uniform or Rayleigh, while estimator assumes that the noise is Gaussian. In addition as in section 5.6 model mismatch with faded AOA was added where 33% of the AOA measurements were altered by random phase $\theta_{fading} \in (0 \ldots \pi/3)$. in practice such alteration of the AOA measurements occur due to fading of the radio signal.

In order to test the different functions presented above for the task of data fusion, the same scenario as in figure 5.16 was used as to provide consistence comparison. Note, that although in previous section fusion of TDOA and two AOA measurements were used, for generalised estimator simulations only AOA measurements were considered, as there is no known procedure of the normalisation of the likelihood before fusion of the different type of data.

In the foregoing, the likelihood function was formulated on the basis of Gaussian measurement errors. In order to test the robustness of the generalised estimator the statistics of the measurement noise, used for the Monte-Carlo simulation, was altered: instead of Gaussian noise distributions, the AOA measurements were corrupted by random values sampled from uniform and Rayleigh distributions. However, important to note the algorithm still assumed that the measurement noise was Gaussian distributed. As in section 5.6 AOA measurements with fading were used in order to determine the optimal value of α. Note that although scenario is the same 5.16 the absence of TDOA measurements made a significant impact on both Bayesian and Hough Transform estimators. It will be noted, that although the

precision of the generalised estimator suffered from this model mismatch the estimator still converges with a reasonably small error on the interval $\alpha \in [0.1 \ldots 0.5]$. From figures 6.16 and 6.17 it is clear that for 78 measurements any $\alpha \in (0.1 \ldots 0.4)$ can provide reasonable estimates, and with small number of measurements like 11 as well. The RMS error calculated as average over 12 simulations and the results are consistent in their repeatability. It should be noted that $\alpha = 0$, which models Bayesian estimator, didn't provide any reasonable estimate in presence of the model mismatch measurement noise with faded AOA. The calculation - "zooming" the

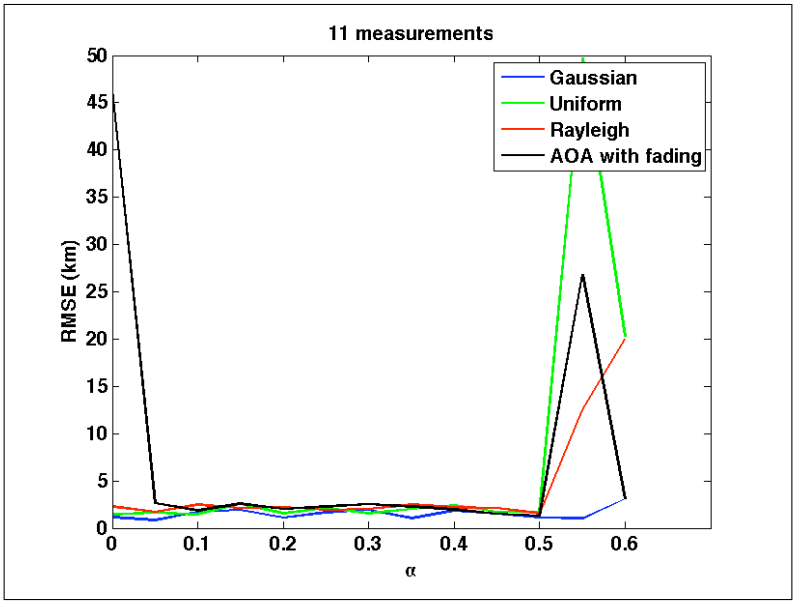

Figure 6.16: RMS error of the generalised estimator with $\alpha \in [0 \ldots 0.6]$ with step 0.05 for 11 measurements for AOA with fading

interval $\alpha \in (0.4 \ldots 0.6$ changing the values of alpha with step 0.0031 was performed. Figures 6.19) and 6.20 presents the results of the simulation in terms of RMS error (Euclidian distance). In figure 6.19 any value of $\alpha \in [0.1 \ldots 0.48]$ gives best estimate in presence of AOA measurement with fading as in figure 6.20, as well for 78 measurements. Exploring results in figures 6.16 and 6.17 with figures 6.19,6.20 zoomed version in the vicinity of $\alpha = 0.5$ and figures 6.22,6.23 zooming $\alpha = 0$, suggest the value to use $\alpha = 0.25$ as basis for the estimator which gives best performance in presence of model mismatch and measurement noise corrupted by fading.

Figures 6.18 provide 3D view of the values RMS error depending on values of α and different number of measurements with AOA measurement noise with fading. Figure 6.21 provides zoomed version of the view in the vicinity of $\alpha \in [0.4 \ldots 0.5]$.

Figure 6.24 provide 3D view for RMS error depending on value α and number of measurements in the vicinity of $\alpha = 0$ for measurement noise AOA with fading. Note that 3D figures are rotated in order to provide better view.

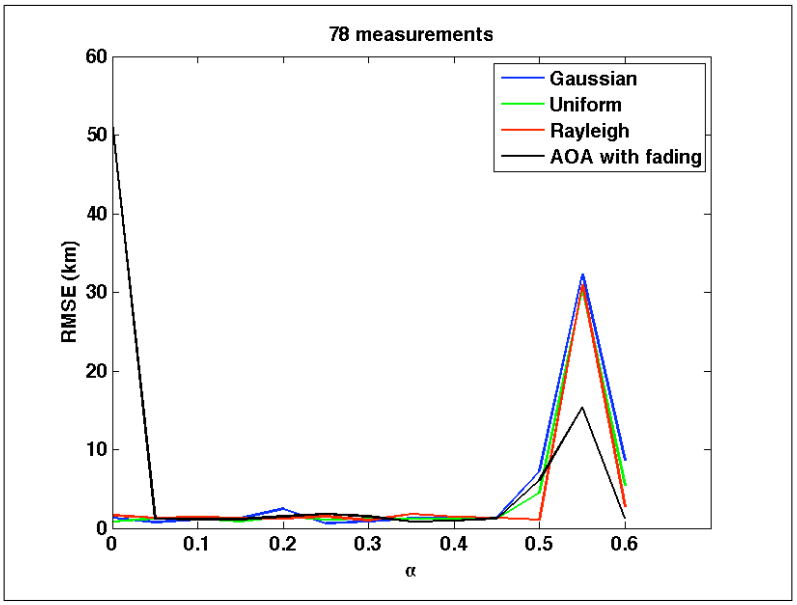

Figure 6.17: RMS error of the generalised estimator with $\alpha \in [0 \dots 0.6]$ with step 0.05 for 11 measurements for AOA with fading

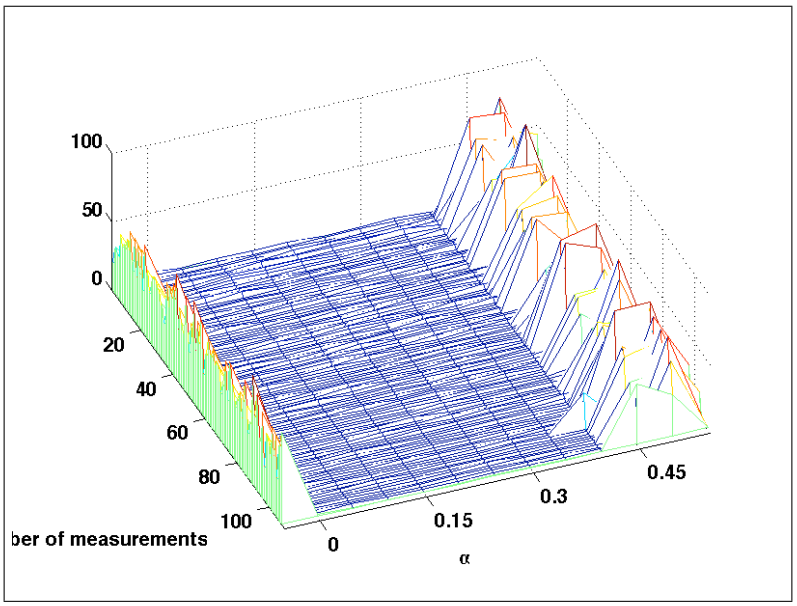

Figure 6.18: 3D representation of RMS error of the generalised estimator with $\alpha \in [0 \dots 0.6]$ with step 0.05 for different number of measurements for AOA with fading

6.4.1 Conclusion

The analysis presented in this section has been carried out in order to derive connections between the Hough Transform based algorithms and Bayesian type algorithms using general probability theory. In this section the generalised estimator based on parameter α, which changes the the estimator's behaviour with parameter $\alpha = 0$ near Bayesian to $\alpha = 0.5$ - Hough Transform equivalent, was proposed and tested on scenario 5.16 with model mismatch, such as: the measurements noise was assumed

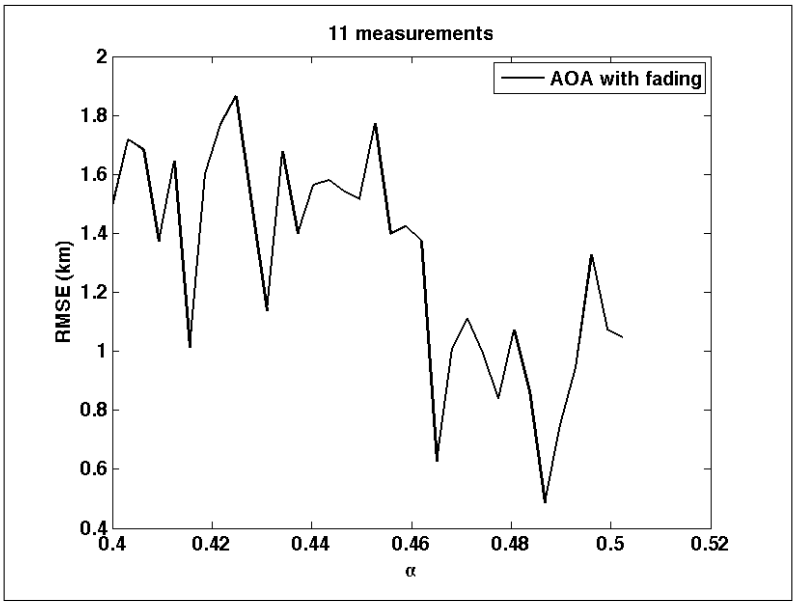

Figure 6.19: RMS error of the generalised estimator with α zoomed in the area of 0.4 till 0.6 with step 0.0031 for 11 measurements for AOA with fading

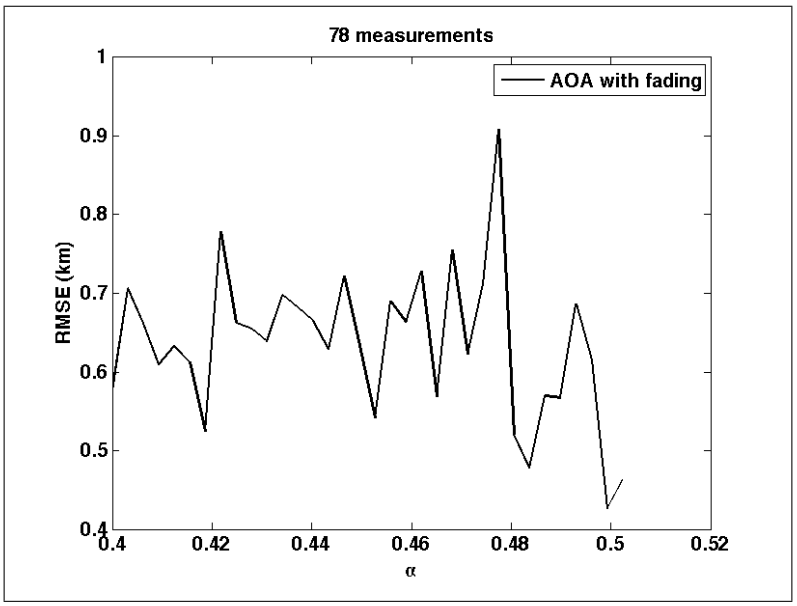

Figure 6.20: RMS error of the generalised estimator with α zoomed in the area of 0.4 till 0.6 with step 0.0031 for 78 measurements for AOA with fading

to be Gaussian and then was tested on Gaussian, Rayleigh and Uniform modelled measurement's noise with additional test using AOA with fading. Measurement's noise may be unknown and may not be Gaussian in practical scenario, thus these tests have a vital practical importance for the application of geolocation.

In this tests $\alpha = 0.5$, which is equivalent of Hough Transform, proved to be fairly robust in terms of sustainability to changing model of the measurements noise. Near Bayesian for $\alpha \in (0 \ldots 0.1)$ proved, as expected, provided higher accuracy in pres-

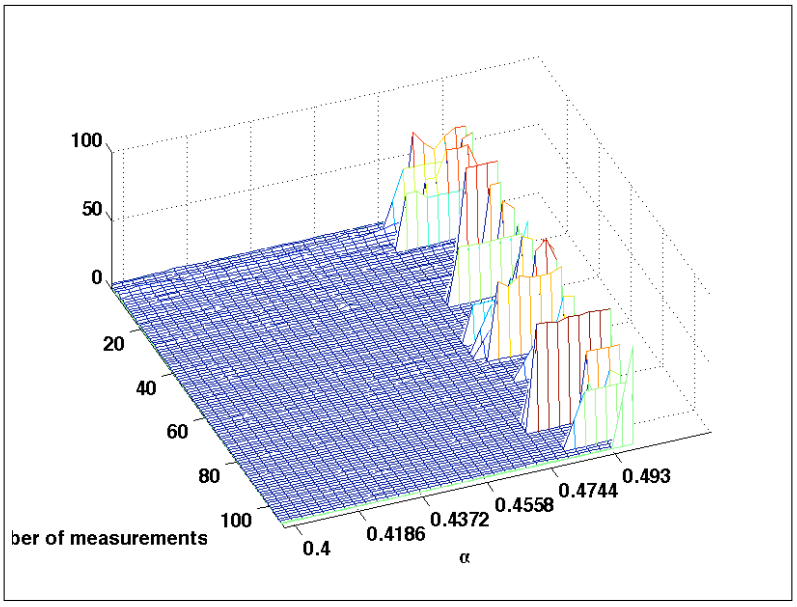

Figure 6.21: 3d plot RMS with relation to α value from 0.4 till 0.5 with number of measurements from 2 till 110 for AOA with fading. Note that the plot is rotated

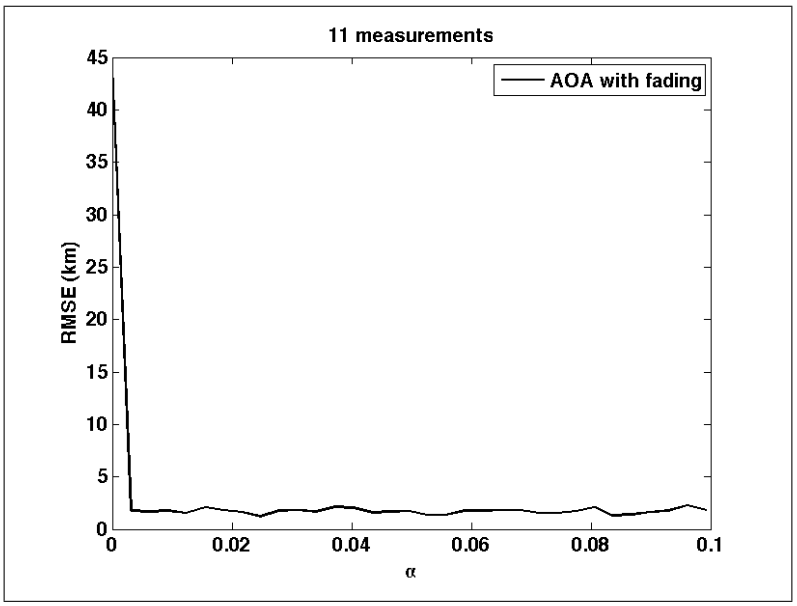

Figure 6.22: RMS error of generalised estimator zoomed around $\alpha \in [0 \ldots 0.1]$ for 11 measurements with AOA measurements in fading conditions

ence of Gaussian measurement's noise. Note that although scenario for generalised estimator Bayesian estimator with $\alpha = 0$ uses only AOA measurements, thus can't be compared directly with particle filter in section 5.6.

It was proposed $\alpha = 0.25$ may be good estimator which performs better then Hough Transform based estimator in presence of measurement noise such as simulated faded AOA, however it should be noted that this will increase the complexity of the estimating algorithm.

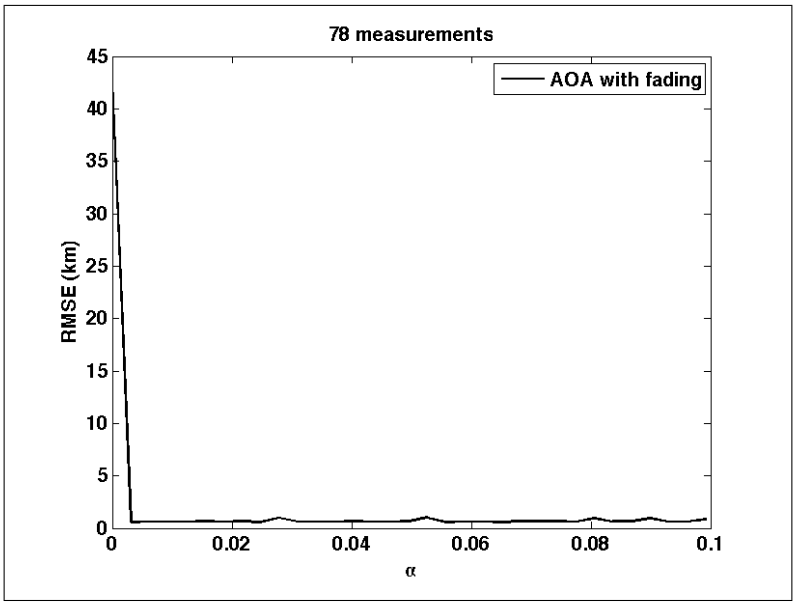

Figure 6.23: RMS error of generalised estimator zoomed around $\alpha \in [0 \dots 0.1]$ for 78 measurements with AOA measurements in fading conditions

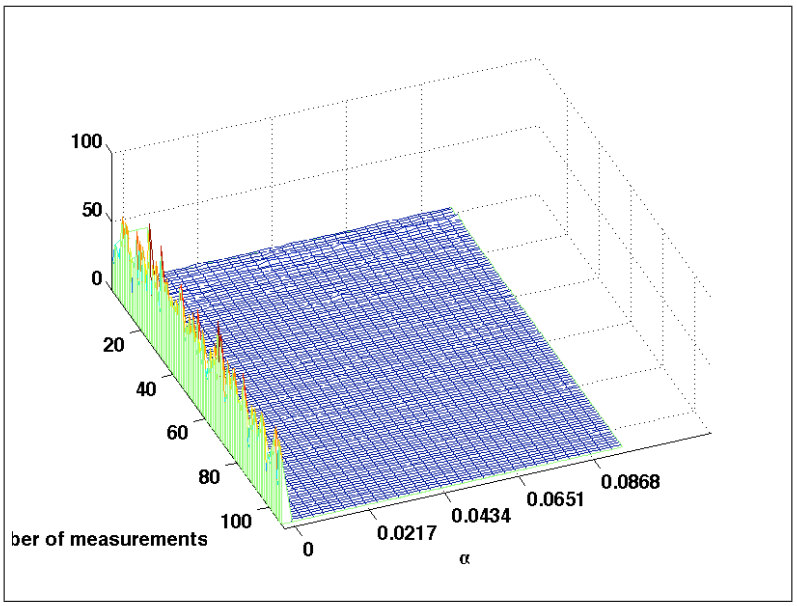

Figure 6.24: 3d plot RMS with relation of α value from 0 till 0.1 with number of measurements from 2 till 110 with AOA measurements in fading conditions

Hough transform equivalent to $\alpha = 0.5$, while not being able to provide the best results during model mismatch test, still was able to locate target with reasonable accuracy. One should keep in mind that Hough Transform estimator is a sum of likelihoods, and as such can be easily programmed or optimised into hardware, while Generalised estimator with $\alpha = 0.25$ will require approximately 4 times more computational operations, so there is a trade-of between simplicity which should be considered in practice. Furthermore, it has been shown that a connection exists between the Hough Transform and Gaussian Mixture model based estimation. How-

ever, further research is required in order to apply the Gaussian Mixture model for the problem of emitter location. Very recent development of the geolocation using Gaussian Mixture model using TDOA and FDOA has been presented in [91]. GMM has also been used as for speaker identification and tracking for example in [92] and [93].

6.5 Generalized Mean estimator

In the previous section, the generalized estimator was derived on basis of mixture of probabilities and tested in order to find an optimal solution for geolocation problem. In this section another approach has been taken in order to derive and test the different functions for building a parameterized space - a generalized mean.

The question remains the same, however: is there a better function for the geolocation estimation that can be used for building a parameterized space, rather then simply using either the sum of likelihoods as in Hough Transform or the product of likelihoods as in the Baysian estimator.

The common definition of the Generalized Mean is given by:

Definition Let $x_1, x_2, \ldots, x_n$ be real numbers, and f a continuous and strictly increasing or decreasing function of the real numbers. If each number x_i is assigned a weight p_i, with $\sum_{i=1}^{n} p_i = 1$, for $i = 1, \ldots, n$, then the *generalized mean* is defined as

$$M_f(x_1, \ldots, x_n) = f^{-1}\Big(\sum_{i=1}^{n} p_i f(x_i)\Big). \tag{6.5}$$

Special cases

1. $f(x) = x$, $p_i = 1/n$ for all i: arithmetic mean, with $i = 1, 2$ then $M_a = \frac{x_1+x_2}{2}$.
2. $f(x) = x$: $p_i = 1$ for all i weighted mean with $i = 1, 2$ then $M_w = x_1 + x_2$, although it would seem that it can be called not normalised mean, as the weights proportional to x itself.
3. $f(x) = \log(x)$, $p_i = 1/n$ for all i: geometric mean, with $i = 1, 2$ then $M_g = \exp^{\frac{log(x_1)+log(x_2)}{2}}$
4. $f(x) = 1/x$ and $p_i = 1/n$ for all i: harmonic mean, with $i = 1, 2$ $M_h = \frac{2}{\frac{1}{x_1}+\frac{1}{x_2}}$
5. $f(x) = x^2$ and $p_i = 1/n$ for all i: root-mean-square, Euclidian mean, also known as quadratic mean, with $i = 1, 2$ then $M_{rms} = \sqrt{\frac{x_1^2+x^2}{2}}$
6. $f(x) = x^d$ and $p_i = 1/n$ for all i: power mean, with $i = 1, 2$ and $d = 3$ then $M_p = (\frac{x_1^3+x_2^3}{2})^{\frac{1}{3}}$, also there are two special cases for power mean, where $p = \inf$, called maximum mean and calculated as maximum value from x, and minimum (non-parametric mean) with $p = -\inf$, calculated as minimum from all values of x (as [85]).
7. $f(x) = x^d$ and $p_i = 1/n$ for all i: weighted power mean, with $i = 1, 2$ then $M_p = (\frac{x_1^3+x_2^3}{2})^{\frac{1}{3}}$

Also it is possible to use any continuous and strictly increasing function as a mean, for example hyperbolic tangent tanh will be used for the simulations as well as

special cases mentioned above. as the only properties required for the function to be used as mean function are (i)it should be continuos,(ii) injective (in order for inverse to exist). Then hyperbolic tangence mean will be:

$$M_{\tanh} = atanh\frac{\tanh(x_1) + \tanh(x_2)}{2} \tag{6.6}$$

Now, assuming that the x from the generalized mean is a likelihood of the probability definition function given the measurement, it is possible to use the generalized mean defined earlier in order to build a parameterized space as in 4.5 and the previous section 6.1 given by (6.7):

$$A_{AOA}(x, y) = M_f(x_1, \ldots, x_n) \tag{6.7}$$

where x_i is a likelihood of the probability definition function as defined by (4.4).

It is worth mentioning, that there has been a recent development in data fusion by Simon Julier where he uses the weighted geometric mean for data fusion in his presentation 'Estimation without Independence' [94], so it is of the interest of research to compare the different means as a fusion function for the purpose of geolocation.

6.5.1 Application of the generalized mean to geolocation

In order to present generalised mean functions in application for geolocation, the same simple scenario similar to one in section 6.1 was set up, with two receivers obtaining AOA measurements from one stationary target plotted in figure 6.25. Both AOA measurements are affected by Gaussian noise. The maximum in the parameterized space was obtained and this was assumed to provide a position estimate of the target as before. This simple scenario used only for illustrative purpose. The examples of the parameterized space, built for these two AOA measurements can be seen in figures 6.26-6.36. It will be noted that the Hough Transform can be viewed as the use of the arithmetic mean, or, if Hough Transformed is not normalised by the number of measurements, it can be seen as a weighted arithmetic mean. The Bayesian condition probability can be seen as the Geometric mean. Some special cases, like the geometric and harmonic mean require a check for a non-zero value of the probability.

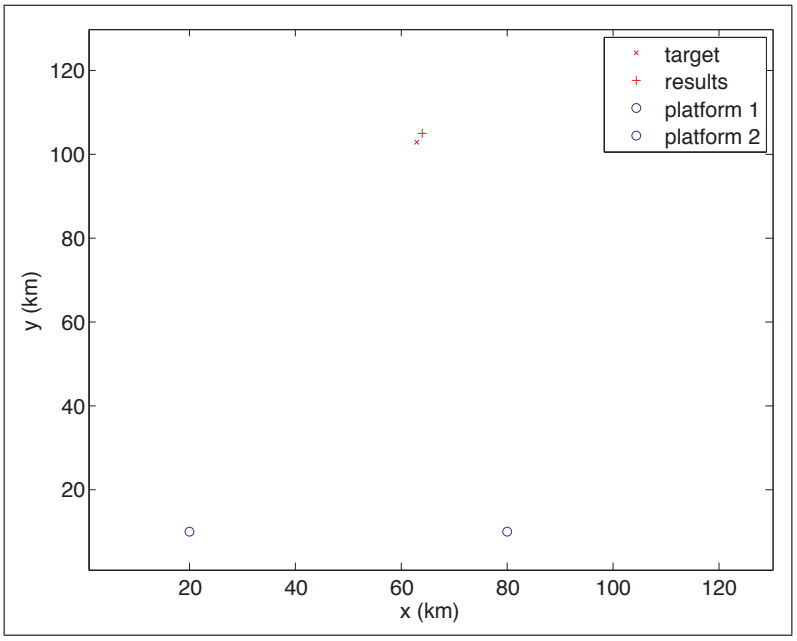

Figure 6.25: Scenario for geolocation using Generalized Mean

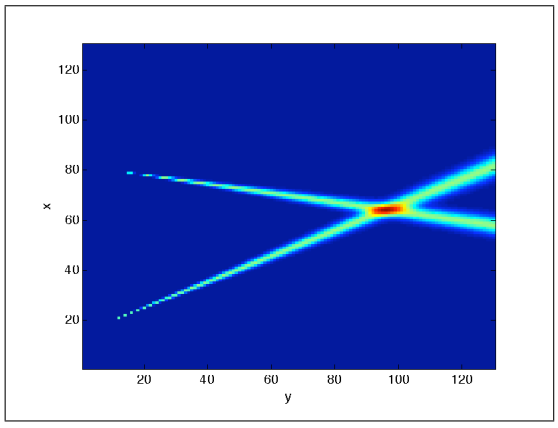

Figure 6.26: 2-D parameterised space for geolocation using arithmetic mean

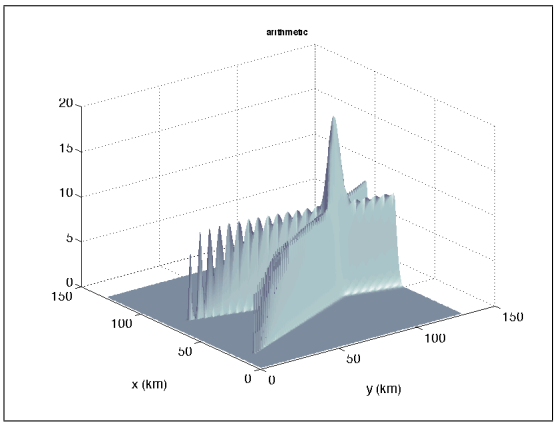

Figure 6.27: 3-D parameterised space for geolocation using arithmetic mean

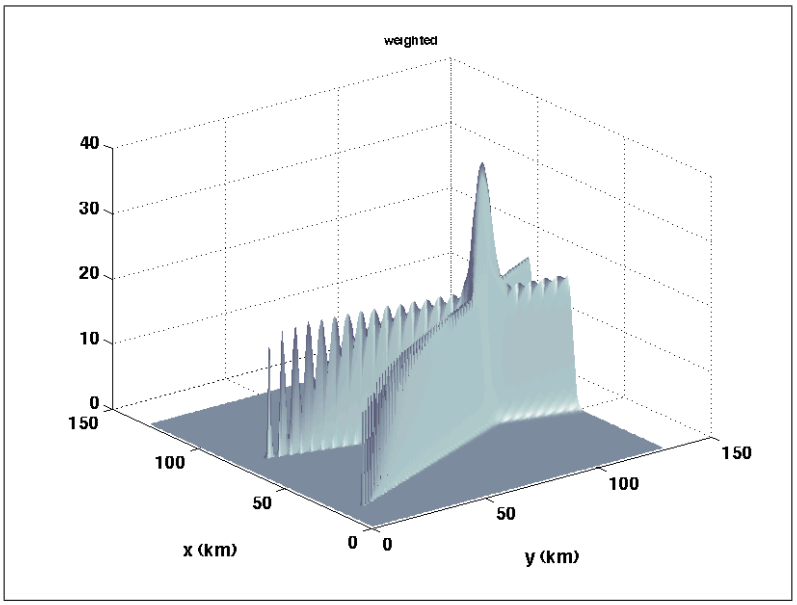

Figure 6.28: 3-D parameterised space for geolocation weighted arithmetic mean

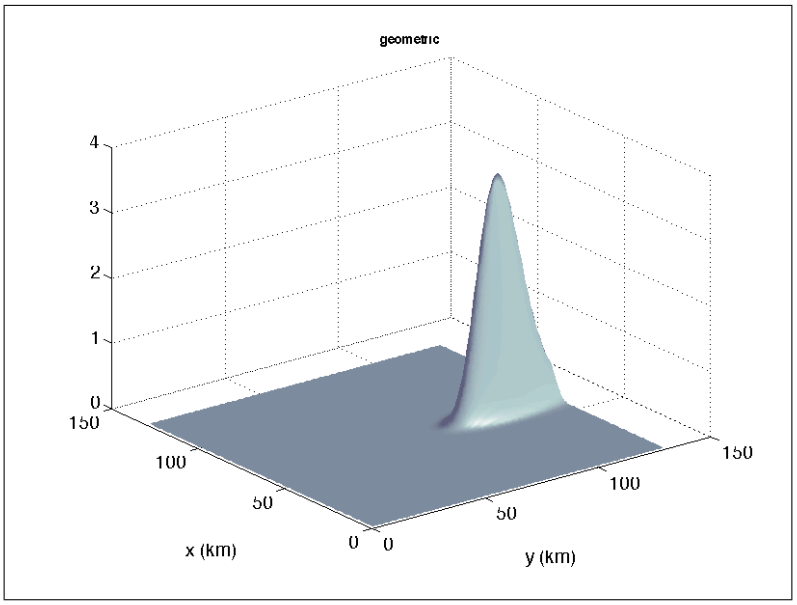

Figure 6.29: 3-D parameterised space for geolocation using geometric mean

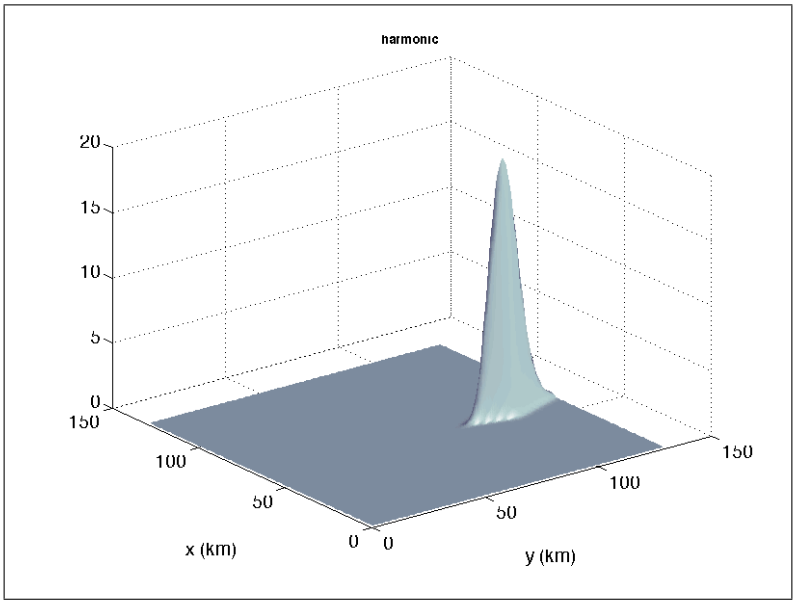

Figure 6.30: 3-D parameterised space for geolocation using harmonic mean

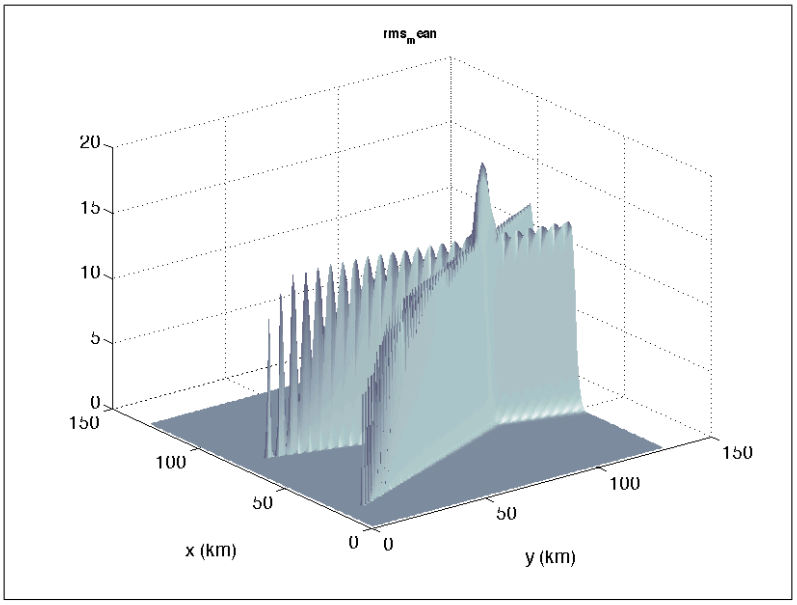

Figure 6.31: 3-D parameterised space for geolocation using root mean square (also known as Euclidian mean and quadratic mean)

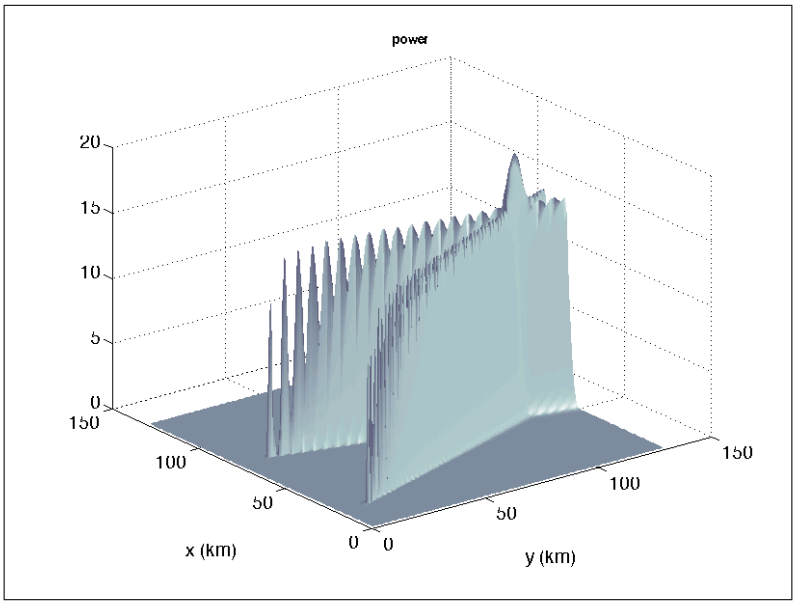

Figure 6.32: 3-D parameterised space for geolocation using power mean with $p = 3$

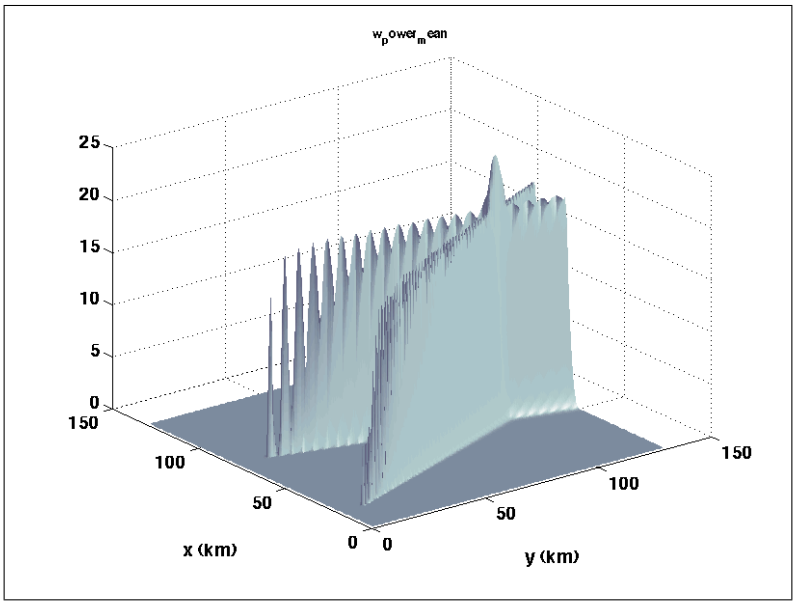

Figure 6.33: 3-D parameterised space for geolocation using weighted power mean with $p = 3$

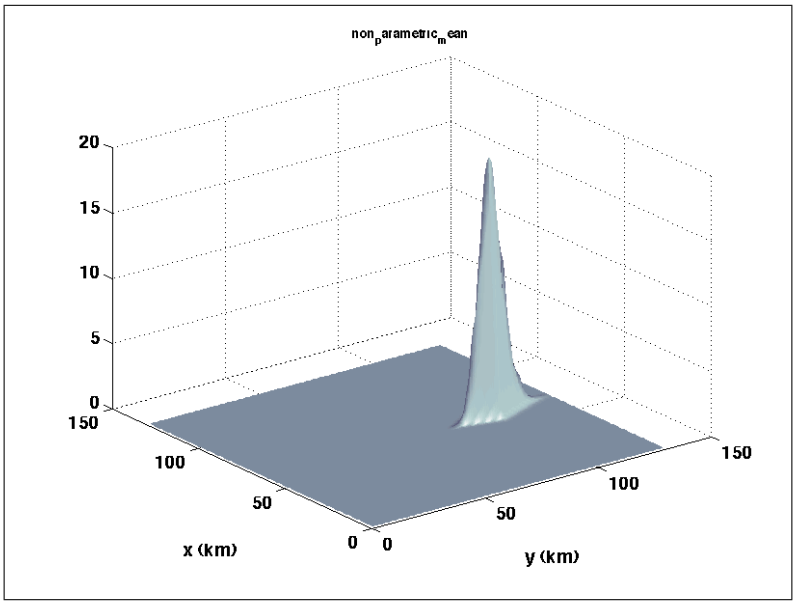

Figure 6.34: 3-D parameterised space for geolocation using non-parametric mean, power mean with $p = -\infty$

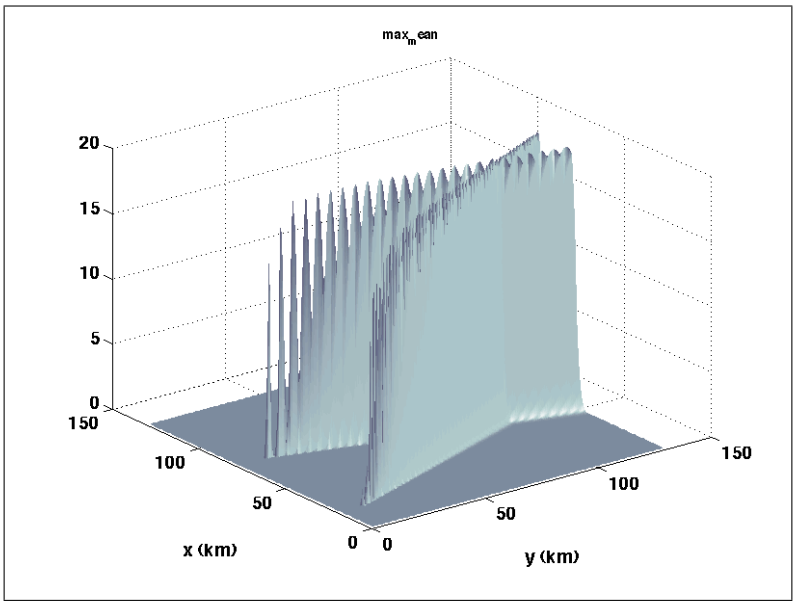

Figure 6.35: 3-D parameterised space for geolocation using power mean with $p = \infty$

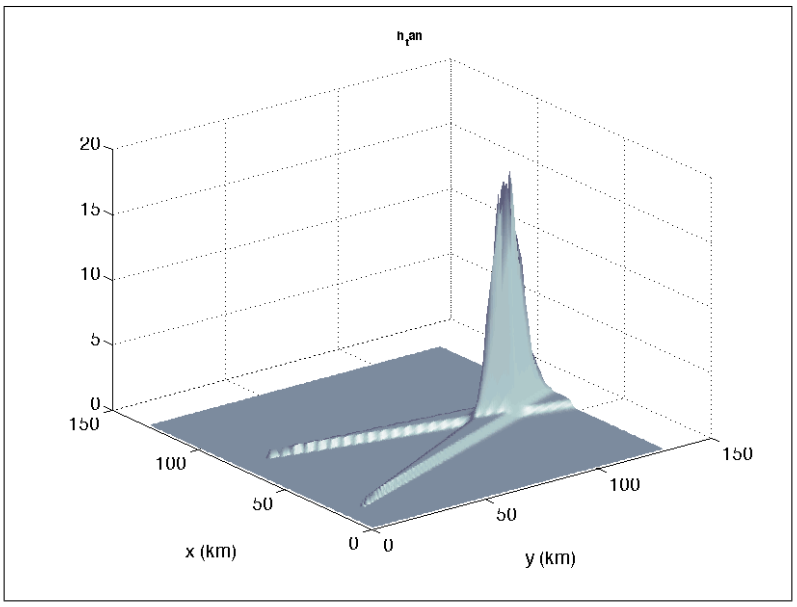

Figure 6.36: 3-D parameterised space for geolocation using hyperbolic tangent, $f = \tanh$

In order to test the fusion capabilities of the proposed functions, the scenario was changed to the common comparison scenario 5.16. Only AOA measurements used, due to the absence of normalisation in Generalised mean functions. The results of the application of Generalized mean functions to (6.7) for the scenario in figure 5.16 using only two AOA measurements, with a root mean square error as metric against number of measurements are presented in figures 6.37 6.46. Note that the same data were used for model mismatch as in section 5.6 for testing model mismatch performance.

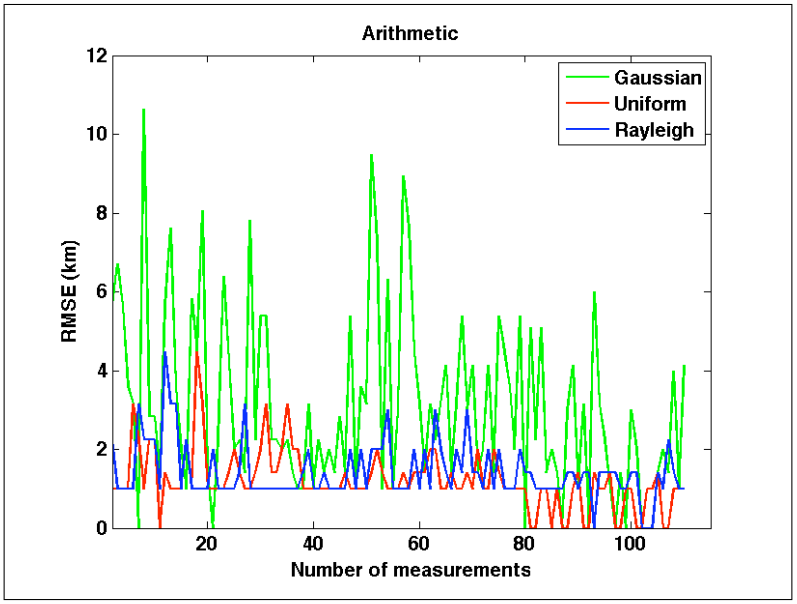

Figure 6.37: RMS error over number of measurements using arithmetic mean in generalised estimator, averaged over 12 simulations

Exploring figures 6.37 6.46 it is possible to see that arithmetic mean in figure 6.37 (Hough transform equivalent) and geometric mean 6.39 (Bayesian equivalent) are good estimators, with weighted arithmetic mean 6.38 as equivalent of non-normalised Hough Transform are performing well in presence of the model mismatch noise. There are several candidate functions with reasonable performance such as hyperbolic tangence based estimator in figure 6.44 and harmonic mean in figure 6.40. Also power mean in figure 6.42 and RMS (Euclidian) mean in figure 6.41 demonstrated interesting performance in presence of uniform or Rayleigh noise. Non parametric mean 6.45 and power mean with $p = \infty$ didn't performed as estimators. Figure 6.38 dominates the generalised mean based estimators as in presence of uniform noise RMS is a flat like on zero and produce good results in presence of Rayleigh and Gaussian measurements noise. However, the application of the weighted arithmetic mean to data fusion between different types of measurement will lead to the problem that due to the fact that the values in parameterised space are not normalised, it will be difficult to fuse different types of measurements together. Fusion of the different type of measurements using Hough Transform is one of the main points of the next chapter.

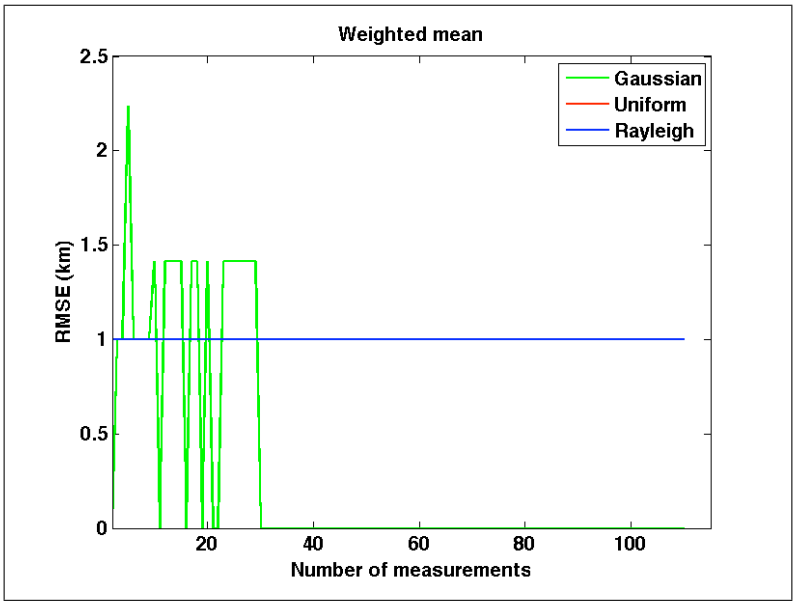

Figure 6.38: RMS error over number of measurements using weighted mean in generalised estimator, averaged over 12 simulations. RMS error for uniform distribution is zero

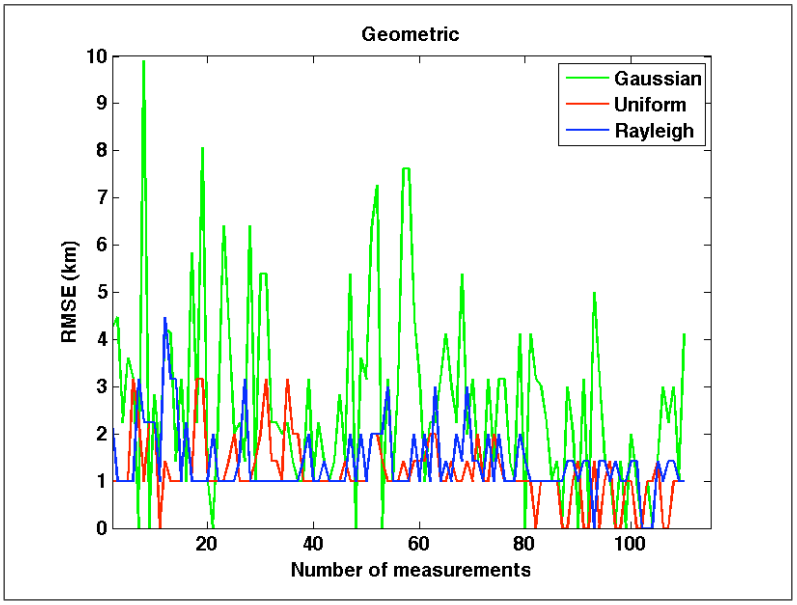

Figure 6.39: RMS error over number of measurements using geometric mean in generalised estimator, averaged over 12 simulations

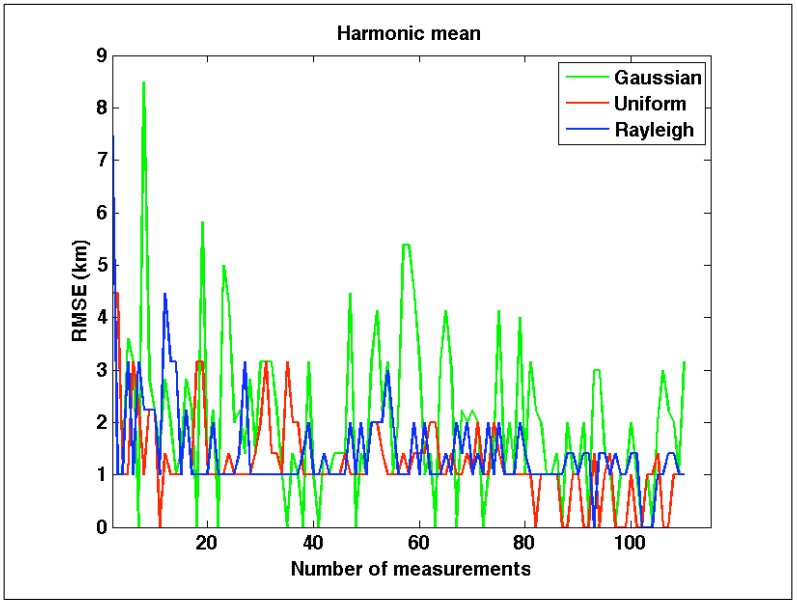

Figure 6.40: RMS error over number of measurements using harmonic mean in generalised estimator, averaged over 12 simulations

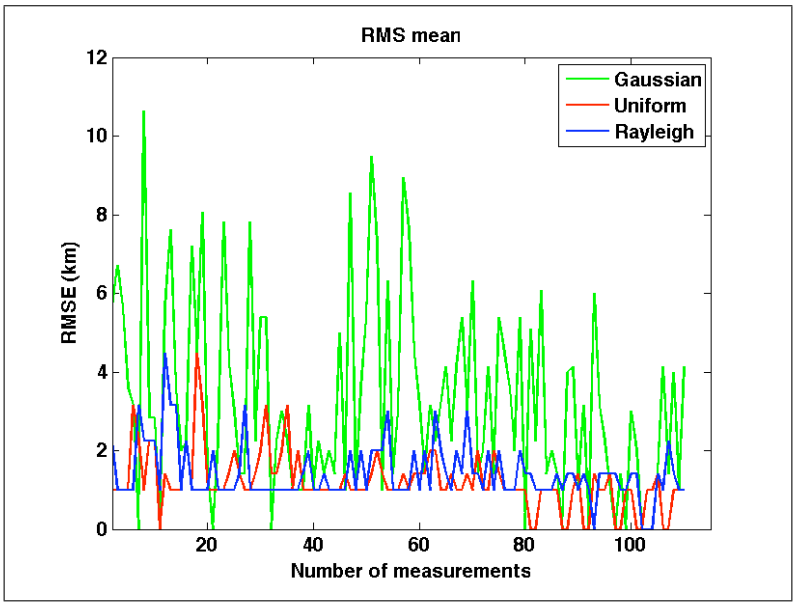

Figure 6.41: RMS error over number of measurements using root-mean square mean in generalised estimator, averaged over 12 simulations

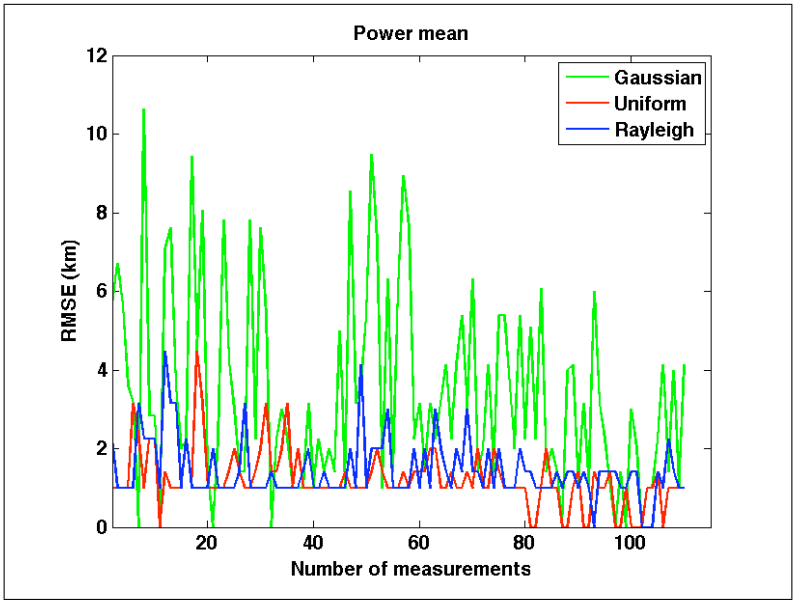

Figure 6.42: RMS error over number of measurements using power mean $p = 3$ in generalised estimator

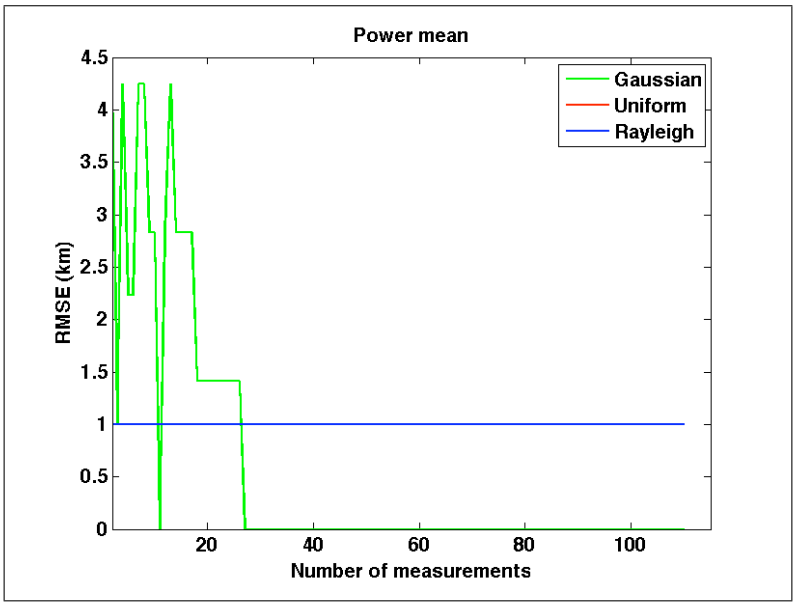

Figure 6.43: RMS error over number of measurements using weighted power mean with $p = 3$ in generalised estimator, average over 12 simulations

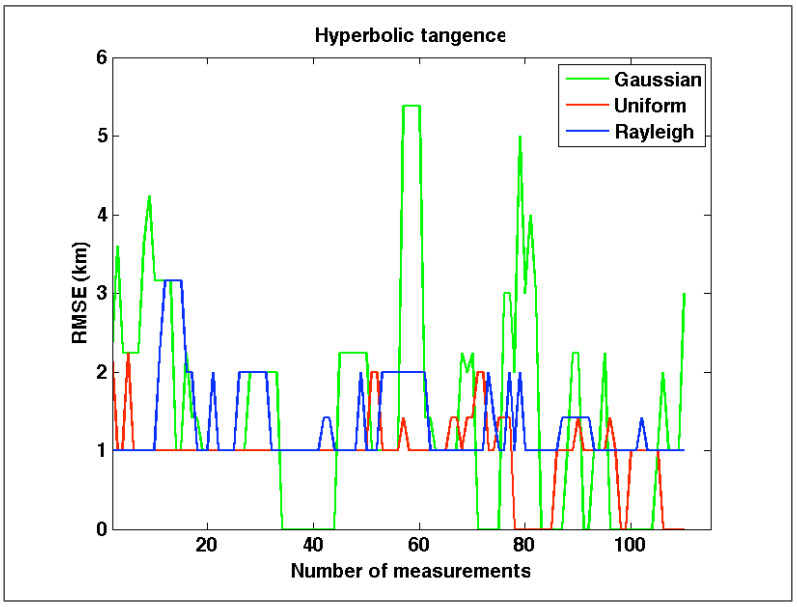

Figure 6.44: RMS error over number of measurements using hyperbolic tangence in generalised estimator, averaged over 12 sumulations

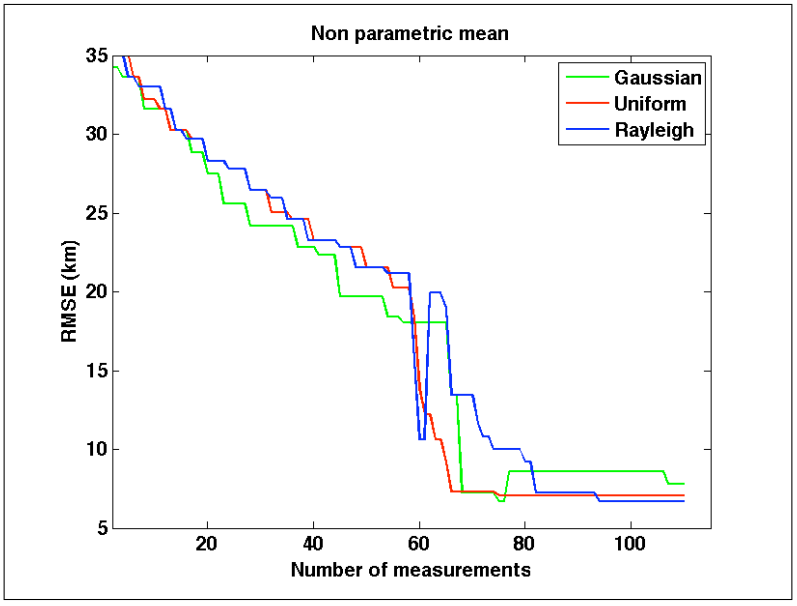

Figure 6.45: RMS error over number of measurements using non parametric mean ($p = -\infty$) in generalised estimator, averaged over 12 simulations

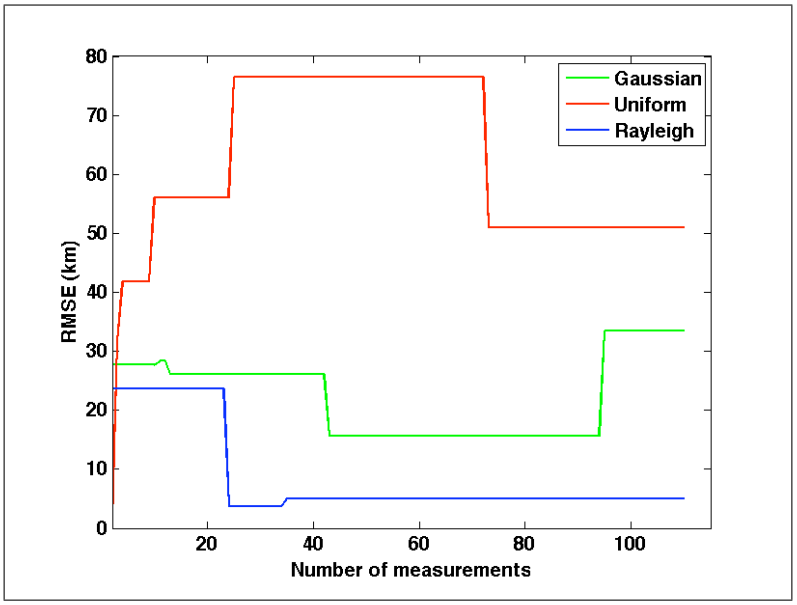

Figure 6.46: RMS error over number of measurements using power mean with $p = \infty$ in generalised estimator, averaged over 12 simulations

Chapter 7

Agent-Based Data fusion

7.1 Introduction

In chapter 4 a new method of emitter geolocation was presented based on a image processing technique rather then the more usual classical methods based on triangulation and hyperbolic location [10] or statistical methods [23][32][95]. The new method is based on the Generalized Hough Transform (GHT) and one of its key features is that it is able to fuse different types of measurement data (such as angle of arrival measurements (AOA) and time difference of arrival measurements (TDOA)) by transforming them into conditional probabilities and storing them in a unified parameterized space. In this chapter, the Hough Transform algorithm is improved by weighting the data appropriately and a novel method of providing the weights is presented. Then the concept of an agent will be introduced followed by the application of the weighted Hough Transform for geolocation using agents. The final part of this chapter will demonstrate cluster level fusion of information and a decision making process for the agents.

7.2 A Method of Weighted Fusion

When fusing different measurement types, it is usual to weight the individual contributions of the measurements according to their measurement error [32]. However, for emitter geolocation, the problem is extremely non-linear and the effect of the measurement errors on the position error is augmented by the GDOP for that emitter/sensor platform scenario. It is important to recognise that each type of measurement (AOA, TDOA and FDOA) provide their own, different, contributions to the GDOP and simply weighting according to measurement error does not represent the true impact of the error on the positional accuracy of the emitter position estimate. It is also important to note, that in practical applications some sensors can be damaged, or obstructed by obstacles and thus provide unreliable estimate. The contribution of such sensor can improve overall estimate, however if such measurement added and fused with other, more reliable measurements according to the

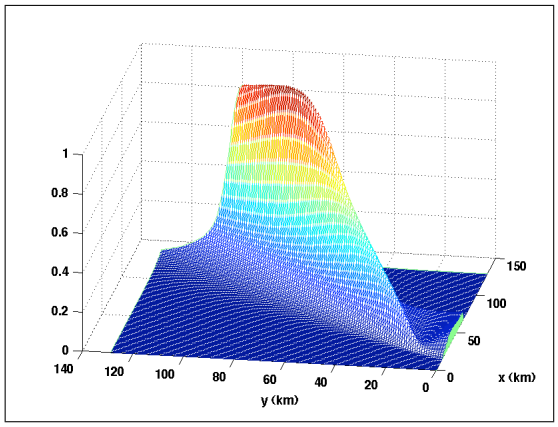

Figure 7.1: Hough Transform space for TDOA only measurements (TDOA agent)

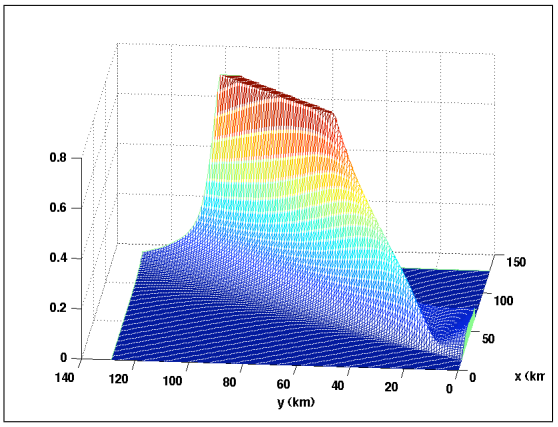

Figure 7.2: Hough Transform space for TDOA only measurements, thresholded at a level corresponding to 75% of the maximum likelihood value

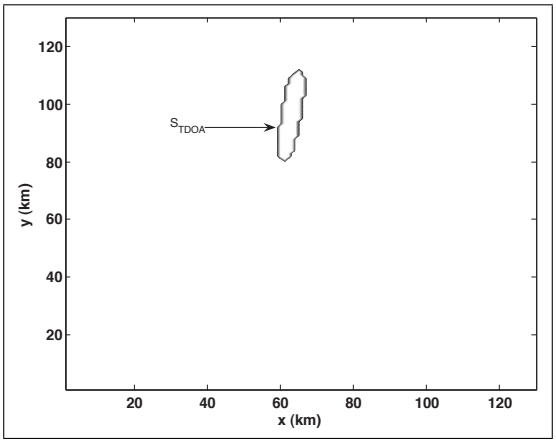

Figure 7.3: Plot of the 75% contour of (4.13) for TDOA set at a threshold of 75% of the maximum likelihood value

measurement error and GDOP it can worsened the estimate.

A novel form of obtaining the weights has been proposed in this research, where the aim is to compensate for the different contributions to the emitter position error from each of the different measurement types according to their GDOP and their contributions to the estimate, for that scenario.

In this case, the accumulated pdf for a particular measurement type, such as TDOA, given by (4.13) is first normalized by its peak value (pictured in figure 7.1) and then thresholded at some appropriate value to create a contour at that threshold, as shown in figures 7.2-7.3 for a threshold set at 75% of the maximum. Threshold selection at a level of 75% was using the properties of the Hough Transform, demonstrated in section 6.2, with an assumption that 95 % area is too small and 50 % area too large to provide a weighting criteria. The area contained within this contour, S_{TDOA}, is then obtained. This is repeated for the case of the AOA measurements whose accumulated pdf is given by (4.5) and the FDOA measurements whose accumulated pdf is given by (4.18). The areas contained within the

respective contours are: S_{AOA} and S_{FDOA}. It is clear that the larger the area of the contour, the greater the contribution of these measurements to the positional error and hence a smaller weight is required. It can also be seen that these contours contain the effect of GDOP as well as the measurement error. Hence the weights are given by:

$$w_{AOA} = \frac{S_{tot}}{S_{AOA}} \tag{7.1}$$

$$w_{TDOA} = \frac{S_{tot}}{S_{TDOA}} \tag{7.2}$$

$$w_{FDOA} = \frac{S_{tot}}{S_{FDOA}} \tag{7.3}$$

where S_{tot} is the area of the total search space. Now it is possible to fuse different kind of the measurements, weighting them during the process:

$$\begin{aligned} A(x,y) \quad = \quad & \frac{w_{TDOA}}{L}\sum_{l=1}^{L} p(x,y|\tau_{l,1}) + \\ & \frac{w_{AOA}}{M}\sum_{m=1}^{M} p(x,y|\theta_m) + \\ & \frac{w_{FDOA}}{N}\sum_{m=1}^{N} p(x,y|f_{d_i}) \end{aligned} \tag{7.4}$$

where, w_{TDOA}, w_{AOA} and w_{FDOA} are the weights for the three types of measurement which are calculated according to the impact that both the measurement variance *and* GDOP has on them. It can be seen that this approach provides the opportunity to self-weight the measurements. This is the key requirements for agent-based data fusion.

7.2.1 Definition of agents

What are Agents?

Agent-based systems are of increasing importance in a wide range of spheres. They are regarded as a new paradigm enabling an important step forward in empirical sciences, technology and theory. Recently, this topic has become applicable to modern wireless network simulation. An agent is characterized by some, or all, of the following properties [96]:

- *Autonomous Behaviour*: Every agent is characterised by autonomous behaviour.
- *Individual World View*: Every agent has its own model of the external world that surrounds it which maybe incomplete or even incorrect.

- *Communicative and Cooperative Capacity*: Intelligent agents can exchange information with other intelligent agents and this is how it builds up its own world model. Communication with other intelligent agents is the precondition for common action in pursuit of a goal.
- *Intelligent Behaviour*: Intelligent Agents have the capacity to learn, make logical deductions to modify their own world model in the light of new information that is supplied to it, or which it obtains from the environment
- *Spatial mobility*: Intelligent agents are required to display spatial mobility.
- *Strategies and Decentralised Control*: Agents should be able to develop individual strategies to ensure the achievement of a common goal, even without central regulation.
- *Emergent Behaviour*: Cooperation (feedback) and interactions between intelligent agents can produce a stable system that displays new global behaviour on the next higher level of abstraction.

For this research it is possible to use agents as a model for simulating *ad-hoc* networks in difficult terrains. This model will allow us to simulate agents behaviour, their agenda and, most important, their communicative and cooperative capacities.

In the context of the emitter location problem, the agent comprises the measurements, communications between the two platforms and a suitable algorithm rather than the sensor platform. For example, two platforms are necessary to take a TDOA measurement and this corresponds to a single agent capable of geolocating using TDOA measurements. The same pair of platforms may, independently, make a frequency difference of arrival (FDOA) measurement and this will correspond to a second agent capable of geolocating using FDOA measurements. A platform may be able to make bearing only measurements and this produces an agent that geolocates using AOA.

7.3 Agent-based Data Fusion

As mentioned earlier, it is the *type* of measurement taken, is assumed to be an agent rather than the sensor platform. For example, two platforms may be able to take both TDOA measurements and FDOA measurements and this corresponds to the case where there are two agents: one capable of geolocating using TDOA measurement and one capable of geolocating from FDOA measurements. A third agent geolocates using AOA. It will be shown how these agents can geolocate independently and collaboratively.

In order to illustrate the new method, consider the scenario shown in figure 7.4. In this scenario, two platforms are moving North at 40 m/s according to a wavy path and they are able to take several TDOA measurements (Agent 1) along this path, whereas the platform moving East at 40 m/s is only able to take AOA

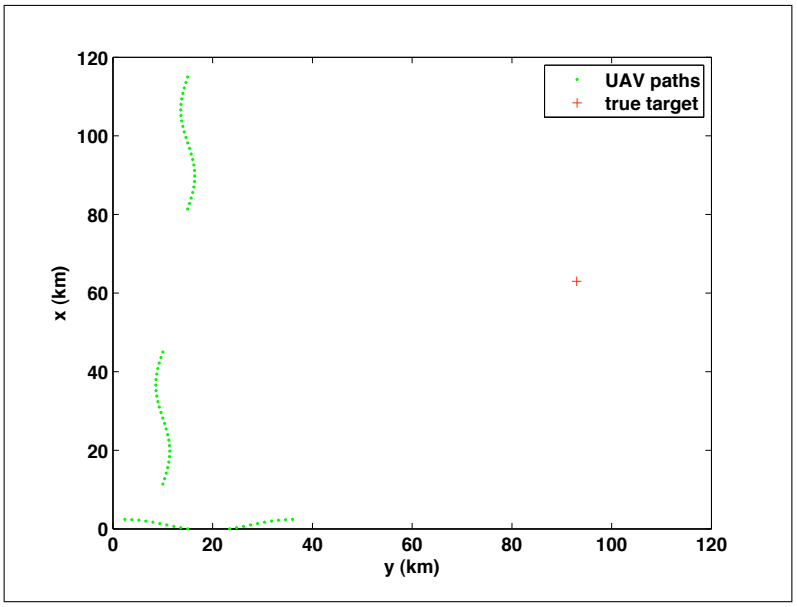

Figure 7.4: Scenario used for agent-based emitter geolocation, showing the flight paths of the different sensor platforms

measurements (Agent 2). The standard deviation of the TDOA measurement error as used in section 4.3.1, in this simulation is defined by:

$$\sigma_{TDOA} \approx \frac{1}{W\sqrt{\text{SNR}}} \tag{7.5}$$

where W is the noise bandwidth of the receiver set at 7×10^{-7}s. The standard deviation of the AOA error is given by:

$$\sigma_{\theta}^{2} \geq \left(\frac{c}{2\pi f_0 d\cos(\theta)}\right)^{2}\left(\frac{1}{SNR}\right) \tag{7.6}$$

if $\theta < \pi/2$ or $\sigma_\theta = 0.02$ otherwise, where f_0 is the carrier frequency of the received signal, d is the maximum separation between antenna elements of interferometer antennas, and θ is the true bearing angle.

The true target position is at (92km,62km). Each measurement is taken on 10th second corresponding to 0.4 km step in simulation. Figure 7.5 shows how each agent can geolocate the emitter independently using the average RMS position error as a metric. In particular, the figure shows the effect of the number of measurements on the the average RMS error as the platforms move along their respective flight paths. In order to obtain the average RMS error the simulations were repeated 50 times and the average taken. It is clear for this scenario that TDOA measurements generally provide a more accurate position estimate.

Figure 7.5 shows how accurately each agent can independently geolocate the emitter using the average RMS position error as a metric. In this figure, the average RMS error is plotted as a function of the TDOA and AOA measurements taken as the platforms move along their respective flight paths. In order to obtain the

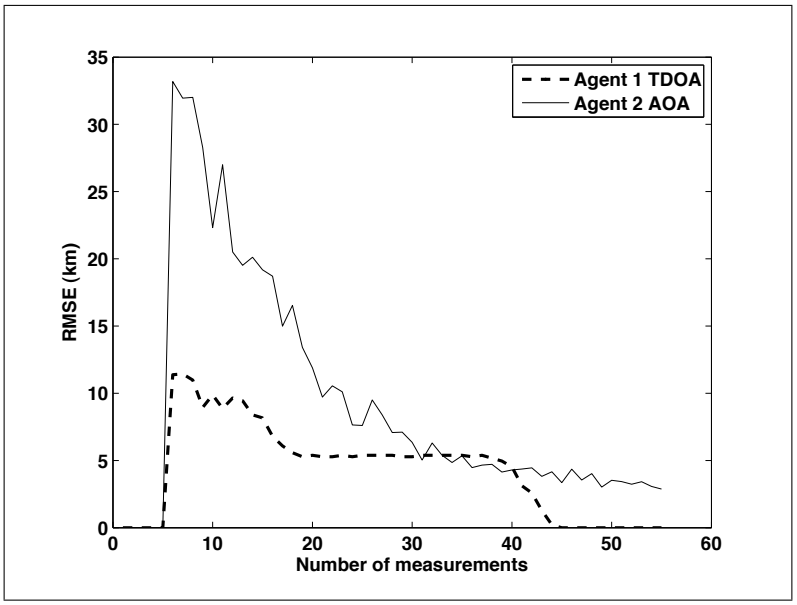

Figure 7.5: Effect of number of measurements on the average RMS positional error. In this case each agent separately geolocates. Agent 1 uses TDOA only, Agent 2 uses AOA only

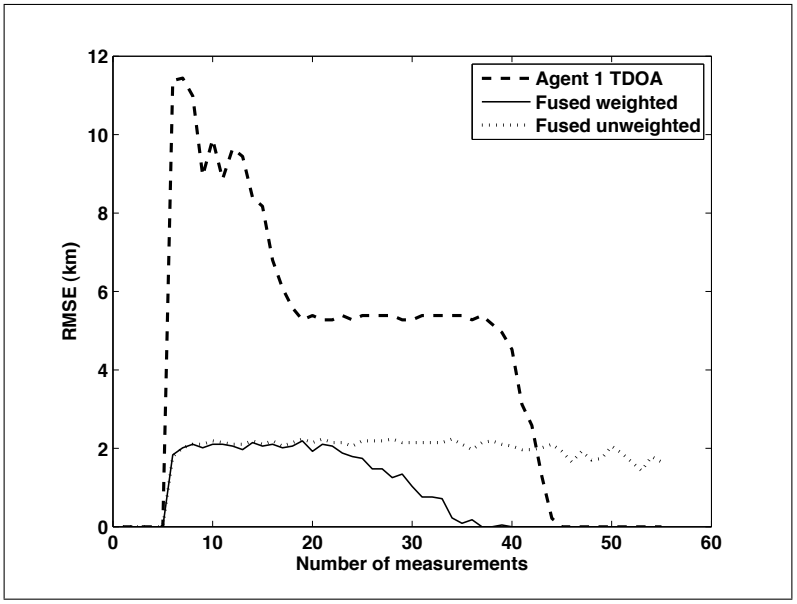

Figure 7.6: Effect of number of measurements on the average RMS positional error, showing effect of both unweighted and weighted fusion

average RMS error the simulations were repeated 50 times and the average taken. It is clear for this scenario that TDOA measurements generally provide a more accurate position estimate. However, it should be noted that the precise results of RMS position error are strongly dependent upon the platform/emitter geometry, and hence the scenario, because this affects the GDOP. This is true for all the results presented in this section.

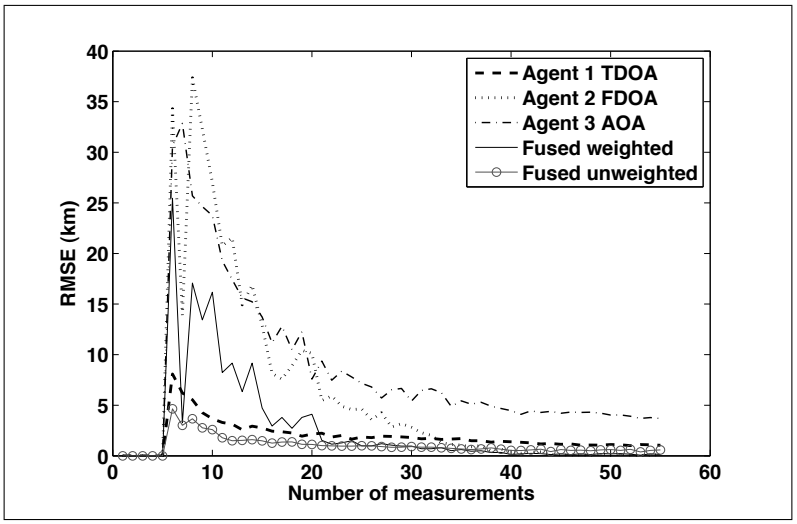

Figure 7.7: Effect of number of measurements on the average RMS positional error, showing effect of both unweighted and weighted fusion for AOA, TDOA and FDOA Measurements

Figure 7.6 shows the benefit of fusing the TDOA and AOA measurements for both weighted and unweighted cases and the results are compared with the case for TDOA-only emitter geolocation for the scenario above. In this figure, the average RMS error using AOA-only measurements (Agent 2) was not plotted in order to demonstrate the advantage of weighting, however the contribution from these agent was used in fusion calculations. Two observations can be made. First, fusion of the measurements improves the positional accuracy of the geolocation algorithm. Second, the impact of weighting is also clear because the weighted result tends to be much more accurate in terms of RMSE as after > 25 measurements. There is an observation that for this particular scenario TDOA only measurements without fusion presents better results, so fusion algorithm does not provide any benefit. The information that TDOA only measurements will provide better estimate is not available *a priori* and dependent on relative target and platform positions. As it was demonstrated in earlier chapters, the estimator is usually benefit from fusion in terms of better convergence and accuracy on average for a larger number of scenarios. In this scenario unweighted fusion remained close to the best available measurement in this case TDOA and didn't improved when position AOA agent changed significantly enough to improve estimate, while weighted fusion attempted to take best contribution out of both type of measurements.

The scenario in figure 7.4 was altered in a way, that the platforms travelling North are now able to perform TDOA and FDOA measurements so that the model consist of TDOA agents, FDOA agents and AOA agents. Figure 7.7 demonstrates the results of fusion for all three types of measurement, using the RMS positional error as the metric. This figure shows quite clearly how both weighted and unweighted fusion improves the positional accuracy of the emitter location estimate when additional measurements from FDOA agent are made. The advantages of the weighted fusion can not be observed in this particular case, on contrary, an attempt of weighted

fusion to TDOA and FDOA type of measurements as more precise estimates lead to much worse estimates when number of measurements were relatively low.

In this section it was shown that the Hough Transform has properties that can be exploited which allow it to be used as a framework for agent-based fusion, thus connecting low level measurement fusion to higher more 'abstract', levels, that can be used for decision making. Furthermore, using the method of self- weighting, it is possible to provide each geolocation agent with a method to calculate their own contribution to the final goal of emitter geolocation; In this section, all agents were constrained to operate within a single cluster, due to restrictions placed on the information exchange by the wireless communication network they shared. In the next section the concept of agents will be taken one step further where agents naturally form multiple clusters.

7.4 Clustered agent data fusion

In this section each cluster is assumed to consist of multiple agents where communications assumed to be good. However, communications between clusters is assumed to exist but may be sporadic. This creates a fusion hierarchy: each agent is able to geolocate individually, a cluster of agents can refine the emitter position using fusion and clusters of agents can further refine the position estimate by taking advantage of the different view of the target by each cluster. In this section, the benefits of providing fusion between clusters of agents will be examined.

In this case, the Agents within each cluster generate a cluster-level model for that cluster and this is used to obtain the weight, $w_{cluster_i}$ for that cluster (assumed here to be the ith). These weights are used to weight the cluster-level models. The overall model is the weighted combination of cluster-level models, given by:

$$A_{multi} = \frac{1}{w_{cluster_1}} A_{cluster_1} + \cdots \frac{1}{w_{cluster_i}} A_{cluster_i} \tag{7.7}$$

The scenario in figure 7.8 has been set up in order to illustrate this. Here, three UAVs are used, as in the previous scenario, and form cluster 1. In this cluster, two UAVs fly North and follow a wavy path, whilst one UAV flies East. The North flying UAVs act as a TDOA agent and the East flying UAV acts as an AOA agent. In addition, three more UAVs are added to the scenario. One flies in a tight circular path, a second flies in an oval racetrack path whilst the third flies generally in an Easterly direction. The UAV flying along the oval path takes AOA measurements, with an RMS error using equation 7.6 whilst the other two platforms act as a TDOA agent with an RMS error of 10^{-7}s timing error. Each cluster has good communications so that agents within that cluster can fuse their results as described above. However, communications between clusters is sporadic. This means that each cluster carries out individual cluster-level fusion, and the clusters can only fuse their cluster levels together when the communications between them is assumed to be good.

Figure 7.9 and figure 7.10 show the effect of using two clusters to geolocate a single emitter. Figure 7.9 represents the RMS error of the emitter position for Cluster 1 and figure 7.10 shows the RMS error for Cluster 2. In each figure, the RMS positional error is plotted as a function of the number of measurements made in each cluster. This forms the cluster-level world model (this is shown as the red solid line in each figure). Only after this model has been created by each cluster are the two cluster models fused to form a high level model. It is theoretically possible to fused cluster level models at any time, however if communications between clusters are sporadic, it is necessary to be able to minimise inter-cluster communications and thus hierarchical fusion model presented.

The result of fusing the weighted cluster-level models is shown as the red crosses in both figures. It is clear that the weighted high-level world model has a much higher accuracy than the weighted cluster-level models for either cluster. Furthermore, the use of cluster level fusion results in a much faster 'convergence' of the RMS error as a function of number of measurements. There is improvement in emitter geolocation performance by adopting a cluster-level fusion strategy is most certainly due to the effect of minimising the effect of GDOP and unreliable measurements, by using different 'look' directions for each cluster even though the fusion at this level takes place relatively infrequently.

In this section the concept of agents was developed into hierarchical model, where agents naturally form multiple clusters. Each cluster is assumed to consist of multiple agents that forms a fusion hierarchy: each agent is able to geolocate individually, clusters of agents can refine the emitter position using fusion and clusters of agents can further refine the position estimate by taking advantage of the different view of the target by each cluster. In the next section the use of the weight for self-awareness and decision making will be demonstrated.

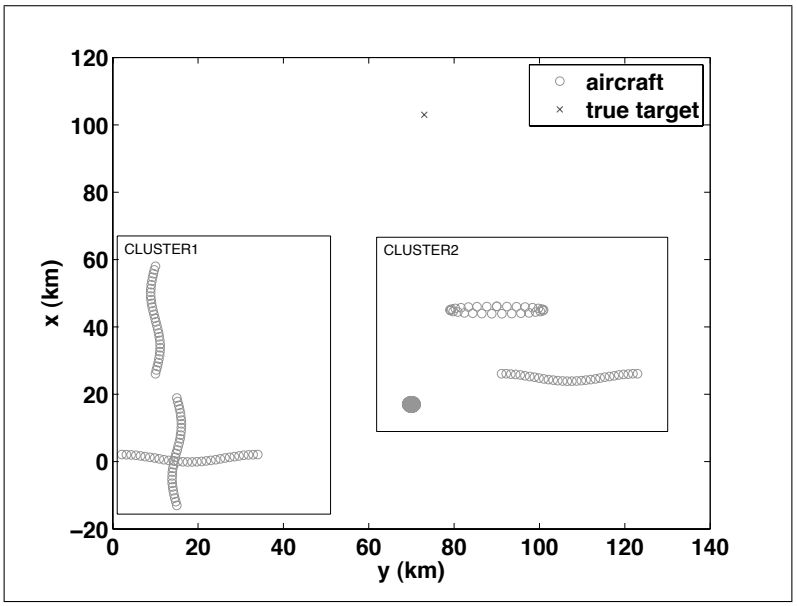

Figure 7.8: Scenario for cluster-level data fusion, using two clusters, illustrated as rectangles

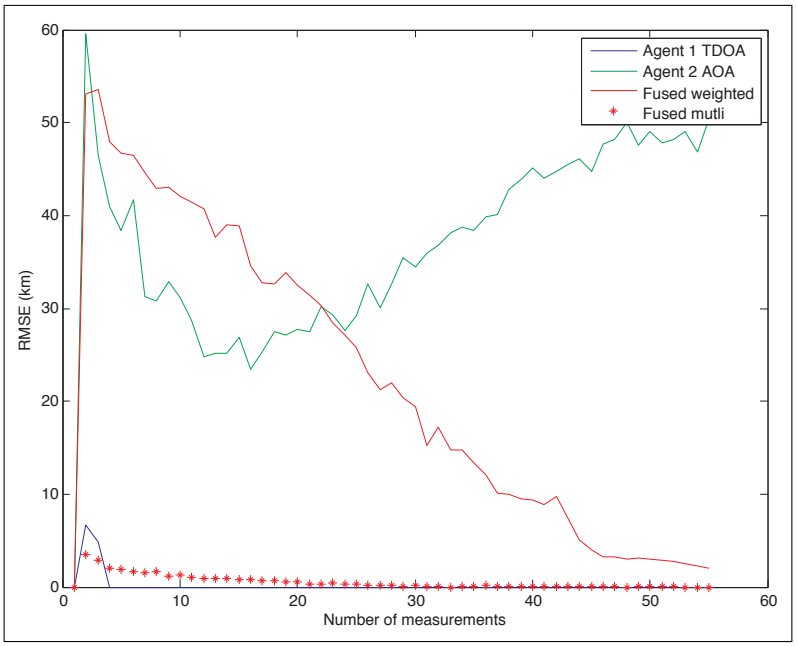

Figure 7.9: Average RMS error over 50 simulations for the scenario shown in figure 7.8 for cluster 1

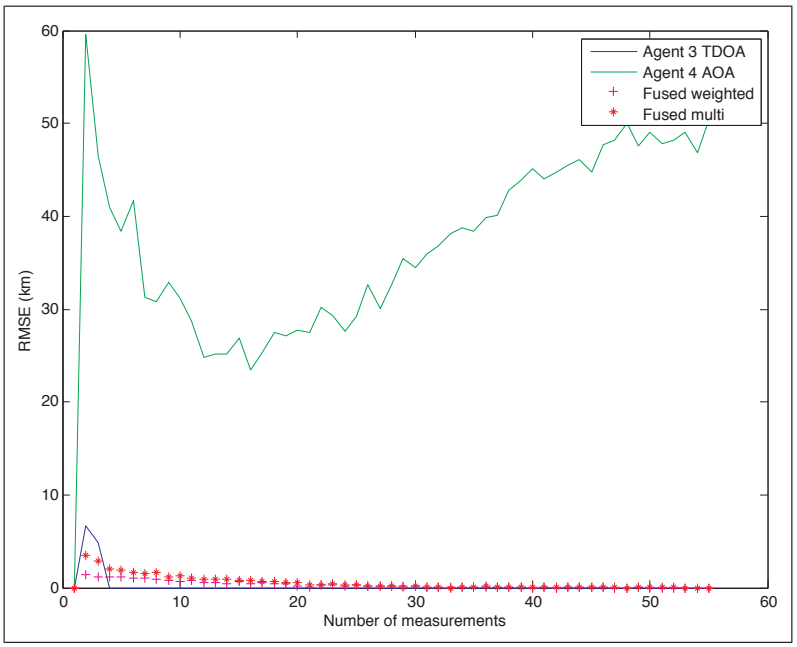

Figure 7.10: Average RMS error over 50 simulations for the scenario shown in figure 7.8 for cluster 2. Cluster 2 has a better geometry of the agents and thus can converge quicker to a true target position

Autonomous behavior - minimizing weight

It is possible to add some 'decision making' logic for the agents, based on checking the value of weight and then adjusting the flight path until the value of weight is minimised. Figure 7.11 shows flight paths of the agents. In this scenario, two

platforms heading north obtained TDOA measurements, thus representing one set of TDOA measurement, and the platform moving east was able to obtain only AOA measurements. The following logic was added to agent one:

- Platforms move according to the equation

$$x(t) = x(t-1) + v \sin\theta(\Delta t) \tag{7.8}$$
$$y(t) = y(t-1) + v\Delta t \tag{7.9}$$

  where $(x(t-1), y(t-1))$ is the previous or initial position of the aircraft. $\theta(\Delta t) \in (0, 2\pi)$ is the angle changing on each time step up with step $\Delta\theta = 2\pi/N_m$. Where N_m - duration in simulation, which is equivalent to number of measurements taken during the simulation.

- Maneuver can be performed by changing the direction of the motion in order to minimize the weight.

$$x(t) = x(t-1) - v \sin\theta(\Delta t) \tag{7.10}$$
$$y(t) = y(t-1) - v\Delta t \tag{7.11}$$

- On each 5th step, the agent checks: wether previous the weight is larger, than the current one ($w_{t-1} \geq w_t$) and if not then agent then performs the manoeuvre above.

In this scenario the TDOA agent quickly realised that the platform position was creating excessive GDOP for effective geolocation and has changed the flight path of the one platform, to reduce the measurement weight by reducing the GDOP. In this simulation S_{TDOA} from (7.2) was minimised down to one after thirty measurements has been obtained. Figure 7.11 demonstrates the flight path of the TDOA agent, where one of the platforms employes the method of changing direction of the motion in order to provide better TDOA measurements. It is known that GDOP of the TDOA measurements depend on baseline between platforms relative to target position 2, however as target position is not known the *a priori* optimal motion model of the platforms is not available. This section demonstrated the used of the weighting in parameterised space to adjust motion of the platform with attempt to provide better measurements and target position estimate.

7.5 Conclusion

This chapter has shown how the Generalised Hough Transform can be used to fuse AOA, TDOA, and FDOA measurements. In particular, it has introduced a novel method of weighting the individual sets of measurements according to the impact that they have on the positional error rather than simply according to the measurement error. The results have shown how using weighted fusion has a beneficial effect on reducing the error of the position estimate. Also it was shown that the Hough

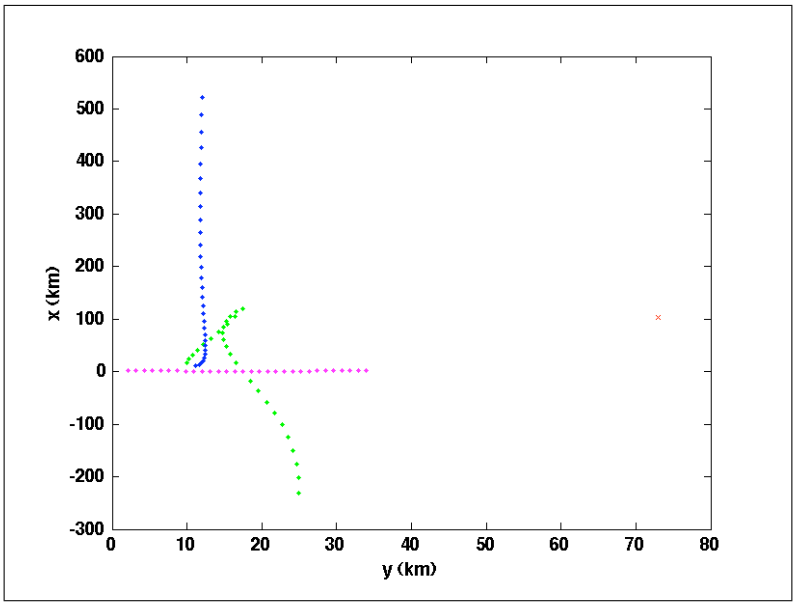

Figure 7.11: Scenario illustrating decision making for agent based on weight minimisation

Transform can be used as a framework for agent-based fusion, thus connecting low level measurement fusion to higher more 'abstract' level, where it can be used for decision making.

The concept of geolocation agents has been developed, where agents naturally form multiple clusters. Each cluster is assumed to consist of multiple agents that forms a fusion hierarchy: each agent is able to geolocate individually, clusters of agents can refine the emitter position using fusion and clusters of agents can further refine the position estimate by taking advantage of the different view of the target by each cluster. In this chapter the benefits of providing fusion between clusters of the agents has been examined and the advantages of the clustered (hierarchical) agent-based data fusion has been demonstrated. Also it was shown that it is possible to add additional capabilities of the agents, where they can perform different manoeuvre, in order to minimise GDOP error.

Chapter 8

Conclusion and future work

In this thesis new estimation and data fusion techniques based on Hough Transform has been shown. The Hough Transform algorithm has been evaluated using the fusion of different type of measurements (angle of arrival, time difference of arrival and frequency difference of arrival), together with higher level fusion with terrain data. There is a good reason to call it a Hough Transform based estimator rather, for example, than 'ad-hoc averaging over Gaussian sum', due to the fact that the Hough Transform, and its related Radon Transform [55], has been used in image processing since 1964 (see [57],[97]). Moreover, there are a fair number of optimisation techniques that can be considered depending on application and resource constraints. Some of these techniques relate to optimisation of the parameterized space, such as the Fuzzy Hough Transform [98] and [80]. Others optimise peak search in parameterized space using genetic algorithms [99]. The research also has been carried out by implementing Hough Transform in hardware as in [78]. Some of these techniques, such as Multiresolution Hough Transform have been tested during this research as has another optimised method, which we call Hybrid Hough Transform, which has been proposed. (Note, there is an ambiguity within image processing community on the names of the optimisation techniques, such as Multiresolution Hough Transform: there are two different implementations of MHT, and there are a number of algorithms called Hybrid Hough Transform). A particle filter algorithm has been applied to the geolocation problem and it was found the non-Bayesian RHT was found to have a broadly similar algorithm to the Bayesian Particle filter. The performance of the Hough Transform based algorithm and the particle filter have been compared and this has formed the basis for a comparison of non-Bayesian and Bayesian type estimators with the Cramer-Rao lower bound, which is representative of the performance of classical estimators. This comparison lead to the development of the generalised estimator. A generalised estimator has been developed, where by changing a single parameter, α, the estimator changes from a Bayesian type to a non-Bayesian type. The analysis has been carried out on the results of this estimator. Some of these results lead back to support the importance of the choice resampling method for the particle filter. In addition, the fusion capability of the Hough Transform has been extended to the development of the weighted fusion algorithm, which can be used to self-weight the measurements from

the sensors according to their GDOP. It would be interesting to see these weighting techniques exploited on command and control level. It is possible to track the value of this weights and provide a controller which will keep them minimal.

The use of these weighting techniques opens the possibility to higher level fusion, where based on the weighted Hough Transform, an agent-based data fusion algorithm for emitter geolocation has been proposed, thus moving the geolocation problem to a higher level of the fusion hierarchy. Agent-based data fusion has been applied to an even higher level of fusion between groups of agents, thus showing the possibility of using cluster level fusion based on the Hough Transform approach to geolocation.Although this aspects has been highlighted in chapter 7 further research is required in this direction.

A comparison with the Bayesian type techniques in chapter 6.1 lead to a number of interesting estimation functions, which are capable of obtaining a position estimate. Although not all of these functions produced a good performance for data fusion, it is in the interest of scientific research to pursue investigations in this area. For example, a Gaussian Mixture based estimator may be a good solution for the application, where it is not only necessary to geolocate but also to track the target after geolocation. Hough Transform, with all its fusion applications, is not capable of tracking, as HT is mostly dealing with static primitives and combines all previous information with one solution.

Some algorithms, which may be applied for the task of geolocation has been left beyond the scope of this thesis and it is in the interest of the scientific research to apply some commonly known algorithms such as Unscented Kalman filter, to the problem of geolocation of radio emitters. Also it would be interesting to see the application of the evolutional algorithms to the task of geolocation of emitters. As it was mentioned before, image processing community uses evolutionary (genetic) algorithms for peak search in Hough Transform, so it would be in the interest of research to extend this concept to the task of geolocation. Especially, if the problem of geolocation will be broaden to geolocation of the multiple emitters and in this case the application of the peak search based on the genetic algorithm can be beneficial. Comparing performance the proposed Hough Transform algorithm with other algorithms, HT have a several advantages: (i) accumulating likelihoods can be done very fast, especially in hardware or using optimised functional programming routines such as *accumarray* in Matlab, (ii) because of the absence of resampling, HT can be used as batch or sequential estimator and may fit modern MapReduce framework[100] [101] and in batch processing form, can take and advantage of parallel processing. MapReduce framework defines in terms of two set of functions **map** and **reduce**, where map function processes data mapping them into key value pairs (for example likelihoods into key (x, y)), while reduce function reduces (accumulating in case of HT) all values with same key into one value. Although **reduce** should be performed after **map** both of these function can be processed in parallel. The Hough Transform in this thesis relies only on the assumption that there is a Gaussian probability function between measurement and the location of the target. However, this assumption is not crucial for the convergence of the algorithm, and in more general cases, something like a lookup table of relative measurement to

position can be used. Moreover, further research is also required in order to extend the Hough Transform based estimator to three-dimensional case. There are multiple ways to explore new areas highlighted in this thesis, but the main goal of the project to propose and develop algorithm for geolocation, robust enough to sustain NLOS effect has been fulfilled by presenting Hough Transform based algorithms and variations of the particle filter.

Chapter 9

Appendix

9.1 AOA estimation using antenna array or interferometer

When AOA measurements are used, a position can be estimated with only two reference nodes, but performance is severely degraded by scattering. Scattering near and around the sender and receiver will alter the measured AOA. Also, the use of antenna arrays corresponds to increased sensor node cost, power consumption, size, and complexity. However, in military applications it is feasible that some nodes (e.g., those mounted on vehicles/aircraft) will be equipped with arrays.

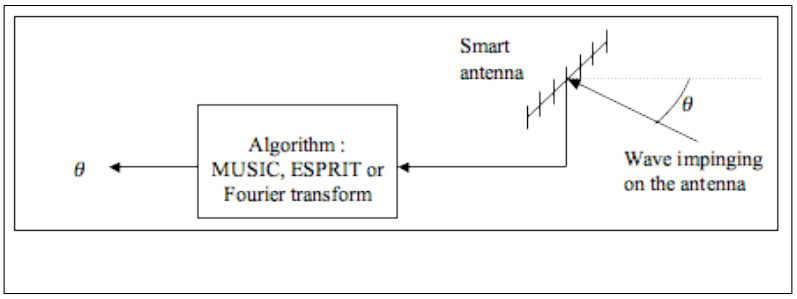

Figure 9.1: AOA antenna array

A receiver can determine the angle at which a wave impinges on an antenna in the receiver. The use of smart antennas (also called phased array antennas) is a very efficient means to determine the AOA of waves impinging on its different elements. A phased array antenna comprises two or more elements. The accuracy of measurements, but also the cost of the antennas increases with the number of elements. It is suggested that an 8 elements antenna can be best trade of for it. An example of antenna array can be seen on picture 9.2. Several signal-processing techniques can be used to determine the AOA from the antenna array such as the Fourier Transform, ESPRIT or MUSIC. The algorithm MUSIC (Multiple Signals Classification) presents multiple advantages over other techniques as a narrow angular resolution and the ability to provide an estimate of the angular error spread

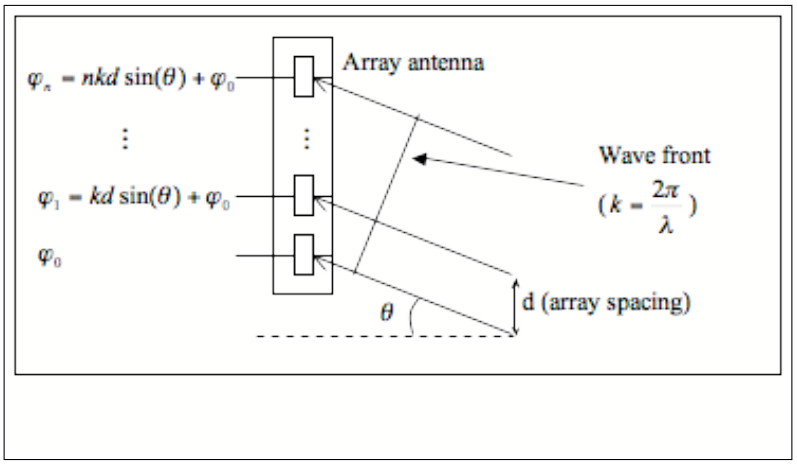

Figure 9.2: Basic principles of antenna array

[20]. Some of the UAV can be equipped with this 8 elements antenna so it is possible to use AoA measurements for position estimation. In the absence of an line of sight (LOS) signal component, the antenna array will lock on to a reflected signal that may not be coming from the direction of the sender. Even if an LOS component is present, multipath will still interfere with the angle measurement. The accuracy of the AOA method diminishes with increasing distance between the sender and receiver due to fundamental limitations of the devices used to measure the arrival angles as well as changing scattering characteristics.

Error covariance for Angle of Arrival

Because of uncertainties in the AOA measurements, uncertainties exist in the estimated emitter location. Thus derivation of the error covariance is required in order to proceed further. In triangulation, angles to the target are measured from two receivers. The example of such a scenario for the error analysis are shown in figure 9.3.

The x-axis may be taken along baseline and the origin to be at the receiver 1. The y-axis lies in the bistatic plane containing two emitter and two receivers. With a baseline length, D, the coordinates of the two receivers are $(0, 0)$ and $(D, 0)$. The coordinates of the emitter (x, y) and the angles to the emitter measured from the baseline at the two sites, are θ_1 and θ_2. The equation for the LOS from target to receiver 1 is then

$$y = x \tan \theta_1 \tag{9.1}$$

Similarly, the equation for LOS2 is

$$y = (D - x) \tan \theta_2 \tag{9.2}$$

The target lies at the intersection of these two lines. Solving the intersection point,

$$x = \frac{D \cos \theta_1 \sin \theta_2}{\sin(\theta_1 + \theta_2)} \tag{9.3}$$

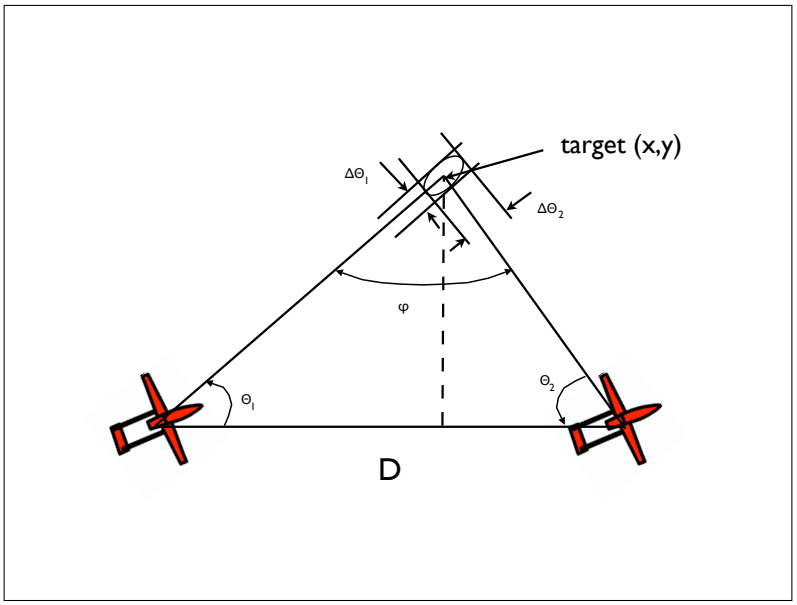

Figure 9.3: Error analysis of the emitter geolocation using Angle of Arrival

and

$$y = \frac{D \sin\theta_1 \sin\theta_2}{\sin(\theta_1 + \theta_2)} \tag{9.4}$$

The variation in the position of the target due to measurement error in the angles θ_1 and θ_2 is given by:

$$\begin{bmatrix} \partial x \\ \partial y \end{bmatrix} = \begin{bmatrix} a & b \\ c & d \end{bmatrix} \begin{bmatrix} \partial\theta_1 \\ \partial\theta_2 \end{bmatrix} \tag{9.5}$$

where

$$\begin{aligned} a &= \frac{-D \sin\theta_1 \sin\theta_2}{\sin(\theta_1 + \theta_2)} - \frac{D \cos\theta_1 \sin\theta_2 \cos(\theta_1 + \cos\theta_2)}{\sin^2(\theta_1 + \theta_2)} \\ b &= \frac{D \cos\theta_1 \cos\theta_2}{\sin(\theta_1 + \theta_2)} - \frac{D \cos\theta_1 \sin\theta_2 \cos(\theta_1 + \theta_2)}{sin^2\theta_1 + \theta_2} \\ c &= \frac{D \cos\theta_1 \sin\theta_2}{\sin(\theta_1 + \theta_2)} - \frac{D \sin\theta_1 \sin\theta_2 \cos(\theta_1 + \theta_2)}{sin^2\theta_1 + \theta_2} \\ d &= \frac{D \sin\theta_1 \cos\theta_2}{\sin(\theta_1 + \theta_2)} - \frac{D \sin\theta_1 \sin\theta_2 \cos(\theta_1 + \theta_2)}{sin^2\theta_1 + \theta_2} \end{aligned} \tag{9.6}$$

The covariance of this variation error is given by:

$$\begin{bmatrix} \partial x \\ \partial y \end{bmatrix} = E \begin{bmatrix} \partial x \\ \partial y \end{bmatrix} E[\partial x, \partial y] \tag{9.7}$$

$$= \begin{bmatrix} a & b \\ c & d \end{bmatrix} E \left\{ \begin{bmatrix} \partial\theta_1 \\ \partial\theta_2 \end{bmatrix} [\partial\theta_1, \partial\theta_2] \right\} \begin{bmatrix} a & b \\ c & d \end{bmatrix}^T \tag{9.8}$$

Because the variations in θ_1 and θ_2 independent,

$$E \left\{ \begin{bmatrix} \partial\theta_1 \\ \partial\theta_2 \end{bmatrix} [\partial\theta_1, \partial\theta_2] \right\} = \begin{bmatrix} \sigma^2_{\theta_1} & 0 \\ 0 & \sigma^2_{\theta_2} \end{bmatrix} \tag{9.9}$$

where σ_{θ_1} and σ_{θ_2} are the standard deviations of the angles, θ_1 and θ_2. Then from (9.7):

$$cov \begin{bmatrix} \partial x \\ \partial y \end{bmatrix} = \begin{bmatrix} a^2\sigma_{\theta_1}^2 + b^2\sigma_{\theta_2}^2 & ac\sigma_{\theta_1}^2 + bd\sigma_{\theta_2}^2 \\ ac\sigma_{\theta_1}^2 + bd\sigma_{\theta_2}^2 & c^2\sigma_{\theta_1}^2 + d^2\sigma_{\theta_2}^2 \end{bmatrix} \tag{9.10}$$

Assume that:

$$\sigma_{\theta_1} = \Delta\theta_1 \tag{9.11}$$

$$\sigma_{\theta_2} = \Delta\theta_2 \tag{9.12}$$

and $\Delta\theta_1 = \Delta\theta_2 = \Delta\theta$[1] thus $\sigma_{\theta_1} = \sigma_{theta_2} = \sigma_\theta$. Then from equation (9.10)

$$cov \begin{bmatrix} \partial x \\ \partial y \end{bmatrix} = \begin{bmatrix} a^2 + b^2 & ac + bd \\ ac + bd & c^2 + d^2 \end{bmatrix} \sigma_\theta^2 \tag{9.13}$$

From the equation (9.6), it is seen that the elements a, b, c and d have the factor $D/\sin(\theta_1 + \theta_2)$ in common. Thus, we may write,

$$a' = -\sin\theta_1 \sin\theta_2 - \cos\theta_1 \sin\theta_2 \cot(\theta_1 + \theta_2) \tag{9.14}$$

$$a = \frac{D}{\sin(\theta_1 + \theta_2)} a' \tag{9.15}$$

$$b' = \cos\theta_1 \cos\theta_2 - \cos\theta_1 \sin\theta_2 \cot(\theta_1 + \theta_2) \tag{9.16}$$

$$b = \frac{D}{\sin(\theta_1 + \theta_2)} b' \tag{9.17}$$

$$c' = \cos\theta_1 \sin\theta_2 - \sin\theta_1 \sin\theta_2 \cot(\theta_1 + \theta_2) \tag{9.18}$$

$$c = \frac{D}{\sin(\theta_1 + \theta_2)} c' \tag{9.19}$$

$$d' = -\sin\theta_1 \cos\theta_2 - \sin\theta_1 \sin\theta_2 \cot(\theta_1 + \theta_2) \tag{9.20}$$

$$d = \frac{D}{\sin(\theta_1 + \theta_2)} d' \tag{9.21}$$

In relation to bistatic angle ϕ (see figure 9.3)

$$\sin(\theta_1 + \theta_2) = \sin\phi \tag{9.22}$$

Thus, equation (9.13) can be written as

$$cov \begin{bmatrix} \partial x \\ \partial y \end{bmatrix} = \frac{D^2}{\sin^2\phi} \begin{bmatrix} p & q \\ q & r \end{bmatrix} \sigma_\theta^2 \tag{9.23}$$

[1] For example in scenario for radar geolocation

where

$$p = a'^2 + b'^2$$
$$q = a'c' + b'd'$$
$$r = c'^2 + d'^2$$

The square root of eigenvalues of covariance matrix gives the major and minor axes of the error ellipse. note that if σ_θ as $\sigma_\theta = 1/2\Delta\theta$, then the square root of the eigenvalues would have yielded the semi-axis.) It is seen that the axis are proportional to $D\sigma_\theta / \sin\phi$, in other words directly proportional to the bistatic angle ϕ.

Error covariance for TDOA

As it was shown before in section 1.4.2, it is possible to measure the time of arrival of the signal on two sites and to use differential of time of arrival located an emitter on an iso-delay curve. In this section the error analysis will be presented.

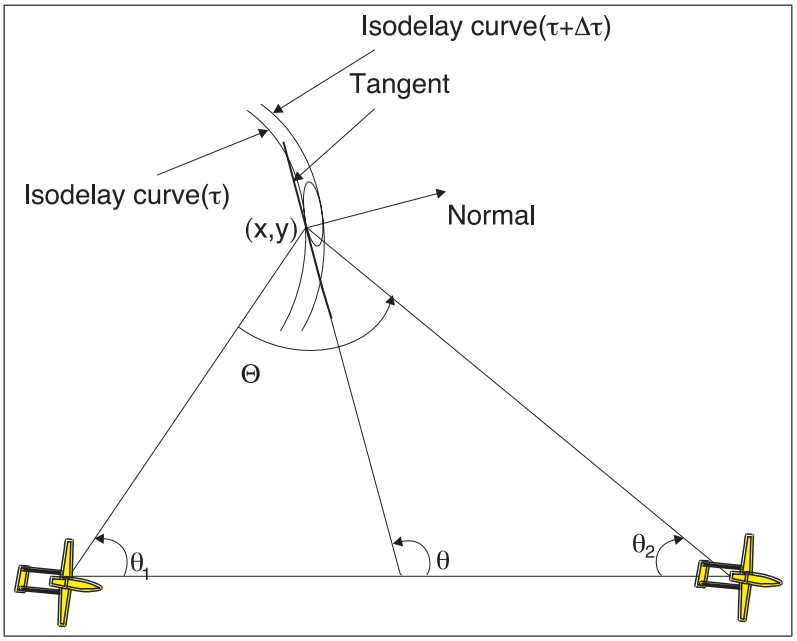

Figure 9.4: Time Difference of Arrival, Error Analysis

As in [19] the geometry, shown on figure 9.4, will be explored. The ranges R_1 and R_2 are given by the following equations:

$$R_1 = \sqrt{x^2 + y^2} \tag{9.24}$$

$$R_2 = \sqrt{(D - x)^2 + y^2} \tag{9.25}$$

The time of arrival delay then is

$$\tau = \frac{R_1 - R_2}{c} \tag{9.26}$$

or

$$\tau = \frac{R_2 - R_1}{c} \tag{9.27}$$

depending upon which site is taken as the reference and where c is the speed of radio wave propagation (speed of light).

Tangent to the Iso-delay Curve

The equation of the iso-delay curve is given by

$$R_2 - R_1 = \tau c = \Delta \tag{9.28}$$

or

$$\sqrt{(D-x)^2 + y^2} - \sqrt{x^2 + y^2} - \Delta = 0 \tag{9.29}$$

The partial derivatives f_x and f_y are

$$f_x = \frac{-(D-x)}{\sqrt{(D-x)^2 + y^2}} - \frac{x}{\sqrt{(x^2 + y^2)}} = -(\cos\theta_2 + \cos\theta_1) \tag{9.30}$$

Then the slope of the tangent to the iso-delay curve is

$$\frac{\partial x}{\partial y} = \tan\theta = -\frac{f_x}{f_y} = \frac{\cos\theta_1 + \cos\theta_2}{\sin\theta_2 - \sin\theta_1} \tag{9.31}$$

It can be shown that the tangent to the iso-delay curve at any point is the bisector to the bistatic angle. From the expression for the slope of the tangent given in equation 9.31, it is seen that a vector $[(\sin\theta_2 - \sin\theta_1), (\cos\theta_1 + \cos\theta_2)]$ lies along the tangent and its magnitude, M, is:

$$\begin{aligned} M &= \sqrt{(\sin\theta_2 - \sin\theta_1)^2 + (\cos\theta_1 + \cos\theta_2)^2} \\ &= \sqrt{2 + 2\cos(\theta_1 + \theta_2)} \\ &= \sqrt{4\cos^2\left(\frac{\theta_1 + \theta_2}{2}\right)} \end{aligned}$$

or

$$M = 2\cos\left(\frac{\theta_1 + \theta_2}{2}\right) \tag{9.32}$$

Now, a vector $(\cos\theta_1, \sin\theta_1)$ lies along the line of sight 1 (LOS1) and has a unity magnitude. Taking the dot product of the tangent vector and the LOS1 vector results in:

$$\begin{aligned} (\sin\theta_2 - \sin\theta_1)\cos\ & \theta_1 + (\cos\theta_1 + \cos\theta_2)\sin\theta_1 \\ = \quad & \sin(\theta_1 + \theta_2) \\ = \quad & 2\sin\left(\frac{\theta_1 + \theta_2}{2}\right)\cos\left(\frac{\theta_1 + \theta_2}{2}\right) \end{aligned}$$

if the angle between these two vectors is δ, then

$$M\cos\delta = 2\sin\left(\frac{\theta_1+\theta_2}{2}\right)\cos\left(\frac{\theta_1+\theta_2}{2}\right) \tag{9.33}$$

or

$$\cos\delta = \frac{2\sin\left(\frac{\theta_1+\theta_2}{2}\right)\cos\left(\frac{\theta_1+\theta_2}{2}\right)}{2\cos\left(\frac{\theta_1+\theta_2}{2}\right)} \tag{9.34}$$

or

$$\cos\delta = \sin\frac{\theta_1+\theta_2}{2} \tag{9.35}$$

and from geometry in figure 9.4, since

$$\frac{\theta_1+\theta_2}{2} = \frac{\pi}{2} - \frac{\Theta}{2} \tag{9.36}$$

and

$$\sin\left(\frac{\theta_1+\theta_2}{2}\right) = \cos\frac{\Theta}{2} \tag{9.37}$$

Hence,

$$\cos\delta = \cos\frac{\Theta}{2} \tag{9.38}$$

or

$$\delta = \frac{\Theta}{2} \tag{9.39}$$

i.e. the tangent of iso-delay curve bisects the bistatic angle Θ.

Maximum gradient

The maximum gradient lies along the normal to the curve and is given by

$$\begin{aligned}
\frac{\partial\tau}{\partial S_n} &= \frac{1}{c}\sqrt{f_x^2+f_y^2} \\
&= \frac{1}{c}\sqrt{(\cos\theta_1+\cos\delta_2)^2+\sqrt{(\sin\theta_2-\sin\delta_1)^2}} \\
&= \frac{1}{c}\sqrt{2(1+\cos(\theta_1+\theta_2))} \\
&= \frac{1}{c}2\cos\left(\frac{\theta_1+\theta_2}{2}\right)
\end{aligned}$$

$$\frac{\partial\tau}{\partial S_n} = \frac{2}{c}\sin\frac{\Theta}{2} \tag{9.40}$$

where S_n is a vector along the normal to the curve. From 9.40 follows:

$$\partial S_n = \frac{c\partial\tau}{2\sin\frac{\Theta}{2}} \tag{9.41}$$

In the next chapter overview of the traditional geolocation methods will be provided, each of them is trying to minimize error and its covariance.

9.2 Gradient Descent Algorithm

Foy presented a geolocation algorithm based on the simple process of using a Taylor-series expansion of the defining equations (also known as Gauss or Gauss-Newton interpolation) [22]. This development provides a convenient introduction to the algorithmic approach to estimate an emitter position from multiple lines of bearing. It is also one of the most general and accurate methods available, according to [10]. The equations express the geometry involved in mathematical terms and are frequently nonlinear, for details see Section 9.1. Expanding the nonlinearities in a Taylor series and retaining only the linear terms allows for employing Newton-Raphson methods of gradient descent to iteratively until an estimated solution is found. At each stage, a correction factor is calculated based on the linear least-sum square error. The principal disadvantages and advantages according to Foy are as shown in Table 9.2

Advantages	Disadvantages
Miltiple independent methods to a single station are averaged naturally	The method is iterative, requires an initial guess
Multiple measurements and mixed-mode measurements are combined properly, that is, with the correct geometric factors, and can be weighted according to their *a priori* accuracy	It is computationally complex compared to simple plotting of lines of position
The statistical spread of the solution can be found easily and naturally	Being a local correction, its convergence is not assured
Experience indicates that the initial position guess can be quite far off without preventing good convergence. Failure to converge is easy to detect	
Simulation is easy so the convergence can be easily tested	
Computational complexity is less than Kalman filter	

Table 9.1: Source [10]. Principal advantages and disadvantages of Gradient Descendent Algorithm

Suppose $x_t = (x_t, y_t)$ represents the true position of the target emitter and $x_k = (x_k, y_k), k = 1, 2, ..., N$ represents the true position of the N sensors. Let m_k

represent ith measurement at sensor k. These measurements, at this point, are not restricted to Angle of Arrival (line of bearing), ranges and so forth, but could represent any measurement useful for calculating the emitter position. Thus,

$$f_i(x_T, y_T, x_k, y_k) = u_i = m_{ki} + \epsilon_i, k = 1, 2..., N \tag{9.42}$$

where m_{ki} = true value of the measured quantity and ϵ_i = error in the m_{ki} measurement

For example, if the measurement is that of an Angle of Arrival from the sensor to the emitter, then

$$f_i(x_T, y_T, x_k, y_k) = tan^{-1}\left(\frac{y_t - y_k}{x_t - x_k}\right) + \epsilon_i \tag{9.43}$$

The goal is to find (x_T, y_T) given the measurements and known locations of the sensors. The errors in the measurements ϵ_i are assumed to be *independent* (of each other) *and identically distributed (i.i.d)* with zero means, $\varepsilon\epsilon_i = 0$, where ε denotes statistical expectation. The *error covariance matrix* is given by

$$R = [r_{ij}] \tag{9.44}$$

with entries

$$r_{ij} = \varepsilon\left(\epsilon_i, \epsilon_j\right) \tag{9.45}$$

Let $(\hat{x}_T, \hat{y}_T)$ be guesses of the true position (x_T, y_T). Then

$$x_T = \hat{x} + \delta_x \tag{9.46}$$

and

$$y_T = \hat{y} + \delta_y \tag{9.47}$$

Unfortunately, because the relation between m_{ki} and (x_T, y_T) nonlinear, as can be seen from AOA example, it is necessary to linearize it using Taylor series expansion. The Taylor series expansion of $f_i()$ around point a is given by

$$f(x) = f(a) + (x-a)f'(a) + \frac{(x-a)^2}{2!}f''(a) + ... + \frac{(x-a)^n}{n!}f^n(a) + ... \tag{9.48}$$

where the notation $f^n(a)$ refers to the nth derivative of $f(x)$ evaluate at point a. In two dimensions, this becomes

$$\begin{aligned} f(a+h, b+k) &= f(a,b) + \left(h\frac{\partial}{\partial x} + k\frac{\partial}{\partial y}\right) f(x,y)|_{y=b}^{x=a,} + \dots \\ &\quad + \frac{1}{n!}\left(h\frac{\partial}{\partial x} + k\frac{\partial}{\partial y}\right)^n f(x,y)|_{y=b}^{x=a,} \dots \end{aligned} \tag{9.49}$$

where the bar and subscripts mean that, after differentiation, x is replaced with a and y is replaced with b. Also, in this notation,

$$\begin{aligned} \left(h\frac{\partial}{\partial x} + k\frac{\partial}{\partial y}\right) f(x,y) &= \left(h\frac{\partial f(x,y)}{\partial x} + k\frac{\partial f(x,y)}{\partial y}\right) \\ \left(h\frac{\partial}{\partial x} + k\frac{\partial}{\partial y}\right)^2 f(x,y) &= h^2\frac{\partial^2 f(x,y)}{\partial x} + 2kh\frac{\partial^2 f(x,y)}{\partial x \partial y} + k^2\frac{\partial f(x,y)}{\partial y} \\ &\dots \end{aligned}$$

For the case at hand, the two-dimensional Taylor expansion, after deleting all terms then linear ones, is

$$\hat{f}_i + \frac{\partial f_i()}{\partial x}|_{y=b}^{x=a,}\delta_x + \frac{\partial f_i()}{\partial y}|_{y=b}^{x=a,}\delta_y \approx m_{ki} + \epsilon_i \tag{9.50}$$

where

$$\hat{f}_i = f_i(\hat{x}_T, \hat{y}_T, x_k, y_k) \tag{9.51}$$

To put this development into matrix form for (easier) manipulation.

$$H = \begin{bmatrix} h_{11} & h_{12} \\ h_{21} & h_{22} \\ \vdots & \vdots \\ h_{N_s1} & h_{N_s2} \end{bmatrix} \begin{bmatrix} \frac{\partial f_1()}{\partial x}|_{y=\hat{y}_T}^{x=\hat{x}_T,} & \frac{f_1()}{\partial y}|_{y=\hat{y}_T}^{x=\hat{x}_T,} \\ \frac{\partial f_2()}{\partial x}|_{y=\hat{y}_T}^{x=\hat{x}_T,} & \frac{f_2()}{\partial y}|_{y=\hat{y}_T}^{x=\hat{x}_T,} \\ \vdots & \vdots \\ \frac{\partial f_{N_s}()}{\partial x}|_{y=\hat{y}_T}^{x=\hat{x}_T,} & \frac{f_{N_s}()}{\partial y}|_{y=\hat{y}_T}^{x=\hat{x}_T,} \end{bmatrix} \tag{9.52}$$

$$\delta = \begin{bmatrix} \delta_x \\ \delta_y \end{bmatrix} \tag{9.53}$$

$$z = \begin{bmatrix} m_{k1} - \hat{f}_1 \\ m_{k2} - \hat{f}_2 \\ \vdots \\ m_{kN_s} - \hat{f}_{N_s} \end{bmatrix} \tag{9.54}$$

and

$$e = \begin{matrix} \epsilon_1 \\ \epsilon_2 \\ \vdots \\ \epsilon_{N_s} \end{matrix} \tag{9.55}$$

then (9.50) can be written

$$H\delta \approx z + e \tag{9.56}$$

The form of delta that yields the least sum squared error with the terms weighted according to the covariance matrix in [102] is:

$$\delta = [H^T R^{-1} H]^{-1} R^{-1} z \tag{9.57}$$

where R is a weighting matrix used to factor one or more parameters. R is arbitrary, but must be positive definite and full rank so that R^{-1} exists. Therefore, during one step of the iteration, δ is computed according to (9.57), and new estimates (guesses) are obtained via

$$\hat{x}_{new} \leftarrow \hat{x}_{old} + \delta_x \tag{9.58}$$

$$\hat{y}_{new} \leftarrow \hat{y}_{old} + \delta_y \tag{9.59}$$

in (9.57) and the iteration is repeated until there is a satisfactory minimization of the change in (x_g, y_g) from one iteration to the next ($\delta = 0$). The covariance matrix of the target estimate is given by

$$Q_0 = [H^T R^{-1} H]^{-1} = \begin{bmatrix} \delta_x & \rho_{xy} \\ \rho_{xy} & \delta_y \end{bmatrix} \tag{9.60}$$

If the error statistics are normal, then the error region is an ellipse, called the *elliptical error probable*(EEP), with semi-major axis a and semi-minor axis b given by [10]

$$a^2 = 2\frac{\sigma_x^2\sigma_y^2 - \rho_{xy}^2}{\sigma_x^2 + \sigma_y^2 - [\sigma_x^2 - \sigma_y^2 + 4\rho_{xy}^2]^{1/2}}C^2 \tag{9.61}$$

$$b^2 = 2\frac{\sigma_x^2\sigma_y^2 - \rho_{xy}^2}{\sigma_x^2 + \sigma_y^2 + [\sigma_x^2 - \sigma_y^2 + 4\rho_{xy}^2]^{1/2}}C^2 \tag{9.62}$$

where $C = -2ln(1-P_e)$, with P_e being the confidence that the target lies within the EEP, (eg., 0,5 for 50%, 0.9 for 90%, and so forth). The tilt angle θ of the semi-major axis relative to the x-axis is given by

$$\theta = \frac{1}{2}\tan^{-1}\frac{2\rho_{xy}}{\sigma_x^2 - \sigma_y^2} \tag{9.63}$$

The circular error probable (CEP) is similar to concept EEP. It is a circle centered on the computed position with an area such as that the target lies within the circle with a prescribed probability. It can be estimated to within 10% by [22]

$$CEP \approx 0.75\sqrt{a^2 + b^2} \tag{9.64}$$

9.2.1 Alternative Estimators

Weighted Least squares

By introducing a weighting matrix, $\mathbf{W}$ into the linear least squares objective function, error contributors to the squaring process can be selectively weighted. This permits the estimator to reduce the square of certain error components more than others, according to the selection of $\mathbf{W}$. In effect, the observations with the greatest importance are allowed to make the greater contributions to the solutions. In this case, the least squares process minimizes $Q(\mathbf{X}) = \epsilon^T\mathbf{W}\epsilon$ and the weighted least squares estimate is:

$$\hat{X} = (A^TWA)^{-1}A^TWY \tag{9.65}$$

where W is symmetric and positive definite. Because the observation residuals are samples of a random process, it is reasonable to base the selection of W on a statistical criterion. The covariance matrix C of the data vector provides a measure of the contribution made by the data. Consequently it is common for W to be inverse of C. In this case, it can be shown that the estimator is the best linear unbiased estimator (if the noise is zero mean Gaussian). This gives a better estimate than linear least least squares, but requires more work to obtain the covariance matrix of the data. Another variant of the least squares estimator that have been used for this type of the problem is the constrained least squares, where *a priori* information about the observations is used. As for the least squares method, it is possible to fuse measurements from different measurement methods, but covariance matrix needs to include all measurements. In this way, if one measurement method is more accurate than another, the weighted least squares method will automatically give stronger

weight to the more accurate method, as well as stronger weight to the most accurate data points for each method.

Constrained least squares estimation

Consider a typical estimation problem, where the raw measurements are contained in the column vector g_0, the requred state to be estimated is $\mathbf{f}$ and the model relating the two is T, such that:

$$\mathbf{g_0} \approx \mathbf{Tf} \tag{9.66}$$

The core of the conventional least squares estimator is the matrix operation:

$$\mathbf{f} = T^T T^{-1} T g_0 \tag{9.67}$$

where, in this application, g_0 is the column vector of the measurements. However, under some conditions, the standard, unconstrained least squares method can give wild over-estimates. The constrained least squares algorithm, tries to overcome this shortcoming. If Φ_i and λ_i denote the ith eigenvector and eigenvalue of matrix $\mathbf{T^T T}$ respectively:

$$[[\mathbf{T^T}]\mathbf{T}]\mathbf{\Phi_i} = \lambda_\mathbf{i}\mathbf{\Phi_i} \tag{9.68}$$

Then the *constrained* least squares approximation of f is given by:

$$f = \sum_{i=1}^{M} \frac{c_i}{\lambda_i + \alpha}\Phi_i \tag{9.69}$$

where

$$c_i = [\Phi_i][\mathbf{T}]g_0 \tag{9.70}$$

The value of α may be found using the Newton-Raphson iterative method, as described in the iterative equation below:

$$\alpha_1 = \alpha_0 - \left(\frac{C - \sum_{i=1}^{M} \frac{|c_i|^2}{(\lambda_i+\alpha_0)^2}}{2\sum_{i=1}^{M} \frac{|c_i|^2}{(\lambda_i+\alpha_0)^3}} \right) \tag{9.71}$$

where the subscript on α refer to the iteration number. In this equation, C is the applied constraint. The value of α for the first iteration can be a guess (for example $\alpha_0 = 1$). However, care must be taken if $\alpha \leq 0$ as the function is discontinuous below zero and the results of the iterative estimator are unpredictable. A possible solution is to replace negative values of α_0 with a positive random number, typically in the range [1,100]. The algorithm then starts at a random position. The square of the norm of vector f, defined as $\|f\|^2 = \sum_{i=1}^{M} |f_i|^2$ is limited by the value of the constraint, C. The concept behind the constrained least squares in the present application is that it would find the squared norm of the measurements representing the position data, which represents C. This algorithm provides improved stability in realistic scenarios where the tails of the measurement error distributions may not be Gaussian but the cost is increased processing.

Brown's estimators

Brown [10] developed an algorithm for calculating the best point estimate of the emitter from measured bearings or line of position (LOP). These included the distance least squares and asymptotic algorithms. His algorithms were designed for determining the location of both stationary and moving emitters based upon a number of angular measurements from a moving platform. The algorithms are particularly useful when there is a appreciable error in the measurement but they are restricted to platform motion that generates a small baseline in comparison to the distance between platform and the emitter. The algorithm minimizes the sum of the squares of the distances to the measured LOPs. The benefit of this method is that the sums are accumulated in memory as the positional fixes are taken. By solving the linear equations the estimate of the target position is achieved. The asymptotic algorithm was developed to minimize the sum of the squares of the angle errors and does not rely on expensive iteration technique as used in Newton-Gauss methods. This method was proposed to deal with a particular set of conditions, where the combined effect of large angle errors and short base line causes the standard algorithms to fail in even approximating the correct emitter position. Emitter location is determined by a pair of linear equations, whereby, the asymptotic algorithm is used to calculate the best point estimate of the target.

Distance Least Squares and Asymptotic Algorithm

The distance to the ith bearing line is given by:

$$d_i = |a_i x + b_i y - c_i| \tag{9.72}$$

where

$$[l]a_i = \sin \xi_i \tag{9.73}$$

$$b_i = -\cos \xi_i \tag{9.74}$$

$$c_i = p_i \sin \xi_i - q \cos \xi_i \tag{9.75}$$

The quantity to be minimised is expressed as:

$$M = \sum_{i=1}^{M} d_i^2 \tag{9.76}$$

Taking partial derivatives of M with respect to x and y to linearise equations:

$$B_1 x + Ay = E \tag{9.77}$$

$$Ax + B_2 y = -D \tag{9.78}$$

where,

$$A = \sum_{i=1}^{M} a_i b_i \tag{9.79}$$

$$B_1 = \sum_{i=1}^{M} a_i^2 \tag{9.80}$$

$$B_2 = \sum_{i=1}^{M} b_i^2 \tag{9.81}$$

$$D = \sum_{i=1}^{M} b_i c_i \tag{9.82}$$

$$E = \sum_{i=1}^{M} a_i c_i \tag{9.83}$$

The simultaneous equations that solve (9.77) and (9.78) are:

$$x = \frac{B_2 E + AD}{B_1 B_2 - A^2} \tag{9.84}$$

and,

$$y = \frac{-B_1 D - AE}{B_1 B_2 - A^2} \tag{9.85}$$

The asymptotic algorithm is a simplification of the quadratic algorithm using an asymptotic approximation and is designed to give better results for small base lines and large angular errors. The transformed equations use the identity

$$A' x'^2 + B' x' y' - A' y'^2 + D' x' + E' y' = 0 \tag{9.86}$$

which results in:

$$x = \frac{GS + DT}{ES + DR} \tag{9.87}$$

and

$$x = \frac{ET - GR}{ES + DR} \tag{9.88}$$

where

$$B = B_2 - B_1 \tag{9.89}$$

$$G = \sum_{i=1}^{N} c_i^2 \tag{9.90}$$

$$\beta = \sqrt{4A^2 - B^2} \tag{9.91}$$

$$R = \beta(\beta - B) \tag{9.92}$$

$$S = 2A\beta \tag{9.93}$$

$$T = E(\beta - B) - 2AD \tag{9.94}$$

The values of A, B_1,B_2 and D are as for the least squares estimator.

Bibliography

[1] "3GPP Specification detail 3GPP TS 02.71 Location Services (LCS) Stage 1.". Available from: `http://www.3gpp.org/ftp/Specs/html-info/0271.htm` [cited 26 May 2008].

[2] C. Drane, M. Macnaughtan, and C. Scott, "Positioning GSM telephones," *IEEE Communications Magazine*, vol. 36, pp. 46–54, April 1998. `http://www.tik.ee.ethz.ch/~beutel/projects/picopositioning/positioning_GSM_phones.pdf`.

[3] A. Finn, K. Brown, and T. Lindsey, "Miniature UAVs and future electronic warfare," tech. rep., DSTO Report, Australia, 2005. Available from: `http://www.aerosonde.com/downloads/Aerosonde_DSTO_EW.pdf`.

[4] N. Patwari, A. Hero, M. Perkins, N. Correal, and R. J. O'Dea, "Relative location estimation in sensor networks," *IEEE Transactions on Signal Processing*, vol. 51, pp. 2137–2148, August 2003. Special Issue on Signal Processing in Networking, `http://www.eecs.umich.edu/~hero/Preprints/patwari_tsp02_final.pdf`.

[5] S. Meyn and R. Tweedie, *Markov Chains and Stochastic Stability*. Springer-Verlag, London, 1993. Available from: `http://probability.ca/MT/`.

[6] A. Doucet, N. de Freitas, and N. Gordon, eds., *Sequential Monte Carlo Methods in Practice*. Statisitics for Engineering and Information Science, New York: Springer-Verlag, 2001.

[7] D. J. Salmond, N. O. Everett, and N. J. Gordon, "Target tracking and guidance using partilcles," *in Proc. of American Control Conference*, vol. 6, no. ISBN: 0-7803-6495-3, pp. 4387–4392, 2001.

[8] L. D. Stone, C. A. Barlow, and T. L. Corwin, *Multiple Target tracking*. Arthech House, INC, 1999.

[9] J.-P. M. G. Linmartz, *Wireless Communication*, vol. 1. Baltzer Science Publishers, 1996.

[10] R. A. Poisel, *Electronic Warfare Target Location Methods*. Artech House Inc, Norwood MA, 2005.

[11] J. J. Caffery and G. L. Stuber, "Overview of radiolocation in cdma cellular systems," *IEEE Communications Magazine*, vol. 36, pp. 38–45, 1999. `http://www.sss-mag.com/pdf/radioloc.pdf`.

[12] J. Caffery and G. Stüber, "Vehicle Location and Tracking for IVHS in CDMA microcells," *Proc. IEEE PIMRC*, pp. 1227–31, 1994.

[13] S. Cho, H. Jwa, J. Chun, J. Lee, and Y. Jung, "Mobile position location with the constrained bootstrap filter in a cellular communication systems," in *46th SPIE Annual Symposium*, (San Diego, CA, U.S.A.), July 2001.

[14] T. Roos, P. Myllymki, and H. Tirri, "A statistical modeling approach to location estimation," *IEEE Transactions on Mobile Computing*, vol. 1, pp. 59–69, January-March 2002. Available from: `http://csdl.computer.org/dl/trans/tm/2002/01/h0059.pdf`.

[15] Y. Chan and K. Ho, "A simple and efficient estimator for hyperbolic location," *IEEE Transactions on Acoustics, Speech, and Signal Processing*, vol. 42, pp. 1905–1915, August 1994.

[16] V. Seshadri, "A Bayesian sampling approach to in-door localization of wireless devices using received signal strength indication," Master's thesis, The University of Texas at Arlington, Department of Computer Science and Engineering, 2003. `http://www.cse.uta.edu/Research/Publications/Downloads/CSE-2003-35.pdf`.

[17] A. Mattioli and M.A.Spirito, "On the Hyperbolic Positioning of GSM Mobile Stations," in *International Symposium on Signals, Systems and Electronics*, no. ISBN: 0-7803-4900-8, (Pisa, Italy), pp. 173–177, October 1998.

[18] M. Spirito, "Further results on GSM mobile station location," *Electronics Letters*, vol. 35, pp. 867– 869, May 1999.

[19] R. G. Wiley, *Electronic Intelligence: the interception of radar signals*. Artech House Inc, Norwood MA, 1985.

[20] J. Zagami, S. Parl, J. Bussang, and K. D. Melillo, "Providing Universal Location Services Using a Wireless E911 Location Network," *IEEE Communications magazine*, April 1998.

[21] "Vera passive sensor," [online]. 2008. Available from: `http://www.icao.int/icao/en/ro/apac/2005/ADSB_SITF4/sp06.pdf`.

[22] W. Foy, "Position-location solutions by taylor-series estimation," *IEEE Trans. Aerospace and Elect. Sys*, vol. vol. AES-12, pp. 187–93, 1976.

[23] D. J. Torrieri, "Statistical theory of passive location systems," *IEEE Trans. on Aerospace and Electronic Systems*, vol. 2, pp. 183–198, 1984.

[24] F. Gustafsson and F. Gunnarsson, "Mobile positioning using wireless networks," *IEEE Signal Processing Magazine*, vol. 41, pp. 41– 53, JULY 2005.

[25] S. M. Kay, *Fundamentals of statistical signal processing: estimation theory*. Upper Saddle River, NJ, USA: Prentice-Hall, Inc., 1993.

[26] T. Smestad, H. Øhra, and A. Knapskog. "ESM-sensors for tactical information in air defence systems," [online]. Available from: `http://ftp.rta.nato.int/public//PubFulltext/RTO/MP/RTO-MP-063/MP-063-09.pdf`.

[27] C. Botteron, A. Host-Madsen, and M. Fattouche, "Cramer-Rao bounds for the estimation of multipath parameters and mobiles' positions in asynchronous ds-cdma systems," *Signal Processing, IEEE Transactions on [see also Acoustics, Speech, and Signal Processing, IEEE Transactions on]*, vol. 52, no. 4, pp. 862–875, April 2004.

[28] C. Botteron, *A Statistical Analysis of the Performance of Radio Location Techniques*. PhD thesis, University of Calgary, 2003.

[29] E. Lehmann and G. Casella, *Theory of Point Estimation*. No. ISBN: 0-471-05849-1 in Probability and Mathematical Statistics, Wiley-Interscience, 1991.

[30] B. Yang and J. Scheuing, "Cramer-Rao bound and optimum sensor array for source localazation from Time Differences of Arrival," *Proc. ICASSP 2005*, vol. 4, pp. 961–964, 2005.

[31] J. Chaffee and J. Abel, "GDOP and the Cramer-Rao bound," *Position Location and Navigation Symposium, 1994., IEEE*, pp. 663–668, 11-15 Apr 1994.

[32] K. F. McDonald and W. S. Kuklinski, "Track Maintenance and Positional Estimation via Ground Moving Target Indicator and Geolocation Data Fusion," *Proc. of the IEEE Radar Conference*, pp. 239–245, 2001.

[33] E. W. Weisstein. ""Local Minimum." from MathWorld–A Wolfram Web Resource.," [online]. Available from: `http://mathworld.wolfram.com/LocalMinimum.html`.

[34] SIGGRAPH, *An Introduction to the Kalman Filter*, 2001. Available from: `http://www.cs.unc.edu/~tracker/media/pdf/SIGGRAPH2001_CoursePack_08.pdf`.

[35] S. E. Hammel, V. J. Aidala, K. F. Gong, and A. G. Lindgren, "Recursive versus batch processing algorithms for bearings-only tracking," *Proc. Oceans*, vol. 50-61, 1983.

[36] K. Spingarn, "Passive Position location estimation using the Extended Kalman filter," *IEEE Transactions of Aerospace and Electronic systems*, vol. 4, pp. 558–567, July 1987.

[37] N. Gordon, D. Salmond, and A. Smith, "Novel approach to nonlinear/non-gaussian bayesian state estimation," in *Radar and Signal Processing, IEE Proceedings F*, vol. 140, pp. 107–113, 1993.

[38] H. Jwa, S. Kim, X. Cho, and J. Chun, "Position tracking of mobiles in a cellular radio network using the constrained bootstrap filter," in *Proc. National Aerospace Electronics Conference*, (Dayton, OH, USA), October 2000.

[39] G. V. Zaruba, M. Huber, and F. A. Kamangar, "Monte Carlo sampling based in-home location tracking with minimal RF infrastructure requirements," Technical Report CSE-2002-6, The University of Texas at Arlington, Department of Computer Science and Engineering, 2002. `http://www.cse.uta.edu/Research/Publications/Downloads/CSE-2002-6.pdf`.

[40] F. Gustafsson and F. Gunnarsson, "Positioning using time-difference of arrival measurements," *Proc. ICASSP 2003*, vol. 6, pp. VI–553 – 556, 2003. Available from: `http://www.control.isy.liu.se/~fredrik/reports/03icasspgustafsson.pdf`.

[41] L. Ljung, "Asymptotic behavior of the extended Kalman filter as a parameter estimator for linear systems," *Automatic Control, IEEE Transactions on*, vol. 24, no. 1, pp. 36–50, Feb 1979.

[42] T. Song and J. Speyer, "A stochastic analysis of a modified gain extended kalman filter with applications to estimation with bearings only measurements," *Automatic Control, IEEE Transactions on*, vol. 30, no. 10, pp. 940–949, Oct 1985.

[43] D. Alspach and H. Sorenson, "Nonlinear Bayesian estimation using Gaussian sum approximations," *Automatic Control, IEEE Transactions on*, vol. 17, no. 4, pp. 439–448, Aug 1972.

[44] R. Bucy and K. Senne, "Digital synthesis of nonlinear filters," *Automatica*, no. 7, pp. 287–298, 1971.

[45] J. E. Handschin and D. Q. Mayne, "Monte Carlo techniques to estimate the conditional expectation in multi-stage non-linear filtering," *International Journal of Control*, vol. 9, no. 5, pp. 547–559, 1969.

[46] G. Kitagawa, "Non-Gaussian state-space modeling of nonstationary time series," *Journal of the American Statistical Association*, vol. 82, pp. 1032–63, 1987.

[47] W. Gilks, S. Richardson, and D. Spiegelhalter, *Markov Chain Monte Carlo in Practice*. Chapman & Hall/CRC, 1996.

[48] J. Geweke, "Bayesian inference in Econometric Models Using Monte Carlo Integration," *Econometrica*, vol. 57, no. 1317-1339, 1989.

[49] B. Efron and R. J. Tibshirani, *An Introduction to the Bootstrap*. Chapman & Hall, 1993.

[50] E. W. Weisstein. ""Random Walk." From MathWorld–A Wolfram Web Resource.," [online]. Available from: `http://mathworld.wolfram.com/RandomWalk.html` [cited 26 May 2008].

[51] Z. Zhang. "Parameter estimation techniques: A tutorial with application to conic fitting," [online]. Available from: `http://research.microsoft.com/~zhang/INRIA/Publis/Tutorial-Estim/node20.html`.

[52] K. M. Alexiev and L. V. Bojilov, "A Hough Transform track initiation algorithm for multiple passive sensors," *Proc. FUSION'2000*, vol. 1, pp. TUB2/11 – TUB2/16, 2000.

[53] R. H. T. Chan and P. K. S. Tam, "A new Hough Transform based position estimation algorithm," *IEEE Proc. Australian and New Zealand Conference on Intelligent Information Systems*, pp. 140–144, 1994.

[54] B. Schiele and J. L. Crowley, "A comparison of position estimation techniques using occupancy grids," in *ICRA*, pp. 1628–1634, 1994.

[55] M. van Ginkel, C. L. Hendriks, and L. van Vliet, "A short introduction to the Radon and Hough transforms and how they relate to each other," *the Quantitative Imaging Group Technical Report Series, Number QI-2004-01*, 2004.

[56] P. V. C. Hough, "Method and means for recognizing complex patterns," *US Patent 3069654*, 1962.

[57] K. J. Illingworth J., "A Survey of the Hough transform," *Computer vision, graphics and image porcessing*, vol. 44(10):87-116, 1988.

[58] R. O. Duda and P. E. Hart, "Use of Hough Transform to Detect lines and Curves in Pictures," *Commun. Ass. Comput.*, vol. 15:11-15, 1972.

[59] A. Quazi, "An overview on the time delay estimate in active and passive systems for target localization," *IEEE Trans. on Acoustics, Speach and Signal Processing*, vol. ASSP-29, no. 3, pp. 527–533, 1981.

[60] H. Wang, H. Lenz, A. Szabo, J. Bamberger, and U. Hanebeck, "Enhancing the map usage for indoor location-aware systems," *Human-Computer Interaction. Interaction Platforms and Techniques*, pp. 151–160, 2007. Available from: `http://dx.doi.org/10.1007/978-3-540-73107-8_17`.

[61] J. Caffery, *Wireless Location in CDMA Cellular Radio Systems*. No. ISBN:0792377036 in The Kluwer International Series in Engineering, Kluwer Academic Publishers, 1999.

[62] G. L. Stuber, *Principles of Mobile Communication*. Kluwer Academic Publishers, 1996.

[63] B. Ibrahim and A. Aghvami, "Direct sequence spread spectrum matched filter acquisition in frequency-selective rayleigh fading channels," *Selected Areas in Communications, IEEE Journal*, vol. 12, no. June, pp. 885 – 890, 1994.

[64] E. Sourour and S. Gupta, "Direct-sequence spread-spectrum parallel acquisition in a fading mobile channel," *Communications, IEEE Transactions on*, vol. 38, no. July, pp. 992 – 998, 1990.

[65] W.-H. Sheen and G. Stuber, "Effects of multipath fading on delay-locked loops for spread spectrum systems," *Communications, IEEE Transactions on*, vol. 42, no. July, pp. 1947 – 1956, 1994.

[66] E. G. Strom, S. Parkvall, and B. E. Ottersten, "Propagation delay estimation of DS-CDMA signals in a fading environment," *Global Telecommunications Conference*, no. December, pp. 85 – 89, 1994.

[67] N. Yousef and A. Sayed, "Detection of fading overlapping multipath components for mobile positioning systems," *Communications, 2001. ICC 2001. IEEE International Conference on*, vol. 10, no. June, pp. 3102 – 3106, 2001.

[68] M. Silventoinen and T. Rantalainen, "Personal wireless communications," *IEEE International Conference on*, vol. 10, no. February, pp. 232 – 238, 1996.

[69] Y. Qi and H. Kobayashi, "Cramer-Rao Lower Bound for Geolocation in Non-line-of-sight Environment," *IEEE International Conference on Acoustics, Speech, and Signal Processing*, vol. 3, no. May, pp. III – 2473 – III – 2476, 2002.

[70] S.-S. W. H. You and J.-S. Koh, "The NLOS mitigation technique for oosition location using IS-95 CDMA networks," *IEEE VTS Fal l VTC 2000*, vol. 6, pp. 2556 –2560, 2000.

[71] M. P. Wylie and J. Holtzman, "The Non-Line of Sight Problem in Mobile Location Estimation," *5th IEEE International Conference on Universal Personal Communications*, vol. 2, pp. 827–831., 1996.

[72] P. Mandayam, N. Borras, and J.Hatrack, "Decision theoretic framework for NLOS identification," *VTC 98. 48th IEEE*, vol. 2, pp. 1583 –1587, 1998.

[73] J. J. You, H.-R. Al-Jazzar, and S. Caffery, "A scattering model based approach to NLOS mitigation in TOA location systems," in *Vehicular Technology Conference*, vol. 2, pp. 861 –865, IEEE 55th, 2002.

[74] P.-C. Chen, "A Non-line-Of-Sight error mitigation algorithm in location estimation," in *Wireless Communications and Networking Conference*, vol. 1, pp. 316 –320, IEEE, 1999.

[75] M. Redl, M. Weber, and M. Oliphant, *GSM and Personal Communication Handbook*. Artech House Inc, Norwood MA, 1998.

[76] J. Parsons, *The Mobile Radio Propagation Channel*. John Wiley and Sons, Chichester, UK, 2002.

[77] C. W. L Hanzo and M. Yee, *Adaptive Wireless Tranceivers*. John Wiley and Sons, Chichester, UK, 2002.

[78] M. Nakanishi and T. Ogura, "A Real-time CAM-based Hough Transform Algorithm and its performance evaluation," *IEEE Proceedings of ICPR*, pp. 516–521, 1996.

[79] W. L. P. Fung and I. King, "A Randomized Generalized Hough Transform for 2-D grayscale object detection," *IEEE Proceedings of 13th International Conference on Pattern Recognition*, vol. 2, p. 511, 1996.

[80] M. Atiquzzaman, "Multiresolution Hough transform - An efficient method of detecting patterns in images," *IEEE Transactions on Pattern Analysis and Machine Intelligence*, vol. 14, no. ISSN:0162-8828, pp. 1090–1095, 1992.

[81] S. Maskell and N. Gordon, "A tutorial on particle filters for on-line nonlinear/non-gaussian bayesian tracking," in *Target Tracking: Algorithms and Applications (Ref. No. 2001/174), IEE*, vol. Workshop, pp. 2/1–2/15 vol.2, Oct. 2001.

[82] M. Arulampalam, S. Maskell, N. Gordon, and T. Clapp, "A tutorial on particle filters for online nonlinear/non-gaussian bayesian tracking," *Signal Processing, IEEE Transactions on*, vol. 50, pp. 174–188, Feb 2002.

[83] J. S. Liu, *Monte Carlo Strategies in Scientific Computing*. Springer, October 2002.

[84] NIST, *NIST/SEMATECH e-Handbook of Statistical Methods*. NIST/SEMATECH, 2006. Available from: `http://www.itl.nist.gov/div898/handbook/`.

[85] E. W. Weisstein. "Bayes' Theorem. From MathWorld–A Wolfram Web Resource.," [online]. Available from: `http://mathworld.wolfram.com/BayesTheorem.html`.

[86] F. Mosteller and J. Tukey, *Data Analysis and Regression*. Addison-Wesley, 1977.

[87] B. Resch. "Mixtures of Gaussians A Tutorial for the Course Computational Intelligence," [online]. Available from: `http://www.igi.tugraz.at/lehre/EW/tutorials/MixtGaussian/`.

[88] J. Kotecha, , J. H. Kotecha, and P. M. Djurić, "Gaussian Sum Particle Filtering For Dynamic State Space Models," in *in Proceedings of the International Conference on Acoustics, Speech, and Signal Processing, (Salt Lake City, UT*, pp. 3465–3468, 2001.

[89] R. van der Merwe and E. Wan, "Gaussian Mixture Sigma-Point Particle Filters For Sequential Probabilistic Inference in Dynamic State-Space Models," in *In Proceedings of the International Conference on Acoustics, Speech, and Signal Processing (ICASSP), Hong Kong*, pp. 701–704, IEEE, 2003.

[90] G. R. Arce, *Nonlinear Signal Processing: a statistical approach*. Wiley-Interscience, 2005.

[91] D. Musicki and W. Koch, "Geolocation using TDOA and FDOA measurements," in *Fusion*, Fusion, 2008.

[92] R. Reynolds, D.A.; Rose, "Robust text-independent speaker identification using gaussian mixture speaker models," *IEEE Transactions on Speech and Audio Processing*, vol. 3, pp. 72 – 83, January 1995.

[93] R. Schmidt, "Multiple Emitter location and signal parameter estimation," *IEEE Transactions on Antennas and Propagation*, vol. 34, pp. 276–280, March 1986.

[94] S. Julier. "Estimation without independence," [online]. Available from: `http://tv.theiet.org/search.cfm?search=1&back=%2Findex.cfm&syear=&schan=&stext=julier`.

[95] D. S. Elaesser and R. G. Brown, "The discrete probability density method for emitter geolocation," *Ottawa Technical Memorandum, Defence Research and Development Canada*, p. June 2003, 2003-068.

[96] J. Ferber, *Multi-agent Systems: Introduction to Distributed Artificial Intelligence*. Addison Wesley, 1999.

[97] A. A. Kassim, T. Tan, and K. H. Tan, "A comparative study of efficient generalised Hough transform techniques," *Image and Vision Computing*, vol. 17, pp. 737–748, 1999.

[98] V. Chatzis and J. Pitas, "Fuzzy cell Hough Transform for curve detection," *Pattern Recognition*, vol. 30, pp. 2031–2042, 1997.

[99] D. J. Montana. "Genetic Search of a Generalized Hough Transform Space," [online]. Available from: `http://vishnu.bbn.com/papers/ght.pdf`.

[100] "Introduction to Parallel Programming and MapReduce," [online]. Available from: `http://code.google.com/edu/parallel/mapreduce-tutorial.html`.

[101] "mapReduce Reduced (and Ported to R)," [online]. Available from: `http://blog.opendatagroup.com/2009/09/10/mapreduce-reduced-ported-to-r/`.

[102] A. Whalen, *Detection of Signal in Noise*. New York: Academic Press, 1971.

Glossary

3G	Third Generation Mobile Radio, 6
AOA	Angle Of Arrival, 11
AWGN	Additive White Gaussian Noise, 105
CCF	Cross-Correlation Function, 103
CEP	Circular Error Probable, 22
COST 207	A Cooperation in the field of Scientific and Technical Research 207 model, 97
CRLB	Cramer-Rao Lower Bound, 8
ES	Electronic Surveillance, 6
FCC	U.S. Federal Communications Commission, 6
FDOA	Frequency Difference of Arrival, 10
GDOP	Geometric Delusion of Precision, 8
GMSK	Gaussian Minimum Shift Keyed signal, 96
GPS	Global Positioning System, 7
GSM	Global System for Mobile communications, 95
HHT	Hybrid Hough Transform, 8
HT	Hough Transform, 8
ITU	The International Telecommunication Union, 97
MC	Monte Carlo, 54
MCMC	Markov Chain Monte Carlo, 55
MHT	Multiresolution Hough Transform, 8
MLE	Maximum Likelihood Estimator, 26
NLOS	Non-Line-Of-Sight, 52
PF	Particle Filter, 58

RF Radio Frequency, 6
RHT Randomized Hough Transform, 8
RMS(E) Root Mean Square (error), 17

TDOA Time Difference of Arrival, 10
TOA Time of Arrival, 10

UAV Unmanned Aerial Vehicles, 7

List of Figures

List of Tables

Multi-Cluster Agent-Based Emitter Geolocation using Hough Transform Data Fusion

Alexander Mikhalev and Richard Ormondroyd
Department of Informatics and Sensors
Cranfield University, The Defence Academy of the UK,
SN6 8LA, UK
Email: a.mikhalev@cranfield.ac.uk

***Abstract*—This paper is concerned with the use of multi-platform agent-based emitter geolocation. Multiple, self-aware, agents representing different types of emitter location method, naturally form clusters, which are controlled by the network connectivity. Each cluster provides a fusion hierarchy: each agent is able to geolocate individually, a cluster of agents can refine the emitter position using fusion and multiple clusters can further refine the position estimate by taking advantage of the different view of the target by each cluster. In this paper, the benefits of providing fusion between clusters of self-aware agents are examined and the advantages of such clustered agent-based data fusion are demonstrated for the scenario where imperfect communication forces the sensor platforms to operate as multiple clusters.**

Keywords: Geolocation, data fusion, agent-based, cluster, Hough Transform.

I. Introduction

In earlier papers [1] [2] [3], a new method of emitter geolocation was presented that was based on image processing techniques rather than the more usual classical methods using triangulation and hyperbolic location [4] or statistical methods [5] [6] [7]. The new method exploits the properties of the Generalized Hough Transform and one of its key features is that it is able to fuse different types of measurement data (such as angle of arrival measurements (AOA), time difference of arrival measurements (TDOA) and frequency difference of arrival measurements (FDOA)) by transforming them into conditional probabilities and storing them in a unified parameterized space. Once in this consistent framework, they can then be fused easily.

In order to optimize data fusion using this method, an extension to the method was described in [8] wherein sets of measurements are weighted according to the impact that they have on the positional error rather than simply according to the measurement error. In this way, the weighting includes the effect of the geometric dilution of precision (GDOP) of a particular geolocation method. The results cited in [8] showed that this reduced the error of the position estimate.

It was also shown in [8] that the Hough Transform has properties that can be exploited which allow it to be used as a framework for agent-based fusion, thus connecting low level measurement fusion to higher, more 'abstract', levels that can be used for decision making. Furthermore, using the method of self-weighting, it is possible to provide each geolocation agent with a method to calculate their contribution to the final goal of emitter geolocation; thus creating the concept of 'self-aware' or cognitive agents.

The paper [8] considered the case where all the agents were constrained to operate within a single cluster due to restrictions placed on the information exchange by the wireless communications network that they shared. In this paper, we take the concept of cognitive agents one step further where agents naturally form multiple clusters. Each cluster is assumed to consist of multiple self-aware agents where communications is assumed to be good. However, communications between clusters is assumed to exist, but is sporadic. This creates a fusion hierarchy: each agent is able to geolocate individually, a cluster of agents can refine the emitter position using fusion and clusters of agents can further refine the position estimate by taking advantage of the different view of the target by each cluster. In this paper, we examine the benefits of providing fusion between clusters of self-aware agents.

II. Agent-based emitter geolocation

In [8], the concept of agents was applied to the problem of emitter geolocation using the Hough Transform space as the model of the environment, where the common goal of the agents was the geolocation of the emitter. An agent is characterized by some, or all, of the following properties [9]:

- *Autonomous Behaviour:* Every agent is characterised by autonomous behaviour.
- *Individual World View:* Every agent has its own model of the external world that surrounds it which maybe incomplete or even incorrect.
- *Communicative and Cooperative Capacity:* Intelligent agents can exchange information with other intelligent agents and this is how it builds up its own world model. Communication with other intelligent agents is the precondition for common action in pursuit of a goal.
- *Intelligent Behaviour:* Intelligent Agents have the capacity to learn, make logical deductions to modify their own world model in the light of new information that is supplied to it, or which it obtains from the environment
- *Spatial mobility:* Intelligent agents are sometimes required to display spatial mobility.

Authorized licensed use limited to: Cranfield University. Downloaded on November 18, 2009 at 05:06 from IEEE Xplore. Restrictions apply.

- *Strategies and Decentralised Control:* Agents should be able to develop individual strategies to ensure the achievement of a common goal, even without central regulation.
- *Emergent Behaviour:* Cooperation (feedback) and interactions between intelligent agents can produce a stable system that displays new global behaviour on the next higher level of abstraction.

In the context of the emitter location problem, the agent does not simply represent the sensor platform. Rather, it represents the ability of one or more platforms to provide a position estimate according to a particular method. For example, two platforms are necessary to take a TDOA measurement and this corresponds to a single agent capable of geolocating using TDOA measurements. The same pair of platforms may, independently, make a frequency difference of arrival (FDOA) measurement and this will correspond to a second agent capable of geolocating using FDOA measurements. A platform may be able to make bearing only measurements and this produces an agent that geolocates using AOA.

In the pursuit of the common goal of emitter location, these agents use the ability of the Hough Transform to weight their individual contributions to the collaborative fused estimate and communicate this to the other agents or central control.

III. The Agent's Local Model of the World

Each agent generates a local model of the emitter location problem. Here three types of agent are of interest: (i) those that locate emitters using AOA, (ii) those that locate emitters using TDOA and (iii) those that locate emitters using FDOA. In the following sections, these models are briefly described.

A. Geolocation using Angle of Arrival

Consider a single mobile platform, whose position is accurately known, that is able to measure the AOA of the emitted signal periodically using an interferometer or antenna array. Let the measured AOA at some instant be θ_i. The conditional pdf, $p(x, y|\theta_i)$, of locating the emitter at some point, (x, y), assuming that the measurement error in the angle of arrival is Gaussian distributed, is given by:

$$p(x, y|\theta_i) = \frac{\exp\left(-\frac{(\xi-\theta_i)^2}{\sigma_{\theta_i}^2}\right)}{\sqrt{2\pi}\sigma_{\theta_i}} \tag{1}$$

where ξ is the calculated angle from the current position of the platform, (x_{r_i}, y_{r_i}), to the point (x, y) and σ_{θ_i} defines the standard deviation of the AOA measurement.

Although the point (x, y) could lie anywhere within the search space, in practice, the search space is split into a regular grid and (x, y) is constrained to lie at one of the grid points and (1) is evaluated at each of these grid points.

The local world model of this AOA agent is updated every time it makes a new measurement and this model is built as follows from (1):

$$A_{AOA}(x, y) = \frac{1}{M}\sum_{m=1}^{M} p(x, y|\theta_m) \tag{2}$$

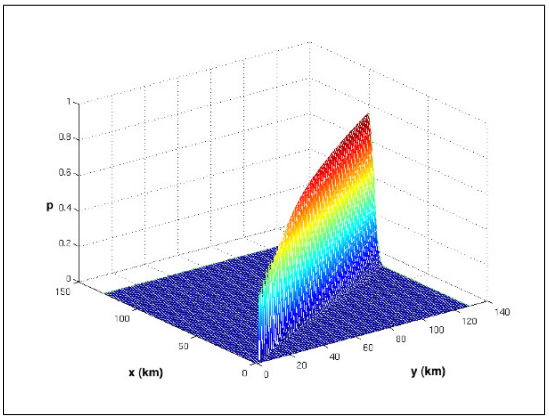

Figure 1. Local world model for AOA agent using equation (2)

where M represents the total number of measurements made. This accumulated pdf now represents the voting array for the Hough Transform.

An example of such a local world model is pictured in figure 1. This shows the probability of locating the emitter using only two AoA measurements that intersect at a very shallow angle. The peak indicates the likely position of the emitter.

B. Geolocation using Time Difference of Arrival

Assume that the emitter signal of interest is received at two spatially separated receivers, r_1 and r_2, whose positions are known. The TDOA, $\tau_{1,2}$ between these receivers can be obtained using signal cross-correlation, or some other delay-estimation technique. In this case, the pdf of the emitter location evaluated at a point (x, y) given $\tau_{1,2}$, and assuming Gaussian distributed timing errors, is given by:

$$p(x, y|\tau_{1,2}) = \frac{\exp\left(-\frac{(R_{1,2}-c\tau_{1,2})^2}{2\sigma_r^2}\right)}{\sqrt{2\pi}\sigma_r} \tag{3}$$

where $R_{1,2}$ is the difference between the range of a particular point on the grid (x, y) to receiver 1 and the range from the same grid point to receiver 2, c is the speed of light and σ_r is the range error for this measurement. A method of calculating σ_r is discussed in [2] and [8]. The local world model of this TDOA agent is built as follows from the conditional pdf (3) using

$$A_{TDOA}(x, y) = \frac{1}{L}\sum_{l=1}^{L} p(x, y|\tau_{1,2_l}) \tag{4}$$

where L represents the actual number of TDOA measurements taken and $\tau_{1,2_l}$ is the lth time difference of arrival measurement. $A_{TDOA}(x, y)$ is equivalent to the voting array (accumulator) for the Hough Transform for the TDOA measurements.

An example of the agent's local world model is shown in figure 2 using a single measurement of $\tau_{1,2}$ for a particular separation of the two sensor platforms.

Authorized licensed use limited to: Cranfield University. Downloaded on November 18, 2009 at 05:06 from IEEE Xplore. Restrictions apply.

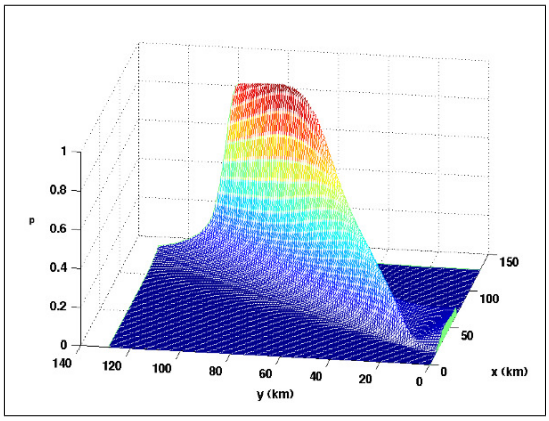

Figure 2. Local world model for TDOA agent using equation (4)

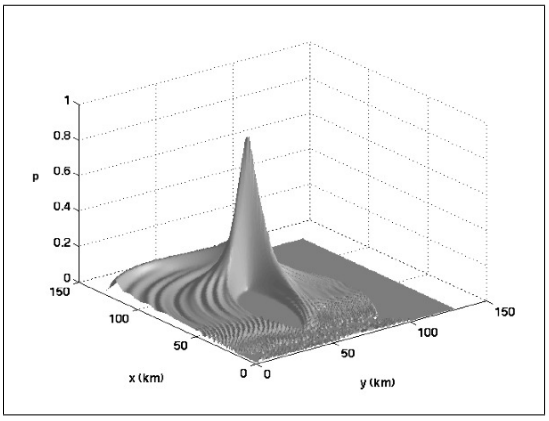

Figure 3. Local world model for FDOA agent using equation (6)

C. Geolocation using Frequency Difference of Arrival

Assume that the emitter signal of interest is received at two spatially separated receivers r_1 and r_2 whose positions are known. The ith FDOA measurement f_{d_i} can be obtained using a Doppler receiver. In this case, the pdf of the emitter location evaluated at a point (x, y) given f_{d_i}, and assuming a Gaussian distributed frequency measurement error, is given by:

$$p\left(x, y|f_{d_i}\right) = \frac{\exp\left(-\frac{(D_{1,2}-f_{d_i})^2}{\sigma_{f_d}^2}\right)}{\sqrt{2\pi}\sigma_{f_d}} \tag{5}$$

where $D_{1,2}$ is the frequency difference between the Doppler measurements calculated from a particular point on the grid (x, y) and receiver 1 and the Doppler measurement from the same point on the grid and receiver 2. σ_{f_d} is the standard deviation of the measurement error for FDOA. The method of calculating σ_{f_d} is discussed in detail in [8].

The local world model of this FDOA agent is updated every time it makes a new measurement and this model is built as follows from (5):

$$A_{FDOA}(x, y) = \frac{1}{N}\sum_{m=1}^{N} p\left(x, y|f_{d_i}\right) \tag{6}$$

where N is the number of measurements.

Figure 3 shows an example of the local world model for 20 FDOA measurements. The sensor platform positions move with time, so the figure shows the most likely emitter position (i.e. the peak value) after these measurements have been fused. This figure clearly shows how an FDOA agent is able to geolocate using a pair of moving platforms.

D. A Method of Weighted Fusion

When fusing different measurement types, it is usual to weight the individual contributions of the measurements according to their measurement error [6]. However, for emitter geolocation, the problem is extremely non-linear and the effect of the measurement errors on the position error is augmented by the GDOP for that emitter/sensor platform scenario. It is important to recognize that each type of measurement (AOA, TDOA and FDOA) provide their own, different, contributions to the GDOP and simply weighting according to measurement error does not represent the true impact of the error on the positional accuracy of the emitter position estimate.

In [8], a novel form of obtaining the weights was proposed, where the aim was to compensate for the different contributions to the emitter position error from each of the different measurement types according to their GDOP, for that scenario.

$$\begin{aligned} A(x, y) \quad = \quad & \frac{w_{TDOA}}{L}\sum_{l=1}^{L} p(x, y|\tau_{l,1}) + \\ & \frac{w_{AOA}}{M}\sum_{m=1}^{M} p(x, y|\theta_m) + \\ & \frac{w_{FDOA}}{N}\sum_{m=1}^{N} p(x, y|f_{d_i}) \end{aligned} \tag{7}$$

where, w_{TDOA}, w_{AOA} and w_{FDOA} are the weights for the three types of measurement which are calculated according to the impact that both the measurement variance *and* GDOP has on them. This is achieved directly from the accumulated pdfs of the Hough Transform.

In this case the accumulated pdf for a particular measurement type, such as TDOA, given by (4), is first normalized by its peak value, as shown in figure 2, and then thresholded at some appropriate value to create a contour at that threshold, as shown in figure 4 for a threshold set at 75% of the maximum. The area contained within this contour, S_{TDOA}, is then obtained. This is repeated for the case of the AOA measurements whose accumulated pdf is given by (2) and the FDOA measurements whose accumulated pdf is given by (6). The areas contained within the respective contours are: S_{AOA} and S_{FDOA}. It will be clear that the larger the area of the contour, the greater the contribution of these measurements to the positional error and hence a smaller weight is required. The weights are given by:

$$w_{AOA} = \frac{S_{tot}}{S_{AOA}} \tag{8}$$

Authorized licensed use limited to: Cranfield University. Downloaded on November 18, 2009 at 05:06 from IEEE Xplore. Restrictions apply.

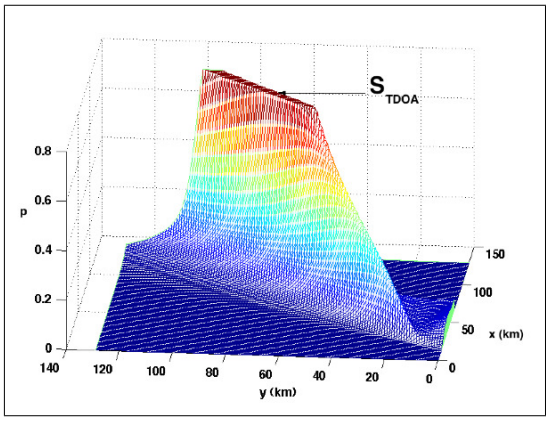

Figure 4. Local world model for TDOA only measurements shown in figure 2, thresholded at the level 75% of maximum likelihood value

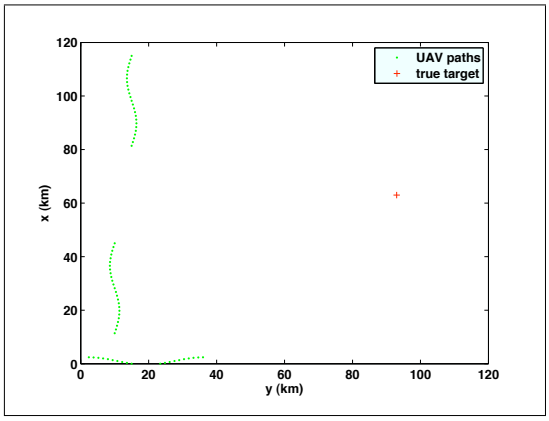

Figure 5. Scenario used for agent-based emitter geolocation, showing the flight paths of the different sensor platforms

$$w_{TDOA} = \frac{S_{tot}}{S_{TDOA}} \tag{9}$$

$$w_{FDOA} = \frac{S_{tot}}{S_{FDOA}} \tag{10}$$

where S_{tot} is the area of the total search space.

E. Agent-based Data Fusion

In order to illustrate the new method, consider the scenario shown in figure 5. In this scenario, two platforms are moving North at 40m/s according to a wavy path and they are able to take TDOA measurements (Agent 1), whereas the platform moving East at 40m/s is only able to take AOA measurements (Agent 2). This represents a cluster of AOA, and TDOA agents. The standard deviation of the TDOA measurement error in this simulation is set at 7×10^{-7}s and the standard deviation of the AOA error was set at a realistic value of 0.02 radians. The true target position is at (93km,63km). Figure 6 shows the cluster-level world model for AOA and TDOA agents after a total of 30 measurements have been taken along the respective flight paths. The peak in this model shows the most likely position of the emitter. Figure 7 shows how

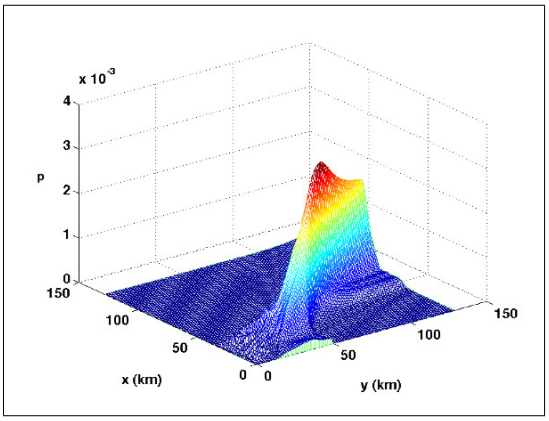

Figure 6. The cluster-level world model for AOA and TDOA agents after a total of 30 measurements have been taken along the respective flight paths

accurately each agent can independently geolocate the emitter using the average rms position error as a metric. In this figure, the average rms error is plotted as a function of the TDOA and AOA measurements taken as the platforms move along their respective flight paths. In order to obtain the average rms error the simulations were repeated 50 times and the average taken. It is clear for this scenario that TDOA measurements generally provide a more accurate position estimate. However, it should be noted that the precise results of rms position error are strongly dependent upon the platform/emitter geometry, and hence the scenario, because this affects the GDOP. This is true for all the results presented in this paper.

Figure 8 shows the benefit of fusing the TDOA and AOA measurements for both weighted and unweighted cases and the results are compared with the case for TDOA-only emitter geolocation. Two observations can be made. First, fusion of the measurements significantly improves the positional accuracy of the geolocation algorithm. Second, the impact of weighting is also clear because the weighted result tends to be much more accurate in terms of rms error.

Figure 9 shows the effect of fusing FDOA with TDOA and AOA for a similar scenario to the previous case. In this case the platforms travelling North are now able to perform TDOA and FDOA measurements so that we now have TDOA agents, FDOA agents and AOA agents. The figure, which is taken for thirty AOA, TDOA and FDOA measurements, shows the cluster-level world model for this situation. It is clear that adding the FDOA measurements ultimately results in improved positional accuracy, compared with the AOA and TDOA result of figure 6. This is indicated by the very sharp peak in the cluster-level world model[1].

Figure 10 quantifies the results of figure 9 using the rms positional error as the metric. This figure shows quite clearly how both weighted and unweighted fusion improves the positional accuracy of emitter location relative to emitter location by just one type of agent. It is found that after about 30

[1]This is not always the case when the number of measurements is relatively few.

Authorized licensed use limited to: Cranfield University. Downloaded on November 18, 2009 at 05:06 from IEEE Xplore. Restrictions apply.

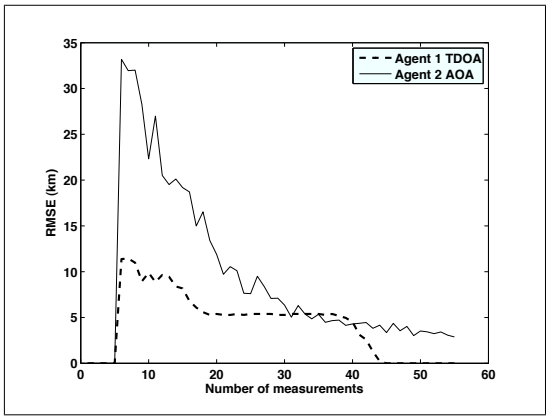

Figure 7. Effect of number of measurements on the average rms positional error. In this case each agent separately geolocates. Agent 1 is TDOA agent, Agent 2 is AoA agent

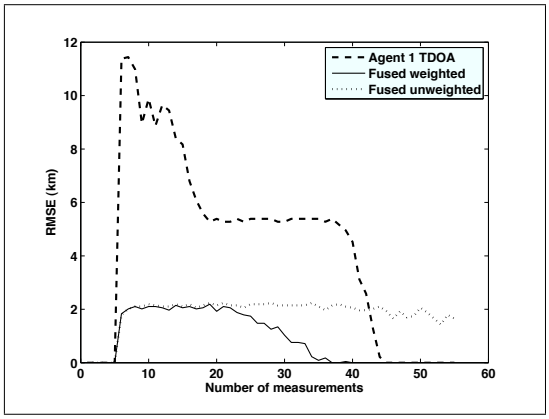

Figure 8. Effect of number of measurements on the average rms positional error, for both unweighted and weighted fusion of AoA and TDOA agents

measurements, the weighted measurements are more accurate than the unweighted measurements, for this scenario.

IV. Clustered agent data fusion

Because the Hough Transform provides a unified environment for the local own-world models of the agents as well as the cluster-level model of the clustered agents, it is possible to apply the same method of weighted data fusion, as described above, at a higher level where there are several clusters of agents.

In this case, the Agents within each cluster generate a cluster-level world model for that cluster and this is used to obtain the weight, $w_{cluster_i}$ for that cluster (assumed here to be the ith). These weights are used to weight the cluster-level world models. The overall model is the weighted combination of cluster-level world models, given by:

$$A_{multi} = \frac{1}{w_{cluster_1}} A_{cluster_1} + \cdots \frac{1}{w_{cluster_i}} A_{cluster_i} \quad (11)$$

The scenario in figure 11 has been set up in order to illustrate this. Here, three Unmanned Aerial Vehicles (UAVs) are used,

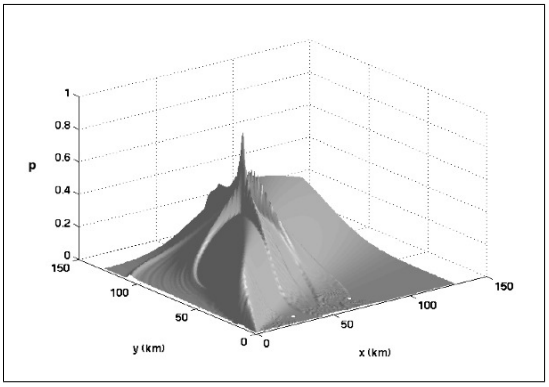

Figure 9. The cluster-level world model for AOA, TDOA and FDOA agents after a total of 30 measurements have been taken along the respective flight paths

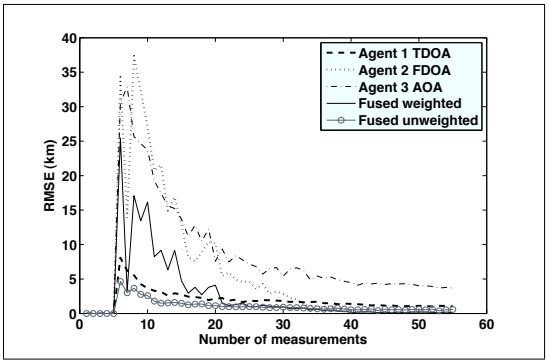

Figure 10. Effect of number of measurements on the average rms positional error, showing effect of both unweighted and weighted fusion for AOA, TDOA and FDOA Measurements

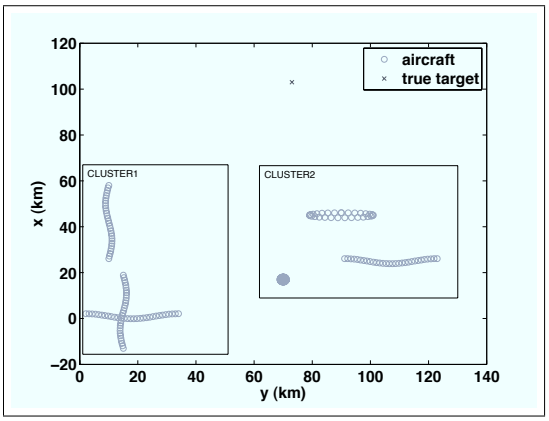

Figure 11. Scenario for cluster-level data fusion, using two clusters, illustrated as rectangles.

Authorized licensed use limited to: Cranfield University. Downloaded on November 18, 2009 at 05:06 from IEEE Xplore. Restrictions apply.

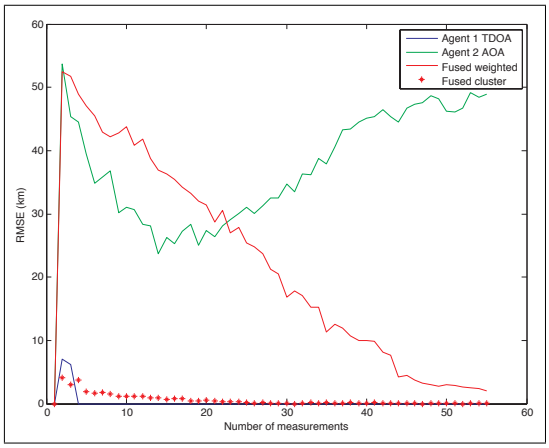

Figure 12. Average RMS error over 50 simulations for the scenario shown in figure 11 for cluster 1

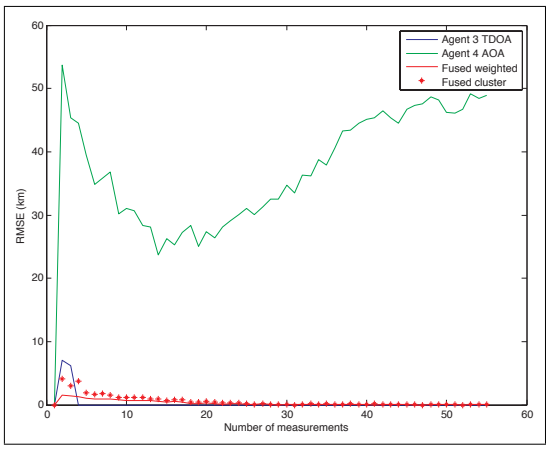

Figure 13. Average RMS error over 50 simulations for the scenario shown in figure 11 for cluster 2. Cluster 2 has a better geometry of the agents and thus can converge quicker to a true target position

as in the previous scenario, and form cluster 1. In this cluster, two UAVs fly North and follow a wavy path, whilst one UAV flies East. The North flying UAVs act as a TDOA agent and the East flying UAV acts as an AOA agent. In addition, three more UAVs are added to the scenario. One flies in a tight circular path, a second flies in an oval racetrack path whilst the third flies generally in an Easterly direction. The UAV flying along the oval path takes AOA measurements, with an rms error of 0.02rad whilst the other two platforms act as a TDOA agent with an rms error of 10^{-7}s timing error. Each cluster has good communications so that agents within that cluster can fuse their results as described above. However, communications between clusters is sporadic. This means that each cluster carries out individual cluster-level fusion, and the clusters can only fuse their cluster levels together when the communications between them is assumed to be good.

Figure 12 and figure 13 show the effect of using two clusters to geolocate a single emitter. Figure 12 represents the rms error of the emitter position for Cluster 1 and figure 13 shows the rms error for Cluster 2. In each figure, the rms positional error is plotted as a function of the number of measurements made in each cluster. This forms the cluster-level world model (this is shown as the red solid line in figures 12-13). Only after this model has been created by each cluster are the two cluster models fused to form a high level model.

The result of fusing the weighted cluster-level models is shown as the red stars in both figures. It is clear that the weighted high-level world model has a much higher accuracy than the weighted cluster-level models for either cluster. Furthermore, the use of cluster level fusion results in a much faster 'convergence' of the rms error as a function of number of measurements. The significant improvement in emitter geolocation performance by adopting a cluster-level fusion strategy is most certainly due to the effect of minimising the effect of GDOP by using different 'look' directions for each cluster even though the fusion at this level takes place relatively infrequently.

V. Conclusion

The paper [8] considered the case where all the agents were constrained to operate within a single cluster due to restrictions placed on the information exchange by the wireless communications network that they shared. In this paper, we have taken the concept of cognitive agents one step further where agents naturally form multiple clusters. Each cluster is assumed to consist of multiple self-aware agents that forms a fusion hierarchy: each agent is able to geolocate individually, clusters of agents can refine the emitter position using fusion and clusters of agents can further refine the position estimate by taking advantage of the different view of the target by each cluster. In this paper, the benefits of providing fusion between clusters of self-aware agents has been examined and the advantages of the clustered (hierarchical) agent-based data fusion has been clearly demonstrated.

References

[1] A. Mikhalev and R. Ormondroyd, "UAV-based Non-line-of-sight geolocation of emitter," *Proc. 21 International UAV Systems Conference*, pp. 25.1–25.9, April 2006.

[2] ——, "Fusion of Sensor Data for Source Localization using the Hough Transform," *Proc. The 9th International Conference on Information Fusion*, p. paper266, July 2006.

[3] ——, "Comparison of Hough Transform and Particle Filter methods of emitter geolocation using fusion of TDOA data," *Proc. of the 4th Workshop on Positioning, Navigation and Communication 2007, (WPNC 2007)*, pp. 121–127, March 2007.

[4] R. A. Poisel, *Electronic Warfare Target Location Methods*. Artech House Inc, Norwood MA, 2005.

[5] D. J. Torrieri, "Statistical theory of passive location systems," *IEEE Trans. on Aerospace and Electronic Systems*, vol. 2, pp. 183–198, 1984.

[6] K. F. McDonald and W. S. Kuklinski, "Track maintenance and positional estimation via ground moving target indicator and geolocation data fusion," *Proc. of the IEEE Radar Conference*, pp. 239–245, 2001.

[7] E. D. S and R. G. Brown, "The discrete probability density method for emitter geolocation," *Ottawa Technical Memorandum, Defence Research and Development Canada*, p. June 2003, 2003-068.

[8] A. Mikhalev and R. Ormondroyd, "Passive emitter geolocation using agent-based data fusion of aoa, tdoa and fdoa measurements," *Information Fusion, 2007 10th International Conference on*, pp. 1–6, 9-12 July 2007.

[9] J. Ferber, *Multi-agent Systems: Introduction to Distributed Artificial Intelligence*. Addison Wesley, 1999.

Authorized licensed use limited to: Cranfield University. Downloaded on November 18, 2009 at 05:06 from IEEE Xplore. Restrictions apply.

Passive Emitter Geolocation using Agent-based Data Fusion of AOA, TDOA and FDOA Measurements

Alex Mikhalev and Richard Ormondroyd
Department of Aerospace Power and Sensors
Cranfield University
The Defence Academy of the UK
Shrivenham, Oxfordshire, SN6 8LA, UK
Email: a.mikhalev@cranfield.ac.uk and r.f.ormondroyd@cranfield.ac.uk

***Abstract*— This paper considers the use of the Hough Transform image processing method applied to the problem of agent-based multi-platform, multi-sensor emitter geolocation. In this paper, improved geolocation is obtained through the fusion of three different types of measurement: angle of arrival, time difference of arrival and frequency difference of arrival. One of the main aims of this paper is to introduce a novel method of obtaining the weights for optimal combining of the different types of measurement during fusion. Comparative results of the new method obtained by simulation are presented.**

Keywords: Emitter geolocation, Agent-based fusion, Hough Transform

I. Introduction

In earlier papers [1] [2] [3], a new method of emitter geolocation was presented based on image processing techniques rather than the more usual classical methods based on triangulation and hyperbolic location [4] or statistical methods [5] [6] [7]. The new method is based on the Generalized Hough Transform (GHT) and one of its key features is that it is able to fuse different types of measurement data (such as angle of arrival measurements (AOA) and time difference of arrival measurements (TDOA)) by transforming them into conditional probabilities and storing them in a unified parameterized space. Thus, they can then be merged easily.

This paper has two main aims. First, the algorithm given in [2] is extended to include fusion of Frequency Difference of Arrival (FDOA) measurement data with AOA and TDOA data. Second the algorithm is improved by weighting each method of emitter geolocation prior to fusion and the paper presents a novel method of providing the weights.

The advantage of adding FDOA measurements is that they produce emitter location estimates whose error ellipse may lie in a different direction to the error ellipses of the other two methods. Consequently, it is possible to minimize the effect of geometric dilution of precision (GDOP) by suitable fusion of the different types of measurement data.

When fusing different types of data, it is usual to weight the contributions to the estimate according to the accuracy of the *measurements*. This is certainly the case with the maximum likelihood method [6]. However, for the case of a non-linear problem, such as emitter geolocation, there is the additional factor of the GDOP that must be taken into account. Here we propose a method of weighting that includes the effect that the measurement errors have on the *position estimate* (i.e. the weight we derive includes the effect of GDOP).

In this paper we assume that it is possible to extract TDOA and FDOA measurements from pairs of platforms using appropriate signal processing equipment. The bandwidth of this equipment is optimized to either the TDOA measurement or the FDOA measurement, since they have different requirements [8]. It is also assumed that in order to make these measurements, broadband data links may be needed between the platforms. AOA measurements are assumed to be made using a third DF receiver, as described below.

II. Use of the Generalized Hough Transform for Emitter Geolocation

A. Adaptation of the Generalized Hough Transform

The Generalized Hough Transform is a transformation of points from the input space, referred to as the feature space (FS), into curves in parameter space (PS) that can be used for the detection of geometric patterns. This method is based on the fact that all points from a straight line (say) positioned in FS can be mapped to a single point in PS. The GHT can be represented by the following algorithm:

1) A fixed grid representing the parameters (x, y) that need to be estimated is created
2) At each point on the grid, the *voting function* is evaluated using the likelihood that the estimated emitter position is at (x, y) given the measurement β, $p(x, y|\beta)$, and then accumulated in an array, A:

$$A(x, y) = \frac{1}{L} \sum_{l=1}^{L} p(x, y|\beta_l) \tag{1}$$

   where β_l is the lth measurement of a total L.
3) The estimate is taken as the grid position corresponding to the peak accumulated likelihood

B. Angle of arrival

Consider a 2D scenario with M receivers (that may be mobile) and one stationary radio emitter. Assume that the receivers can obtain the AOA of the emitted signal using an antenna array and also assume that the measurement errors

Authorized licensed use limited to: Cranfield University. Downloaded on November 18, 2009 at 05:06 from IEEE Xplore. Restrictions apply.

in the AOA are Gaussian (although other distributions can be accommodated easily). The voting function can be defined in terms of the conditional pdf, $p(x, y|\theta_i)$, of the emitter being located at some point (x, y)) within the search space given the measurement θ_i. This conditional probability for the AOA measurements has the form:

$$p(x, y|\theta_i) = \frac{\exp\left(-\frac{(\xi-\theta_i)^2}{\sigma_{\theta_i}^2}\right)}{\sqrt{2\pi}\sigma_{\theta_i}} \quad (2)$$

where θ_i is the measured angle at the ith receiver and ξ is the calculated angle from the ith receiver at point (x_{r_i}, y_{r_i}) to the point (x, y). σ_{θ_i} defines the standard deviation of the AOA measurement error for that receiver.

Although the point (x, y) could lie anywhere within the search space, in practice, the search space is split into a regular grid and (x, y) is constrained to lie at one of the grid points and (2) is evaluated at each of these grid points. Assuming that multiple measurements are made at each receiver, the pdf is evaluated for each measurement for all receivers. In this method, the pdfs due to each measurement are accumulated as follows:

$$A_{AOA}(x, y) = \frac{1}{M}\sum_{m=1}^{M} p(x, y|\theta_m) \quad (3)$$

where M represents the total number of measurements made. This accumulated pdf now represents the voting array for the Hough Transform. As an example, consider two stationary receivers located at (20km,10km) and (20km,30km) respectively and a single emitter located at (60km,80km). At each receiver a single AOA measurement was taken and the standard deviation of each measurement due to the effect of DF receiver noise was taken as $\sigma_\theta = 0.02$ radians. The corresponding Hough Transform space for these AOA measurements is shown in Fig. 1. The z axis of this figure is the accumulated likelihood A_{AOA}. The maximum of the Hough Transform space corresponds to the estimated position of the emitter.

C. Time difference of arrival

The following illustrates the Hough Transform method for the case of emitter geolocation using time difference of arrival (TDOA). Assume that we can obtain the TDOA between two spatially separated receivers, r_1 and r_i using signal cross-correlation, or some other delay-estimation technique, where r_1 represents the first receiver, and r_i is the ith receiver for index $i = 2, 3, ..., M$. The range of the emitter to the ith receiver is:

$$R_i = \sqrt{(x_{r_i} - x)^2 + (y_{r_i} - y)^2} \quad (4)$$

where (x, y) is the emitter location and (x_{r_i}, y_{r_i}) is the known location of the ith receiver. The range difference between receiver R_i and receiver R_1 is:

$$\begin{aligned} c\tau_{i,1} &= R_i - R_1 \\ &= \sqrt{(x_{r_i} - x)^2 + (y_{r_i} - y)^2} \\ &\quad -\sqrt{(x_{r_1} - x)^2 + (y_{r_1} - y)^2} \end{aligned} \quad (5)$$

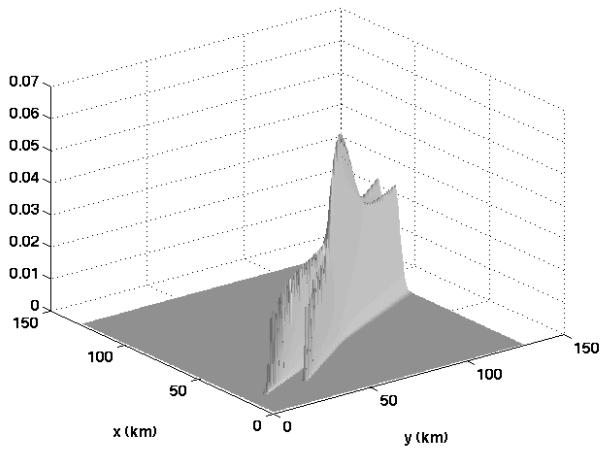

Fig. 1. Hough Transform space for AOA-only measurements

where, $\tau_{i,1}$ is the measured TDOA between the ith receiver and receiver 1 and c is the velocity of light.

The pdf of the emitter location for this case is given by:

$$p(x, y|\tau_{i,1}) = \frac{\exp\left(-\frac{(R_{i,1}-c\tau_{i,1})^2}{2\sigma_r^2}\right)}{\sqrt{2\pi}\sigma_r} \quad (6)$$

where $R_{i,1}$ is the difference between the range of a particular point on the grid to receiver 1 and the range from the same grid point to receiver i and σ_r is the range error for this measurement. The range error is dependent upon the error in the time difference of arrival measurement, σ_{TDOA}, and the geometric dilution of precision (GDOP). According to [8] the range error for a single TDOA measurement is given by:

$$\sigma_r = \frac{c\sigma_{TDOA}}{2sin(\frac{\Theta}{2})} \quad (7)$$

where the numerator represents the timing measurement error and the denominator is the GDOP. Θ is the angle subtended between the two lines of position from receiver 1 to the emitter and receiver i to the emitter, respectively. There are a number of different theoretical approximations for σ_{TDOA} depending upon the assumptions made regarding the SNR of the received signal [4]. For good SNR conditions it is common to assume that the standard deviation of the timing error is given by [4]:

$$\sigma_{TDOA} \approx \frac{1}{W\sqrt{\text{SNR}}} \quad (8)$$

where W is the noise bandwidth of the TDOA receiver. Using (8), the range error becomes:

$$\sigma_r = \frac{c}{2Wsin(\frac{\Theta}{2})\sqrt{\text{SNR}}} \quad (9)$$

Using the conditional pdf (6), the voting array (accumulator) for the Hough Transform can be built using:

$$A_{TDOA}(x, y) = \frac{1}{L}\sum_{l=1}^{L} p(x, y|\tau_{l,1}) \quad (10)$$

Authorized licensed use limited to: Cranfield University. Downloaded on November 18, 2009 at 05:06 from IEEE Xplore. Restrictions apply.

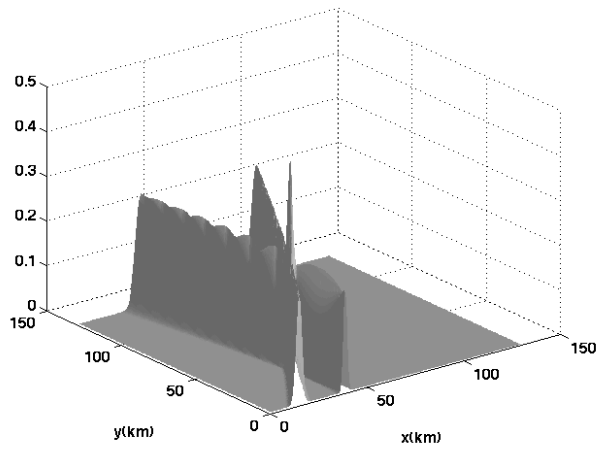

Fig. 2. Hough Transform space for TDOA-only measurements

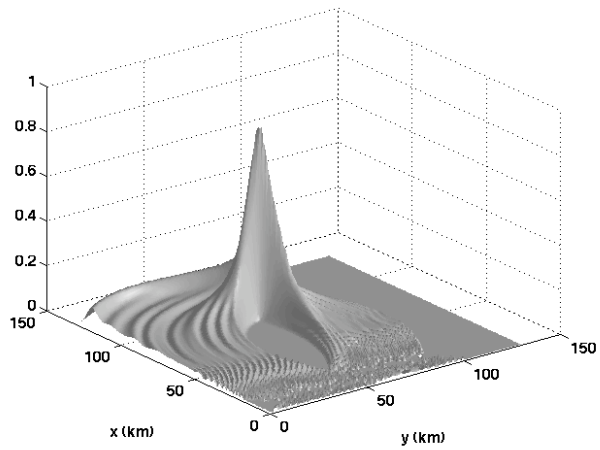

Fig. 3. Hough Transform space for FDOA-only measurements

where L represents the actual number of TDOA measurements taken.

As an example, consider the case of emitter geolocation using three stationary receivers. These are located at: (20km, 10km), (20km, 75km), (60km, 10km). The emitter is located at (40km, 40km). In the simulation, it is assumed that the bandwidth of the received signal is $W = 1$MHz and the SNR +3dB, leading to a value for $\sigma_{TDOA} = 7 \times 10^{-7}$s. Only two TDOA measurements are taken: (i) between receiver 1 and receiver 2 and (ii) between receiver 1 and receiver 3. The resulting Hough Transform space due purely to the provided TDOA information is shown in Fig 2, where the z axis represents A_{TDOA}. The dominant peak in the Hough Transform space denotes the likely emitter position.

D. Frequency difference of arrival

The following illustrates the Hough Transform method for the case of emitter geolocation using frequency difference of arrival (FDOA). Assume that we can obtain the FDOA measurement f_{d_i} between the two spatially separated receivers, r_1 and r_i using a Doppler receiver of bandwidth B. The individual Doppler shifts at r_1 and r_i are given by:

$$D_1 = -\frac{f_0}{c}\frac{v_{x_{r_1}}\left(x - x_{r_1}\right) + v_{y_{r_1}}\left(y - y_{r_1}\right)}{\sqrt{\left(x - x_{r_1}\right)^2 + \left(y - y_{r_1}\right)^2}} \tag{11}$$

$$D_i = -\frac{f_0}{c}\frac{v_{x_{r_i}}\left(x - x_{r_i}\right) + v_{y_{r_i}}\left(y - y_{r_i}\right)}{\sqrt{\left(x - x_{r_i}\right)^2 + \left(y - y_{r_i}\right)^2}} \tag{12}$$

The pdf of the emitter location for this case is given by:

$$p\left(x, y | f_{d_i}\right) = \frac{\exp\left(-\frac{\left(D_i - D_1 - f_{d_i}\right)^2}{\sigma_{f_d}^2}\right)}{\sqrt{2\pi}\sigma_{f_d}} \tag{13}$$

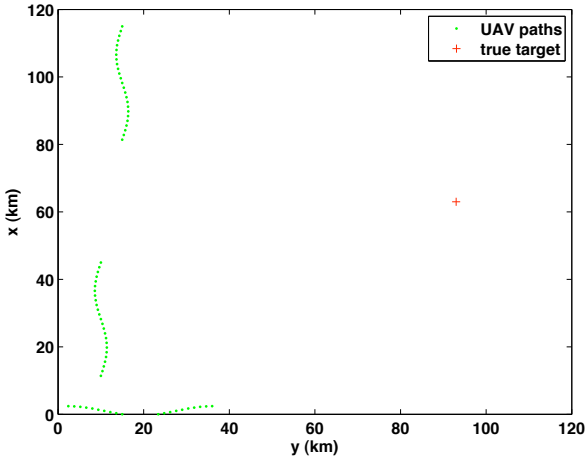

Fig. 4. Scenario for FDOA for emitter geolocation

The resulting accumulator array for N measurements is given by:

$$A_{FDOA}(x, y) = \frac{1}{N}\sum_{m=1}^{N} p\left(x, y | f_{d_i}\right) \tag{14}$$

Fig. 3 shows the ability of two moving platforms to geolocate an emitter, where the z axis represents the accumulated likelihood, A_{FDOA}. In this case, the two platforms of interest are moving North at 40m/s according to a wavy path, as described in Fig. 4; where $\sigma_{f_d} = 12$mHz is taken from [4] as a Cramer-Rao lower bound value for $B = 25$kHz with an integration time $T = 1$s and $SNR = +3$dB. In this case 25 measurements were used, starting at the bottom of the path and terminating at the top of the path.

Authorized licensed use limited to: Cranfield University. Downloaded on November 18, 2009 at 05:06 from IEEE Xplore. Restrictions apply.

III. Fusion of AoA and TDOA with FDOA Measurements

Because the sensor data has been transformed into conditional probabilities and are now in a unified parameterized space, irrespective of the type of measurement, it is possible to merge the TDOA sensor data with the AoA sensor data.

$$A(x,y) = \frac{1}{L}\sum_{l=1}^{L} p(x,y|\tau_{l,1}) + \frac{1}{M}\sum_{m=1}^{M} p(x,y|\theta_m) + \frac{1}{N}\sum_{m=1}^{N} p(x,y|f_{d_i}) \quad (15)$$

Fig. 5 shows the ability of three moving platforms to geolocate an emitter according to the scenario shown in Fig. 6. In Fig. 6, the dots indicate the paths of the three platforms, the large cross indicates the true target position at (92km, 62km). In this case, the two platforms moving North at 40m/s according to a wavy path are able to take twenty five TDOA and FDOA measurements, whereas the platform moving East at 40m/s is able to take twenty five AOA measurements only. The standard deviation of the TDOA measurement error in this simulation is set at 7×10^{-7}s and the standard deviation of the AOA error was set at a realistic value of 0.02 radians and the standard deviation of the FDOA measurement was set at 12mHz. This set of results shows how it is possible to fuse three different measurement types using the Hough Transform, with the very sharp peak in the accumulated likelihood function giving the estimated emitter position.

As well as providing the scenario, Fig. 6 shows the effect of running the simulations several times. The small triangles indicate the estimated position for five different runs of the simulation for AOA-only measurements, and it is clear that there is a large spread in the position estimate. The squares show the position estimates for TDOA-only measurements, also for five simulation runs. Similarly, the diamonds show the position estimates for FDOA-only and the asterisks show the fused results.

In the next section we show how the geolocation accuracy can be improved by weighting the contributions to the accumulator array from the AOA, TDOA and FDOA measurements in (15).

IV. A Method of Weighted Fusion

When fusing different measurement types, it is usual to weight the individual contributions of the measurements according to their measurement error [6]. However, for emitter geolocation, the problem is extremely non-linear and the effect of the measurement errors on the position error is augmented by the GDOP for that emitter/sensor platform scenario. It is important to recognize that each type of measurement (AOA, TDOA and FDOA) provide their own, different, contributions to the GDOP and simply weighting according to measurement

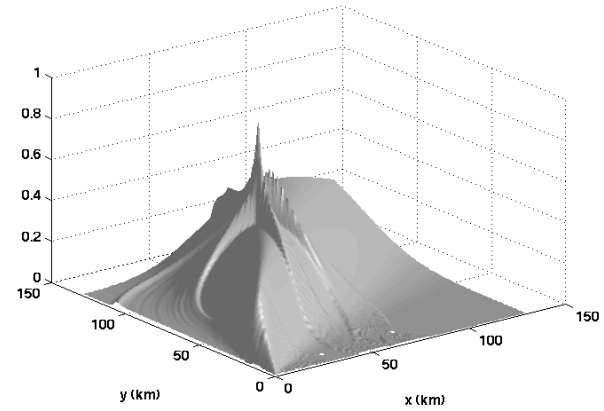

Fig. 5. Hough Transform space for fusion of AOA, TDOA and FDOA measurements

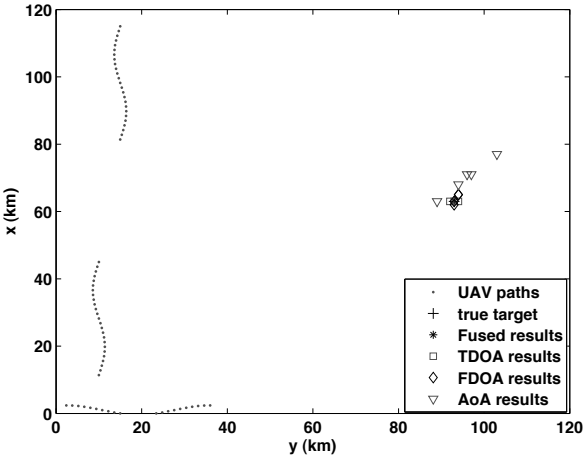

Fig. 6. Scenario for fusion of AOA, TDOA and FDOA measurements

error does not represent the true impact of the error on the positional accuracy of the emitter position estimate.

In this section, we propose a novel form of obtaining the weights, where the aim is to compensate for the different contributions to the emitter position error from each of the different measurement types according to their GDOP, for that scenario.

$$A(x,y) = \frac{w_{TDOA}}{L}\sum_{l=1}^{L} p(x,y|\tau_{l,1}) + \frac{w_{AOA}}{M}\sum_{m=1}^{M} p(x,y|\theta_m) + \frac{w_{FDOA}}{N}\sum_{m=1}^{N} p(x,y|f_{d_i}) \quad (16)$$

where, w_{TDOA}, w_{AOA} and w_{FDOA} are the weights for the three types of measurement which are calculated according to

Authorized licensed use limited to: Cranfield University. Downloaded on November 18, 2009 at 05:06 from IEEE Xplore. Restrictions apply.

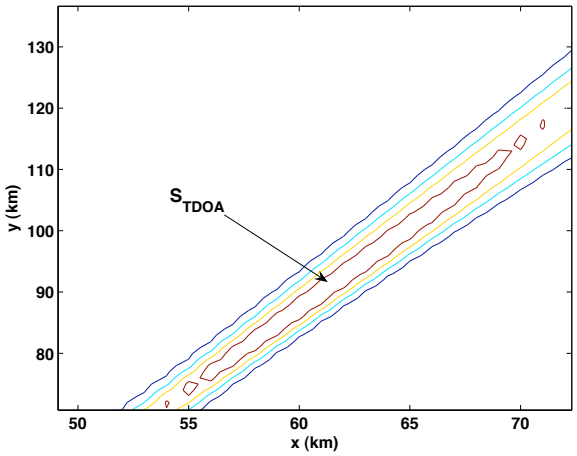

Fig. 7. Contour plot of (10) for the TDOA measurements in the range 55%-75% of the peak value, highlighting the area of the 75% contour

the impact that GDOP has on them. This is achieved directly from the accumulated pdfs of the Hough Transform.

For example, the accumulated pdf for a particular measurement type, such as TDOA, given by (10) is first normalized by its peak value and then generated as a contour plot, as shown in Fig. 7 for several contours in the range 55%-75%. We then threshold this contour plot, (we have chosen this threshold to be set at 75% of the maximum). The area contained within this threshold contour, S_{TDOA}, is then obtained. This is repeated for the case of the AOA measurements whose accumulated pdf is given by (3) and the FDOA measurements whose accumulated pdf is given by (14). The areas contained within the respective contours are: S_{AOA} and S_{FDOA}. It will be clear that the larger the area of the contour, the greater the contribution of these measurements to the positional error and hence a smaller weight is required.

The weights are given by:

$$w_{AOA} = \frac{S_{tot}}{S_{AOA}} \tag{17}$$

$$w_{TDOA} = \frac{S_{tot}}{S_{TDOA}} \tag{18}$$

$$w_{FDOA} = \frac{S_{tot}}{S_{FDOA}} \tag{19}$$

where S_{tot} is the area of the total search space.

V. Agent-based Fusion

Agent-based systems are regarded as a new paradigm which provide a novel approach to sensor fusion. Here, we apply the concept of agents to the problem of emitter geolocation using the Hough Transform space as the model of the environment where the common goal of the agents is the geolocation of the emitter. In order to cooperate in the pursuit of this common goal, these agents use the ability of the Hough Transform method to obtain the weights of the measurements in accordance with their accuracy, as described in the previous section, to self-weight their own measurements and hence obtain their own contribution to their collaborative fused estimate and communicate this to the other agents or central control (i.e. they have the property of self-awareness).

In this paper, we relate the type of measurement taken to be an agent. For example, two platforms may be able to take both TDOA measurements and FDOA measurements and this corresponds to the case where there are two agents: one capable of geolocating using TDOA measurement and one capable of geolocating from FDOA measurements. A third agent geolocates using AOA. In the next section, we show how agents can geolocate independently and collaboratively.

VI. Results

In order to illustrate the new method consider the scenario shown in Fig. 8. In this scenario, two platforms are moving North at 40m/s according to a wavy path and they are able to take several TDOA measurements (Agent 1) along this path, whereas the platform moving East at 40m/s is only able to take AOA measurements (Agent 2). The standard deviation of the TDOA measurement error in this simulation is set at 7×10^{-7}s and the standard deviation of the AOA error was set at a realistic value of 0.02 radians. The true target position is at (92km,62km). Also shown in this figure are the effects of running the simulations a number of times on the estimated emitter position. Here, the triangles represent the result of using AOA measurements only, the square show the effect of using TDOA measurements only and the asterisks the effect of fusing the different measurements.

Fig. 9 shows how each agent can geolocate the emitter independently using the average rms position error as a metric. In particular, the figure shows the effect of the number of measurements on the the average rms error as the platforms move along their respective flight paths. In order to obtain the average rms error the simulations were repeated 50 times and the average taken. It is clear for this scenario that TDOA measurements generally provide a more accurate position estimate.

Fig. 10 shows the benefit of fusing the TDOA and AOA measurements for both weighted and unweighted cases. Two observations can be made. First, fusion of the measurements significantly improves the positional accuracy of the geolocation algorithm. Second, the impact of weighting is also clear because the weighted result tends to be much more accurate in terms of rms error. It should be noted that the precise results of rms position error are strongly dependent upon the platform/emitter geometry, and hence the scenario, because this affects the GDOP.

Fig. 11 shows the effect of fusing FDOA with TDOA and AOA for the scenario of Fig. 8. In this case the platforms travelling North are now able to perform TDOA and FDOA measurements. It is clear that adding the FDOA measurements ultimately results in improved positional accuracy, although

Authorized licensed use limited to: Cranfield University. Downloaded on November 18, 2009 at 05:06 from IEEE Xplore. Restrictions apply.

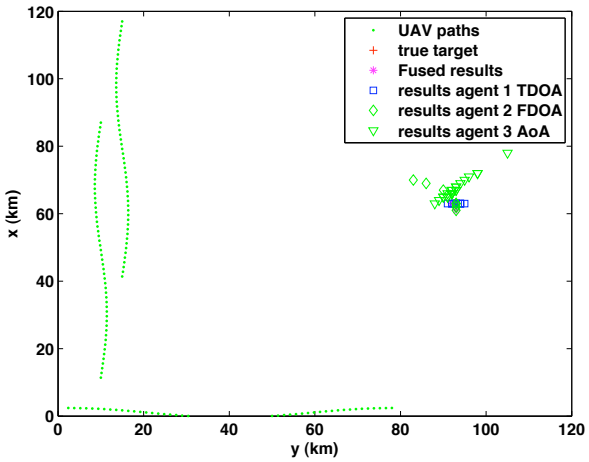

Fig. 8. Agent based scenario

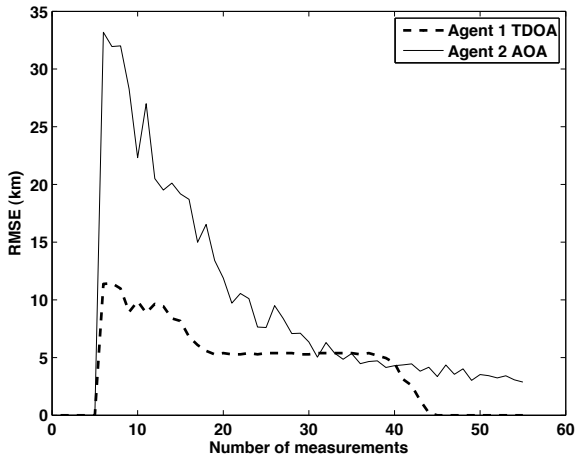

Fig. 9. Effect of number of measurements on the average rms positional error. In this case each agent separately geolocates. Agent 1 uses TDOA only, Agent 2 uses AoA only

this is not immediately the case when the number of measurements is relatively few. The effect of weighting is also shown. It is found that after about 30 measurements, the weighted measurements are more accurate than the unweighted measurements, for this scenario.

VII. Conclusions

This paper has shown how the generalized Hough Transform can be used to fuse AOA, TDOA, and FDOA measurements. In particular, it has introduced a novel method of weighting the individual sets of measurements according to the impact that they have on the positional error rather than simply according to the measurement error. The results have shown how using weighted fusion has a beneficial effect on reducing the error of the position estimate.

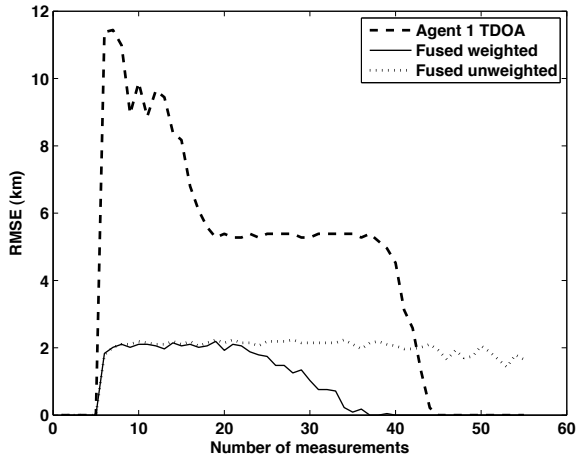

Fig. 10. Effect of number of measurements on the average rms positional error, showing effect of both unweighted and weighted fusion

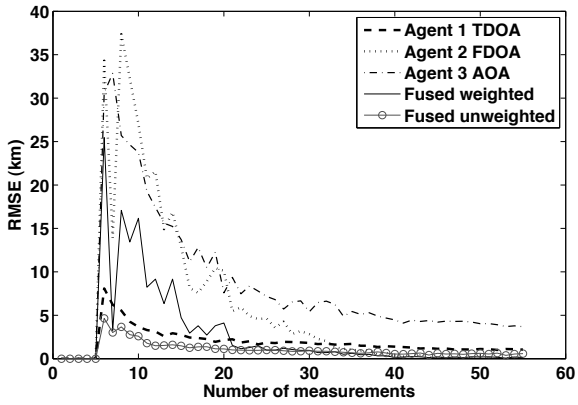

Fig. 11. Effect of number of measurements on the average rms positional error, showing effect of both unweighted and weighted fusion for AOA, TDOA and FDOA Measurements

References

[1] A. Mikhalev and R. Ormondroyd, "UAV-based Non-line-of-sight geolocation of emitter," *Proc. 21 International UAV Systems Conference*, pp. 25.1–25.9, April 2006.

[2] ——, "Fusion of Sensor Data for Source Localization using the Hough Transform," *Proc. The 9th International Conference on Information Fusion*, p. paper266, July 2006.

[3] ——, "Comparison of Hough Transform and Particle Filter methods of emitter geolocation using fusion of TDOA data," *Proc. of the 4th Workshop on Positioning, Navigation and Communication 2007, (WPNC 2007)*, pp. 121–127, March 2007.

[4] R. A. Poisel, *Electronic Warfare Target Location Methods*. Artech House Inc, Norwood MA, 2005.

[5] D. J. Torrieri, "Statistical theory of passive location systems," *IEEE Trans. on Aerospace and Electronic Systems*, vol. 2, pp. 183–198, 1984.

[6] K. F. McDonald and W. S. Kuklinski, "Track maintenance and positional estimation via ground moving target indicator and geolocation data fusion," *Proc. of the IEEE Radar Conference*, pp. 239–245, 2001.

[7] E. D. S and R. G. Brown, "The discrete probability density method for emitter geolocation," *Ottawa Technical Memorandum, Defence Research and Development Canada*, p. June 2003, 2003-068.

[8] R. G. Wiley, *Electronic Intelligence: the interception of radar signals*. Artech House Inc, Norwood MA, 1985.

Authorized licensed use limited to: Cranfield University. Downloaded on November 18, 2009 at 05:06 from IEEE Xplore. Restrictions apply.

Comparison of Hough Transform and Particle Filter Methods of Emitter Geolocation using Fusion of TDOA Data

A Mikhalev, R F Ormondroyd
Department of Aerospace, Power and Sensors, Cranfield University,
The Defence Academy of the UK, Shrivenham,Oxfordshire, SN6 8LA, UK
a.mikhalev@cranfield.ac.uk, r.f.ormondroyd@cranfield.ac.uk

***Abstract*— This paper compares the performance of RF emitter geolocation algorithms based on the Hough Transform and the particle filter. Three Hough Transform methods are considered: (a) the generalized Hough Transform, (b) the Randomized Hough Transform and (c) the Hybrid Hough Transform. In each case, the emitter is assumed to provide a signal from which time difference of arrival measurements can be made by pairs of mobile receiving platforms, such as fixed-wing UAVs or fast jets as well as rotorcraft. Typical emitters include cellphones and other types of communication equipment. The paper shows that the Hough Transform outperforms the particle filter both in terms of the RMS positional error and the computational processing requirements.** [1]

I. Introduction

Location of communication emitters has always been of vital importance in military applications and it is now gaining in importance in civilian applications such as: homeland security, summoning the emergency services and the provision of location-based value-added services. Traditional methods of passive RF emitter location are often based on geometrical techniques such as triangulation and hyperbolic location [1]. Recently, a number of statistical methods have been proposed to provide improved accuracy [2][3][4]. In this paper we examine the use of time difference of arrival (TDOA) data obtained from multiple mobile platforms, such as unmanned airborne vehicles (UAV), fast jets and rotorcraft, that are fused using either the Hough Transform (HT) [5] [6] or the particle filter [7] [8] to provide the position estimate.

The Generalized Hough Transform (GHT) [9] is an image processing technique for arbitrary shape detection and Alexiev and Bojilov [10] have proposed it for the elimination of ghost detections in target tracking using multi-sensor data fusion. Others [11] have used it for self-positioning of robots using map matching. Here, we propose the novel application of the Generalized Hough Transform to the task of emitter geolocation.

Particle filters (also known as sequential Monte Carlo methods) are estimation techniques based on simulation used to estimate the parameters of Bayesian models.

[1]This work was funded by the Data and Information Fusion Defence Technology Centre, UK, Project 12.3.2

The paper is arranged as follows. In Section II, the use of three different variants of the Hough Transform to estimate the position of the emitter from the TDOA data is provided. In Section III, the use of the particle filter as a means of estimating the emitter position from TDOA data is given and Section IV presents the emitter location scenario that has been used and provides the main results.

The essence of our paper is to compare whether the non-Bayesian approach of the Randomized Hough Transform can outperform the particle filter in terms of RMS positional error and computational efficiency.

II. Use of the Hough Transform and its Variants for Emitter Geolocation

A. Adaptation of the Generalized Hough Transform

The Hough Transform was patented in 1962 [12] as a mathematical transformation of points from the input space, referred to as the feature space (FS), into curves in parameter space (PS) that can be used for the detection of geometric patterns. This method is based on the fact that all points from a straight line (say) positioned in FS can be mapped to a single point in PS.

Let our sets of hypotheses exist in some coordinate framework (an N-dimensional array). An event can occur within this coordinate system and can indicate with its conditional probabilities a set of hypotheses whose parameters are fixed relative to the event. The conditional probability table of the event can then also be considered as an *N*-dimensional array centered on the event, where *N* is the dimensionality of the hypothesis space. This array is called the *voting array* for the event. It contains the logs of the normalized conditional probabilities and so each event will simply add its own voting array into the accumulator representing the hypothesis space.

Imagine that the hypothesis space is a particular point located in two dimensions. In this case, the hypothesis space is then a 2D array of numbers representing the conditional probability of the event. In this application, the events that are of interest are the observations (i.e. the measurements of the parameters of the source). Associated with each measurement is a probability that the emitter is located at a particular point (x, y) within the search space. This is equivalent to assigning

1-4244-0871-7/07/$25.00 ©2007 IEEE

Authorized licensed use limited to: Cranfield University. Downloaded on November 18, 2009 at 05:07 from IEEE Xplore. Restrictions apply.

the event to a particular part of the hypothesis space. We can obtain the conditional probability voting array for each measurement by placing the emitter into each position in turn and calculating the conditional probability and adding these values to the voting array. The Generalized Hough Transform (GHT) can be represented by the following algorithm:

1) A fixed grid representing the parameters (x, y) that need to be estimated is created
2) At each point on the grid, the likelihood of the estimate being (x, y) given the measurement β, $p(x, y|\beta)$, is evaluated and accumulated in an array, A:

$$A(x, y) = \frac{1}{L} \sum_{l=1}^{L} p(x, y|\beta_l) \tag{1}$$

where β_l is the lth measurement of a total L.
3) The estimate is taken as the grid position corresponding to the peak accumulated likelihood

The following illustrates the Hough Transform method for the case of emitter geolocation using time difference of arrival (TDOA). Assume that we can obtain the TDOA between two spatially separated receivers, r_1 and r_i using signal cross correlation or some other delay-estimation technique, where r_1 represents the first receiver, and r_i is the ith receiver for index $i = 2, 3, ..., M$. The range of the emitter to the ith receiver is:

$$R_i = \sqrt{(x_{r_i} - x)^2 + (y_{r_i} - y)^2} \tag{2}$$

where (x, y) is the emitter location and (x_{r_i}, y_{r_i}) is the known location of the ith receiver. The range difference between receiver R_i and receiver R_1 is:

$$\begin{aligned} c\tau_{i,1} &= R_i - R_1 \\ &= \sqrt{(x_{r_i} - x)^2 + (y_{r_i} - y)^2} \\ &\quad -\sqrt{(x_{r_1} - x)^2 + (y_{r_1} - y)^2} \end{aligned} \tag{3}$$

where, $\tau_{i,1}$ is the measured TDOA between the ith receiver and receiver 1 and c is the velocity of light.

The pdf of the emitter location for this case is given by:

$$p(x, y|\tau_{i,1}) = \frac{\exp\left(\frac{R_{i,1}^2 - c^2\tau_{i,1}^2}{2\sigma_r^2}\right)}{\sqrt{2\pi}\sigma_r} \tag{4}$$

where $R_{i,1}$ is the difference between the range of a particular point on the grid to receiver 1 and the range from the same grid point to receiver i and σ_r is the range error for this measurement. The range error is dependent upon the error in the time difference of arrival measurement, σ_{TDOA}, and the geometric dilution of precision (GDOP). According to [13] the range error for a single TDOA measurement is given by:

$$\sigma_r = \frac{c\sigma_{TDOA}}{2sin(\frac{\Theta}{2})} \tag{5}$$

where the numerator represents the timing measurement error and the denominator is the GDOP. Θ is the angle subtended between the two lines of position from receiver 1 to the emitter and receiver i to the emitter, respectively. There are a number

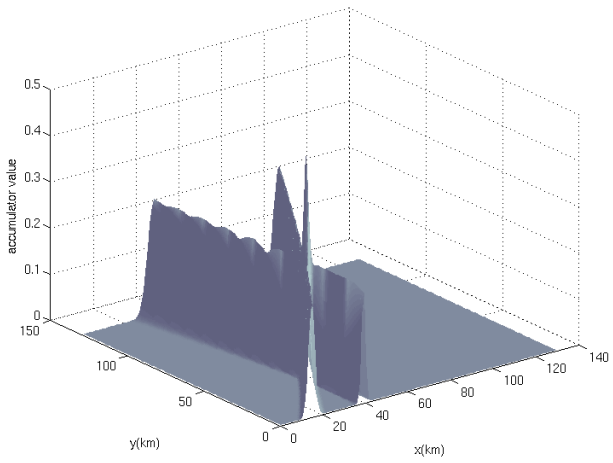

Fig. 1. Hough Transform space for TDOA-only measurements

of different theoretical approximations for σ_{TDOA} depending upon the assumptions made regarding the SNR of the received signal [1]. For good SNR conditions it is common to assume that the standard deviation of the timing error is given by:

$$\sigma_{TDOA} \approx \frac{1}{W\sqrt{\text{SNR}}} \tag{6}$$

where W is the noise bandwidth of the receiver. Using (6), the range error becomes:

$$\sigma_r = \frac{c}{2Wsin(\frac{\Theta}{2})\sqrt{\text{SNR}}} \tag{7}$$

Using the conditional pdf (4), the voting array (accumulator) for the Hough Transform can be built using:

$$A_{TDOA}(x, y) = \frac{1}{L} \sum_{l=1}^{L} p(x, y|\tau_{l,1}) \tag{8}$$

where L represents the number of TDOA measurements taken from the M receivers.

As an example, consider the case of emitter geolocation using three stationary receivers. These are located at: (20km, 10km), (20km, 75km), (60km, 10km). The emitter is located at (40km, 40km). In the simulation, it is assumed that the bandwidth of the received signal is $W = 1$ MHz and the SNR +3dB, leading to a value for $\sigma_{TDOA} = 7 \times 10^{-7}$s. Only two TDOA measurements are taken - between receiver 1 and receiver 2 and receiver 1 and receiver 3. The resulting Hough Transform space due purely to the provided TDOA information is shown in Fig. 1. The dominant peak in the Hough Transform space denotes the likely emitter position.

B. Randomized Hough Transform

Whereas the Generalized Hough Transform considers *every* point on the grid of possible emitter locations, the Randomized Hough Transform (RHT) examines a smaller subset of these points based on probabilistic methods. Our implementation of the Randomized Hough Transform works as follows.

Authorized licensed use limited to: Cranfield University. Downloaded on November 18, 2009 at 05:07 from IEEE Xplore. Restrictions apply.

1) A number of samples representing points on the grid of the parameterized space are generated randomly with a uniform distribution
2) At each selected point on the grid, the likelihood corresponding to each TDOA measurement is evaluated and stored in an array as in (8)
3) The estimated emitter position is taken as the grid position corresponding to the peak accumulated likelihood.

Because the likelihoods are evaluated at fewer grid positions than for the Generalized Hough Transform the computational time and storage requirements are reduced. However, because the effective grid spacing is increased (albeit in a statistical way), the accuracy of the method can be compromised.

When viewed in this way, it will be immediately apparent that there are parallels between the Randomized Hough Transform and the particle filter. However, it is worthy of comment that whereas the particle filter uses a Bayesian approach, the Randomized Hough Transform is non-Bayesian, as indicated by (8).

The particle filter algorithm using multivariate resampling is described in Section III

C. Hybrid Hough Transform

In this paper, we propose the use of a further variant of the Hough Transform, which we call the Hybrid Hough Transform (HHT), that is inspired by the particle filter algorithm and the Multiresolution Hough Transform [14] [6]. The performance of this algorithm will be shown in Section IV to be much better than either the particle filter or the Randomized Hough Transform, on which it is based.

The Randomized Hough Transform algorithm is modified as follows:

1) A number of samples representing points on the grid of the parameterized space are generated randomly with a uniform distribution
2) At each selected point on the grid, the likelihood corresponding to each TDOA measurement is evaluated and stored in an array, as in (8)
3) The grid position (x, y) of the parameterized space corresponding to the peak accumulated likelihood is obtained
4) A fixed grid Generalized Hough Transform is performed around (x, y) using a fixed tile size (for example 10×10 points in our case)
5) The estimate corresponds to the maximum of the updated parameterized space, as shown in Fig. 2

III. Emitter Geolocation using TDOA Data with a Particle Filter Estimator

The following illustrates the method for the case of emitter geolocation using TDOA with a particle filter. As before, it is assumed that the TDOA can be obtained between two spatially separated receivers using the signal cross correlation or some other delay estimation technique and that the equations defining the problem are identical to equations (2) - (7).

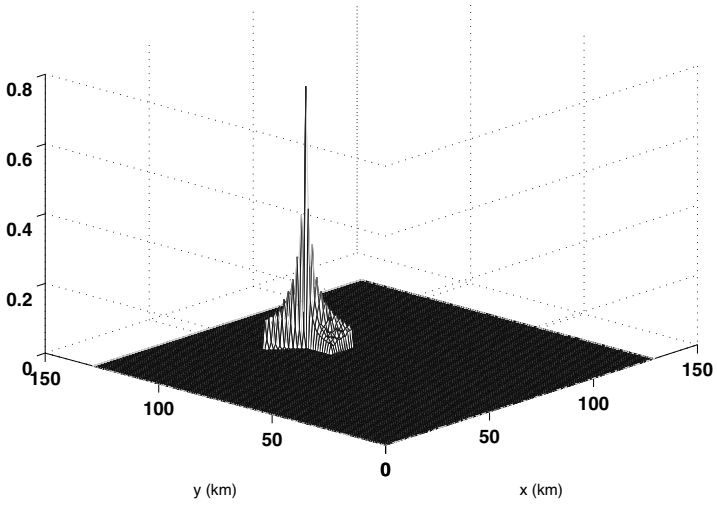

Fig. 2. Parameterized space of the Hybrid Hough Transform

The particle filter has been widely used for target tracking and other applications, such as state or model estimation. In this paper, the particle filter is applied to the problem of geolocation of a radio emitter in multi-path conditions. Although this application looks similar to target tracking, there is a significant difference. In our case the state of the target doesn't change with time which means that a static framework has to be applied, as highlighted in [15].

In order to implement the particle filter to estimate the state vector representing the emitter position, $[\hat{x}, \hat{y}]^T$, using TDOA measurements, the following algorithm was applied [7].

1) For the ith TDOA measurement, $\tilde{\tau}_{i,1}$, generate L particles, each with random position, (x_{p_p}, y_{p_p}) (for $p = 1, \cdots L$), drawn from the 2D search space with uniform distribution.
2) Initialize the weight of each particle: $w_0(x_{p_p}, y_{p_p}) = 1$ for $p = 1 \cdots L$
3) Evaluate the probability of the emitter being located at each of the particle positions given the ith measurement, $p(x_{p_p}, y_{p_p}|\tilde{\tau}_{i,1})$, using the likelihood equation (4)
4) Update the weights of all the particles:

$$w_i(x_{p_p}, y_{p_p}) = w_{i-1}(x_{p_p}, y_{p_p}) \cdot p(x_{p_p}, y_{p_p}|\tilde{\tau}_{i,1}) \quad (9)$$

and normalize it:

$$w_i(x_{p_p}, y_{p_p}) = \frac{w_i(x_{p_p}, y_{p_p})}{\sum_{p=1}^{L} w_i(x_{p_p}, y_{p_p})} \quad (10)$$

for $p = 1 \cdots L$
5) Resample the indices of the particles using multinomial resampling [7]
6) Make copies of resampled particles according to previous step
7) Resample the particles (described below)
8) Repeat from step 1 for next measurement

Authorized licensed use limited to: Cranfield University. Downloaded on November 18, 2009 at 05:07 from IEEE Xplore. Restrictions apply.

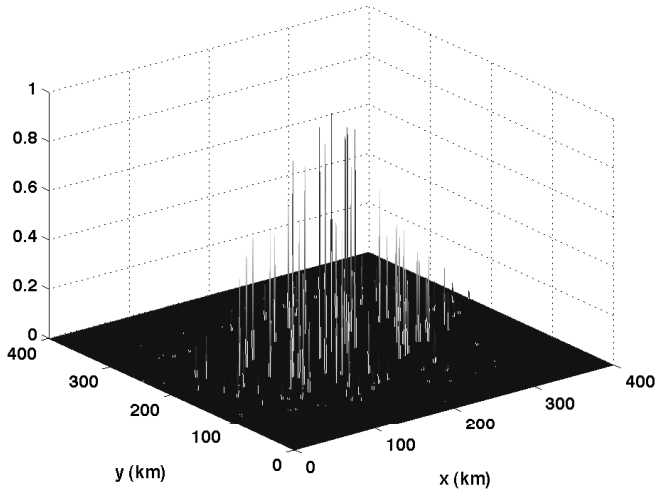

Fig. 3. The distribution of weighted particles after the Mth measurement using multivatiate resampling for the particle filter

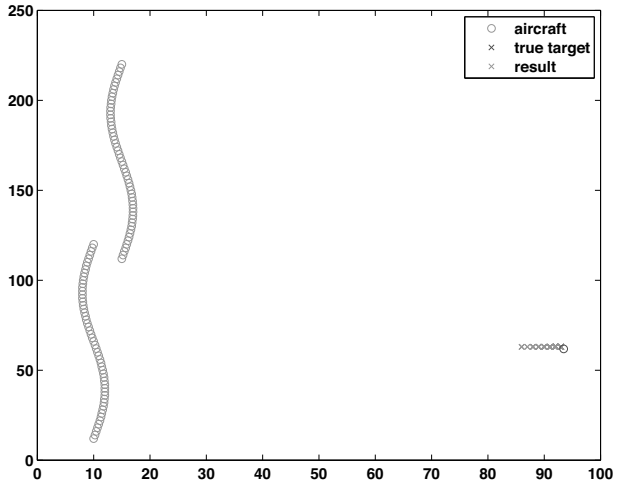

Fig. 4. Scenario of multiplatform emitter geolocation showing the flight paths of 3 UAV platforms and the emitter of interest. The crosses show the estimated emitter position

After all M measurements have been used, the estimated emitter location $(\hat{x}, \hat{y})$ corresponds to the mean position of the particles.

A. Resampling

The resampling method generates new particles from a two-dimensional Gaussian distribution with a mean centered on the position, (x_p, y_p), of the survivor particle from the previous measurement and with covariance matrix $\mathbf{P}$. The resampled particles are generated using:

$$\mathbf{x} = \mathbf{SX} + \mathbf{x}_p\mathbf{I}; \tag{11}$$

where $\mathbf{x}$ is the array of the particle position vectors, $\mathbf{X}$ is the array of zero-mean normally distributed values, $\mathbf{S} = chol(\mathbf{P})^T$ is a matrix of scaling factors for x and y directions determined by the covariance of the distribution (where $chol$ is the Cholesky factorisation of the covariance matrix of the bivariate distribution of $\mathbf{X}$), $\mathbf{x}_p$ is the position vector of the survivor particle from the previous measurement and $\mathbf{I}$ is a $(1 \times L)$ unity matrix. It is usual for:

$$\mathbf{P} = \begin{bmatrix} 0 & 1 \\ 1 & 0 \end{bmatrix} \tag{12}$$

Figure 3 shows the weighted particles after the Mth measurement using multivatiate (Gaussian) resampling.

IV. Simulation Scenario and Results

Fig. 4 shows a simplified scenario in which two UAVs are used to geolocate a single transmitter, denoted as a circle at (93km, 40km). The two UAVs can have arbitrary flight paths, shown here with wavy paths. The speed of the platforms is 60m/s.

Fig. 5 shows the RMS error performance of three estimators as a function of the number of TDOA measurements taken. These were: the Generalized Hough Transform, the Randomized Hough Transform and the particle filter based on [7]. In this figure, the x axis represents the number of measurements taken and the y axis is an average root mean square error over 500 simulation runs for a given number of measurements. For this particular set of simulations the number of particles for the Randomized Hough Transform and particle filter were the same, $N = 8450$. This corresponded to half the number of grid points used in the Generalized Hough Transform. As expected, the RMS error tends to fall as the number of measurements taken increases. It should be noted that the RMS error for the Generalized Hough Transform and the particle filter are very close, even though the particle filter evaluates the position likelihood at half the number of grid points than the Generalized Hough Transform.

However, the average computational time for the three methods, as shown in Fig. 6 shows quite clearly that the Generalized Hough Transform has a much lower computational overhead than the particle filter. Although the error performance of the Randomized Hough Transform is worse than for the Generalized Hough Transform, it offers the lowest computational overhead. In Fig. 7, the number of particles was adjusted so that the RMS error performance of the particle filter and the Randomized Hough Transform were approximately the same. In this case, the number of particles used for the particle filter was 20% of the number of grid points and 75% for the Randomized Hough Transform. Fig, 8, shows that the computational overhead for the particle filter is still substantially more than for the Randomized Hough Transform.

In considering these results, it should be noted that the magnitude of the RMS position accuracy depends quite critically on the relative position of the emitter to the platforms because of the effect of GDOP and different platform/target scenarios

Authorized licensed use limited to: Cranfield University. Downloaded on November 18, 2009 at 05:07 from IEEE Xplore. Restrictions apply.

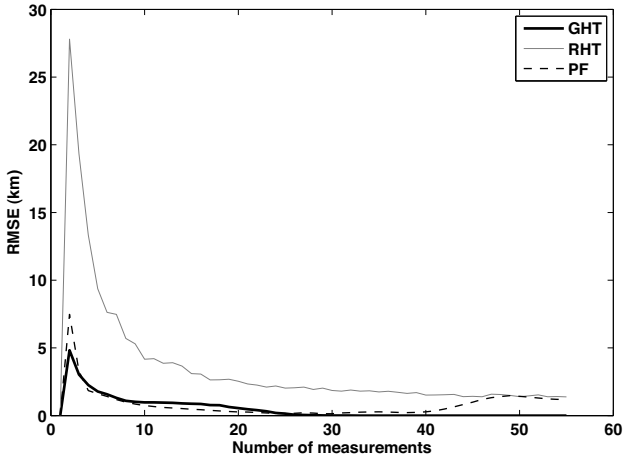

Fig. 5. Average RMS positional error obtained over 500 simulations for different number of measurements. For the Randomized Hough Transform and the PF, the number of particles ($N = 8450$) was 50% of the total number of grid points

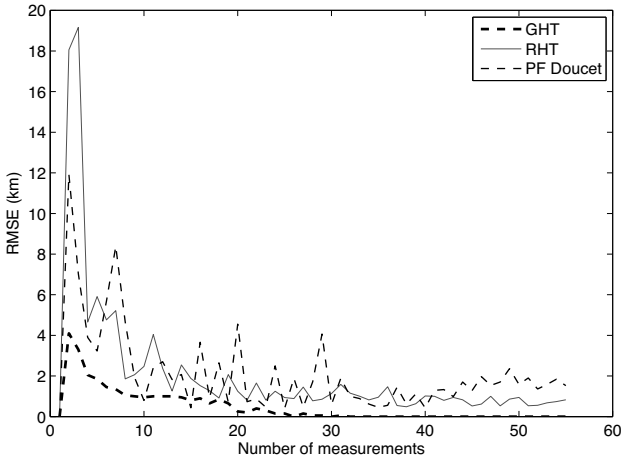

Fig. 7. Average RMS positional error obtained over 20 simulations for different number of measurements. For the particle filter $N = 3380$ (corresponding to 20% of the grid) and for the Randomized Hough Transform $N = 12675$ (corresponding to 75% of the total number of grid points)

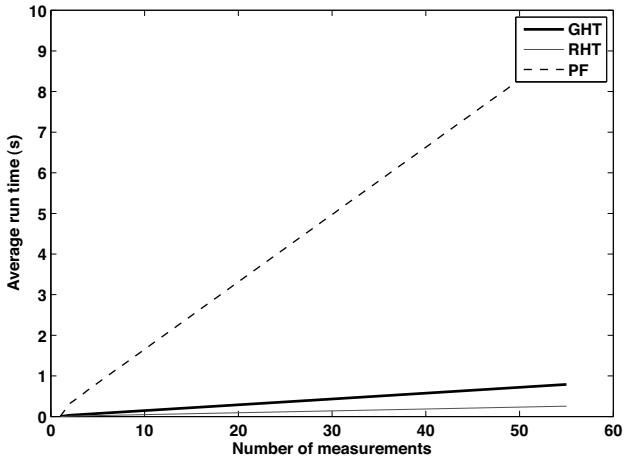

Fig. 6. Average computation time over 500 simulations for different number of measurements for the different estimators

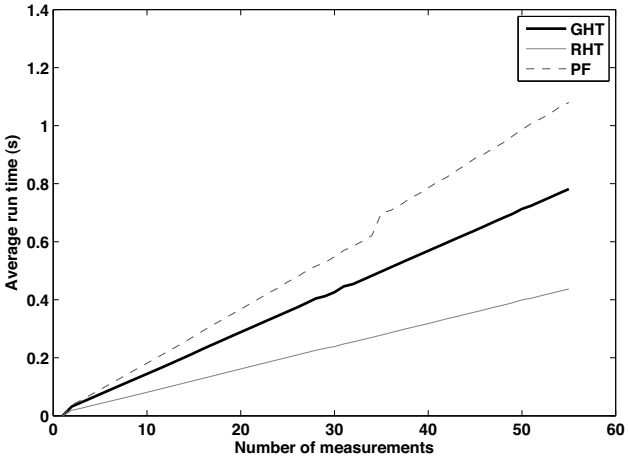

Fig. 8. Average computation time over 20 simulations for different number of measurements for the different estimators

may produce better or worse RMS error, depending on the GDOP but the trends across the three types of estimator remain the same.

The foregoing has shown that the randomized Hough Transform has a low computational overhead, but this is at the expense of accuracy. In contrast, the Generalized Hough Transform has a high accuracy. The Hybrid Hough Transform provides the reduced computational overhead of the Randomized Hough Transform with the accuracy of the Generalized Hough Transform and this is clearly shown in Fig. 9, which compares the RMS positional accuracy of the three Hough Transform methods and Fig. 10 shows the calculation time for the three Hough Transform variants.

The results show that the computational overhead of the Hybrid Hough Transform is slightly higher then Randomized Hough Transform but accuracy of the algorithm is almost indistinguishable from the Generalized Hough Transform.

A. Bayesian Randomized Estimator

It is possible to construct a Bayesian estimator using a similar approach to the Randomized Hough Transform in which the accumulation of likelihoods by arithmetic addition is replaced by taking the product. Such an estimator has been implemented here for comparison with the Hough transform estimators. In this implementation of the Bayesian Randomized estimator, no resampling is carried out on each measurement update cycle. This must be contrasted with the particle filter, where resampling is an important part of the algorithm to prevent degeneracy. The consequence of this on the performance of the Bayesian Randomized estimator will be shown in this section. An example of degeneracy is shown

Authorized licensed use limited to: Cranfield University. Downloaded on November 18, 2009 at 05:07 from IEEE Xplore. Restrictions apply.

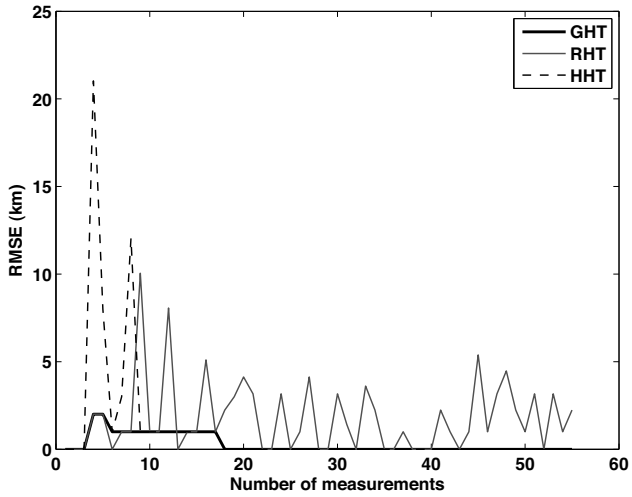

Fig. 9. Average RMS error over 500 simulations, Hybrid Hough transform using fixed grid 10×10 sizes

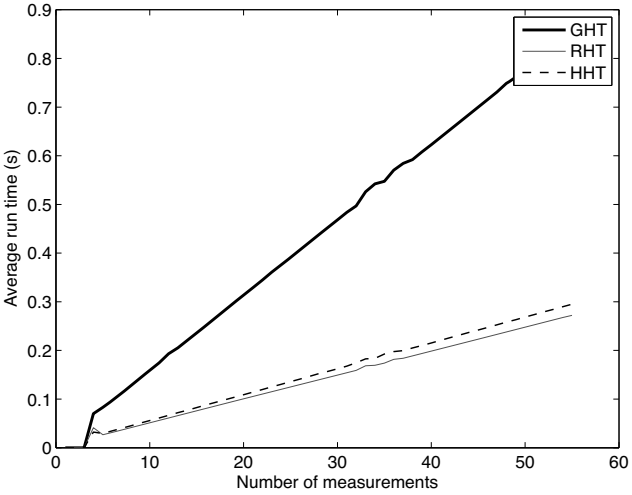

Fig. 10. Average time obtained over 500 simulations for different number of measurements for the same scenario. Hybrid Hough transform using 10×10 fixed grid.

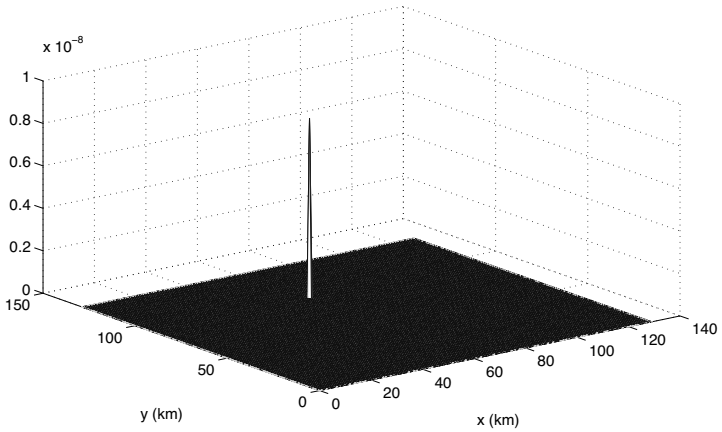

Fig. 11. Parameterized space of the Bayesian Randomized estimator after 55 measurements, showing degeneracy

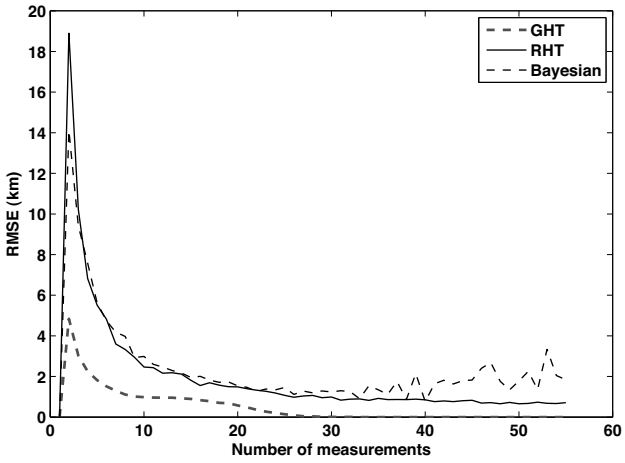

Fig. 12. Average RMS positional error over 500 simulations for the Randomized Hough Transform and Bayesian estimator using the same number of particles (75% of the grid size used for the GHT)

in Fig. 11, which shows the parameterized space after 55 measurements have been used.

The comparison of results are presented in Fig. 12. As can be seen, the RMS positional error performance of the Randomized Hough Transform and the Bayesian estimator are identical. The performance of the two algorithms in terms of computation time are shown in Fig. 13 and again, the computational overhead is identical. However, it is clear from Fig. 12 that the RMS positional error of the Bayesian Randomized estimator starts to diverge with increasing number of measurements, whereas the Randomized Hough Transform and the Generalized Hough Transform continue to converge. Although not shown here, other results for larger numbers of measurements confirm that the RMS error performance of the Bayesian Randomized estimator diverges.

One of the advantages of the Hough Transform approach to dealing with the accumulation of the likelihoods is that it does not require reinitialization of the parameterized space on each measurement update cycle, hence it can be used as both a sequential and a batch estimator at the same time. However, it is impossible to modify the Bayesian Randomized transform in the same way and still have an improved accuracy.

In the same way that the Randomized Hough Transform was modified to form the Hybrid Hough Transform, an attempt was made to improve the accuracy of the Bayesian Randomized estimator using a similar approach whereby a fixed grid search was incorporated with the Bayesian Randomized estimator. Fig. 14 compares the performance of this modified Bayesian estimator with the three Hough Transform variants. It is clear from this result that this approach does not lead to improved results.

It is also possible to implement uniform resampling and

Authorized licensed use limited to: Cranfield University. Downloaded on November 18, 2009 at 05:07 from IEEE Xplore. Restrictions apply.

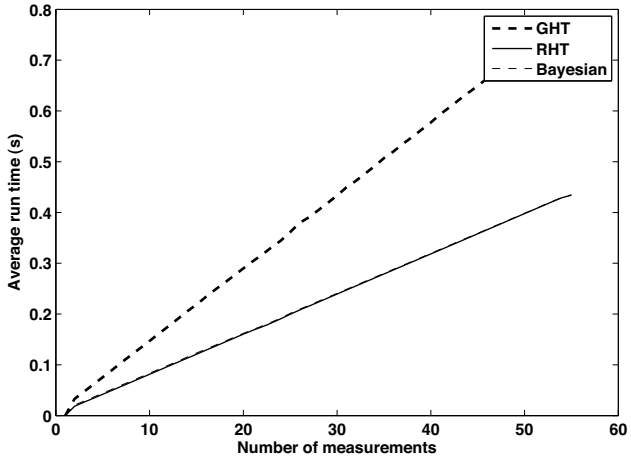

Fig. 13. Average computational time over 500 simulation runs run for the Generalized Hough Transform, Randomized Hough Transform and the Bayesian Randomized estimator

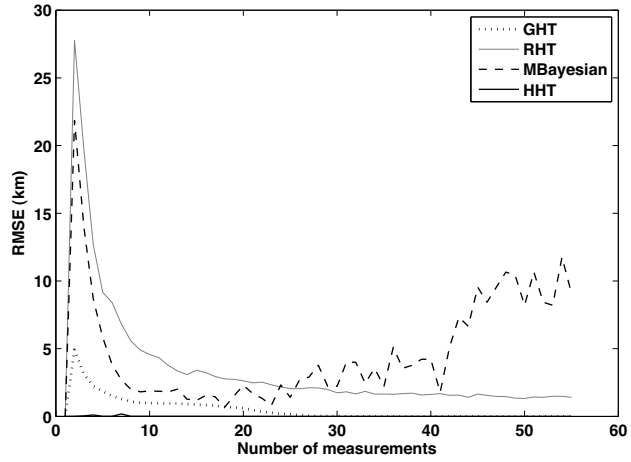

Fig. 14. Average RMS positional error obtained over 500 simulations for different number of measurements for the Generalized Hough Transform, Randomized Hough Transform, modified Bayesian Randomized estimator and the Hybrid Hough Transform

reinitialization of the parameterized space before updating it with each measurement. However it will lead to an algorithm that is very close to a particle filter, the performance of which has already been presented earlier.

V. Conclusions

In this paper we have compared five different geolocation algorithms. Three of these are based on the Hough Transform,one on the particle filter and one on the Bayesian Randomized estimator. After performing the comparisons under identical conditions, it was found that whilst all five estimators were able to geolocate the target successfully, there were important tradeoffs between the positional accuracy of the estimate and the computational overhead such that the choice of the estimator may depend entirely on the application rather than whether one estimator is more 'accurate' than another. In attempting to reduce the computational overhead of the Generalized Hough Transform, the performance of the Randomized Hough Transform has been obtained. Whilst it is seen that the RMS positional error of the Randomized Hough Transform is not as good as the Generalized Hough Transform, the reduction in computational overhead is substantial. The Hybrid Hough transform, provides an excellent compromise that results in an RMS error performance that is indistinguishable from the Generalized Hough Transform, for a computational overhead that is marginally worse that the Randomized Hough Transform.

It was identified that there are many structural similarities between the Randomized Hough Transform and the particle filter, except that the latter uses a Bayesian approach and the former is non-Bayesian. After examining these results, it is clear that a non-Bayesian approach to emitter geolocation using the Generalized or Hybrid Hough Transform is superior to the two Bayesian estimators. For the case of the Bayesian Randomized estimator, in particular, and the particle filter to a lesser extent, it was observed that after a critical number of measurements had been input into the estimator, the average RMS positional error starts to grow, which is not observed for any of the Hough Transform estimators.

References

[1] R. A. Poisel. *Electronic Warfare Target Location Methods*. Artech House Inc, Norwood MA, 2005.

[2] D. J. Torrieri. Statistical theory of passive location systems. *IEEE Trans. on Aerospace and Electronic Systems*, 2:183–198, 1984.

[3] K. F. McDonald and W. S. Kuklinski. Track maintenance and positional estimation via ground moving target indicator and geolocation data fusion. *Proc. of the IEEE Radar Conference*, pages 239–245, 2001.

[4] Elaesser D. S and R. G. Brown. The discrete probability density method for emitter geolocation. *Ottawa Technical Memorandum, Defence Research and Development Canada*, page June 2003, 2003-068.

[5] A. Mikhalev and R.F. Ormondroyd. UAV-based Non-line-of-sight geolocation of emitter. *Proc. 21 International UAV Systems Conference*, pages 25.1–25.9, April 2006.

[6] A. Mikhalev and R.F. Ormondroyd. Fusion of Sensor Data for Source Localization using the Hough Transform. *Proc. The 9th International Conference on Information Fusion*, page paper266, July 2006.

[7] N. de Freitas A. Doucet and N. Gordon, editors. *Sequential Monte Carlo Methods in Practice*. Statisitics for Engineering and Information Science. Springer-Verlag, New York, 2001.

[8] T. Bailey. Tim Bailey Source Code. http://www.acfr.usyd.edu.au/homepages/academic/tbailey/.

[9] D. H. Ballard. Generalizing the Hough Transform to detect arbitrary shapes. *Pattern Recognition*, 13(2):111–122, 1981.

[10] K. M. Alexiev and L. V. Bojilov. A Hough Transform track initiation algorithm for multiple passive sensors. *Proc. FUSION'2000*, 1:TUB2/11 – TUB2/16, 2000.

[11] R. H. T Chan and P. K. S. Tam. A new Hough Transform based position estimation algorithm. *IEEE Proc. Australian and New Zealand Conference on Intelligent Information Systems*, pages 140–144, 1994.

[12] P. V. C. Hough. Method and means for recognizing complex patterns. *US Patent 3069654*, 1962.

[13] R. G. Wiley. *Electronic Intelligence: the interception of radar signals*. Artech House Inc, Norwood MA, 1985.

[14] M. Atiquzzaman. Multiresolution Hough transform - An efficient method of detecting patterns in images. *IEEE Transactions on Pattern Analysis and Machine Intel ligence*, 14(11):109010951095 1992.

[15] F. Gustafsson and F. Gunnarsson. Positioning using time-difference of arrival measurements. *Proc. ICASSP 2003*, 6:VI–553 –556, 2003.

Authorized licensed use limited to: Cranfield University. Downloaded on November 18, 2009 at 05:07 from IEEE Xplore. Restrictions apply.

Fusion of Sensor Data for Source Localization using the Hough Transform

A. Mikhalev and R. F. Ormondroyd
Department of Aerospace, Power and Sensors
Cranfield University, The Defence Academy,
Shrivenham, Swindon, SN6 8LA, UK,
a.mikhalev@cranfield.ac.uk r.f.ormondroyd@cranfield.ac.uk

Abstract - ***This paper describes a novel source localization algorithm based on the Hough Transform that allows different types of sensor data, such as angle of arrival and time difference of arrival data to be fused together by means of a transformation into a consistent parameterized space. A particular advantage of this method is that terrain data can also be fused with the various types of sensor data to aid accurate source localization.****

Keywords: Emitter localization, data fusion, position estimation, Generalized Hough Transform.

1 Introduction

Source localization of radio frequency (RF) emitters is of vital importance in both civilian and military applications. Traditional methods of passive RF source localization are often based on geometrical techniques such as triangulation and hyperbolic location [1]. Recently, a number of statistical methods have been proposed that fuse several types of sensor data to provide improved accuracy. These include the use of the least mean squares estimator (LMS) [2], the discrete probability density function method [3], the likelihood method [4] and the particle filter [5].

The Generalized Hough Transform [6] is an image processing technique for arbitrary shape detection and Alexiev and Bojilov [7] have proposed it for the elimination of ghost detections in target tracking using multi-sensor data fusion. Others [8] have used it for self-positioning of robots using map matching. Here, we propose the novel application of the generalized Hough Transform to the task of source localization.

2 Adaptation of the Generalized Hough Transform for Source Localization

The Hough Transform was patented in 1962 [9] as a mathematical transformation of points from the input space, referred to as the feature space (FS), into curves in parameter space (PS) that can be used for the detection of geometric patterns. This method is based on the fact that all points from a straight line (say) positioned in FS can be mapped to a single point in PS.

Let our sets of hypotheses exist in some coordinate framework (an N-dimensional array). An event can occur within this coordinate system and can indicate with its conditional probabilities a set of hypotheses whose parameters are fixed relative to the event. The conditional probability table of the event can then also be considered as an N-dimensional array centered on the event, where N is the dimensionality of the hypothesis space. This array is called the *voting array* for the event. It contains the logs of the normalized conditional probabilities and so each event will simply add its own voting array into the accumulator representing the hypothesis space.

Imagine that the hypothesis space is a particular point located in two dimensions. In this case, the hypothesis space is then a 2D array of numbers representing the conditional probability of the event. In this application, the events that are of interest are the observations (i.e. the measurements of the parameters of the source). Associated with each measurement is a probability that the source is located at a particular point (x, y) within the search space. This is equivalent to assigning the event to a particular part of the hypothesis space. We can obtain the conditional probability voting array for each measurement by placing the source into each position in turn and calculating the conditional probability and adding these values to the voting array. This approach is described for two different measurement techniques in the following sections.

2.1 Angle of arrival measurements

Consider a 2D scenario, with M receivers (that may be mobile) and one stationary radio source. Assume that the receivers can obtain the Angle of Arrival (AOA) of the source emission using an antenna array and also assume that the measurement errors in the AOA are Gaussian (although other distributions can be accommodated easily). The voting function can be defined in terms of the conditional probability density function (pdf), $p(x, y|\theta_i)$, of the source being located at

*This work was funded by General Dynamics through DTC DIF Project 12.3.2

Authorized licensed use limited to: Cranfield University. Downloaded on November 18, 2009 at 05:07 from IEEE Xplore. Restrictions apply.

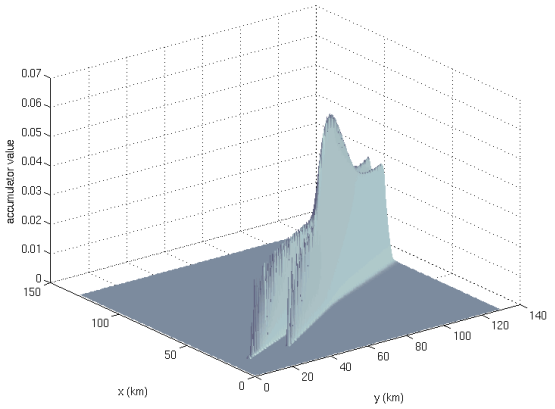

Figure 1: HT space for AOA-only measurements

some point (x, y) within the search space given the measurement θ_i. This conditional probability for the AOA measurements has the form:

$$p(x, y|\theta_i) = \frac{\exp\left(\frac{(\xi-\theta_i)^2}{2\sigma_{\theta_i}^2}\right)}{\sqrt{2\pi}\sigma_{\theta_i}} \quad (1)$$

where θ_i is the measured angle at the ith receiver and ξ is the calculated angle from the ith receiver at point (x_{r_i}, y_{r_i}) to the point (x, y). σ_{θ_i} defines the standard deviation of the AOA measurement error for that receiver.

Although the point (x, y) could lie anywhere within the search space, in practice, the search space is split into a regular grid and (x, y) is constrained to lie at one of the grid points and (1) is evaluated at each of these grid points. Assuming that multiple measurements are made at each receiver, in the usual way, the pdf is evaluated for each measurement for all receivers. In this method, the pdfs due to each measurement are accumulated as follows:

$$A_{AOA}(x, y) = \frac{1}{M}\sum_{m=1}^{M} p(x, y|\theta_m) \quad (2)$$

where M represents the total number of measurements made. This accumulated pdf now represents the voting array for the Hough Transform. As an example, consider two stationary receivers located at (20km,10km) and (20km,30km) respectively and a single source located at (60km,80km). At each receiver, a single AOA measurement was taken and the standard deviation of each measurement due to the effect of receiver noise was taken as $\sigma_\theta = 0.02$ radians. The corresponding Hough Transform space for these AOA measurements is shown in Fig. 1. The maximum of the Hough Transform space corresponds to the estimated position of the source. The localization error using this method is discussed in Section 4.

Within the context of the Hough Transform, the combination of many weak constraints has generated a stronger constraint, represented by the peak in the hypotheses space. The degree of constraint contributed by an event (measurement) depends on how many different hypotheses it votes for (its specificity). For example, if the event's voting array consisted of sharp peaks then this would correspond to a strong constraint. However, if the voting array is completely uniform, corresponding to event voting equality for all hypotheses, then it offers no constraint at all.

2.2 Time difference of arrival measurements

The following illustrates the method for the case of source localization using time difference of arrival (TDOA). Assume that we can obtain the TDOA between two spatially separated receivers (using signal cross correlation or other delay estimation technique, for example). Referring all TDOAs to the first receiver, which is assumed to be the first to receive the transmitted signal, let the index $i = 2, 3, ..., M$ unless otherwise specified, (x, y) be the source location and (x_{r_i}, y_{r_i}) be the known location of the ith receiver. The range of the source to the ith receiver is:

$$R_i = \sqrt{(x_{r_i} - x)^2 + (y_{r_i} - y)^2} \quad (3)$$

and the range difference between receiver R_i and receiver R_1 is:

$$\begin{aligned} c\tau_{i,1} &= R_i - R_1 \\ &= \sqrt{(x_{r_i} - x)^2 + (y_{r_i} - y)^2} \\ &\quad -\sqrt{(x_{r_1} - x)^2 + (y_{r_1} - y)^2} \end{aligned} \quad (4)$$

where, $\tau_{i,1}$ is the measured TDOA between the ith receiver and receiver 1 and c is the velocity of light.

The pdf of the source location for this case is given by:

$$p(x, y|\tau_{i,1}) = \frac{\exp\left(\frac{R_{i,1}^2 - c^2\tau_{i,1}^2}{2\sigma_r^2}\right)}{\sqrt{2\pi}\sigma_r} \quad (5)$$

where $R_{i,1}$ is the difference between the range of a particular point on the grid to receiver 1 and the range from the same grid point to receiver i, σ_r is the range error for this measurement. The range error is dependent upon the error in the time difference of arrival measurement, σ_{TDOA}, *and* the geometric dilution of precision (GDOP). According to [10] the range error for a single TDOA measurement is given by:

$$\sigma_r = \frac{c\sigma_{TDOA}}{2sin(\frac{\Theta}{2})} \quad (6)$$

where the numerator represents the timing measurement error and the denominator is the GDOP. Θ is the angle subtended between the two lines of position from receiver 1 to the source and receiver i to the source, respectively. There are a number of different theoretical approximations for σ_{TDOA} depending upon the assumptions made regarding the SNR of the received signal [1]. For good SNR conditions it is common to assume that the standard deviation of the timing error is given by:

$$\sigma_{TDOA} \approx \frac{1}{W\sqrt{\text{SNR}}} \quad (7)$$

Authorized licensed use limited to: Cranfield University. Downloaded on November 18, 2009 at 05:07 from IEEE Xplore. Restrictions apply.

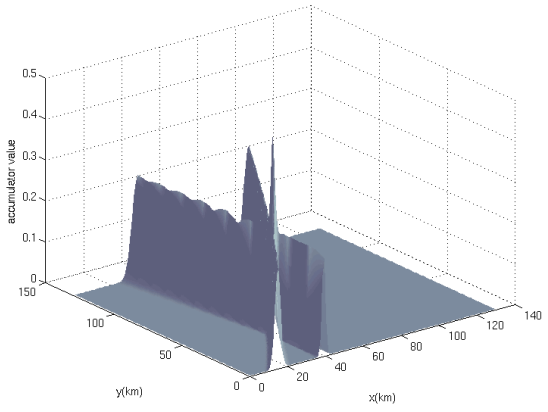

Figure 2: HT Space for TDOA-only measurements

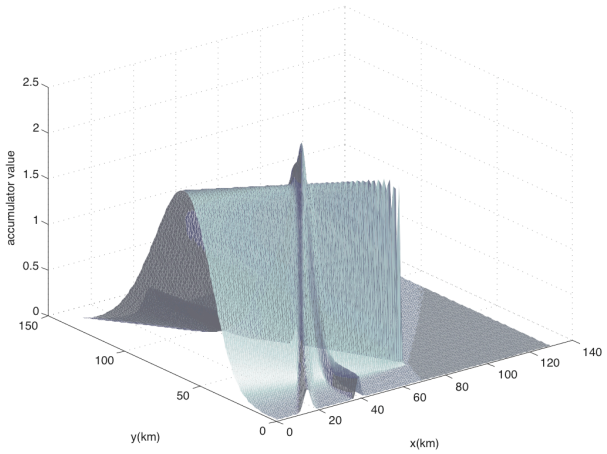

Figure 3: HT space for fusion of AOA with TDOA measurements

where W is the noise bandwidth of the receiver, whereas for low SNR the achievable timing error is often given by [11]:

$$\sigma_{TDOA} \geq \sqrt{\frac{3}{8\pi^2 T}} \frac{1}{\text{SNR}} \frac{1}{\sqrt{f_2^3 - f_1^3}} \tag{8}$$

where T is the integration time used in the receiver and $W = f_2 - f_1$. Using, for the sake of example, the high SNR case given by (7), the range error becomes:

$$\sigma_r = \frac{c}{2W sin(\frac{\Theta}{2})\sqrt{\text{SNR}}} \tag{9}$$

Using the conditional pdf (5), the voting array can be built, as per the earlier case for the AOA measurements (2) using:

$$A_{TDOA}(x,y) = \frac{1}{L} \sum_{l=1}^{L} p(x,y|\tau_{l,1}) \tag{10}$$

where L represents the number of TDOA measurements taken from the M receivers.

As an example, consider the case of source localization using three stationary receivers. These are located at: (20km, 10km), (20km, 75km), (60km, 10km). The source is located at (40km, 40km). In the simulation, it is assumed that the bandwidth of the received signal is $W = 1$ MHz and the SNR +3dB, leading to a value for $\sigma_{TDOA} = 7 \times 10^{-7}$s. Only two TDOA measurements are taken - between receiver 1 and receiver 2 and receiver 1 and receiver 3. The resulting Hough Transform space due purely to the provided TDOA information is shown in Fig. 2. Again, the dominant peak in the Hough Transform space denotes the likely source position.

2.3 Fusion of AOA with TDOA Measurements

Because the sensor data has been transformed into conditional probabilities and are now in a unified parameterized space, irrespective of the type of measurement, it is possible to merge the TDOA sensor data with the AOA sensor data.

$$A(x,y) = \frac{1}{M} \sum_{m=1}^{M} p(x,y|\theta_m) + \frac{1}{L} \sum_{l=1}^{L} p(x,y|\tau_{l,1}) \tag{11}$$

The results of fusing the two TDOA measurements described in the previous section with one AOA measurement from the receiver at (20km, 75km) are shown in Fig. 3. The standard deviation of the TDOA measurement error in this simulation is set at $\sigma_{TDOA} = 7 \times 10^{-7}$s and the standard deviation of the AOA error is set at a realistic value of $\pi/16$ radians. The strong single peak in the Hough transform space, coincides with the maximum likelihood of the source position and it is clear how the additional AOA data has provided further information to improve the accuracy of localizing the source position.

2.4 Fusion of sensor data with terrain data

The new HT method is also very convenient for adding terrain data. In this case, the terrain data is first processed to give a first order likelihood that the emitter can be located at a particular map reference on the basis of *a priori* knowledge. This terrain-based likelihood map is then transformed into the Hough transform space where is is merged with the Hough transforms due to TDOA data and the AOA data. For example, in Fig. 4 the likelihood that our target is *not* likely at a particular point on the map is shown as the darkened areas. The influence of this additional information on the Hough Transform space, and hence the likelihood of location the emitter is shown in Fig. 5

3 Complexity Reduction of the Hough Transform

The complexity of the Hough transform depends on the grid size and is of order $(n \times m)$ where n and m are the grid dimensions. However, it is possible to

Authorized licensed use limited to: Cranfield University. Downloaded on November 18, 2009 at 05:07 from IEEE Xplore. Restrictions apply.

Figure 4: Illustration of map data showing regions where the source is unlikely to be (increasing level of grey)

perform a real-time Hough transform using real-time content addressable memory [12] or to use optimized Hough Transform algorithms, such as the Randomized Generalized Hough Transform [13]. It is also possible to reduce the computational load by dividing the parameterized space into overlapping 'tiles' that provides a multi-resolution Hough transform [14], and this approach was used here. In this method, the parameterized space is first divided into a coarse grid and the likelihood function is evaluated for this grid. The maximum for this coarse grid is then obtained and this is used to refine the search space to a region of 2×2 tiles centered on the tile containing the maximum. This ensures that the new search space overlaps the neighbouring tiles of the previous search and still contains the wanted maximum when subject to a higher resolution search. For this new search space, the grid size is refined to provide a much higher resolution. Clearly, this method can be iterated several times, achieving progressively higher spatial resolution at each stage. For example, if the original parameterized space had an $n \times n$ grid, the computational complexity of calculating the likelihood is $O(n^2)$ for the standard Hough transform. However, for the multi-resolution Hough Transform, let the number of grid points for the first iteration be scaled down by a factor of p. In this case, the

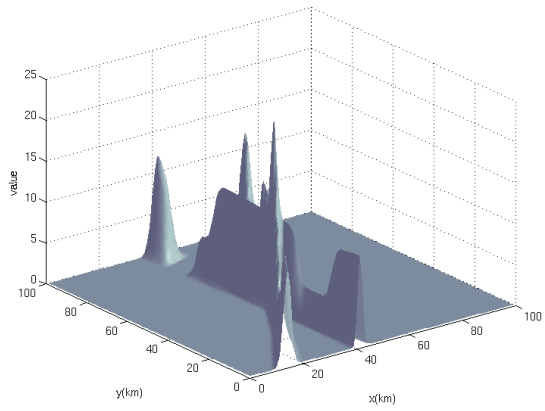

Figure 5: Fusion of TDOA data with map data

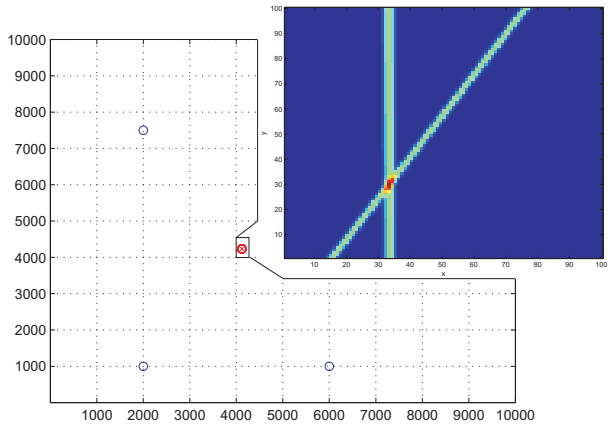

Figure 6: An example of the use of the Multi-resolution HT for emitter localization using TDOA measurements

order of complexity for the first iteration is $O\left(\frac{n\times n}{p}\right)$, whilst the order of complexity for the second iteration $O\left(4\frac{n\times n}{p}\right)$, where in this case, the factor four arises because for the second iteration we choose a total of four tiles centered on the peak obtained from the first iteration. Consequently, for just two iterations, the overall order of complexity is $O\left(\left(\frac{n\times n}{p}\right)+\left(4\frac{n\times n}{p}\right)\right)$ for the same overall resolution.

An example of the use of the multi-resolution Hough transform method is shown in Fig. 6. In this case, the source is located at (4.13km, 4.13km) (marked with a cross) within a search space of (10km, 10km) and the platforms are located at (1km, 2km), (1km, 6km) and (2km, 7.5km) (marked with circles). The number of grid points used for the first iteration was 100×100 (i.e 10,000 tiles with a separation between grid points of 0.1km). For the second iteration, an area equivalent to 2×2 tiles centered on the grid with the maximum in the accumulator was used, and each tile was split into 100×100 grid points (corresponding to a separation between grid points of 1m).

4 Comparison with CRLB

The Cramer-Rao inequality sets a lower bound for the variance of any unbiased parameter estimations. Hence it is of interest to compare the performance of the Hough Transform algorithm with the optimum. Here, one of the forms of the CRLB derived in [15] is used:

$$tr(J^{-1}) = (c\sigma_{TDOA})^2 tr\left[(GG^T)^{-1}\right] \qquad (12)$$

where

$$\begin{aligned} G &= \nabla R_{ij}^T = [\bar{g_{ij}}.....], \\ \bar{g_{ij}} &= \bar{g}_i - \bar{g}_j, \\ \bar{g}_i &= \underline{\nabla} R_i(\bar{p}) = \frac{\bar{p}-\bar{q}_i}{||\bar{p}-\bar{q}_i||} \end{aligned}$$

Here, $\bar{p}$ represents source coordinates in vector form and $\bar{q}_i$ represents the coordinate vector of the ith receiver. Clearly, $\bar{g}_i$ is a unit length vector with $||\bar{g}_i|| = 1$.

Authorized licensed use limited to: Cranfield University. Downloaded on November 18, 2009 at 05:07 from IEEE Xplore. Restrictions apply.

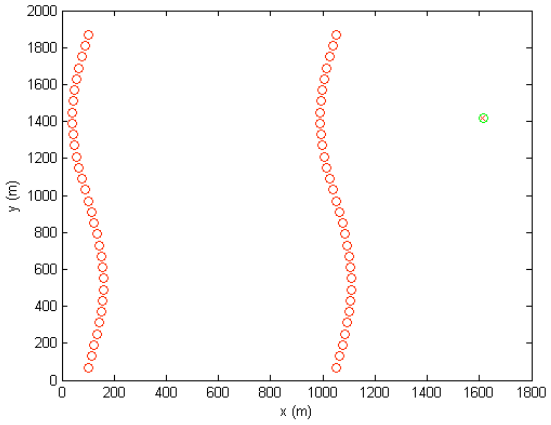

Figure 7: Moving platform scenario

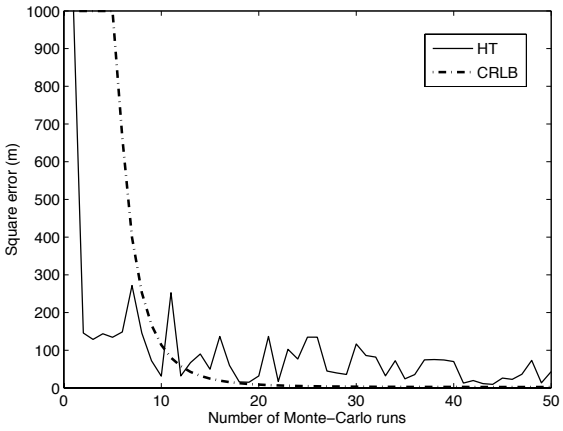

Figure 8: RMS error performance for moving platform scenario of Fig. 7 as a function of the number of measurements taken compared with the corresponding CRLB

It points from receiver i to the emitter. G depends on: (i) the source position (ii) receiver position and (iii) the set of receiver pairs which are used for source localization.

The scenario that is used here to compare the performance relative to the CRLB is one where two mobile receivers are used to geolocate a fixed target using TDOA. Fig. 7 shows the simulation scenario in which the source is denoted as a cross at (1900m, 1400m), and the two platforms (moving with a wavy path) are denoted as circles. Measurements are taken every second for 50 seconds. The speed of the platforms is 60m/s. The standard deviation of the measurement error is $\sigma_{TDOA} = 7.4\times10^{-9}$ s. The circle surrounding the cross represents the estimate of the source position after 30 measurements using the Hough Transform. Figure 8 compares the average rms error of the Hough transform method with the CRLB, as measurement data is accumulated along the flight path. In this case, the rms error was averaged over 20 independent runs. It is clear that the Hough Transform method comes quite close to the CRLB for this scenario. However, it will be realized that both the CRLB and the average rms error obtained using the Hough Transform depend quite critically upon the scenario used.

5 Conclusion

A new source localization algorithm based on the Hough Transform has been presented. It has the following advantages over traditional estimator algorithms: (i) the algorithm does not require an initial guess of the emitter position, (ii) it is easy to fuse data from different sensors, (iii) terrain data can be incorporated with the sensor data, (iv) the method can have a flexible error model (e.g. the error model may be Gaussian or other distribution), (v) it is robust. The results have shown that this new approach provide average rms errors that are close to the CRLB.

References

[1] R. A. Poisel. *Electronic Warfare Target Location Methods*. Artech House Inc, Norwood MA, 2005.

[2] K. F. McDonald and W. S. Kuklinski. Track maintenance and positional estimation via ground moving target indicator and geolocation data fusion. *Proc. of the IEEE Radar Conference*, pages 239–245, 2001.

[3] Elaesser D. S and R. G. Brown. The discrete probability density method for emitter geolocation. *Ottawa Technical Memorandum, Defence Research and Development Canada*, page June 2003, 2003-068.

[4] P. J. D. Gething. *Radio Direction Finding and Superresolution*. Peter Peregrinus Ltd, 1978.

[5] F. Gustafsson and F. Gunnarsson. Positioning using time-difference of arrival measurements. *Proc. ICASSP 2003*, 6:VI–553 –556, 2003.

[6] D. H. Ballard. Generalizing the Hough Transform to detect arbitrary shapes. *Pattern Recognition*, 13(2):111–122, 1981.

[7] K. M. Alexiev and L. V. Bojilov. A Hough Transform track initiation algorithm for multiple passive sensors. *Proc. FUSION'2000*, 1:TUB2/11 – TUB2/16, 2000.

[8] R. H. T Chan and P. K. S. Tam. A new Hough Transform based position estimation algorithm. *IEEE Proc. Australian and New Zealand Conference on Intelligent Information Systems*, pages 140–144, 1994.

[9] P. V. C. Hough. Method and means for recognizing complex patterns. *US Patent 3069654*, 1962.

[10] R. G. Wiley. *Electronic Intelligence: the interception of radar signals*. Artech House Inc, Norwood MA, 1985.

Authorized licensed use limited to: Cranfield University. Downloaded on November 18, 2009 at 05:07 from IEEE Xplore. Restrictions apply.

[11] A.H. Quazi. An overview on the time delay estimate in active and passive systems for target localization. *IEEE Trans. on Acoustics, Speach and Signal Processing*, ASSP-29(3):527–533, 1981.

[12] M. Nakanishi and T. Ogura. A Real-time CAM-based Hough Transform Algorithm and its performance evaluation. *IEEE Proceedings of ICPR*, pages 516–521, 1996.

[13] W. Lee P. Fung and I. King. A Randomized Generalized Hough Transform for 2-D grayscale object detection. *IEEE Proceedings of ICPR*, 1996.

[14] M. Atiquzzaman. Multiresolution Hough transform - An efficient method of detecting patterns in images. *IEEE Transactions on Pattern Analysis and Machine Intel ligence*, 14(11):10901095 1992.

[15] B. Yang and J. Scheuing. Cramer-Rao bound and optimum sensor array for source localazation from time differences of arrival. *Proc. ICASSP 2005*, 4:961–964, 2005.

Authorized licensed use limited to: Cranfield University. Downloaded on November 18, 2009 at 05:07 from IEEE Xplore. Restrictions apply.